Magnetic Resonance Imaging of tissue microcirculation in experimental studies

Jane F. Utting

Department of Medical Physics and Bioengineering,
University College London

Submitted for the degree of Doctor of Philosophy
University of London

May 2002

ProQuest Number: U642323

All rights reserved

INFORMATION TO ALL USERS
The quality of this reproduction is dependent upon the quality of the copy submitted.

In the unlikely event that the author did not send a complete manuscript
and there are missing pages, these will be noted. Also, if material had to be removed,
a note will indicate the deletion.

ProQuest U642323

Published by ProQuest LLC(2015). Copyright of the Dissertation is held by the Author.

All rights reserved.
This work is protected against unauthorized copying under Title 17, United States Code.
Microform Edition © ProQuest LLC.

ProQuest LLC
789 East Eisenhower Parkway
P.O. Box 1346
Ann Arbor, MI 48106-1346

Abstract

Magnetic resonance images may be sensitised to tissue perfusion and oxygenation, providing functional information about organs in the body. These MR techniques are of great value for the assessment of ischaemic conditions, both for clinical diagnosis and to investigate disease processes in animal models. Perfusion may be studied completely non-invasively using arterial spin labelling (ASL) to magnetically label blood. The presence of deoxyhaemoglobin (dHb) influences spin-spin relaxation times, producing blood-oxygen-level-dependent (BOLD) contrast in images. ASL and BOLD MRI are investigated in this thesis in rat brain and liver.

Theoretical and practical aspects of labelling blood by velocity driven adiabatic fast passage (AFP) for continuous ASL (CASL) are considered. A computer model of the modified Bloch equations facilitated optimisation of velocity driven AFP under various experimental and physiological conditions in humans and animals. The computer model was extended to investigate the amplitude modulated (AM) control pulse for multiple-slice CASL. The effect of the AM control on moving spins and some of the reasons for the non-ideal performance of the technique are explained. The AM control was implemented and results in rat brain *in-vivo* demonstrate that the technique is significantly less sensitive to perfusion than the standard control technique for single slice CASL imaging. BOLD was employed in an animal model of intestinal ischaemia-reperfusion (I/R). This is a devastating condition that affects remote organs, including the liver, lungs, heart, kidney and central nervous system, and may lead to multiple-organ-dysfunction-syndrome. BOLD MRI of the liver during intestinal I/R showed that R_2* increases throughout reperfusion. This suggests that dHb accumulates in the liver, consistent with the triggering of the failure of hepatic energy metabolism by intestinal reperfusion following ischaemia.

Acknowledgements

Many people have generously shared their scientific expertise and enthusiasm with me in the course of completing this work. I should like to thank my principle supervisor Roger Ordidge, who gave me the opportunity to be involved in this exciting field at UCL and my second supervisor David Gadian, who allowed me to work in his laboratory at the Institute of Child Health. I have been privileged to have such thoughtful and thought-provoking colleagues as David Thomas and Paisarn Vejchapipat, who have been of great assistance throughout. I also thank Gaby Pell, Robert Helliar, Martin King, Fernanado Calamante, Sue Williams, Mark Lythgoe, Edward Proctor, Quyen Nguyen, Enrico DeVita, Neil Harris and Dan West for their invaluable contributions. I am grateful for the support and encouragement of all my colleagues, especially Sally Dowsett, Sati Sahota, Jo Perthen, Donald Tournier, John Thornton and Marzena Arridge.

Friends and family make everything possible and special thanks must go to my Mum for her support and genuine interest in everything I do, as well as to my Dad and Hugh. Thanks to all my friends, near and far, for all moral and practical support, and in particular to Anand Madhvani, Sue Williams and Faye Jones, who have enriched these years enormously.

Contents

1 Introduction

2 Magnetic Resonance Imaging

3 Computer modelling of velocity driven adiabatic fast passage for continuous arterial spin labelling

3.2 Theory

3.3 Method

3.4 Results

3.5 Discussion

4 Computer modelling of the amplitude modulated control for multiple-slice continuous arterial spin labelling

4.4 Results

5 Implementation of amplitude modulated control for multiple-slice continuous arterial spin labelling

6 MRI of liver during intestinal ischaemia-reperfusion

6.2 Methods

6.3 Results

7 Final discussion and future work

Appendices

Figures

Tables

1 Introduction

Twenty first century scientists would agree with much in the description of the role of the blood and its circulation given by Thomas Willis in 1684:

> "the offices of the blood" "are divers and manifold, viz. to instil matter in the Brain and nervous stock for the animal Spirits, to dispense the nutritious Juyce into all the solid parts, to suggest to the motive parts an elastic Copula, and besides to separate all recrements and worn out Particles, and to put them aside into convenient Emuntories."
>
> "[the blood's] undiscontinued motion is required both for the conservation of the disposition of the blood itself, whole liquor would otherwise be subject to stagnation and putrefaction, as also that being carried about in the whole body, it might be able to give a due tribute to all parts."

Willis relied on anatomical observations to infer the functions of the blood (Willis T 1684). Two centuries were to pass before it was possible to monitor the movement of blood in organs, and a further century before perfusion imaging in humans became a standard tool for clinical diagnosis.

In this thesis magnetic resonance techniques for imaging perfusion and oxygenation are investigated. The sensitivity of perfusion imaging by continuous arterial spin labelling (CASL) to microvascular flow was studied, both theoretically and experimentally in rat brain *in-vivo*. In a separate set of experiments oxygenation changes in the liver resulting from intestinal ischaemia-reperfusion (I/R) were monitored in a rat model, using magnetic resonance imaging (MRI) with blood-oxygen-level-dependent (BOLD) contrast.

In this chapter MRI techniques that are sensitive to perfusion and oxygenation are introduced and the advantages and disadvantages of these methods are highlighted in relation to alternative techniques. Then the motivations for the work described in subsequent chapters are discussed. The theoretical bases of perfusion and BOLD contrast are introduced in Chapter 2.

The delivery and utilisation of oxygen may be considered in three stages. Firstly, oxygen is carried by the bulk flow of blood from the heart through the arterial system to every tissue and organ in the body. Secondly, oxygen is delivered to capillary exchange sites as blood perfuses organs and tissues. Finally, oxygen enters tissues and is metabolised. Each of these stages is vital for normal cellular function and ultimately for the survival of cells. Imaging of bulk flow may be performed by angiography: plane-film x-ray, computed tomography (CT), Doppler ultrasound or magnetic resonance angiography (MRA). The second and third stages of oxygen delivery and utilisation, and MR techniques to image these processes are considered in this thesis.

1.1 Magnetic Resonance Imaging

MRI developed in the 1970s after Paul Lauterbur recognised the possibility of discriminating between magnetic nuclei at different positions in a sample by applying magnetic field gradients (Lauterbur P 1973). It was first applied in clinical practice only two decades ago, but since then MRI has become established as an important tool for clinical and experimental investigations of some of the most serious medical conditions, including stroke and cancer.

MRI may be employed to visualise function in addition to anatomy, mainly through diffusion- and perfusion- weighted imaging and BOLD contrast. In ischaemic disease, the combination of diffusion- and perfusion- weighted MRI has the potential to discriminate between infarcted tissue and salvageable tissue that is suffering from vascular insufficiency but has not proceeded to infarction (Østergaard L et al. 2000; van Dorsten FA et al. 2002). Diffusion weighted imaging highlights changes that are indicative of abnormal cell energy metabolism (Busza AL et al. 1992). However, once ischaemia is sufficiently severe to change cellular energy metabolism, it is often too late for intervention to save the tissue. Earlier identification of tissue that is at risk may be provided in perfusion-weighted or BOLD contrast images.

BOLD contrast is best known in the context of brain imaging, where it is employed either to identify areas of the brain that are activated during a particular cognitive task (Dijkhuizen RM et al. 2001; Holloway V et al. 2000) or to map cerebrovascular reserve (Harris NG et al. 2001; Ono Y et al. 1997). However it has also been used in studies of other organs, including kidney (Prasad PV et al. 1996).

1.2 Historical perspective on perfusion imaging

Definitions of perfusion include:

"*Surgery*. 1. the passage of a liquid over or through an organ or tissue." (Academic Press Dictionary of Science and Technology)

"The act of pouring over or through, especially the passage of a fluid through the vessels of a specific organ." (Online dictionary of cancerweb@www.graylab.ac.uk).

Perfusion is blood flow within an organ, at the capillary level. The distribution of this microvascular flow may change in pathological states. Therefore the measurement of perfusion is an invaluable diagnostic tool for diseases of the circulation. In addition to clinical applications, perfusion measurements have an important role in experimental models of disease to identify pathophysiological changes in tissue and inform proposed treatment strategies.

There are several factors that affect the choice of technique for measuring perfusion. Is perfusion of the whole organ, or regional perfusion of interest? What degree of spatial localisation is necessary or desirable? Are multiple measurements required (for example in a time series study)? How long may a single measurement take? Is an invasive technique acceptable? And if so, how invasive? Is absolute quantification required, or is a relative measure adequate? The availability and cost of different methods are also important considerations. A brief history of developments in perfusion imaging serves as an introduction to the techniques that are currently available.

The earliest studies of perfusion were performed by highly invasive techniques requiring, for example, insertion of electromagnetic flow probes into blood vessels (Rein H 1929) or insertion of cooled thermocouples directly into tissue (Schmidt CF and Pierson JC 1934), or even drainage of cerebrospinal fluid and the application of a pressure cuff around the neck (Ferris EB 1941). Electromagnetic flow probes may be employed today to measure bulk flow or whole organ perfusion, especially in experimental studies in animal models (for example Horn EP et al. 1997; Majid DS et al. 1997), but they do not provide regional information. Thermocouples are also employed for specific applications (Thome C et al. 2001; Klar E et al. 1999), but they measure perfusion within a very localised region and other approaches are more common.

The first quantitative measurements of cerebral blood flow (CBF) in humans yielded values for whole brain perfusion (Kety S. and Schmidt CJ.1945). Kety and Schmidt introduced nitrous oxide (N_2O) as a tracer by inhalation, and measured concentrations of N_2O in the jugular vein and femoral artery. They calculated the total flow of blood through the whole brain by adapting the Fick Principle (originally devised for oxygen passing through the lungs (Fick A 1870)).

These whole organ measurements yielded no information on the distribution of blood flow within the brain. Then in 1955 Landau et al. used autoradiography to measure regional CBF in cat brain (Landau WH et al. 1955). For autoradiography, the distribution of a radioactive tracer (e.g. ^{99m}Tc or ^{14}C) is imaged by sacrificing the animal, slicing the brain immediately and placing the slices onto x-ray film. Autoradiography has the highest spatial resolution of any perfusion imaging technique, limited only by the resolution of the x-ray film. However, it yields only a single time point per animal after slicing the brain.

Radio-labelled microspheres were first employed in 1967 to study foetal circulation (Rudolph AM and Heyman MA 1967). The microspheres become trapped in capillaries, and after appropriate correction for radioactive decay, the quantity and distribution of blood in the microcirculation may be quantified. Microspheres may be introduced into the circulation repeatedly (four or six times), using different isotopes to distinguish separate time points in a single animal (Capuro NL et al. 1979).

Regional measurements of flow by autoradiography or the use of radioactive microspheres necessitate destruction of the sample. A different approach is required for regional measurements in humans, and in 1961 Ingvar and Lassen made quantitative measurements of regional CBF (rCBF) in a patient undergoing craniotomy to remove a tumour. They made a cranial window out of glass, through which β emissions from ^{85}Kr were detected from one section of the cortex (Ingvar DH and Lassen NA.1961).

Measurement of regional perfusion within whole organs became possible with the development of external monitoring techniques to map distributions of γ-emitting radioisotopes (for example Mallett B.L. and Veall N.1963; Conn HL.1955). Blood tracers may be introduced by intra-arterial injection, permitting detection of flow in the territory of a single artery or by inhalation of a radioactive gas, which produces signal from every perfused tissue in the body.

Computed tomography offers better spatial specificity than planar imaging, as demonstrated by Fazio et al. (Fazio F et al. 1979). Emission scans may detect either single γ-emissions or the coincident photons resulting from positron annihilation. These approaches form the basis of single photon emission tomography (SPECT) and positron emission tomography (PET) respectively. The recorded radioactivity in the body must be calibrated against the activity in samples of arterial blood drawn during the measurement. PET also offers information on haemodynamic or metabolic function through images of local blood volume, oxygen and glucose consumption, using different radio-labelled pharmaceuticals.

The development of transmission CT led to the introduction of Xe-enhanced CT perfusion mapping, which exploits the high atomic number of Xe to show the distribution of perfusion after inhalation of Xe gas (for example Drayer BP et al. 1978). Xe CT also provides anatomical information, which is not obtained in SPECT and PET.

Although transmission CT, SPECT and PET are tolerated by many patients, each carries the risks associated with the use of ionising radiation. MRI, on the other hand, does not employ ionising radiation and offers equivalent or better spatial resolution. The first MRI technique to measure microvascular blood flow employed a paramagnetic contrast agent as a blood tracer (Villringer A et al. 1988). The magnetic susceptibility difference generated by the contrast agent resulted in rapid loss of phase coherence and reduced T_2 as blood passed through microvessels in tissue. Regional blood flow may be calculated by tracking the passage of the bolus through tissue.

Arterial spin labelling (ASL) is an alternative MRI technique, in which ^{1}H nuclei in water in blood are magnetically labelled before they enter tissue (Williams DS et al. 1992). For ASL, endogenous water is the tracer, and hence this approach is completely non-invasive. The rapid clearance of labelled blood also permits repeated measurements within a few seconds.

Other techniques to detect regional blood flow include hydrogen clearance, Laser Doppler, confocal microscopy, optical imaging and near–infrared spectroscopy (NIRS). All of these methods give information on only a localised region of tissue (although a tomographic approach for NIRS is under development (Hillman EM et al. 2001)). Therefore, at present CT, SPECT, PET and MRI are the only techniques employed in standard clinical practice to image the distribution of regional blood flow. MRI is the only one that does not employ ionising radiation and ASL MRI is the only one that does not require an exogenous contrast agent.

1.2.1 Perfusion imaging studies in this thesis

The sensitivity of ASL is inherently low because protons in blood constitute only a few percent of the total number of protons that produce signal in an MR image. Maximising the sensitivity of perfusion measurements is critical to the efficacy of the technique, especially in the study of pathology associated with low perfusion, or when trying to detect small changes in regional blood flow. The focus of Chapters 3, 4 and 5 is on the process of velocity driven adiabatic fast passage (AFP) to magnetically label ^{1}H spins for continuous ASL (CASL) (see Chapter 2 for a description of the theory).

In Chapter 3 a thorough investigation of several factors that determine the sensitivity of CASL is presented, using a computer model of velocity driven AFP.

For multiple-slice CASL the labelling process must be modified and the most widely used approach is the amplitude modulated (AM) control (Alsop DC and Detre JA.1998). The advantage of multiple-slice perfusion images is offset by the disadvantage of a smaller flow-dependent signal with the AM control. In Chapter 4 a computer modelling study is presented in which the causes of the relative insensitivity of multiple-slice ASL using the AM control are explored.

In Chapter 5 an experimental evaluation of CASL imaging with the AM control is described. The three sets of investigations were designed to: 1) verify the absence of apparently flow-dependent signal in samples of meat; 2) demonstrate the efficacy of multiple-slice CASL images in rat brain, *in-vivo* with the AM control, and 3) compare the flow-sensitivity of single-slice and multiple-slice versions of CASL.

1.3 Blood-Oxygen-Level-Dependent (BOLD) MRI

The vast majority of oxygen in blood is contained in haemoglobin (Hb), within red cells. Typically, 19.4 ml of oxygen is bound to Hb, whereas only 0.39 ml of oxygen is dissolved in plasma per 100 ml of arterial blood (Harper HA.1971). Fully oxygenated Hb is carried to tissues, where the relatively low partial pressure of oxygen causes the Hb to release oxygen and become deoxygenated Hb (dHb). The amount of dHb present in the microvasculature is determined by the oxygenation of the blood delivered and local oxidative metabolism.

dHb is paramagnetic and within the static magnetic field of the MRI scanner, it sets up local magnetic field gradients in tissue. The presence of these gradients increases the transverse relaxation rates R_2 and R_2*, producing blood-oxygen-level-dependent (BOLD) contrast. Subject to appropriate calibration, it is possible that BOLD may provide a quantifiable means of sensitising images to oxidative metabolism and a means for quantifying changes in the rate of oxygen consumption (Davis TL et al. 1998; Hoge RD et al. 1999).

There is a range of other techniques for measuring oxygenation, including measurements of arterial and venous blood gases, pulse oximetry, NIRS, tonometry and PET. Pulse oximetry and blood gas measurements are employed as indicators of oxygenation in a whole organ, or systemically. NIRS makes local measurements, but calibration must be performed against a state with zero blood oxygen saturation and complicated analysis is required to calculate concentrations of Hb and dHb. Tonometry has uses only for specific applications in the lumen of the stomach or colon.

PET is employed to monitor the regional uptake of positron emitting $^{15}O_2$, from which regional rates of oxygen consumption may be calculated (Frackowiak RS et al. 1980; Ohta S et al. 1992). PET is the only real alternative to BOLD at the moment for mapping the distribution of tissue oxygen metabolism. However, MRI has the advantages of more rapid image acquisition, it does not require administration of a radio-active tracer and it provides anatomical as well as functional information.

1.3.1 BOLD imaging studies in this thesis

The study presented in Chapter 6 was designed to exploit the dependence of R_2^* on the presence of dHb as an indication of temporal changes in the availability of oxygen in the liver during intestinal ischaemia-reperfusion (I/R). Intestinal I/R causes severe derangement of hepatic energy metabolism, possibly linked to inadequate oxygen supply (Vejchapipat P et al. 2001a). This is a serious clinical condition, affecting both adults and children, whose most life-threatening injuries are not due to the primary insult to the intestine, but to the damage and eventual failure of remote organs. The liver is one of the first organs to be affected after intestinal I/R, possibly due to its intimate dependence on vascular outflow from the gut, through the portal vein. The temporal changes in hepatic oxygenation and the inflow of blood to the liver have not been studied fully and the influence of the oxygenation of the liver on hepatic damage during intestinal I/R is not well understood. This provided the motivation for the MRI studies described in Chapter 6.

ASL and BOLD MRI offer invaluable insight into the delivery of oxygen and nutrients to tissue, a process that is compromised in numerous disease states. Maximising the sensitivity of these techniques is vital both for maximum diagnostic benefit in patients, and in order to yield information about the nature of pathology in animal models. This thesis describes investigations of both continuous ASL and BOLD imaging. A series of studies was designed to gain a deeper understanding of the labelling technique for CASL MRI so that the sensitivity of perfusion measurements may be maximised. Another set of investigations were performed, using BOLD MRI to study the effects of intestinal ischaemia-reperfusion on the liver in an animal model of this life-threatening condition.

2 Magnetic Resonance Imaging

2.1 Nuclear Magnetic Resonance

In this chapter emphasis is placed on those aspects of the theoretical basis of MRI that pertain to the work described in subsequent chapters. The processes of spin-lattice and spin-spin relaxation are discussed, the formalism of k-space is introduced, rapid imaging using echo planar imaging (EPI) is described, and arterial spin-labelling (ASL) techniques for imaging microvascular blood flow are outlined.

The phenomenon of nuclear magnetic resonance is the result of quantum interactions of magnetic nuclei within an externally applied magnetic field. Information about these nuclei and their molecular environment may be obtained by applying energy in the form of oscillating magnetic fields, referred to as radio-frequency (RF) pulses, to excite nuclear spins. The absorption and emission of energy by nuclear spins are resonance phenomena, that is to say they only occur at a specific frequency in a given nuclear species at a given magnetic field strength. This resonance frequency is known as the Larmor frequency, ω_0.

The concept of nuclear spin was introduced by Wolfgang Pauli to account for ultra-fine structure in atomic spectra (Pauli W.1924). It is the basis of NMR phenomena. Nuclear spin is quantised and individual protons and neutrons have spin quantum number $I = ½$. In a nucleus the spins of individual nucleons combine in such a way as to minimise the total energy of the system. Nuclei with $I \geq ½$ have a dipole magnetic moment, $\mu = \gamma(h/2\pi)I$, where γ is the gyromagnetic ratio, a characteristic property of each nuclear species.

Nuclei with magnetic moments undergo quantum interactions with an external magnetic field and the characteristic energy of these interactions is determined by the Larmor frequency, ω_0. In a field with flux density B_0, the amplitude of the Larmor frequency of nuclear spins is $\omega_0 = \gamma B_0$. Perturbations of the system are most often considered in a frame that rotates at ω_0, which is known as the "rotating reference frame". A sample containing a large number of magnetic nuclei may be treated as an "ensemble", whose mean behaviour is described by the expectation value of the interaction between an individual nucleus and B_0. This mean behaviour is described by the bulk magnetisation, M, that tends to align with B_0 at equilibrium.

Nuclei with magnetic dipole moments that are used to study biological systems include ^{31}P, ^{13}C, and ^{19}F. However, most magnetic resonance imaging (MRI) is based on the detection of ^{1}H nuclei (protons) in water for two main reasons. Firstly free water comprises between 60 % and 80 % of most body tissues. In comparison ^{31}P, the second most abundant magnetic nuclear species in biological tissue, is contained in metabolites at millimolar concentrations. Secondly, ^{1}H has a large magnetic moment due to a large gyromagnetic ratio ($\gamma = 26.8 \times 10^{7}\,T^{-1}s^{-1}$ compared with $\gamma = 10.8 \times 10^{7}\,T^{-1}s^{-1}$ for ^{31}P). All work presented in this thesis is based on MRI of water and the following description of MRI theory is pertinent to ^{1}H nuclei.

2.2 Relaxation times

The relaxation times of nuclear spins, T_1 and T_2, combined with proton density, provide contrast between different tissues in MRI. T_1 is the "spin-lattice" relaxation time, characteristic of the rate of transfer of energy between nuclear spins and their environment, the "lattice". T_2 is the "spin-spin" relaxation time, caused by interactions between spins without any exchange of energy with the lattice.

T_1 and T_2 are absolute measures, which provide an objective means of comparing measurements in different samples or subjects, in the same subject over time, or using different MR scanners. T_1 and T_2 provide characteristic contrast in a range of conditions. For example, T_1 tends to increase in tumour tissue and T_1-weighted images are employed to assess the lesion load in multiple sclerosis. T_2 also changes in tumours and T_2 is reduced in the early stages of ischaemia, for example in affected regions of the brain after a stroke.

T_1 and T_2 depend on the static magnetic field and the molecular environment of nuclear spins in a particular sample or tissue. Pulse sequence parameters are selected to emphasise differences due to proton density, T_1 or T_2 relaxation, or a combination, depending on which provides the best contrast between particular anatomical, functional or pathological features.

2.2.1 Spin-lattice relaxation

Magnetic dipoles align approximately parallel or anti-parallel to an external magnetic field, $\underline{B}_0$. The energy of this interaction is $-\underline{\mu}.\underline{B}_0 = -\mu_z B_0$ where μ_z is the component of the magnetic moment parallel to $\underline{B}_0$. It is energetically favourable for magnetic dipoles to align parallel to the field, but thermal energy constantly promotes spins to the higher energy state. The Boltzmann distribution relates the number of spins in the higher energy state, N_+, (with energy + $\mu_z B_0$), to the number of spins in the lower energy state, N_-, (with energy - $\mu_z B_0$) at a given temperature T (in Kelvin).

$$N_+ / N_- = \exp(-2\,\mu_z B_0/kT) \qquad \text{equation [2.1]}$$

where k is the Boltzmann constant.

The bulk magnetisation of a sample, M, is proportional to (N_- - N_+).

After an RF pulse excites spins in a sample that is held in a magnetic field, energy is exchanged between nuclear spins and the lattice to re-establish an equilibrium state. The time it takes to restore equilibrium is characterised by the spin-lattice relaxation time, T_1.

The dominant mechanism for T_1 relaxation in biological tissues is the dipole-dipole interaction. Fluctuations in the magnetic field at one nucleus due to the field of another magnetic dipole (another nucleus or an unpaired electron) induce transitions between nuclear spin states. The strength of the magnetic field due to a magnetic moment μ at a distance r is proportional to μ/r^3. If magnetic dipoles are close together or if μ is large, T_1 is short. The fact that magnetic moments of unpaired electrons are 685 times greater than those of protons is exploited to observe paramagnetic contrast agents, such as gadolinium-based compounds, or deoxyhaemoglobin.

Any nuclear species in a particular type of molecule has a spectral density function associated with the molecular motions within it (*Figure 2.1*). The correlation time, τ_c, is a measure of the random motions of molecules (the mean time for a molecule to change direction by one radian). $1/\tau_c$ is a measure of the rate of fluctuations due to rotational tumbling of molecules and if $1/\tau_c$ is close to the Larmor frequency energy transitions occur rapidly and T_1 is short. Small, freely moving molecules have short τ_c, corresponding to a greater weighting of the spectral density to higher frequencies. This is the fast regime, and it is typical of free water (*Figure 2.1*). At the field strengths commonly employed for MRI, biological tissues are in the intermediate regime (*Figure 2.1*).

2.2.2 Spin-spin relaxation

T_1 processes re-establish an equilibrium energy state, whereas T_2 processes destroy phase coherence between individual spin isochromats, without necessarily affecting the energy of the system.

In a perfectly homogeneous magnetic field the Larmor frequencies of spins in a sample are exactly the same. After a 90^0 pulse the bulk magnetisation, M, lies along a single axis in the transverse plane. All isochromats have the same phase and precess at the frequency of rotation of the rotating frame (ω_0). However, random processes destroy the phase history of individual spins, and the coherence of the spins in the sample is lost. The most common of these processes is the dipole-dipole interaction, which is also the main mechanism for T_1 relaxation. Other, low frequency oscillations cause T_2, but not T_1, relaxation, which explains the divergent behaviour of T_1 and T_2 at frequencies lower than ω_0 (*Figure 2.2*).

In practice, T_2 is not measured in a perfectly homogeneous magnetic field. Additional dephasing of isochromats occurs due to destructive interference between spins with slightly different Larmor frequencies. After an excitation pulse, echoes may be formed by applying a 180^0 pulse to produce a spin-echo, or by reversing the polarity of a de-focussing gradient to form a gradient-echo. A spin echo restores the phase coherence that is lost due to a static distribution of Larmor frequencies, whereas a gradient-echo does not. The relaxation times measured with spin-echo and gradient-echo pulse sequences are denoted T_2 and $T_2{}^*$ respectively and

$$1/T_2{}^* = 1/T_2 + 1/T_2` \qquad \text{equation [2.2]}$$

where $1/T_2`$ accounts for dephasing due to a spread of Larmor frequencies.

A third T_2 process occurs when magnetic nuclei diffuse through an inhomogeneous magnetic field. A spin that diffuses through local magnetic field gradients has a randomly varying Larmor frequency, which introduces irreversible dephasing if there is a significant change in the Larmor frequency before the MR signal is acquired.

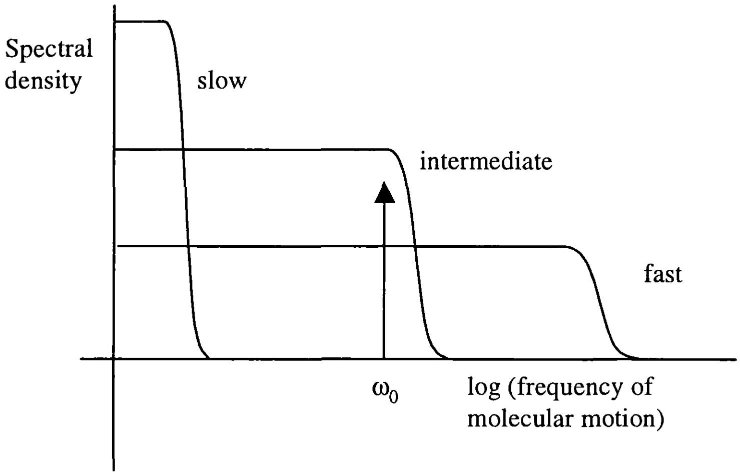

Figure 2.1

Spectral density functions.

Fast, intermediate and slow molecular motions correspond to short, intermediate and long correlation times, τ_c. In the intermediate regime, with the magnetic field strength corresponding to the ω_0 shown here, the spectral density is high at ω_0 and T_1 relaxation is rapid.

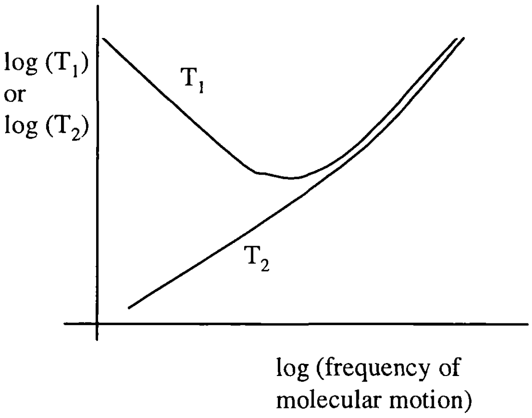

Figure 2.2

The frequency dependencies of T_1 and T_2.

Spin lattice relaxation is most effective at the Larmor frequency. Spin-spin relaxation is enhanced at low frequencies, reducing T_2 relative to T_1.

2.2.3 T_1 and T_2 weighted images

In order to observe contrast due primarily to T_1 relaxation, fairly short repetition times (TR) and short echo times (TE) are selected. Provided TR is short enough to prevent a full return of the longitudinal magnetisation, M_z, to its equilibrium value, M_z in nuclear species with different T_1 values recovers by different amounts, to produce T_1-dependent contrast. Short TE prevent significant dephasing, maximising signal-to-noise-ratio and minimising T_2 contrast between tissues.

For T_2 weighted images long repetition times are preferred to minimise T_1-dependent contrast. Echo times must be long enough to allow differences between transverse magnetisation, M_{xy}, in different tissues to evolve.

A "rule of thumb" that may be applied to obtain the greatest T_1 contrast with a flip angle of 90^0 is to set TR equal to the shortest T_1 of interest for a particular study (Edelstein WA et al. 1983). Similarly, to obtain maximum T_2 contrast, TE should be approximately the same as the shortest T_2 of interest.

2.2.4 Measuring T_1 and T_2

T_1 and T_2 are measured by sampling the relevant decay curve. In order to measure T_1, M_z is sampled at different times after inversion or saturation, by tipping the magnetisation into the transverse plane (*Figure 2.3*). Provided that the repetition time between saturation or inversion pulses is long enough to permit full relaxation of the sample (at least 5 times T_1), M_z returns to its equilibrium value, M_0, according to

$$M_z = (M_z(t=0) - M_0)\, e^{-t/T1} + M_0 \qquad \text{equation [2.3]}$$

where $M_z(t=0) = 0$ for saturation and $- M_0$ for inversion.

In order to measure T_2, spin-echoes are acquired at a range of echo times, TE. M_{xy} is reduced according to

$$M_{xy} = M_0\, e^{-TE/T2} \qquad \text{equation [2.4]}$$

The Carr-Purcell-Meiboom-Gill sequence was designed to provide a rapid means of measuring T_2 accurately and with the minimal effects from spin diffusion (*Figure 2.4*) (Meiboom S and Gill D 1958).

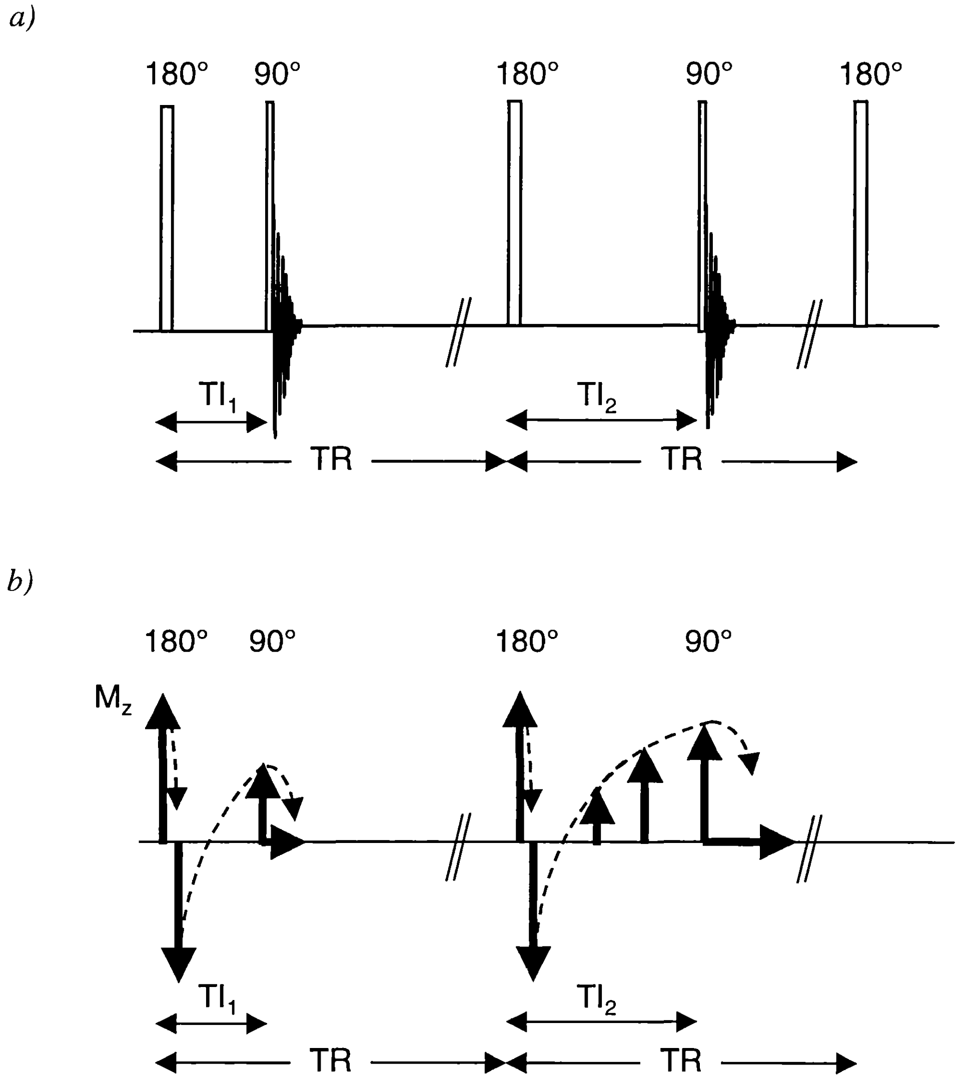

Figure 2.3

The inversion recovery sequence

The pulse sequence is shown in (a). TI is the time between inversion and excitation. TR is the repetition time. The evolution of the longitudinal magnetisation, M_z is shown in (b). M_z recovers after inversion, as equilibrium is restored during TI. It is sampled by applying a 90^0 pulse. The magnitude of the resulting FID is proportional to M_z (adapted from Thomas DL 1999).

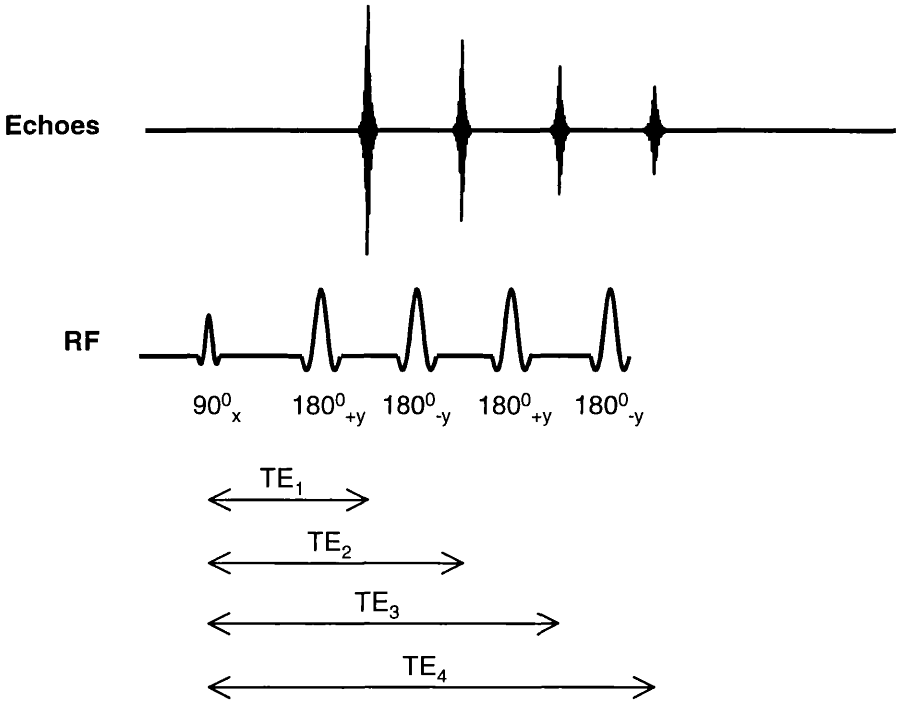

Figure 2.4

The Carr-Purcell-Meiboom-Gill sequence.

Repeated 180^0 pulses are applied in phase quadrature to the 90^0 pulse in order to avoid imperfect refocusing by inaccurate 180^0 pulses. The magnitude of the spin-echo after each refocusing pulse is proportional to M_{xy} and from a series of such echoes, T_2 may be determined.

2.3 The Bloch Equations

The equation of motion for the bulk magnetisation, $\underline{M}$, of a sample in the presence of a magnetic field, $\underline{B}$, may be expressed as a differential equation (Bloch F. 1946). The effects of spin relaxation may be included and in general:

$$d\underline{M} / dt = \gamma (\underline{M} \times \underline{B}) + (M_0 - M_z) / T_1 - (M_x + M_y) / T_2 \qquad \text{equation [2.5]}$$

where M_z is the longitudinal component of $\underline{M}$, parallel to the static magnetic field, $\underline{B}_0$.
M_x, M_y are the transverse components of magnetisation

2.4 Magnetisation transfer contrast

Protons are present in many different forms in biological tissues and the observed magnetisation and T_1 values depend on interactions between protons in different molecular environments. Despite the variety and complexity of these interactions, a simplifying assumption of two proton pools is generally valid; the free or solvent pool and the bound or restricted motion pool (for example Henkelman RM et al. 1993). The majority of the signal in MR images originates from protons in free water, but it is affected by protons bound to large molecules, including proteins, cell membranes and other macromolecules. This bound pool has broad resonances and correspondingly short relaxation times, (approximately 10^3 times shorter than free water), so that in most experiments signals from these protons may not be observed directly. However, exchange (or transfer) of magnetisation between the bound and free pools occurs, which may be approximately described by analogy with chemical exchange, according to

$$\frac{dM_f}{dt} = \frac{(M^0_f - M_f)}{T_{1f}} - k_{for} M_f + k_{rev} M_b \qquad \text{equation [2.6]}$$

where M_f is the magnetisation of the free water pool

M^0_f is the equilibrium magnetisation of the free water pool

k_{for} and k_{rev} are the forward and reverse rate constants for exchange between the free and bound pools

M_b is the magnetisation of the bound pool

T_{1f} is the spin-lattice relaxation time of the free pool

Protons in the bound pool may be selectively excited by an off-resonance RF pulse (*Figure 2.5*). The excitation reduces M_b and thereby reduces M_f through exchange (equation [2.6]). Thus, contrast in MR images may be manipulated by selective excitation of the bound pool. Differences in the proportions of free and bound protons, or in T_1 values in either species are highlighted in an image acquired after an off-resonance pulse.

Magnetisation transfer (MT) imaging has a number of important clinical applications, including in angiographic studies, the detection of lesions in multiple sclerosis and the discrimination of tumour from normal tissue. MT also reduces the signal intensity in CASL images, as discussed in Chapter 5.

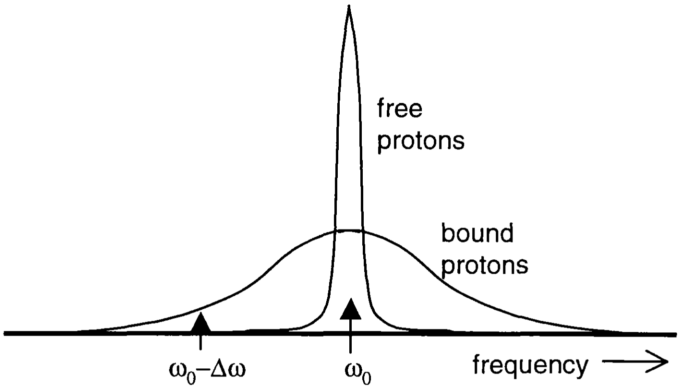

Figure 2.5

Resonance line shapes of free and bound proton pools

A pulse applied at ω_0 excites the protons in both the free and bound pools. A pulse at $\omega_0 - \Delta\omega$ excites mainly the bound pool.

2.5 Image formation and the concept of k space

The MR signal, S(t), is

$$S(t) = \exp(-t/T_2^*) \int_V \rho(r) \exp(i\phi(t))\, dV \qquad \text{equation [2.7]}$$

where $\rho(r)$ is the proton density,

ϕ is the phase of the magnetisation,

V is the volume of integration.

Spatial information may be gained from NMR through the application of magnetic field gradients to separate positions in space according to their resonance frequency, as follows: ϕ evolves over time at the Larmor frequency, ω_0, and in the presence of a gradient, $\underline{G}$, the phase that accumulates from the time of excitation depends on position, $\underline{r}$. In the rotating frame of reference,

$$\phi(t) = \gamma \int_0^t \underline{G}.\underline{r}\, dt$$

If the time between excitation and acquisition is much less than T_2*, we may write:

$$S(t) = \int_V \rho(r) \exp(i\underline{k}(t).\underline{r})\, dV \qquad \text{equation [2.8]}$$

where spatial frequency, k, is defined as: $\underline{k}(t) = \gamma \int_0^t \underline{G}\, dt$

We see from equation [2.7] that the spatial distribution of proton density is the inverse Fourier transform of the signal, excluding the effect of T_2 relaxation. The concept of k-space was developed in the early 1980's (Twieg DB.1985; Ljunggren S.1983) to provide a way of assessing the sensitivity of MR pulse sequences to different spatial frequencies and comparing pulse sequences. An example of a pulse sequence is shown in *Figure 2.6* for a conventional, gradient-echo imaging sequence.

If all of k-space were to be sampled ($-\infty < k < +\infty$), a complete description of the distribution of proton density would be obtained. In practice, k is sampled at discrete intervals. Sampling the FID while a constant gradient, G_x, is applied gives information in one dimension, k_x, which may be visualised as scanning along the k_x-axis (*Figure 2.6b*). This is known as frequency encoding.

In order to acquire a second dimension, another gradient must be applied in a direction orthogonal to the first. This is done by phase encoding, as first introduced by Kumar (Kumar A et al. 1975). Spins are dephased coherently after excitation by a phase-encoding gradient of constant duration τ and amplitude $+G_y$. The frequency encoding gradient is applied during the acquisition to place the peak of the echo at the centre of k-space, as the line $k_x = 0$ is crossed, as shown in *Figure 2.6*. A complete set of k_y may be acquired by repeating the phase encoding with a series of values of τ or a series of values of G_y with a constant τ. Early developments in spatial encoding employed variations in τ (Kumar A et al. 1975) but varying G_y has the advantage of introducing the same amount of T_2* relaxation as every line of k-space is acquired (Edelstein WA et al. 1980). Negative regions in k-space are covered by reversing the gradient.

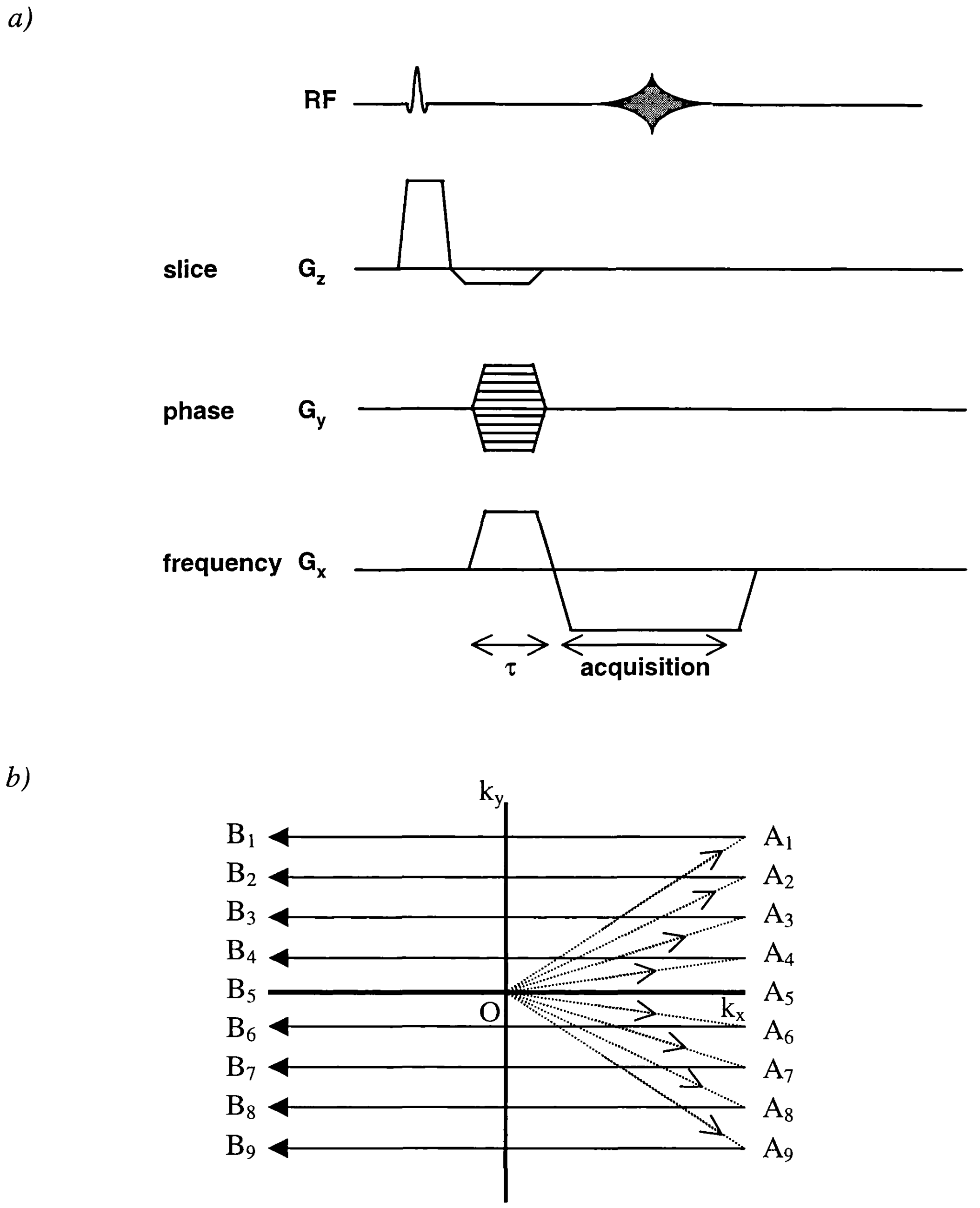

Figure 2.6

Gradient echo sequence.

Pulse sequence diagram (a) and k-space coverage (b)

Gradients, + G_x and G_{y1} move the trajectory through k-space from O to A_1 before the acquisition starts. The first line of k_x is acquired between A_1 and B_1 by applying the gradient $-G_x$ to reduce k_x as time evolves. A smaller phase encoding gradient, G_{y2}, is applied before the second line is acquired from A_2 to B_2 and so on, until the whole plane has been sampled.

2.6 Echo Planar Imaging

Rapid imaging is desirable to permit tracking of dynamic processes, to reduce artifacts in images due to motional blurring and to reduce examination times in clinical practice. A major limitation to reducing imaging times is allowing sufficient relaxation of longitudinal magnetisation between the excitation pulses applied to acquire each line of k-space. This limitation is overcome if a complete image is acquired after a single excitation, which requires sampling all of k-space in a single acquisition. Echo planar imaging (EPI), introduced by Mansfield in 1977 (Mansfield P 1977), produces images in a few tens of milliseconds. It has become more widely available for rapid imaging in clinical practice and has numerous applications in neuro-imaging. Images shown in Chapter 5 were acquired using EPI.

The whole k plane may be sampled after a single excitation, by applying a series of 180^0 pulses to effect repeated reflections through one of the axes, k_x or k_y, (as in turbo-spin-echo (TSE) or RARE) or by repeatedly reversing the frequency encoding gradient direction to scan alternate lines in k-space in opposite directions. The EPI technique employs the second approach.

The pulse sequence diagram for EPI is shown in *Figure 2.7.* A series of gradient recalled echoes is acquired after a single RF excitation. The first line of k-space is acquired as per conventional gradient-echo MRI (*Figure 2.6*). At the end of the first line a brief gradient pulse (or 'blip') in the phase encoding direction and a reversal of the gradient in the frequency encoding direction prepare for the next line in k-space to be scanned in the opposite direction (*Figure 2.7*).

EPI has high time resolution but there are some disadvantages. Echo planar images are inherently T_2* weighted, which limits the number of echoes that may be recalled before the signal has decayed to the noise level. The image matrix size, and hence image resolution, is thus restricted. Long acquisition times make EPI especially sensitive to inhomogeneities in B_0. Variations in B_0 introduce gross distortions into images and signal loss in regions where B_0 inhomogeneity is particularly great. The high acquisition bandwidths make EPI prone to noise and place great demands on the receiver electronics.

However, improvements in hardware over the last two decades have provided the powerful, linear amplifiers and coils necessary for gradients to ramp up and down very rapidly, and EPI has become a standard technique for research and clinical MRI.

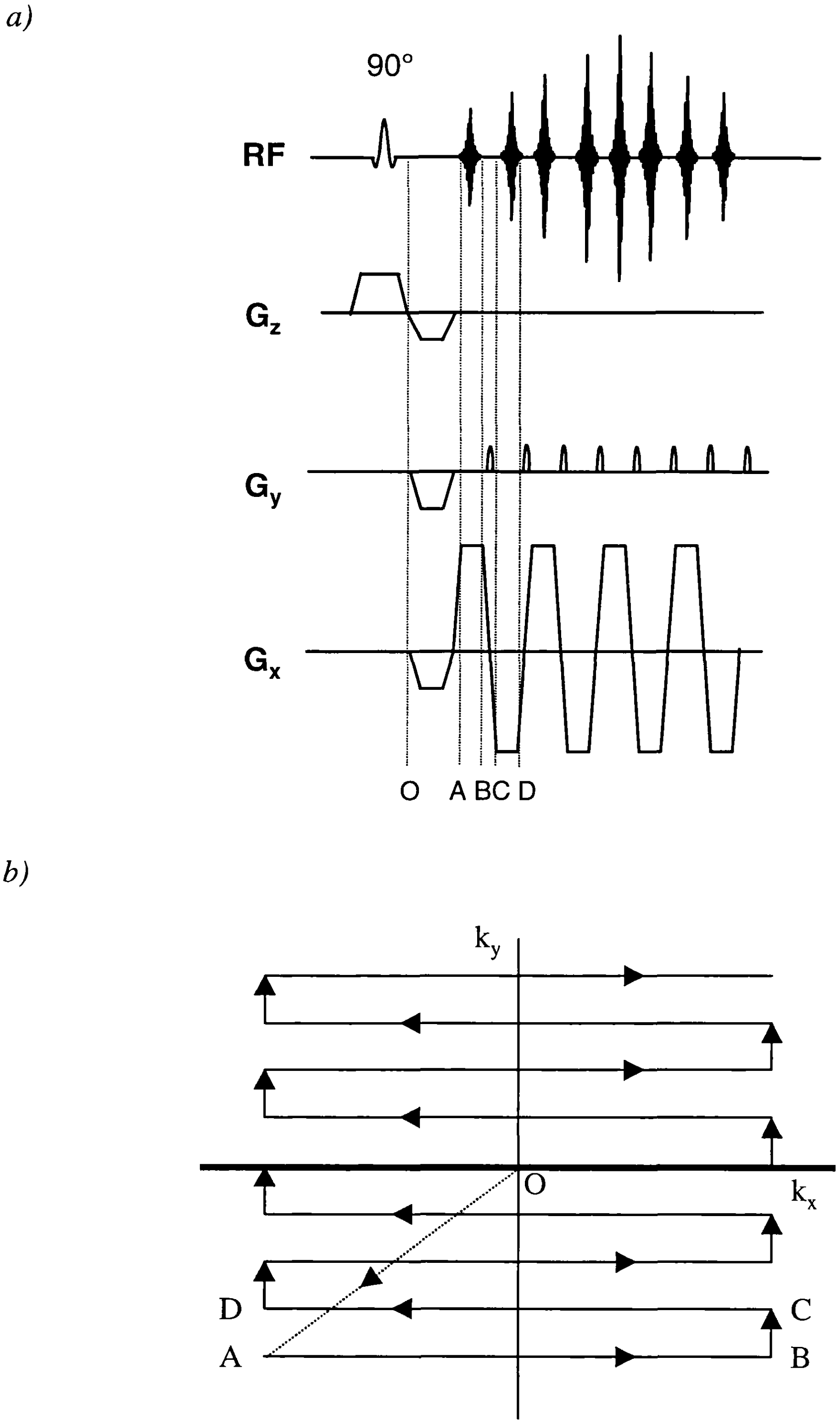

Figure 2.7

Echo planar imaging

Pulse sequence (adapted from Thomas DL 1999) (a) and k-space coverage (b). After the excitation pulse, de-focussing gradients move the trajectory through k-space from O to A. Points from A to B are acquired before a blip in the phase encoding gradient (G_y) takes the path from B to C. A change in sign of the frequency encoding gradient (G_x) takes the path from C to D. Further blips of G_y and reversals of G_x form echoes whenever the line $k_x = 0$ is crossed.

2.7 Perfusion imaging by arterial spin labelling

Arterial spin labelling (ASL) refers to the process of changing the magnetisation of water in arterial blood. Exchange of this 'labelled' water into tissue changes the magnetisation of the tissue. Proton spins in blood thus become an endogenous contrast agent, making ASL a truly non-invasive way of measuring microvascular blood flow.

ASL is a subtraction technique, relying on the acquisition of one image after labelling blood and one image without the label (the control image). An image formed by subtraction of the labelled image from the control image has signal only where blood perfuses tissue. Typical positions of labelling and imaging regions for detection of regional cerebral blood flow, rCBF, are shown in *Figure 2.8.*

The label is applied by saturation or inversion of the magnetisation of inflowing blood. In some implementations, saturation has been the method of choice, either to reduce RF power deposition (Francis ST et al. 1999) or to facilitate multiple slice imaging (Williams DS et al. 2001). However, inversion is preferred in most cases because the difference in signal in subtraction images, and hence the sensitivity of the technique, is twice as great as with saturation.

There are two main classes of ASL techniques. The first to be introduced was continuous ASL (CASL) (Detre JA et al. 1992; Williams DS et al. 1992). Pulsed ASL (PASL) was proposed to overcome some of the difficulties associated with CASL (Edelman RR et al. 1994). For CASL a long period of labelling establishes a steady state between labelled blood and the tissue perfused by this blood, reflected by the reduced magnetisation of the tissue. For PASL a short RF pulse is applied proximal to the imaging slice(s) to form a bolus of labelled blood. The exchange of the bolus into tissue alters the magnetisation of the tissue, which may be detected in the same way as for CASL.

2.7.1 Continuous ASL

The first implementation of continuous ASL imaging employed a train of RF pulses to saturate inflowing spins (Detre JA et al. 1992). Velocity driven adiabatic fast passage (AFP), a technique introduced from MR angiography (Dixon WT et al. 1986), was first employed for CASL by Williams et al. (Williams DS et al. 1992) and it has become the most widely applied technique for CASL. The process of velocity driven AFP and its application in CASL is described in Chapter 3.

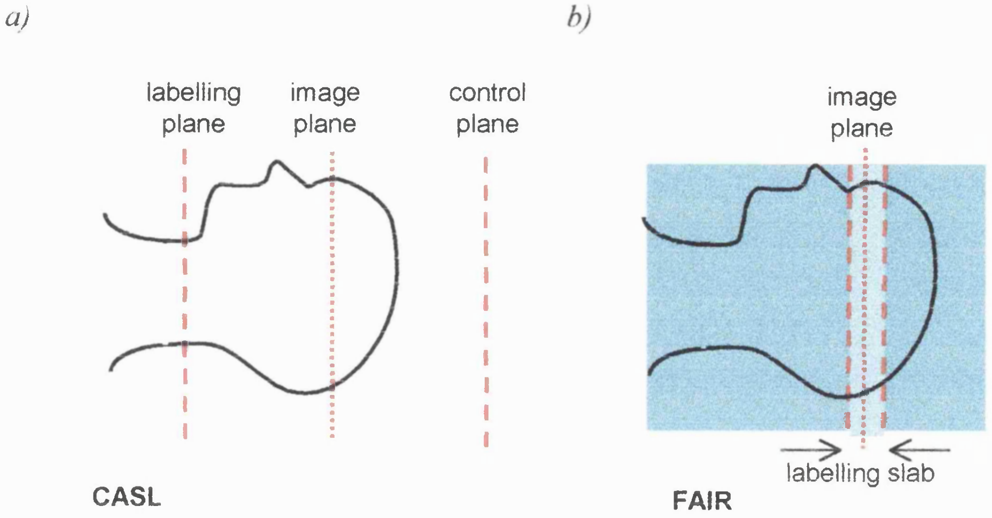

Figure 2.8

Geometry for label and control images using ASL

CASL (a) and the PASL variant, FAIR (b). CASL is performed by continuously inverting the magnetisation of blood that flows through a plane proximal to the imaging plane. This is the labelling plane and the control plane is at the same distance from, but distal to, the imaging plane. FAIR is performed by applying alternately slice selective and non-selective inversions. After a selective inversion of a slab of tissue around the image plane, the inflow of fully relaxed blood provides flow-dependent contrast. The control is a non-selective inversion so that inflowing blood has approximately the same magnetisation as tissue in the imaging slice.

In addition to the inversion of moving protons, the long RF pulse for velocity driven AFP (of a few seconds) introduces magnetisation transfer (MT) contrast to the image. The MT effect varies with offset frequency, and therefore with distance from the labelling plane in the presence of a gradient. The unlabelled (control) image must have identical MT contrast to the labelled image, if the subtraction is to accurately reflect tissue perfusion. Alternatively, MT effects may be eliminated by using a separate, localised RF coil for labelling (Zhang W et al. 1995). However, a two coil system introduces additional hardware complications and the non-uniform RF field of a surface coil may not label blood flowing through all feeding vessels uniformly. In most implementations of CASL, a single coil is used for labelling and imaging and cancellation of MT effects is an important consideration.

CASL is the more sensitive of the ASL techniques (Wong EC et al. 1998a), but it has some limitations. The most important of these are 1) relatively long transit times from the labelling plane to the imaging plane; 2) frequency (and hence position) dependent magnetisation transfer effects, which hinder extension to multiple slices; and 3) long RF pulses for labelling, which impose considerable demands on RF amplifiers and result in high power deposition in subjects.

2.7.2 Pulsed ASL

Pulsed ASL requires a labelling pulse with a sharp profile and large bandwidth to create a well defined bolus, of adequate duration. Adiabatic pulses are most commonly employed to satisfy these demands. Gradient modulated, adiabatic pulses, such as FOCI (Ordidge RJ et al. 1996) have been shown to confer significant improvement over more conventional hyperbolic secant pulses, especially in human studies (Yongbi M and Duyn J.1999).

There are several versions of PASL. One group of techniques labels blood proximal to the imaging plane. These are EPISTAR (echo planar imaging with signal targeted averaging (Edelman RR et al. 1994)), PICORE (proximal inversion with control for off-resonance effects (Wong EC et al. 1997)) and QUIPSS II (quantitative imaging of perfusion using a single subtraction (second version) (Wong EC et al. 1998b)). A second group of PASL techniques label blood simultaneously proximal and distal to the imaging slice. These are FAIR (flow sensitive alternating inversion recovery (Kwong KK et al. 1995; Kim SG 1995)) or the variants UNFAIR (Un-inverted FAIR (Helpern JA et al. 1997)) and FAIRER (FAIR excluding radiation damping (Zhou J et al. 1998)). The control preparations for the proximal labelling techniques are applied distal to the slice(s) of interest, as for CASL. FAIR uses a slice-selective inversion for the label and a global inversion as the control. A bolus of fully relaxed spins washes in to give a flow-dependent signal, following the slice selective inversion.

PASL has the advantages of ready combination with BOLD acquisitions for functional imaging and negligible MT effects of the labelling pulse. However, transit times introduce possible errors into flow calculations using either CASL or PASL and PASL is less sensitive to CBF than CASL, especially in more distal slices. The relative merits of the two ASL variants have been investigated by Wong et al. (Wong EC et al. 1998a).

2.7.3 Quantification of flow from ASL

The standard model for quantifying microvascular blood flow, introduced by Detre et al. (Detre JA et al. 1992) has been adapted to incorporate the numerous parameters that affect ASL images. The model considers the contribution of blood flow to the rate of change of magnetisation in tissue. In its most simple form, excluding the effects of MT, the model is described by the equation:

$$\frac{dM_t}{dt} = \frac{(M_{0sat} - M_t)}{T_{1sat}} + f\,M_a(t) - \frac{f\,M_t}{\lambda} \qquad \text{equation [2.9]}$$

where M_t is the tissue magnetisation per 100g of tissue

M_{0sat} is the equilibrium value of M_t in the presence of the labelling pulse

M_a is the magnetisation of inflowing (arterial) blood per 100 ml of blood

f is microvascular blood flow	(ml /100g tissue/sec)
λ is the blood / brain partition coefficient	$\frac{\text{(ml of water / g of tissue)}}{\text{(ml of water / g of blood)}}$

T_{1sat} is the spin-lattice relaxation time of the tissue in the presence of the labelling pulse.

Assuming that the labelling pulse saturates the magnetisation of macromolecules in the imaging plane(s),

$$f = \frac{\lambda}{T_{1app}} \frac{(M_{control} - M_{label})}{2\,\alpha\,M_0} \qquad \text{equation [2.10]}$$

where T_{1app} is the apparent T_1 of tissue, $1/T_{1app} = 1/T_{1sat} + f/\lambda$

M_0 is the equilibrium magnetisation of the tissue

"sat" refers to the state when the magnetisation of macromolecules is saturated

"label" and "control" refer to the magnetisation after the label and control preparations

α is the degree of inversion produced by the labelling pulse ($\alpha = 1$ for perfect labelling and zero for the perfect control).

More detailed derivation of the equations for calculating perfusion are given in Appendix E, where the effect of a delay between the end of the labelling pulse and image acquisition is also considered.

A more direct way of considering flow was adopted by Buxton et al. (Buxton RB et al. 1998). They modelled the magnetisation of inflowing blood, $M_a(t)$, as it exchanges into tissue. This "general kinetic model" is described by the relationship:

$$\Delta M_a(t) = 2M_{0a}\, f \int c(t')r(t-t')m(t-t')\, dt' \qquad \text{equation [2.11]}$$

where c(t`) is the delivery function, for blood arriving in the imaging plane

m(t - t`) is the magnetisation relaxation function

r(t - t`) is the residue function

t` is the time at which blood moves into the imaging plane (the delivery time).

Continuous and pulsed ASL are distinguished by their respective delivery functions,

$$c(t')_{PASL} = \alpha\, e^{-t'/T1a} \quad \text{and} \quad c(t')_{CASL} = \alpha$$

where T_{1a} is the T_1 relaxation time of arterial blood

The delivery functions differ because the bolus for PASL is assumed to appear instantaneously and decay due to T_1 relaxation, as the bolus moves into tissue, whereas for CASL, labelled blood is supplied continuously throughout the labelling period.

The general kinetic model may be shown to be equivalent to the standard model. It follows the history of the blood itself, but ultimately we measure the magnetisation of tissue. Both models depend on the blood–brain partition coefficient, λ, for which constant values throughout the brain are commonly assumed.

There are several parameters, which affect the accuracy of quantification. These include: i) transit delays (δ), the time it takes for blood to move from the plane in which it is labelled into the imaging region (Alsop DC and Detre JA.1996); ii) the exchange time (T_{ex}), the time between a spin arriving in the imaging plane and the time at which it exchanges into tissue (Wong EC et al. 1998a; Parkes LM and Tofts PS 2001); iii) signal from intravascular spins that do not perfuse tissue in the imaging slice; iv) efficiency of labelling α; v) variations in λ between grey and white matter and in disease states; and vi) accurate measurement of T_{1app}.

A "post-labelling delay" was proposed by Alsop and Detre to reduce sensitivity to transit time and to allow the wash out of labelled blood that passes through the imaging slice, but does not perfuse it (Alsop DC and Detre JA.1996). Alternatively, low amplitude bipolar gradients may be applied after the labelling pulse and before imaging to crush out vascular signal. Greater amplitude gradients are required to eliminate signal from blood in smaller vessels. T_{1app} may be measured in each pixel and α may be estimated from measurements of the signal in a feeding artery (Zhang W et al. 1993).

An overview of the basic theory of MRI and approaches for perfusion and oxygen sensitive imaging has been given in this chapter. Investigations into the performance of the ASL technique and the application of ASL and BOLD are detailed in the following chapters.

3 Computer modelling of velocity driven adiabatic fast passage for continuous arterial spin labelling

3.1 Introduction

The development of arterial spin labelling (ASL) MRI has made it possible to study microvascular blood flow completely non-invasively, offering a means to investigate tissue perfusion in numerous functional and pathological states. The non-invasive nature of the technique makes it attractive for human subjects, as well as for longitudinal measurements in experimental models of disease (van Dorsten FA et al. 2002; Lythgoe MF et al. 2000; Zaharchuk G et al. 1999a). Much work has been performed to assess and improve the accuracy of perfusion values from ASL (Wong EC et al. 1998b; Calamante F et al. 1996; McLaughlin AC et al. 1997; Ye FQ et al. 1997; Alsop DC and Detre JA 1996). However, its inherently low sensitivity remains one of the most significant limitations of the technique.

For ASL, labelled protons in water in arterial blood wash in to the brain, where they exchange into the parenchyma. Such a flow-weighted image is subtracted from an image without flow weighting to produce a map of perfused tissue. These images are referred to as the label and control images respectively. The subtraction images, from which perfusion values are calculated, have inherently low contrast to noise ratios of only a few percent of the signal intensity in a control image. In order to maximise this signal difference, the most effective method for labelling arterial blood must be employed. Blood may be labelled by saturation or inversion. Saturation was used in the first implementations of CASL, in which images were acquired after a train of RF pulses saturated protons in blood in the neck (Detre JA et al. 1992). Velocity driven AFP was applied initially for MR angiography (Dixon WT et al. 1986) and in some of the first perfusion studies using ASL (Williams DS et al. 1992; Roberts DA et al. 1994). Now it is widely regarded as the preferred method for continuous ASL (CASL).

The RF pulse for labelling also excites the broad resonances of macromolecules within the imaging slice. The transfer of this magnetisation to the tissue water reduces image signal intensity, producing magnetisation transfer contrast (MTC), which must be accounted for by modelling (Zhang W et al. 1995) or by applying a suitable pulse prior to the acquisition of the control image. The MT effects of CASL are considered in Chapter 5.

Velocity driven AFP provides a continuous supply of blood, labelled by inversion. However, the degree of inversion is limited by several factors, including the amplitudes of the magnetic field gradient and RF pulse used for AFP, the velocity of blood and its spin relaxation times, T_1 and T_2. The duration of RF pulses is often limited by RF amplifiers, especially on some clinical scanners, and therefore the relatively long pulse required for labelling in CASL experiments (2 or 3 seconds) must be divided into a series of short pulses. It has been assumed that the effectiveness of AFP is proportional to the duty cycle of the train of RF pulses (Ye FQ et al. 1997; Silva AC and Kim SG 1999), but this assumption has not been tested previously.

This study of velocity driven AFP used a computer model to establish optimal RF pulse parameters, and to determine the effects of pulsatile variations in the velocity of blood, the influences of spin relaxation in blood and the duty cycle of discontinuous RF during labelling. The computer modelling was performed with one set of parameters for imaging humans in a clinical scanner and a second set of parameters for imaging rats in a small bore, animal system, to model the conditions for *in-vivo* experiments, as described in Chapter 5. Unlike experiments in flow phantoms or *in-vivo*, the computer modelling approach offers the possibility of turning on or off any number of confounding effects which influence the degree of inversion and thereby may cause substantial errors in the measurements.

3.2 Theory

3.2.1 Velocity driven Adiabatic Fast Passage

To invert moving spins by AFP, a radio-frequency pulse, $\underline{B}_1$, is applied in the presence of a magnetic field gradient, $\underline{G}$, which is ideally along the direction of motion of the spins. A nuclear spin, moving at a velocity, $\underline{v}$, is thus subject to a linear frequency sweep through the frequency of the $\underline{B}_1$ pulse. The pulse may be analysed in a frame of reference that rotates at the Larmor frequency, the "rotating frame of reference". The offset of the spin from resonance is ΔB. The rate of the frequency sweep for adiabatic fast passage is related to the rate of change of ΔB as follows:

$$\gamma\, d\Delta B/dt = \gamma\, \underline{G}.\underline{v}$$

Moving spins experience an effective magnetic field, B_{eff} (*Figure 3.1b*, page 31), where

$\underline{B}_{eff} = \underline{B}_1 + (\underline{G}.\underline{v})\ (\underline{z}/z)$

When a spin is far from the labelling plane, $\underline{\Delta B}$ is the dominant component of $\underline{B}_{eff}$ and the angle between $\underline{\Delta B}$ and $\underline{B}_{eff}$, θ, is close to zero (*Figure 3.1b*). As the spin approaches the labelling plane, the $\underline{B}_1$ component becomes more significant and $\underline{B}_{eff}$ rotates until it is aligned with either $\underline{B}_1$, for a 'half passage' experiment ($\theta = -\pi/2$), or $-\underline{\Delta B}$ for 'full passage' ($\theta = -\pi$).

In a CASL experiment the frequency of $\underline{B}_1$ is selected to produce a resonance in a plane proximal to the imaging plane. Adiabatic inversion is achieved if the magnetisation of a spin, $\underline{m}$, remains closely aligned with $\underline{B}_{eff}$ throughout the frequency sweep and if spin relaxation during inversion is negligible. This is the adiabatic condition, which may be expressed as:

$$1/T_1,\ 1/T_2 << d\theta/dt << \gamma B_{eff} \qquad \text{equation [3.1]}$$

where: $\cos\theta = \Delta B / B_{eff}$ equation [3.2a]

$\sin\theta = -B_1 / B_{eff}$ equation [3.2b]

Differentiation of [3.2a] with respect to time, t, and substitution of [3.2b] yields:

$$d\theta/dt = (1/B_1)*[d(\Delta B)/dt - (\Delta B / B_{eff})*d(B_{eff})/dt] \qquad \text{equation [3.3]}$$

In the case where the velocity of the spin has the same direction as the gradient, the magnetic fields and their time derivatives at a displacement z (z = 0 at the resonance of $\underline{B}_1$, in the presence of $\underline{G}$) are:

$$\Delta B = Gz$$

$$d(\Delta B)/dt = Gv$$

and

$$B_{eff} = ((Gz)^2 + (B_1)^2)^{1/2}$$

$$dB_{eff}/dt = Gv(Gz)/B_{eff} \qquad (\text{because } dB_1/dt = 0)$$

Substitution into equation [3.3] yields:

$$d\theta/dt = [Gv/B_1] * [1- (Gz)^2/B_{eff}^2]$$

$$d\theta/dt = GvB_1 / B_{eff}^2$$

The adiabatic condition for velocity driven AFP is then (Garwood M and Ugurbil K 1992):

$$1/T_1,\ 1/T_2 << GvB_1/B_{eff}^2 << \gamma B_{eff} \qquad \text{equation [3.4]}$$

The right hand side of the adiabatic condition is often simplified by considering the smallest value of $\underline{B}_{eff}$, at the centre of the inversion, where $z = 0$ and $\underline{B}_{eff} = \underline{B}_1$ (Bloch F.1946; Abragam A). Thus a lower limit for B_1 is defined by:

$$Gv << \gamma B_1^2 \qquad \text{equation [3.5]}$$

Equation [3.5] states that $\gamma B_1^2/(Gv) >> 1$ for adiabatic inversion. The adiabaticity factor, β, provides a quantitative measure of how well a given set of parameters meets the right hand side of the adiabatic condition (Roberts DA et al. 1994). β is defined as:

$$\beta = \gamma B_1^2/(Gv)$$

The left hand side of the adiabatic condition may be written (assuming $T_1 > T_2$):

$$B_{eff}^2 << GvB_1T_2 \qquad \text{equation [3.6]}$$

This condition is most difficult to satisfy when B_{eff} has its greatest amplitude, which is at the beginning and at the end of AFP, where $B_{eff} \approx Gvt$ ($t = 0$ when $z = 0$ at the resonance frequency of B_1). If the magnetisation of the spin, $\underline{m}$, follows $\underline{B}_{eff}$ throughout the AFP, then at any time the longitudinal component of $\underline{m}$, m_z, is:

$$\begin{aligned} m_z &= \cos\theta \\ m_z &= Gvt / (B_1^2 + (Gvt)^2)^{1/2} \\ (Gvt)^2 &= B_1^2 * m_z^2 / (1 - m_z^2) \qquad \text{equation [3.7]} \end{aligned}$$

Substituting [3.7] into [3.6] in the limit $B_{eff} \approx Gvt$ yields:

$$B_1 << GvT_2 / k^2$$

where $k^2 = m_{z\_start}^2 / (1 - m_{z\_start}^2)$

m_{z_start} is m_z at the start of the AFP (when it first moves away from $m_z = 1$)

The adiabatic condition may now be written:

$$GvT_2 / k^2 >> B_1 >> \sqrt{[(Gv)/\gamma]} \qquad \text{equation [3.8]}$$

From equation [3.8] we see that at larger values of Gv there is a greater range of B_1 values that satisfy both sides of the adiabatic condition.

If the value of m_z at the end of the AFP is m_{z_end} and $m_{z\_end} = - m_{z\_start}$, an expression for the duration of the AFP may be found from equation [3.7]:

$$\Delta t = 2\,k\,B_1 /(Gv) \qquad \text{equation [3.9]}$$

Δt increases at higher B_1 and decreases when higher values of G or v increase the duration of the frequency sweep.

3.2.2 Spin-relaxation during AFP

If $\underline{m}$ remains closely aligned with $\underline{B}_{eff}$ throughout AFP, $\underline{m}$ is 'locked' to $\underline{B}_{eff}$, in which case it may be argued that the appropriate relaxation times for AFP would be those associated with a spin-locking experiment, $T_{1\rho}$ and $T_{2\rho}$. The amplitude and orientation of a locking field determine the amplitudes of $T_{1\rho}$ and $T_{2\rho}$ and the orientation of the axes along which they act. $\underline{B}_{eff}$ changes constantly throughout adiabatic fast passage. Therefore the equilibrium state to which $T_{1\rho}$ restores $\underline{m}$ changes constantly and the relaxation rates are not well defined at any single point during AFP.

The model employed for these studies uses the relaxation parameters T_1 and T_2. This may be justified on two counts. Firstly, T_1 and T_2 are the appropriate relaxation times at the beginning and end of the passage through resonance, and at any other time when $\underline{m}$ is not locked to $\underline{B}_{eff}$. Secondly, at the centre of an inversion $T_{1\rho}$ acts in a plane orthogonal to $\underline{B}_0$. This is the plane in which T_2 relaxation occurs and $T_{1\rho}$ in this plane is generally very similar to T_2 in the absence of a locking field (Blicharski JS 1972).

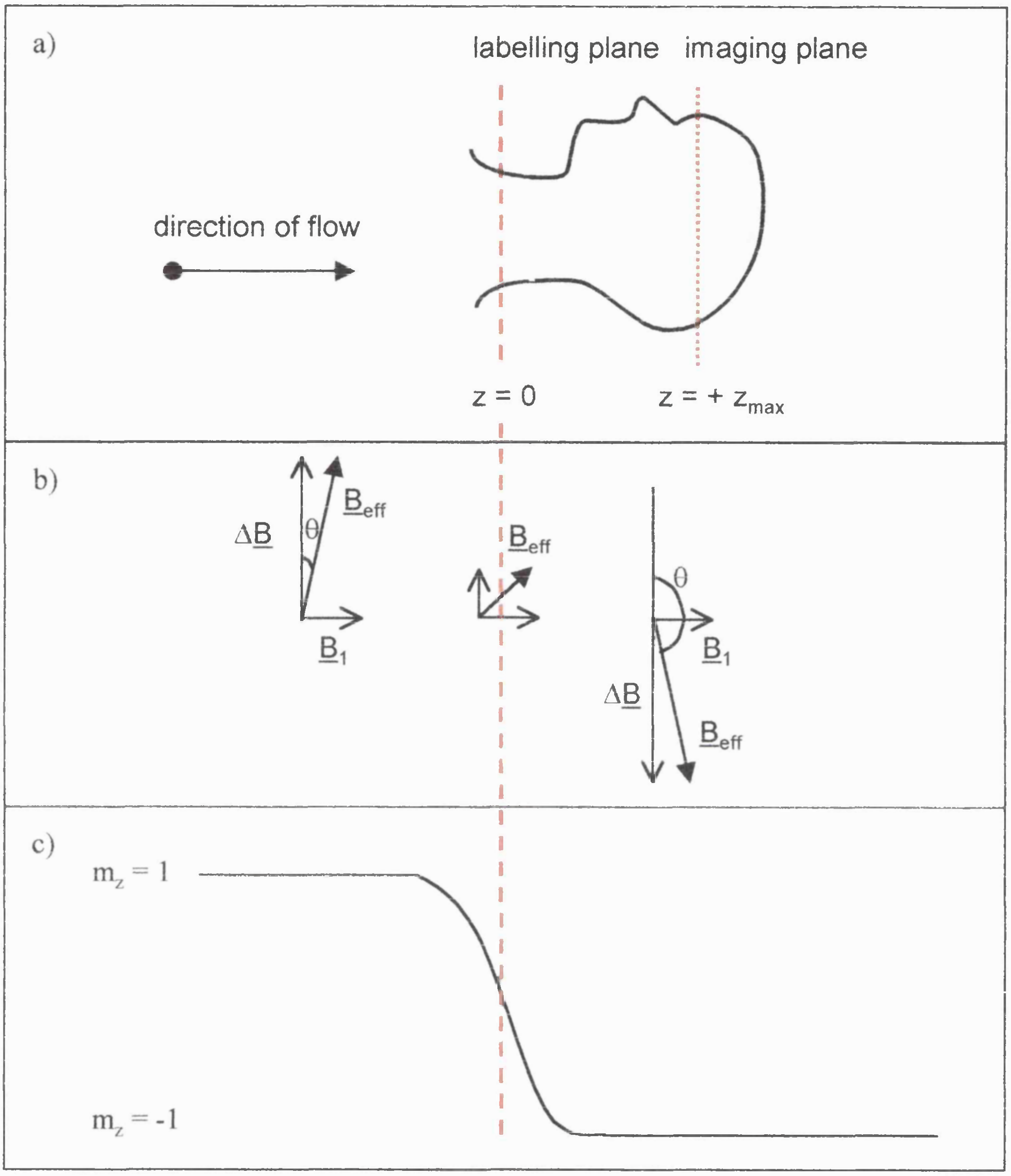

Figure 3.1

Velocity driven AFP for CASL

Blood flows through the labelling plane in the neck or lower part of the brain and into the tissue before images are obtained (a). The effective magnetic field experienced by an individual spin, $\underline{B}_{eff}$, evolves as it moves towards and through the labelling plane (b). The normalised longitudinal magnetisation of the spin, m_z, sweeps from +1 to –1 as it follows $\underline{B}_{eff}$ (c).

3.3 Method

3.3.1 The computer model

A computer model was developed using the C programming language, to solve numerically the modified Bloch equations for velocity driven AFP. This is similar to the model of Maccotta et al. (Maccotta L et al. 1997). The gyromagnetic ratio, γ, does not appear in calculations performed by the computer model because magnetic field strengths, $\underline{B}_1$ and $\underline{\Delta B}$, are expressed as a function of proton frequency throughout.

The change in magnetisation with precession about $\underline{B}_{eff}$ is calculated in the frame of reference that rotates at the frequency of $\underline{B}_{eff}$. The change in $\underline{m}$ may be expressed in terms of the rotation operators, $\mathbf{R}_\theta$ and $\mathbf{R}_\phi$. $\underline{m}$ is calculated at 100,000 points during the passage of a spin, moving at velocity, v, through the plane where B_1 is on resonance (see *Figure 3.2*). After each step, n:

$$\underline{m}_n = \mathbf{R}_\theta \, \mathbf{R}_\phi^{-1} \, \mathbf{R}_\theta^{-1} \, \underline{m}_{n-1} \qquad \text{equation [3.10]}$$

where: $\underline{m}_n$ is the normalised magnetisation at the nth step

θ is the angle between $\underline{\Delta B}$ and $\underline{B}_{eff}$

$\phi = 2\pi \, B_{eff} (\delta t)$ is the nutation angle of $\underline{m}$ about $\underline{B}_{eff}$ in a time increment δt

$$\mathbf{R}_\theta = \begin{pmatrix} \cos\theta & 0 & \sin\theta \\ 0 & 1 & 0 \\ -\sin\theta & 0 & \cos\theta \end{pmatrix} \qquad \mathbf{R}_\phi = \begin{pmatrix} \cos\phi & -\sin\phi & 0 \\ \sin\phi & \cos\phi & 0 \\ 0 & 0 & 1 \end{pmatrix} \qquad \text{equation [3.11]}$$

The steps performed by the computer programme are shown in a flow diagram in *Figure 3.2*. $\underline{B}_1$ is applied along the y-axis and the first transformation, $\mathbf{R}_\theta^{-1}$, maps $\underline{m}$ to $\underline{m}`$ in the reference frame where $\underline{B}_{eff}$ lies along the z`-axis. $\mathbf{R}_\phi^{-1}$ performs the rotation of $\underline{m}`$ about $\underline{B}_{eff}$ and $\mathbf{R}_\theta$ maps $\underline{m}`$ back to $\underline{m}$ in the laboratory reference frame.

A spin moves a specified distance along a linear magnetic field gradient, $\underline{G}$. At any position, z, between $- z_{max}$ and $+ z_{max}$, the offset frequency is $\Delta B = Gz$. The centre of the AFP is the labelling plane, where $z = 0$ and $\Delta B = 0$ (*Figure 3.1*). In the animal model v = 100 mm/s, consistent with velocities measured in the carotid artery by Zhang (Zhang W et al. 1993). In the human model v = 200 mm/s, which is within the normal range of velocities measured by Doppler Ultrasound (US) in the human carotid artery (Holdsworth DW et al. 1999). The time resolution depends on the velocity of the spin. For example, when a spin moves at a velocity of 100 mms^{-1} from a displacement of –20 mm to +20 mm in the model for CASL in rats, the time resolution is 4 μs. When a spin moves at 200 mms^{-1} from a displacement of – 100 mm to + 100 mm in the model for CASL in humans, the time resolution is 10 μs. Spin relaxation effects are calculated at each of the 100,000 points.

If the initial increment in θ is greater than the increment in ϕ, $\underline{m}$ cannot follow $\underline{B}_{eff}$ at the start and the process becomes non-adiabatic. A linear ramp was applied to $\underline{B}_1$ over the first and last 20% of the path of a spin to avoid a large jump in θ when a spin begins its passage through the labelling plane at $z = -z_{max}$. In practice, this is a valid assumption because the $\underline{B}_1$ field transmitted by an RF coil does not have a square profile, but tapers off at the end of the coil, as modelled by the ramp.

The final value of the longitudinal magnetisation (m_z) was used as a measure of the degree of inversion. This is the normalised m_z of water protons in blood when they reach the imaging plane, at $+ z_{max}$. $m_z(z = z_{max})$ determines the contribution of blood flow to the contrast in perfusion images.

Standard parameters were selected to model velocity driven AFP in animals at 2.35 T and in humans at 1.5 T (*Table 3.1*). One parameter was varied in each of a series of studies to assess its effect on the degree of inversion.

3.3.2 Optimisation of B_1

The dependence of m_z on B_1 was calculated in both the animal and human models, with and without spin relaxation. Values of z_{max} were fixed and G was selected to produce frequency offsets of between 4 kHz and 16 kHz, typical of those employed for CASL imaging (Ye FQ et al. 1997; Roberts DA et al. 1993; Detre JA et al. 1998; Calamante F et al. 1999). Calculations were performed without spin relaxation by setting $T_1 = T_2 = 10^6$ ms (as an approximation to $T_1 = T_2 = \infty$), and the optimum B_1 was defined as the lowest value of B_1 at which $m_z = -0.999$. When spin relaxation of arterial blood was included in the model (T_1 = 1000 ms, T_2 = 200 ms in the human model and T_1 = 1500 ms, T_2 = 150 ms in the animal model), m_z never reached – 0.999 and the optimum B_1 was defined as the value that produced the minimum m_z in the imaging plane (where $z = + z_{max}$).

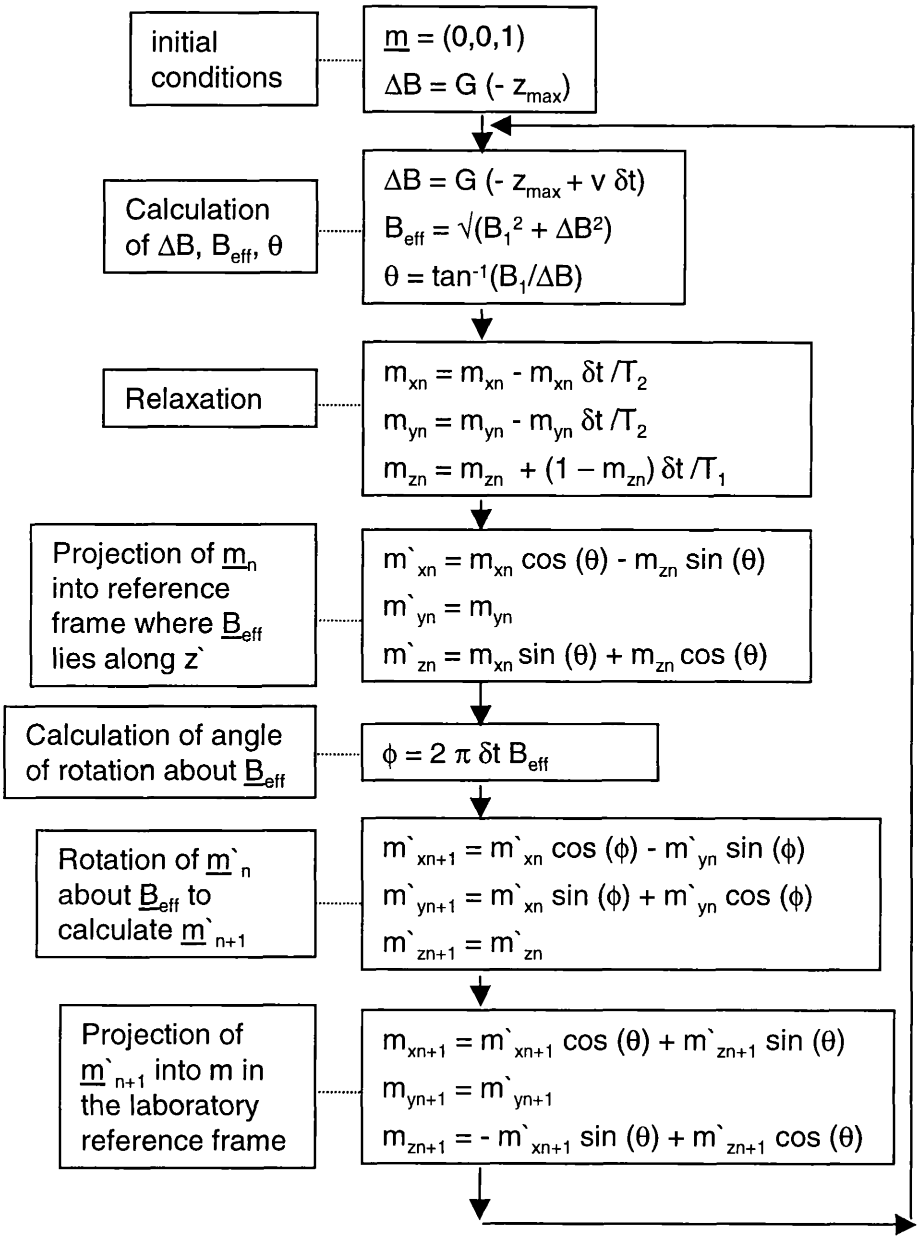

Figure 3.2

Calculations performed by the computer model of velocity driven AFP

The total number of iterations of these calculations is N = 100 000.

The time it takes for a spin to move from $-z_{max}$ to $+z_{max}$ at velocity v is $T = 2\,z_{max}/v$ and the time represented by each step in the model is $\delta t = T/N$

Parameter	Animal Model (2.35 T)	Human Model (1.5 T)
distance travelled	40 mm	200 mm
frequency offset	10 kHz, 5 kHz	10 kHz, 5 kHz
gradient (G)	500, 250 Hz/mm	100, 50 Hz/mm
spin velocity (v)	100 mm/s	200 mm/s
relaxation times of arterial blood	$T_1 = 1500$ ms $T_2 = 150$ ms	$T_1 = 1000$ ms $T_2 = 200$ ms

Table 3.1

Parameter values employed in the computer model of velocity driven AFP

The distance travelled is twice as great as the separation of the labelling and imaging planes (z_{max}). The frequency offsets are comparable with values in common use.

3.3.3 Spin relaxation at different static magnetic field strengths

Higher magnetic field strengths, B_0, are typically associated with longer T_1 and shorter T_2 values. T_1 values of arterial blood quoted in the literature range from 1100 ms to 1400 ms in humans at 1.5 T or 2 T (Gonzalez-At JB et al. 2000; Ye FQ et al. 1999; Walsh EG et al. 1994), and from 1340 ms to 2000 ms in rats at B_0 between 4.7 T and 8.5 T (Calamante F et al. 1999; Barbier EL et al. 2001; Zhang W et al. 1992). In order to assess the effect of T_1 on the degree of inversion by velocity driven AFP, T_1 was set at values representative of, and extending beyond, the range at currently employed B_0. The values of B_1 and v were fixed for two different values of G to produce frequency offsets of 5 kHz and 10 kHz. A similar procedure was performed for a range of T_2 values, representative of the same range of B_0.

3.3.4 Sensitivity of CASL to velocity

The degree of inversion was measured (i) at a range of constant blood velocities, v, and (ii) using the cardiac cycle-dependent velocity of blood flowing through the carotid artery to model more closely the conditions *in-vivo*. m_z in the imaging plane was calculated at constant v between 60 and 400 mm/s in the human model and 20 and 360 mm/s in the animal model.

The effect of variations in the velocity of blood on the degree of inversion was assessed initially using a randomly varying velocity. This showed that variations in v might have a significant effect on the value of m_z when a spin reaches the imaging plane. However, a closer approximation to the variation of v *in-vivo* was required.

Physiological variations in v were taken from a typical Doppler ultrasound (US) scan of blood flow through a normal human carotid artery (*Figure 3.3*). Doppler US scans include measurements of the velocity of blood at all positions within the artery, whereas the computer model of AFP requires a single velocity value at each time point. Points in the US scan with the highest intensity, corresponding to the velocity at which most of the blood was moving, were selected at 16 ms intervals and fitted linearly between these points. The data were normalised using normal values for the peak velocity (v_{peak}) and the duration of cardiac cycle (RR interval) of 1082 mm s^{-1} and 0.917 s respectively (Holdsworth DW et al. 1999). Velocities and RR intervals at the extremes of normal inter-subject ranges were investigated with the computer model by employing values at mean ± standard deviation, as measured by Holdsworth et al. (Holdsworth DW et al. 1999) (v_{peak} = 900 mm s^{-1} and 1260 mm s^{-1}; RR interval = 0.798 s and 1.036 s). Very high flow velocity was modelled using v_{peak} = 2000 mm s^{-1}. Spins pass through the centre of the inversion, where $z = 0$, at different phases of the cardiac cycle. This was modelled by moving the origin of the time axis for the velocity waveform relative to the start of the passage of a spin through the resonance of the AFP. The mean m_z of protons when they arrived in the imaging plane (where $z = + z_{max}$) was calculated for spins starting at 52 evenly spaced time intervals over the course of a single cardiac cycle. The mean m_z in the imaging plane of these 52 spins was compared with m_z of a proton moving at a constant v, equal to the time-averaged mean velocity over the RR interval. The time-averaged mean was 361 mm s^{-1} when v_{peak} was 1082 mm s^{-1}.

The average m_z of protons in blood water when they arrived in the imaging plane was calculated ($M_{z\_carotid}$). m_z was also calculated for a spin travelling at a constant velocity, equal to the mean velocity over the cardiac cycle (M_{z_vconst}). The efficiency of inversion with pulsatile flow, relative to the efficiency with constant velocity was calculated using the relationship:

$$\text{relative efficiency} = \frac{100 * (1 - M_{z\ carotid})}{(1 - M_{z\ vconst})} \qquad \text{equation [3.12]}$$

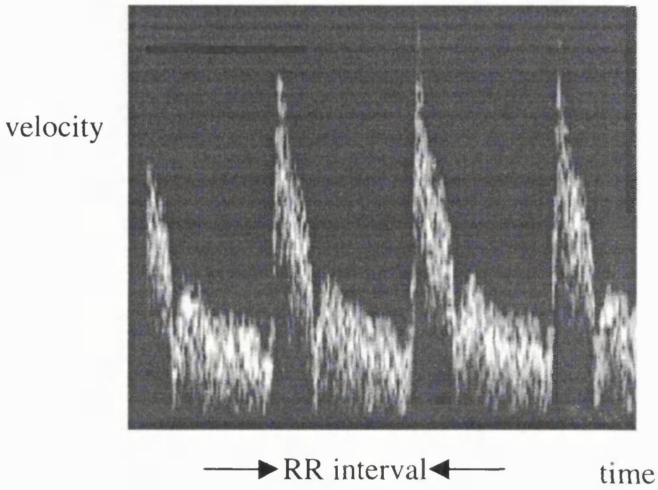

Figure 3.3

Doppler ultrasound scan of blood flow through a human common carotid artery. The velocity waveform is shown over three cardiac cycles. Ultrasound signal is reflected from blood cells as they move, producing a velocity dependent shift in the frequency of the reflected signal, which is detected. If more cells move at one particular velocity, a stronger signal is detected at the corresponding ultrasound frequency but signal is obtained from blood moving at any velocity. The range of velocity within the vessel is greater during systole than diastole.

3.3.5 CASL with a train of B_1 pulses

Radio-frequency pulse amplifiers used with clinical MRI scanners often have limits on the maximum duration of any single RF pulse. As a result, the relatively long pulse required for continuous ASL must be broken up to form a train of pulses. It has been assumed that the efficiency of AFP is proportional to the duty cycle at which the RF pulse train is applied (Ye FQ et al. 1997). This study was designed to test this assumption.

The effect of dividing B_1 into a train of RF pulses was assessed at a range of duty cycles, with periods of 100 ms, 50 ms and 20 ms (a duty cycle of 70 % with a period of 100 ms means that the RF is on for 70 ms and off for 30 ms). The mean value of m_z in the imaging plane (where $z = + z_{max}$) was calculated for spins starting their passage through the resonance of the AFP at 1000 different time points over a single B_1 pulse period.

The relative efficiency of labelling by velocity driven AFP when a train of RF pulses is employed for B_1 may be defined as

$$\text{relative efficiency} = \frac{100 * (1 - M_{z\,\mathrm{RF\,train}})}{(1 - M_{z\,\mathrm{Bconst}})} \qquad \text{equation [3.13]}$$

where $M_{z\,\mathrm{RF\,train}}$ is the mean m_z in the imaging plane over a complete pulse period (time for a single on-off cycle of B_1)

$M_{z\,\mathrm{Bconst}}$ is m_z in the imaging plane with constant B_1.

3.4 Results

3.4.1 Optimisation of B_1 with and without relaxation effects

Figure 3.4a shows m_z values of protons in the imaging plane after velocity driven AFP in the animal model. The values are shown at a range of different B_1 values, using a frequency offset of 5 kHz (G = 250 Hz mm^{-1}) both with spin relaxation (T_1 = 1500 ms, T_2 = 150 ms) and without spin relaxation ($T_1 = T_2 = 10^6$ ms). When there is no spin-relaxation, the degree of inversion increases with B_1 up to B_1 = 150 Hz, when m_z = -0.999 in the imaging plane. In the presence of T_2 relaxation, the degree of inversion reaches a maximum at B_1 = 110 Hz, and then declines at higher B_1 values. T_1 relaxation also reduces the degree of inversion, but a higher B_1 continues to improve the degree of inversion gradually when B_1 is greater than 100 Hz. The combination of T_1 and T_2 relaxation produces the smallest degree of inversion, with a single minimum m_z at the optimum value of B_1.

Less efficient inversion is achieved in the human model (*Figure 3.4b*) than in the animal model, largely as a result of more significant T_1 relaxation over the greater distance between the labelling plane and the imaging plane.

Optimum B_1 values depend on G and hence on the frequency offset, when z_{max} is fixed. In order to study the relationship between G, v and B_1 for minimum m_z, optimum values of B_1 were determined in both the animal model and the human model at a range of frequency offsets. These data are shown in *Figure 3.5* along with the corresponding optimum B_1 values for the most efficient inversion without relaxation effects. Optimum B_1 values are consistently lower with spin relaxation than without spin relaxation.

a) animal model

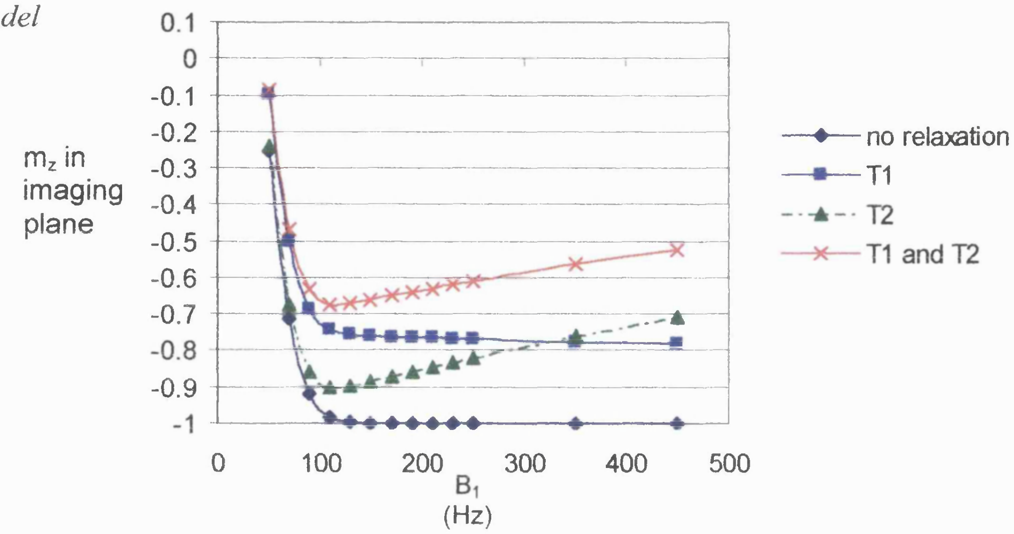

b) human model

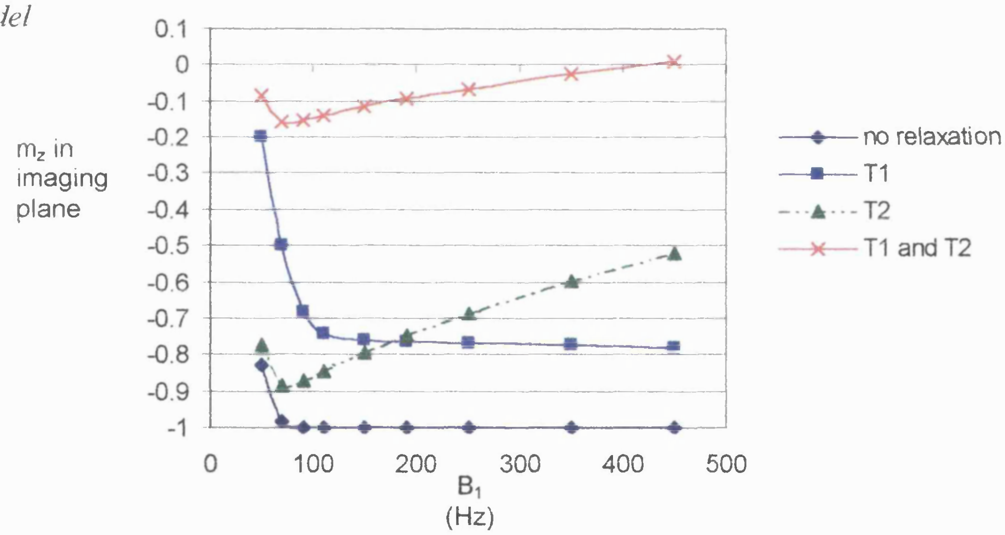

Figure 3.4

Efficiency of inversion at different B_1 amplitudes with spin-relaxation

frequency offset = 5 kHz,

v = 100 mm/s, T_1 = 1500 ms, T_2 = 150 ms in the animal model (a).

v = 200 mm/s, T_1 = 1000 ms, T_2 = 200 ms in the human model (b).

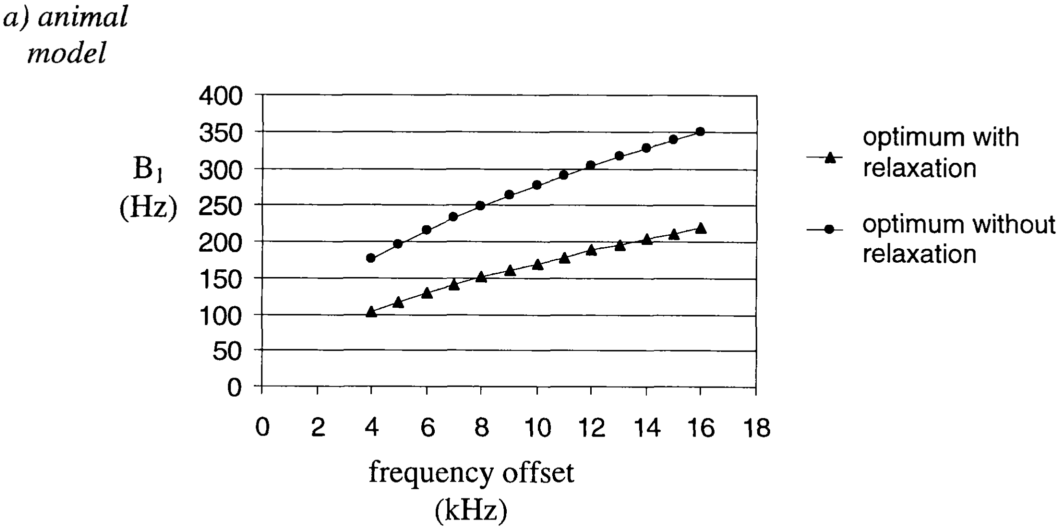

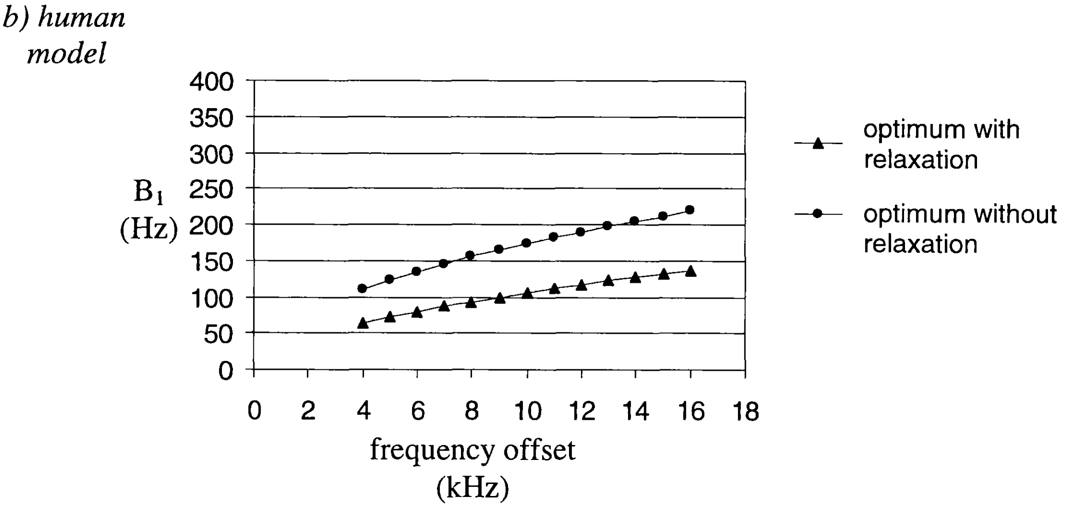

Figure 3.5

Optimum B_1 amplitudes with and without spin-relaxation

The optimum B_1 is the value required for the greatest degree of inversion

$v = 100$ mm/s, $T_1 = 1500$ ms, $T_2 = 150$ ms in the animal model (a).

$v = 200$ mm/s, $T_1 = 1000$ ms, $T_2 = 200$ ms in the human model (b).

When optimum values of B_1^2 are plotted with respect to Gv, a straight line may be fit (*Figure 3.6*). The slope of this line is the optimal value of the adiabaticity factor, β. In the absence of spin relaxation, the square of the optimum value of B_1 was found to depend linearly on the product Gv, with constants of proportionality of 1.50 ($r = 0.9999$) and 1.53 ($r = 0.9999$) in the human and animal models respectively. The constants of proportionality with T_1 and T_2 relaxation are 0.64 ($r = 0.9999$) and 0.65 ($r = 0.9999$) in the human and animal models. These constants are the optimal values of β.

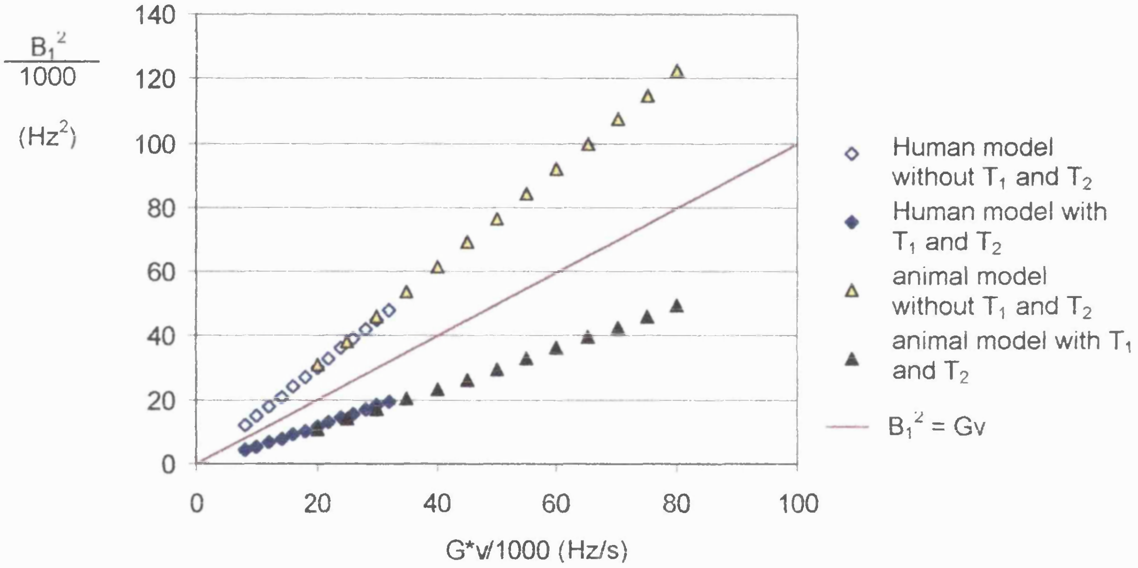

Figure 3.6

Relationships between optimum B_1 values and the product of the gradient amplitude and velocity, Gv. Results are shown with and without relaxation. Without relaxation, the adiabatic condition demands $B_1^2 > Gv$.

$v = 200$ mm/s, $T_1 = 1000$ ms, $T_2 = 200$ ms in the human model

$v = 100$ mm/s, $T_1 = 1500$ ms, $T_2 = 150$ ms in the animal model

Slightly better inversion is achieved at higher G, but at the expense of higher optimum B_1 values and hence greater RF power deposition (*Figure 3.7*). For example, the lowest values of m_z in the imaging plane with frequency offsets of 5 kHz and 10 kHz are – 0.67 and – 0.69 respectively in the animal model (*Figure 3.7a*). However, the amplitudes of B_1 required to achieve these m_z values are 118 Hz and 172 Hz, resulting in more than twice as much RF power deposition at a frequency offset of 10 kHz as at a frequency offset of 5 kHz.

3.4.2 Spin relaxation at different static magnetic field strengths

The degree of inversion increases at greater T_1 values (*Figure 3.8*). There is negligible dependence on frequency offset, but inversion is consistently more efficient in the animal model than in the human model because the separation of the labelling plane from the imaging plane is considerably smaller in the animal model, reducing the time available for T_1 relaxation.

T_2 has a smaller effect on the degree of inversion than T_1 (compare *Figure 3.9* with *Figure 3.8*). There is less T_2 relaxation at a frequency offset of 10 kHz than at 5 kHz because the larger G for the 10 kHz offset produces a more rapid frequency sweep, reducing the time $\underline{m}$ spends in the transverse plane. T_2 effects are less significant in the animal model than in the human model because values of $\underline{G}$ are five times greater than in the human model to produce the same frequency offsets.

a) *animal model*

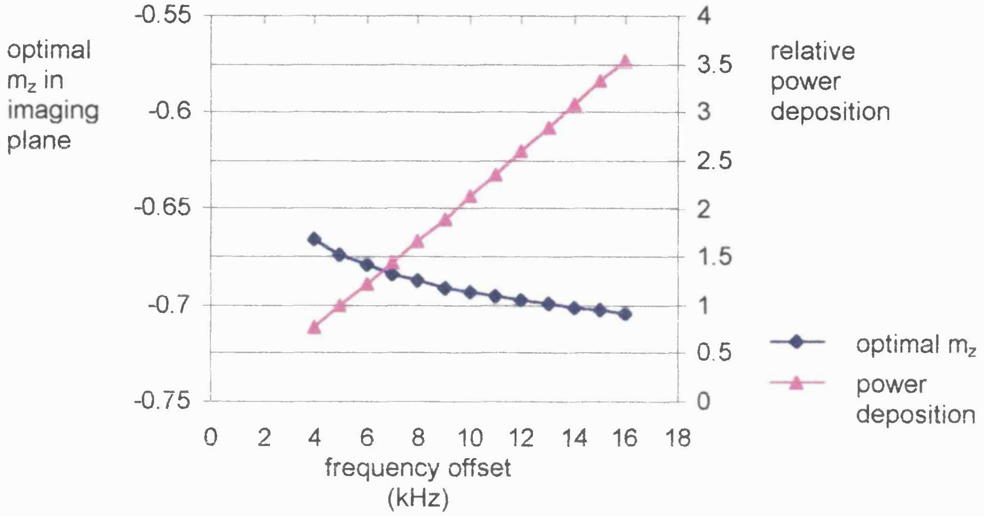

b) human model

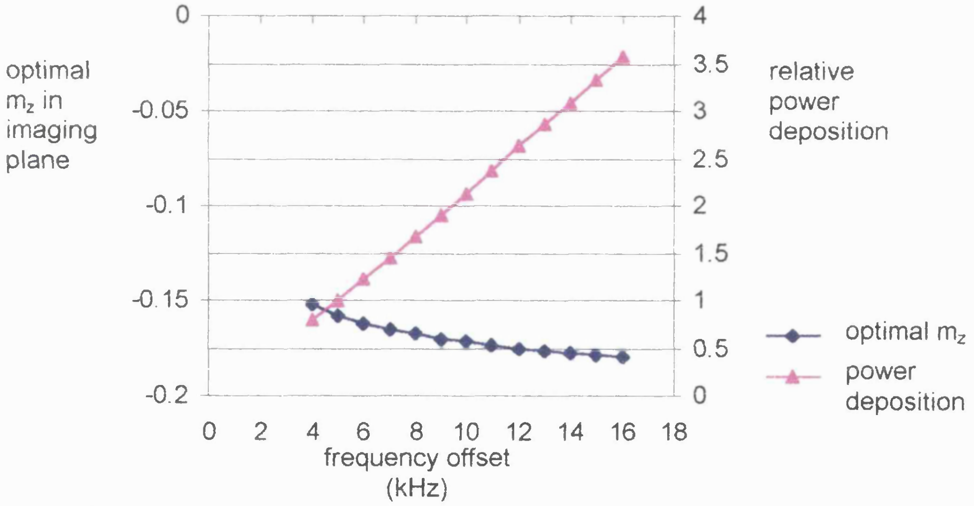

Figure 3.7

Optimal m_z values and relative power deposition at a range of frequency offsets. Values of the power deposition are quoted relative to the power deposition with the optimal B_1 for an offset of 5 kHz.

$v = 100$ mm/s, $T_1 = 1500$ ms, $T_2 = 150$ ms in the animal model (a).

$v = 200$ mm/s, $T_1 = 1000$ ms, $T_2 = 200$ ms in the human model (b).

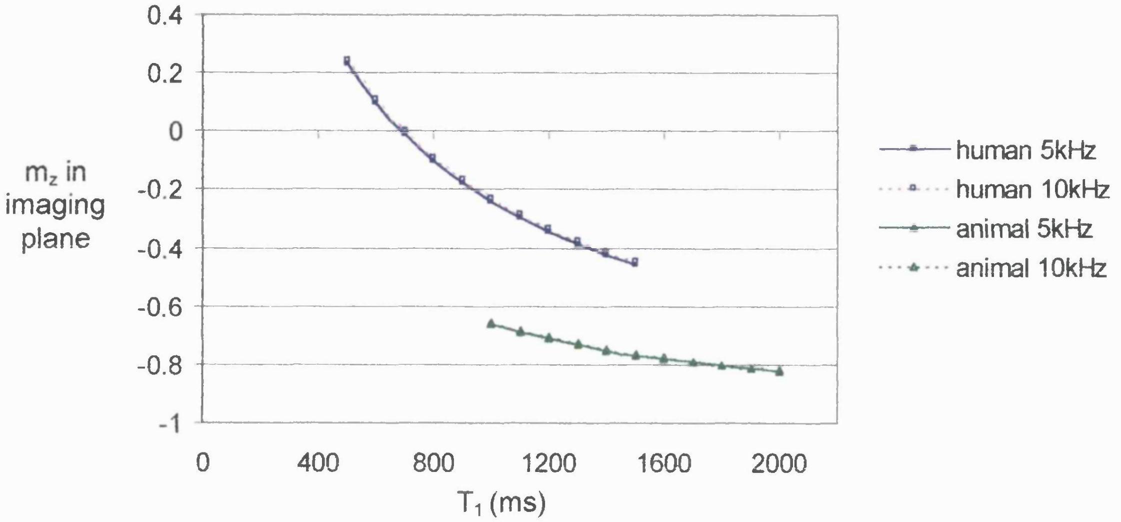

Figure 3.8

Sensitivity of velocity driven AFP to T_1 Relaxation.

In the human model, v = 200 mm/s, B_1 = 150 Hz and B_1 = 190 Hz at frequency offsets of 5 kHz and 10 kHz respectively. In the animal model v = 100 mm/s, B_1 = 210 Hz and B_1 = 300 Hz at frequency offsets of 5 kHz and 10 kHz respectively. $T_2 = 10^6$ ms

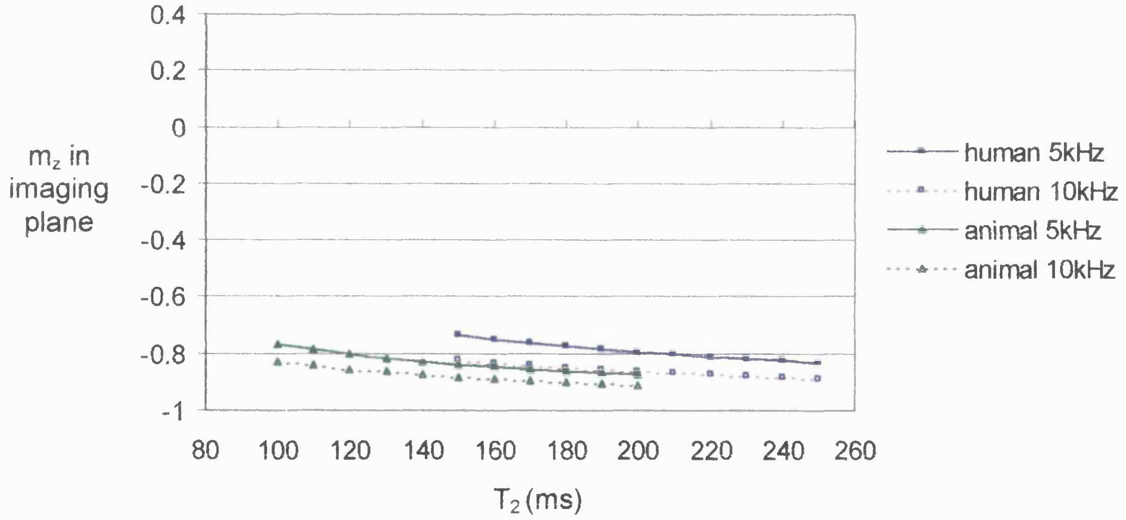

Figure 3.9

Sensitivity of velocity driven AFP to T_2 Relaxation

In the human model, v = 200 mm/s, B_1 = 150 Hz and B_1 = 190 Hz at frequency offsets of 5 kHz and 10 kHz respectively. In the animal model v = 100 mm/s, B_1 = 210 Hz and B_1 = 300 Hz at frequency offsets of 5 kHz and 10 kHz respectively. $T_1 = 10^6$ ms.

3.4.3 Sensitivity of CASL to velocity

Constant Velocity

In the absence of spin relaxation, there is no significant dependence of the degree of inversion on v, over a large range of constant velocities (*Figure 3.10*). Spin relaxation reduces the degree of inversion, but at higher v the effects of T_1 and T_2 are smaller. The amount of T_1 relaxation is more strongly dependent on v in the human model than in the animal model, largely because there is more time for T_1 relaxation between the labelling and imaging planes.

Variable Velocity

Spins move through the labelling plane at different times in the cardiac cycle. *Figure 3.11* shows that m_z in the imaging plane for individual spins varies from $m_z \approx 0.00$ to $m_z \approx -0.75$ with a frequency offset of 10 kHz. The degree of inversion is greatest when blood moves through the labelling plane at the peak velocity. The velocity of blood flowing through the human carotid artery in the data set employed to produce *Figure 3.11* varied between approximately 200 and 400 mm s^{-1} during diastole and up to 1082 mm s^{-1} during systole. Variations in m_z immediately after inversion are amplified by significant T_1 relaxation between the labelling and imaging planes, especially for slower spins.

Values were calculated of the average m_z in the imaging plane over a cardiac cycle ($M_{z\ carotid}$) and the corresponding value of m_z for a spin moving with a constant velocity equal to the time averaged mean ($M_{z\ vconst}$). From these values the relative efficiency of labelling with pulsatile blood flow was calculated (equation [3.12]). Table 3.2 shows the results with mean v_{peak} (1082 mm s^{-1}) and RR interval (0.917 s) and with v_{peak} and RR intervals at the extremes of normal ranges (± inter-subject standard deviation (Holdsworth DW et al. 1999)). $M_{z\ carotid}$ is generally slightly lower with a 10 kHz offset than a 5 kHz offset, corresponding to a greater degree of inversion. The degree of inversion is strongly dependent on v_{peak}, and therefore on the mean v, ranging from $M_{z\ carotid} = -0.327$ when $v_{peak} = 900$ mm s^{-1} to -0.646 when $v_{peak} = 2000$ mm s^{-1} (5 kHz offset). However, the mean efficiency of labelling is equal to that for a spin moving at constant v, equal to the time-averaged mean, to within ± 2.3 % in nearly all cases. The exception is at $v_{peak} = 2000$ mm s^{-1} with an offset of 10 kHz, when the relative efficiency of labelling is 96.4 %. This may be because the amplitude of B_1 is too low to invert spins moving through the labelling plane during systole at this high velocity.

a) animal model

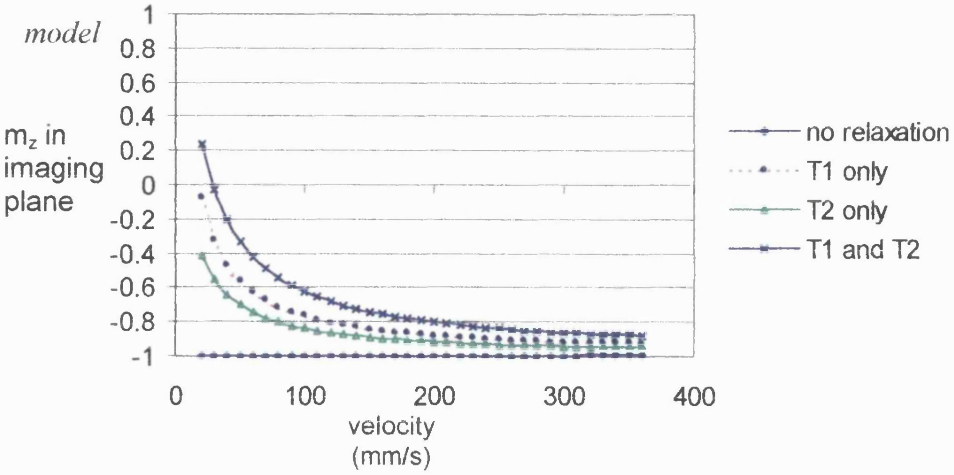

b) human model

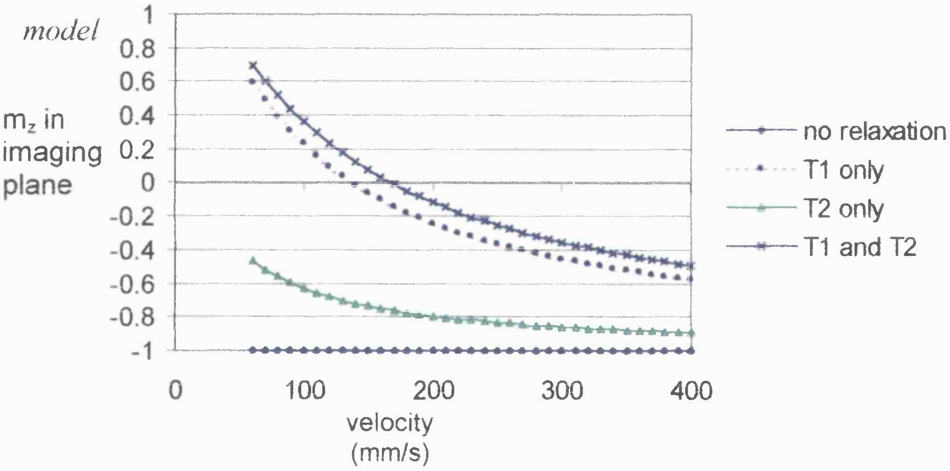

Figure 3.10

Sensitivity of Velocity Driven AFP to Velocity

5 kHz offset, $B_1 = 220$Hz, $T_1 = 1500$ ms, $T_2 = 150$ ms in the animal model (a).

5 kHz offset, $B_1 = 150$Hz, $T_1 = 1000$ ms, $T_2 = 200$ ms in the human model (b).

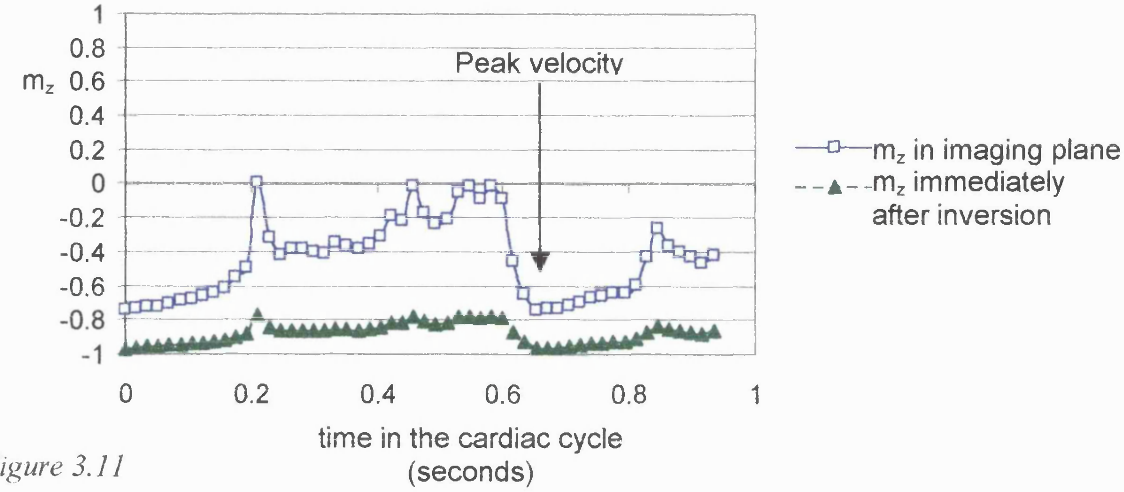

Figure 3.11

Degree of inversion by velocity driven AFP at intervals throughout the cardiac cycle. Values of m_z immediately after inversion and m_z in the imaging plane are shown for each spin. The time is indicated at which the velocity reaches its peak amplitude. Frequency offset of imaging plane from labelling plane = 10 kHz, B_1 = 190 Hz, T_1 = 1000 ms, T_2 = 200 ms.

		[a] 5 kHz offset		[b] 10 kHz offset	
Peak Velocity (mm s^{-1})	RR Interval (seconds)	$M_{z\ \mathrm{carotid}}$	[c] Relative Efficiency (%)	$M_{z\ \mathrm{carotid}}$	[c] Relative Efficiency (%)
1082	0.928	-0.425	98.7	-0.445	98.3
1082	0.808	-0.415	98.0	-0.436	97.7
1082	1.049	-0.458	100.9	-0.475	100.4
900	0.928	-0.327	98.1	-0.352	97.9
1260	0.928	-0.523	100.7	-0.535	100.0
2000	0.928	-0.646	98.3	-0.624	96.4

Table 3.2

Degree of inversion by velocity driven AFP over the course of a single cardiac cycle.

[a] B_1 = 150 Hz at a frequency offset of 5 kHz.

[b] B_1 = 190 Hz at a frequency offset of 10 kHz.

[c] relative efficiency = $\dfrac{100 * (1 - M_{z\ \mathrm{carotid}})}{(1 - M_{z\ \mathrm{vconst}})}$

3.4.4 CASL with a train of B_1 pulses

Results are shown for RF pulse periods of 20 ms, 50 ms and 100 ms at frequency offsets of 5 kHz (*Figure 3.12a*) and 10 kHz (*Figure 3.12b*). The assumption of linearity between duty cycle and efficiency clearly is not valid. Inversion efficiency may be as low as 65 % with a 95 % duty cycle. Even with a duty cycle of 99 %, the relative efficiency is approximately only 90 % at any pulse period. If linearity between the degree of inversion and duty cycle were to be assumed, labelling efficiency would tend to be over-estimated, which would lead to under-estimation of perfusion in a CASL experiment.

Figure 3.13 illustrates the most likely cause of the non-linear dependence of labelling efficiency on the RF duty cycle. An ideal AFP might be described as one that occurred instantaneously, to produce a step in magnetisation from $m_z = +1$ to $m_z = -1$. Real AFP occurs over a finite period of time, characterised by an initially gradual change in m_z with an increasing rate of change towards the centre of the inversion.

When an RF pulse train is employed the ideal AFP would produce no inversion if a spin went through the inversion plane (where $z = 0$) when the amplitude of B_1 was zero. However, a real AFP may have begun before B_1 was turned off and although the inversion would be incomplete, m_z would be reduced to less than +1, resulting in partial labelling. Similarly if B_1 was non-zero as the spin passed the centre of the AFP, but became zero immediately afterwards, an ideal AFP would produce full inversion but the real AFP would be interrupted, m_z would not reach –1, and again partial labelling would result.

An ideal AFP would result in either $m_z = -1$ or $m_z = +1$. The number of spins inverted by such an ideal pulse would be proportional to the duty cycle of the RF pulse train and it would be possible to predict the average inversion efficiency. In practice, AFP does not produce a step change in m_z. After AFP with a train of B_1 pulses, m_z may have any value between –1 and +1, and the degree of inversion has a complicated non-linear dependence on the duty cycle of the RF pulse.

a) 5 kHz offset

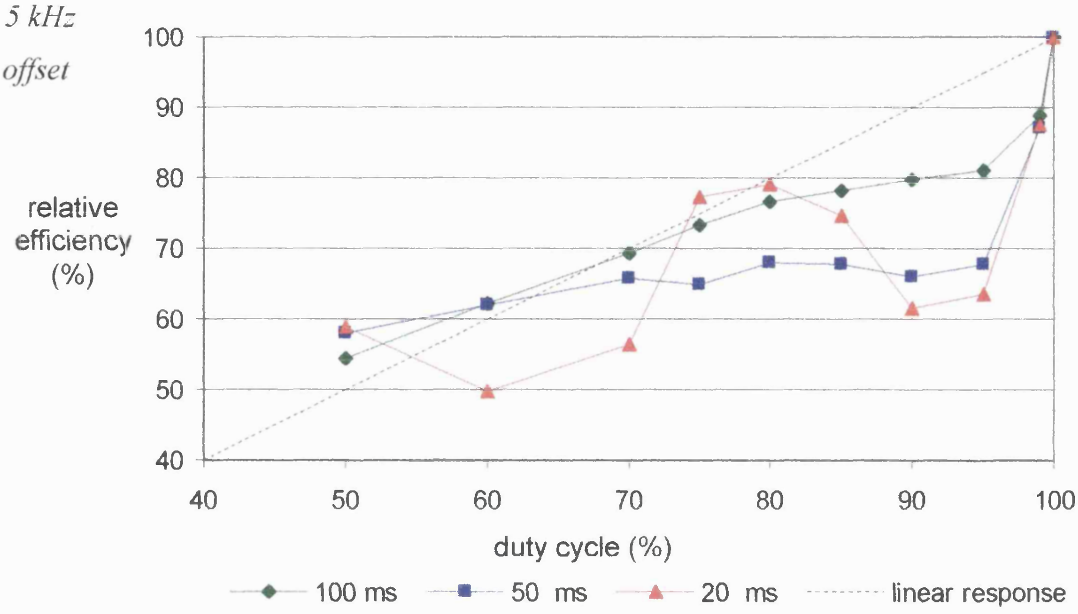

b) *10 kHz offset*

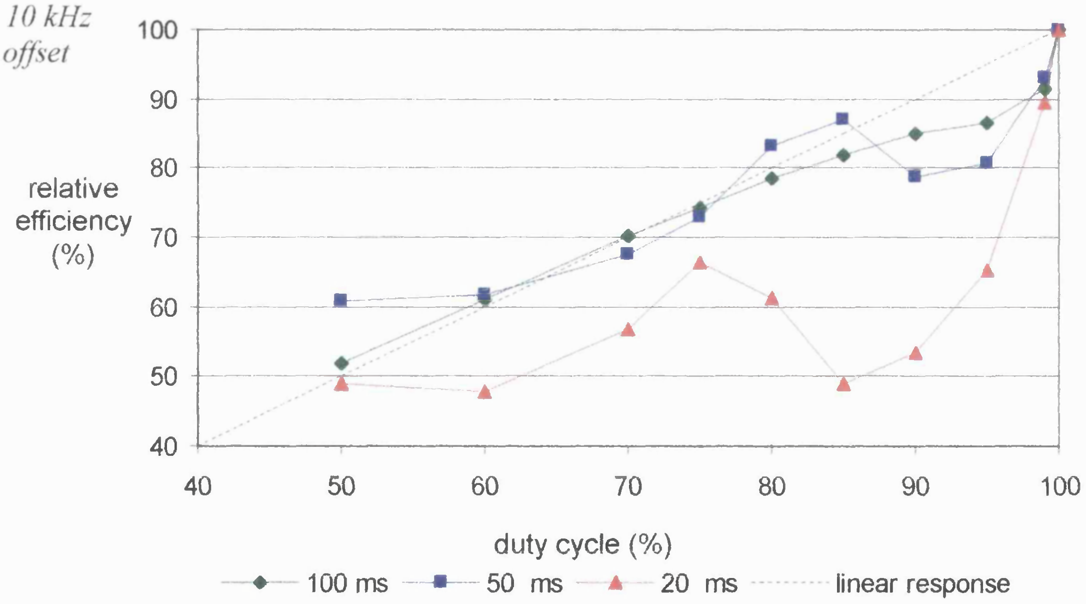

Figure 3.12

Relative efficiency of inversion with a train of RF pulses

Inversion efficiency at three different pulse periods is shown at an offset of 5 kHz with $B_1 = 150\text{Hz}$ (a) and at an offset of 10 kHz with $B_1 = 190$ Hz (b) with v = 210 mm/s, $T_1 = T_2 = 10^6$ ms. A linear response to duty cycle is shown for comparison.

$$\text{relative efficiency} = \frac{100 * (1 - M_{z\ rf\_train})}{(1 - M_{z\ Bconst})}$$

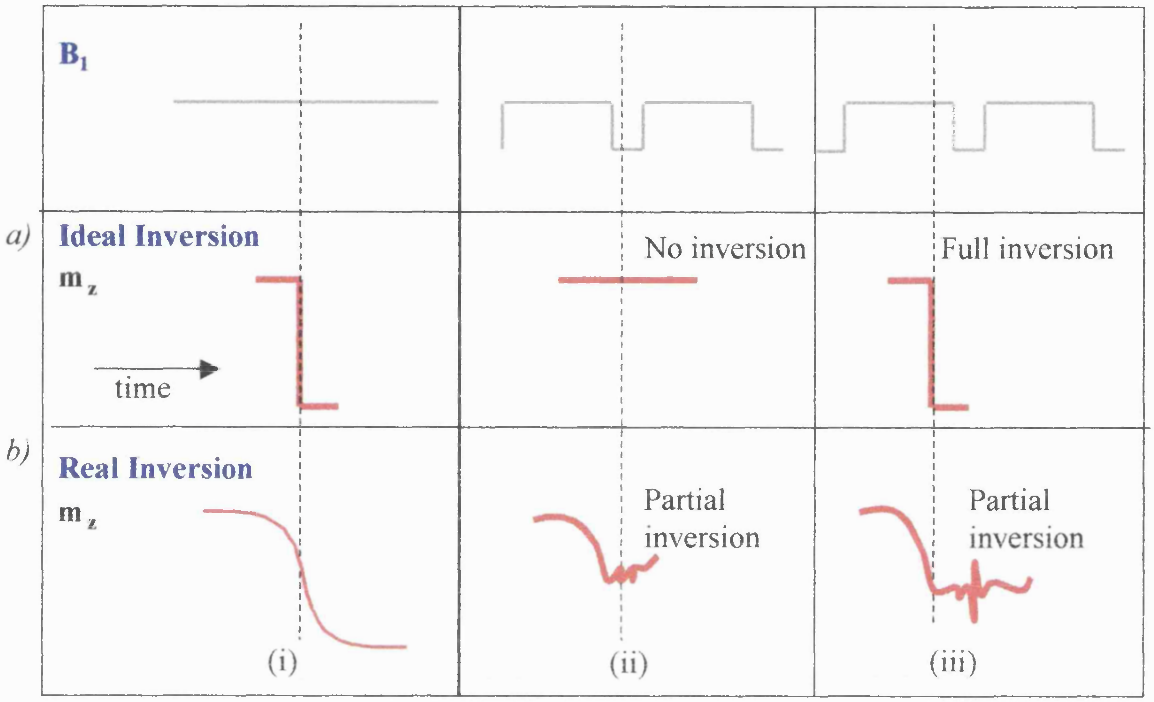

Figure 3.13

Non-linear dependence on RF duty cycle of relative efficiency of inversion by AFP

m_z is shown for an ideal, instantaneous AFP (a) and a realistic AFP (b), of finite duration. The change in m_z in three cases is shown, constant B_1 (i); B_1 off as the spin passes through the centre of the labelling plane (ii); B_1 on as the spin passes through the labelling plane, but off immediately afterwards (iii).

3.5 Discussion

3.5.1 Optimisation of B_1

The adiabatic condition (equation [3.4]) states that the rate of change of the effective magnetic field, $\underline{B}_{eff}$, must be much less than the rate of precession of magnetisation about this field and much greater than the spin relaxation rates. In order to optimise pulse parameters it is useful to know what is meant by "much less than" in quantitative terms, which may be done in terms of the dimensionless adiabaticity factor, β, where $\beta = \gamma B_1^2/(Gv)$ (Roberts DA et al. 1994).

At the centre of the AFP, or in the absence of spin-relaxation, the adiabatic condition may be expressed as $\beta >> 1$. In view of this, it is interesting to note that the minimum β for full inversion by velocity driven AFP is only 1.5 in the absence of relaxation. In practice, however, relaxation effects cannot be ignored and the greatest degree of inversion with typical relaxation times for blood is achieved when β is only 0.64 in the human model and 0.65 in the animal model. The low values of β when spin relaxation is included may be explained by considering the left hand side of the adiabatic condition, which may be expressed as in equation [3.8]. This condition is most difficult to satisfy at the beginning and end of the frequency sweep. Excessive $\underline{B}_1$ amplitudes reduce the degree of inversion by increasing the duration of the AFP, and hence introducing more T_2 relaxation (*Figure 3.4*). Higher values of G result in a more rapid frequency sweep, smaller Δt (equation [3.9]), and hence much less pronounced T_2 relaxation. The effect of higher G is seen by comparison of results in the animal and the human models, in *Figure 3.9* where G is 5 times greater in the animal model than in the human model.

If B_1 is greater than the optimum, then relaxation effects reduce the degree of inversion (*Figure 3.4*). However, if B_1 is slightly too large, the reduction is not as significant as if B_1 is slightly too small, as seen by comparison of m_z values with $B_1 =$ 130 Hz and $B_1 = 90$ Hz in *Figure 3.4a*, for which the optimum B_1 is approximately 110 Hz. This dependence on B_1 is particularly important when the $\underline{B}_1$ field is non-uniform.

A large frequency offset is required to reduce magnetisation transfer contrast in CASL images. Results presented here show that the minimum achievable m_z for a fixed spatial separation of inversion and imaging planes depends on the choice of frequency offset, but only weakly (*Figure 3.7*). Higher values of G result in slightly lower m_z, but at the expense of greater RF power deposition. For example, doubling the frequency offset from 5 kHz to 10 kHz in the animal model achieves an increase in the degree of inversion of approximately 1 %, but RF power deposition more than doubles.

Maccotta et al. investigated velocity driven AFP using a similar computer model to the one presented here (Maccotta L et al. 1997). By calculating β for the parameters employed in that study, it may be shown that their results are consistent with the prediction $\beta = 0.64$ for the maximum degree of inversion. Maccotta et al. assumed laminar flow, and averaged m_z values over the corresponding distribution of velocities within an artery. Taking the mean velocity of approximately v = 200 mm/s with a gradient amplitude of 0.25 G/cm (106.5 Hz/mm), $\sqrt{(0.64\ Gv)} = 117$ Hz. The optimum value of B_1 found by Maccotta et al. with these parameters was 22 mG (94 Hz). Results from the model of Marro et al. are less consistent with the prediction $\beta = 0.64$ for the optimum degree of inversion (Marro KI et al. 1997). In a gradient of 0.2 G/cm (85 Hz/mm) with a velocity of 600 mm/s, $\sqrt{(0.64\ Gv)} = 181$ Hz. The optimum B_1 derived by Marro et al. was 150 mG (approximately 630 Hz), giving $\beta = 8.0$. The model employed by Marro et al. differed from that of Maccotta and the model presented here in two important respects. Firstly, relaxation effects were not included and the phantom employed to verify results from the computer model was filled with distilled water, which has much longer T_1 and T_2 values than blood. Secondly, Marro et al. modelled velocity driven AFP for a two-coil experiment, employing a separate surface coil for labelling, with a significantly non-uniform $\underline{B}_1$ distribution. A recent report by Gach et al. shows optimum values of β of approximately 4 in a flow phantom, over a range of velocities (Gach HM et al. 2002). However, direct comparison of their results with this chapter is complicated by at least two factors. The data shown by Gach et al. were acquired with a train of RF pulses with a duty cycle of 95 % and the value of T_2 in the fluid filling the phantom is not quoted. Results in this chapter show that both of these factors influence the degree of inversion (*Figure 3.12* and *Figure 3.4*).

3.5.2 Effects of different T_1 and T_2

The higher T_1 values of arterial blood at high B_0 fields produce greater degrees of inversion and smaller losses through relaxation in transit to the imaging plane, resulting in greater sensitivity of CASL images to perfusion, as demonstrated by Franke et al. (Franke C et al. 2000). The relatively small dependence of m_z on T_2 (*Figure 3.9)* implies that the loss in the degree of inversion due to increased T_2 relaxation at high B_0

is outweighed by the gain associated with higher T_1 values. This is more significant in humans, where the T_1 relaxation in blood before it arrives in the imaging plane is substantial. However, at high B_0, greater RF power deposition is necessary to produce a given B_1 amplitude and this may prove to be the most significant limitation of CASL for human studies at high B_0.

3.5.3 Sensitivity to velocity

The velocity of blood determines both the speed of the frequency sweep and the time it takes for spins to travel from the labelling plane to the imaging plane. There are three competing effects as v increases. Firstly, the degree of inversion is reduced when v is too high to satisfy the right hand side of the adiabatic condition (equation [3.4]). This effect is not significant within the range of velocities typical of flow through the carotid arteries (observed in data sets without spin relaxation in *Figure 3.10*). Secondly, protons in faster moving blood experience less T_2 relaxation during the inversion. Finally, at higher velocities spins arrive in the imaging plane sooner after labelling, allowing less time for T_1 relaxation of the label. This is a more important consideration in humans than in small animals, because of the greater distance between the labelling and imaging planes.

T_1 relaxation in the time it takes for blood to travel from the labelling plane to the imaging plane has the greatest effect on m_z. The arterial transit time may be reduced by placing the labelling plane closer to the imaging plane. However, the velocity of blood tends to decrease in smaller vessels, closer to the capillary bed and the most significant T_1 relaxation occurs within arterioles closest to the imaging plane. In subjects with normal cerebral vascular supply, positioning the labelling plane closer to the imaging plane may not significantly reduce the arterial transit time, and may introduce more T_2 relaxation due to the slower frequency sweep during AFP.

The influence of physiological variations in velocity on labelling for ASL has not been studied previously. The velocity of blood in arteries changes constantly over the cardiac cycle and results presented here demonstrate the consequent significant variations in the degree of inversion by velocity driven AFP (*Figure 3.11*). Differences in m_z immediately after labelling are accentuated by T_1 relaxation in blood as it moves to the imaging plane. However, it has been found that the average m_z over a complete cardiac cycle is approximately the same as m_z of a spin moving at a constant velocity, equal to the time-averaged mean, except at very high peak velocities (*Table 3.2*). The greater degree of inversion during systole tends to compensate for the lower efficiency of labelling during diastole. Therefore an assumption of constant v to predict the degree of inversion may be justified, unless B_1 is too small, at a given G, to label a significant proportion of the fastest spins.

In general, many averages are employed for CASL image acquisitions, including dozens of cardiac cycles in each measurement, so that an assumption of constant velocity is not likely to affect the accuracy of perfusion values. However, for some recent ASL techniques, which intersperse short labelling pulses with rapid image acquisitions (Silva AC and Kim SG 1999; Barbier EL et al. 2001; Williams DS et al. 2001), there may be a case for cardiac gating to ensure that measurements of apparent changes in perfusion are not confounded by changes in m_z, due to variations in blood velocity during the cardiac cycle.

3.5.4 RF pulse train for B_1

Clinical MRI scanners often impose upper limits on the duration of the output from their RF pulse amplifiers. As a result, the relatively long B_1 pulse required for CASL must be divided into a train of pulses. It has been assumed that the relative efficiency of AFP is proportional to the duty cycle of the RF pulse train (Ye FQ et al. 1997; Silva AC and Kim SG 1999). However, the results of this chapter show that m_z has a highly non-linear dependence on RF duty cycle (*Figure 3.12*). This finding may be explained by partial labelling of spins. AFP occurs over a finite period of time and partial inversion results when B_1 is off at any time during the AFP process. In the case where $B_1 = 0$ as the spin passes through the labelling plane, some degree of inversion might be achieved if B_1 were non-zero immediately before or after this point. Alternatively, in the case where B_1 is on as the spin passes through the labelling plane, but becomes zero before the inversion is complete, m_z is unlikely to reach the lowest value possible with a constant B_1 pulse.

At the majority of RF duty cycles an assumption of proportionality between labelling efficiency and duty cycle would lead to over-estimation of the degree of inversion and hence under-estimation of tissue perfusion. Comparison of results with frequency offsets of 10 kHz and 5 kHz shows a closer approximation to a linear relationship between relative inversion efficiency and duty cycle at 10 kHz, for which G is larger (*Figure 3.12*). Comparison of results with pulse periods of 50 ms and 100 ms shows a closer approximation to a linear relationship with the longer pulse period.

When G is larger, or the pulse period is longer, fewer spins undergo partial inversion because it is more likely that the whole AFP will be completed within the time for which B_1 is on, and the assumption of linearity between duty cycle and relative efficiency is a closer approximation to the real situation. Data have been presented for the human model, although this finding also may have implications for animal studies using dynamic (Barbier EL et al. 2001) or pseudo-continuous (Silva AC and Kim SG 1999) ASL.

The effect of a train of RF pulses on the degree of inversion by velocity driven AFP has been considered in this chapter. The amplitude of the perfusion-dependent signal depends also on subsequent relaxation of labelled spins and this may warrant further examination. Labelled spins in blood arrive in tissue with magnetisation:

$$m_z = \alpha\, e^{(-\delta/T1a)}$$

where α is the efficiency of labelling,

δ is the arterial transit time,

T_{1a} is the longitudinal relaxation time of arterial blood.

Labelled spins then exchange into tissue, and continue to relax with the T_1 relaxation time of the tissue. In the case of a train of RF pulses, the tissue relaxation time changes periodically from T_{1sat} to T_1, where T_{1sat} is the relaxation time in the presence of the labelling pulse. The mixture of spins with different relaxation histories may have a significant effect on the signal intensity for techniques that rapidly cycle between labelling and acquisition phases to provide high temporal resolution.

3.6 Summary and conclusions

The results from this chapter may be employed to maximise the sensitivity of CASL measurements. A simple protocol for selecting pulse parameters for labelling blood by velocity driven AFP may be summarised as follows:

- Choose a labelling plane orthogonal to the direction of flow, which intersects the major vessels supplying the organ to be studied.
- Choose the lowest gradient amplitude, G, to obtain a frequency offset between the labelling and imaging planes that is sufficient to reduce magnetisation transfer contrast in the ASL images.

- Estimate the mean velocity of blood that is to be labelled, v.
- Set $B_1 = \sqrt{(0.64Gv)}$, where B_1, G and v are expressed is in Hz, Hz mm^{-1} and mm s^{-1} respectively.

If a train of RF pulses must be employed for velocity driven AFP, ideally the degree of inversion would be measured with the RF pulse train employed for the CASL experiment. If this measurement is not possible, our results suggest that larger G and the longest possible pulse period may be desirable for a more linear dependence of the degree of inversion on the RF duty cycle.

In conclusion, a computer model has been developed and used to establish optimum parameters for velocity driven AFP. Optimum values of the adiabaticity factor, β, are lower than unity, emphasising the importance of the spin relaxation component of the adiabatic condition. Longer T_1 values at higher static magnetic field strengths increase the efficiency of labelling significantly, especially for studies in humans. Pulsatile flow has been shown to profoundly affect the degree of inversion of individual spins. However, the mean effect of velocity driven AFP over the course of the cardiac cycle may be predicted from the behaviour of a spin, travelling at the time-averaged mean velocity of the blood. Dividing the labelling pulse, B_1, into a train of RF pulses has been shown to result in a degree of inversion with a highly non-linear dependence on the duty cycle of the RF pulse, contrary to previous assumptions.

4 Computer modelling of the amplitude modulated control for multiple-slice continuous arterial spin labelling

4.1 Introduction

Continuous arterial spin labelling (CASL) is performed by velocity driven adiabatic fast passage (AFP), as described in Chapter 3. Labelled blood changes the magnetisation of tissue it perfuses, producing images with perfusion-weighted contrast. The frequency offset of the off-resonance RF pulse for labelling, B_1, is usually great enough that direct excitation of the water signal in the imaging slices(s) is negligible. However, protons in macromolecules, such as proteins and cell membranes have broad resonances and even at offsets of several kHz, the nuclei of these molecules are excited by B_1. Magnetisation transfer (MT) between macromolecules and free water reduces the magnetisation of free water, introducing magnetisation transfer contrast (MTC) in CASL images. A control preparation is required to produce the same MTC as the labelling preparation, but without any perfusion weighting.

Velocity driven AFP is achieved by applying B_1 in a plane through which arterial blood flows parallel to a magnetic field gradient, $\underline{G}$, on the way to the imaging plane(s). The standard control technique for CASL is to reverse the sign of either $\underline{G}$ or the frequency offset of B_1 to define a control plane, which is above the head for cerebral blood flow imaging (see *Figure 2.8* in Chapter 2) (Williams DS et al. 1992). Assuming that blood enters tissue only from vessels proximal to the imaging plane, inflowing blood is not labelled by the control preparation

The standard control ensures equivalent static tissue irradiation by the labelling and control schemes at a single slice position, half way between the label and control planes. An alternative control scheme is required for multiple slice imaging. Several strategies have been suggested, including separate labelling and imaging coils (Zhang W et al. 1995), simultaneous proximal and distal inversion, SPDI (Talagala SL et al. 1998), and an amplitude modulated (AM) control (Alsop DC and Detre JA 1998).

A separate labelling coil produces no excitation, and hence no MT, outside its own sensitive volume. Separate labelling coils are commonly surface coils, and non-uniformity of the B_1 field is likely to result in different degrees of labelling in arteries at different positions relative to the coil. This may be exploited to map the territory of a single artery with a small labelling coil (Zaharchuk G et al. 1999b), but is of limited use for studies of whole brain perfusion. The requirement that the RF fields of the labelling and imaging coils must be isolated from one another restricts the choice of labelling position.

SPDI and the AM control were designed to produce equivalent MT effects in label and control images, so that differences between images at any slice position are due to blood flow alone.

SPDI is implemented by sine modulation of the amplitude of an RF pulse, applied on resonance. In the presence of $\underline{G}$ two labelling planes are produced simultaneously. The modulation frequency is selected to place one plane in the conventional position for labelling and the other above the head (in the position of the standard control). The control preparation comprises the same RF pulse without $\underline{G}$, to produce the same average power deposition, and hence MTC. In the absence of G, protons in blood are not subject to a frequency sweep and hence they are not labelled. In practice, MTC cancellation deteriorates with increasing distance from the central imaging slice, because the MT does not vary linearly with frequency offset. Modifications have been proposed (Kam AW and Talagala SL 2000; Talagala SL et al. 2001), but limited spatial coverage remains the major disadvantage of the technique.

The amplitude modulated (AM) control is the most widely applied technique for multiple slice CASL measurements. A constant RF pulse, B_1, is applied off resonance to label moving blood in the conventional way. For the control, B_1 is applied at the same frequency as for the label but the amplitude of B_1 is modulated by a sine function to produce two proximal inversions of moving blood. Ideally the effect of the first inversion is reversed by the second inversion, so that there is no overall change in magnetisation of water protons in flowing blood (*Figure 4.1*).

CASL images have been acquired successfully in several slices using the AM control (e.g. Wong EC et al. 1998a; Chalela JA et al. 2000). However, there have been consistent reports of reduced sensitivity, relative to the standard control for CASL (Alsop DC and Detre JA 1998; Ye FQ et al. 1999). Several groups have alluded to the role of the changing phase of the B_1 modulation and 'interference' between the frequency components of B_1 (Wong EC et al. 1998a; Alsop DC and Detre JA 1998). However, neither the reasons for the low sensitivity of the AM control, nor the roles of the pulse parameters and blood velocity in determining the efficiency of the AM control are fully understood, providing the motivation for the work described in this chapter.

4.1.1 The ideal AM control

The AM control scheme, proposed by Alsop and Detre (Alsop DC and Detre JA 1998) is designed to produce two inversions, the second one to reverse the effect of the first. For a labelling pulse, a single AFP is centred on the position where B_1 is on resonance ($\Delta B = 0$). The displacement of a spin at this point may be referred to as $\underline{z} = 0$, and $\Delta B = \underline{G}.\underline{z}$ at any $\underline{z}$. A sine modulation divides the labelling pulse into two frequency components at ± f from the frequency of the labelling pulse, which produce spatially separate effects in the presence of $\underline{G}$.

$$B_1(t) = B_{10} \sin(2\pi f t + \phi) \qquad \text{equation [4.1]}$$

$$B_1(t) = \tfrac{1}{2} B_{10} [\exp(2\pi f t + \phi) + \exp(-(2\pi f t + \phi))]$$

where

ϕ is the phase of $B_1(t)$ at $t = 0$, when the spin passes through the position where $\underline{z} = 0$

The ideal AM control inverts proton spins in arterial blood by velocity driven adiabatic fast passage (AFP) as they flow through the first resonance (where $\Delta B = - f/\gamma$ and $z = - f/(\gamma G)$) and re-inverts them as they flow through the second resonance (where $\Delta B = + f/\gamma$ and $z = + f/(\gamma G)$) (*Figure 4.1*). In this case spins arrive at the imaging plane(s) with no net change in normalised longitudinal magnetisation, m_z, i.e. $m_{z\_control} = + 1$. If the labelling pulse is also ideal, m_z after the label, $m_{z\_label} = -1$ and the labelling efficiency for the AM experiment is $\alpha_{AM} = 1$, where

$$\alpha_{AM} = (m_{z\_control} - m_{z\_label}) / 2 \qquad \text{equation [4.2]}$$

MT effects of the sine modulated pulse are equivalent to those of the labelling pulse provided that f is much smaller than the frequency offset of the labelling pulse and the same mean RF power is deposited by the AM control and the labelling pulse.

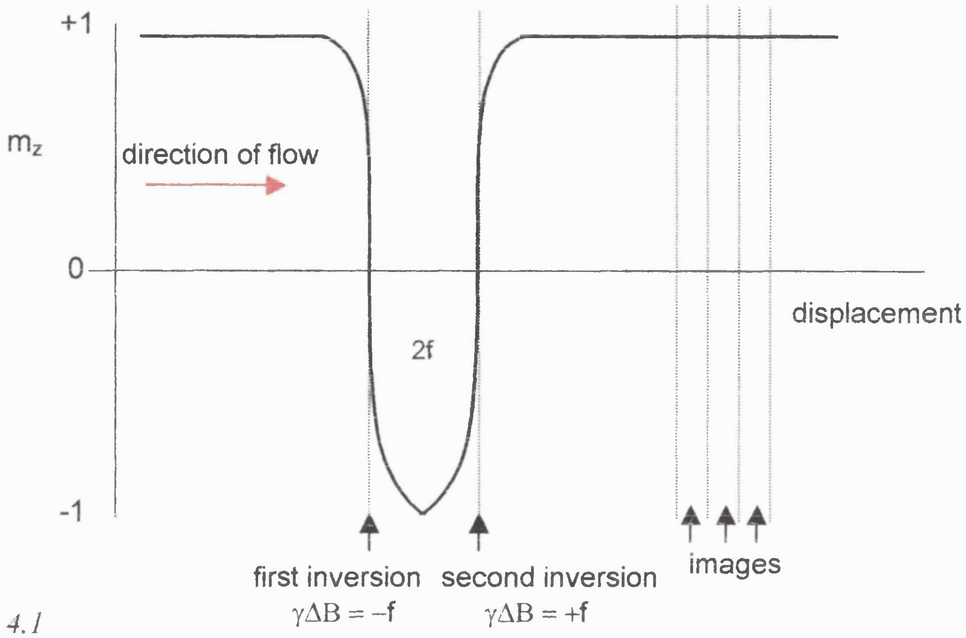

Figure 4.1

Ideal double inversion by the AM control pulse

The magnetisation of a spin is inverted and re-inverted as it moves through two consecutive velocity driven AFPs. The spin arrives in the imaging planes with no overall change in m_z

4.1.2 Parameters of the AM Pulse

All of the variables for the labelling pulse (the subject of Chapter 3) affect the AM control. In addition, the modulation of B_1 by $\sin(2\pi ft + \phi)$ introduces two new parameters, the phase (ϕ) and frequency (f) of the modulation function. ϕ, f, T_1 and T_2, B_1 and v are all considered in this Chapter.

ϕ is defined as the phase of the modulation function when $t = 0$. At this point the spin is half way between the centres of the two AFPs of the AM control. A CASL preparation pulse (for labelling or control) typically lasts for two or three seconds. In this time several periods of the modulation function (1/f) are completed, and spins at all ϕ contribute to the mean magnetisation of blood perfusing tissue in the imaging plane. Therefore the efficiency of the control is determined by the mean behaviour of spins over the whole range of ϕ. Ideally, the control would achieve maximum efficiency at all ϕ.

The value of f determines the separation of the inversions. When f = 0 the control is equivalent to the labelling pulse. As f increases, the two inversions of the AM control move further apart to produce two inversions.

The separation of the inversion planes also determines the amount of spin relaxation that occurs before blood reaches the imaging plane. T_1 relaxation is most effective immediately after inversion when m is furthest from equilibrium. T_2 losses are greatest during AFP, as m passes through the transverse plane. f must be large enough to produce two distinct inversions, but not so large as to allow excessive T_1 relaxation between the AM control planes.

In Chapter 3 optimum B_1 values were found to be significantly lower for the labelling pulse when spin-relaxation was included in the model. The optimal B_1 values for both the label and the control, produce m_{z_label} as close to -1 as possible, $m_{z\_control}$ as close to +1 as possible, and the same MTC in label and control images. When the technique was introduced a ratio of B_1 for the control to B_1 for the label of $\sqrt{2}$ was employed and equivalent MTC in label and control images was achieved (Alsop DC and Detre JA.1998). This ratio was selected because RF power deposition from a constant RF pulse depends on B_1^2 (Eng J et al. 1991). At small f, the AM pulse may be assumed to behave like a single RF component at $\Delta B = 0$, and the time-averaged mean of $(B_{10} \sin(2\pi ft))^2$ over a complete cycle is $B_{10}^2 / 2$.

The velocity of blood affects the degree of inversion for a single AFP (Chapter 3, *Figure 3.10*) and v is expected to influence the performance of the AM control. In an artery blood flows at a range of v. In order to gain maximum α_{AM} (equation [4.2]), the pulse parameters must produce the best double inversion at all v within the relevant physiological range.

4.2 Aim

The aim of this work is to develop an understanding of the dependence of the AM control technique on the parameters of the AM pulse and properties of the blood. These parameters are the phase, ϕ, and frequency, f, of the modulation of B_1, the amplitudes of B_1, and the labelling gradient, $\underline{G}$, the spin velocity, v, and relaxation times of blood, T_1 and T_2.

4.3 Method

A computer model of the Bloch equations for velocity driven AFP was modified to model the AM control technique. A detailed description of the model is given in Chapter 3. Briefly, the change in the magnetisation of a spin that follows $\underline{B}_{eff} = \underline{B}_1 + \underline{\Delta B}$ is calculated at 100,000 time points as the spin covers a specified distance, from $-z_{max}$ to $+z_{max}$. The final position reached by the spin is defined as the imaging plane and the frequency offset between the labelling and imaging planes is $\gamma G z_{max}$. Spin relaxation effects are incorporated by calculating T_1 and T_2 contributions at each of the 100,000 time points. In all these respects the model for the AM control is identical to the model for the labelling pulse. The modification required for the AM pulse is multiplication of the amplitude of $\underline{B}_1$ by the function, $\sin(2\pi ft + \phi)$ (equation [4.1]).

In the computer model, variables are expressed in the following units: Hz for $\underline{B}_1$, Hz/mm for $\underline{G}$, Hz for f, mm/s for v and seconds for T_1 and T_2. Parameters will be expressed in these units in the rest of this Chapter (for example, the centres of the AFPs are at $z = \pm f/G$).

A series of studies was carried out to assess the influence of each pulse parameter and the spin velocity on the performance of the AM control. Values of z_{max}, v and G were selected to be representative of those required to image rCBF in the human brain. Studies of the dependence of the AM control on B_1 and v were also performed with values of z_{max} and G appropriate for imaging rCBF in the rat brain.

The performance of the AM control was assessed by calculating m_z in the imaging plane. The details of methods for individual studies are now given.

The influence of ϕ on the efficiency of the AM control was investigated by calculating m_z in the imaging plane at 100 values of ϕ at intervals of $2\pi/100$ in the range $0 < \phi < 2\pi$. This was performed at different f without relaxation effects ($T_1 = T_2 = 10^6$ ms).

The dependence of m_z on f was studied without relaxation ($T_1 = T_2 = 10^6$ ms) and with relaxation ($T_1 = 1000$ ms and $T_2 = 200$ ms) in the human model. m_z was calculated at 100 values of ϕ at intervals of $\pi/100$, in the range $0 < \phi < \pi$. The mean of these m_z was determined as a measure of the average performance of the AM pulse.

The influences of T_1 and T_2 spin relaxation were considered separately over a range of f in the human model. T_1 relaxation was considered by setting $T_2 = 10^6$ ms and $T_1 = 1000$ ms. T_2 relaxation was considered by setting $T_1 = 10^6$ ms and $T_2 = 200$ ms.

The combined effect of T_1 and T_2 was also considered. Phase effects were minimised by setting $\phi = 0$.

The dependence of the AM control on B_1 was studied over a range of f with one set of parameters appropriate for imaging humans at 1.5 T and with a separate set of parameters for imaging rats at 2.35 T (see Chapter 3 for details of the animal model). G and v were constant and in order to assess the average effect of the AM control, the mean of 100 m_z values was calculated at a range of ϕ, at intervals of $\pi/100$.

A similar procedure was employed to study the dependence of the AM control on spin velocity in both the human and animal models.

4.4 Results

4.4.1 Phase of the modulation function (ϕ)

The effect of variations in ϕ is demonstrated in *Figure 4.2* at a range of f with constant G and v, without spin relaxation ($T_1 = T_2 = 10^6$ ms). When $\phi = n\pi$, $m_z = 1$ in the imaging plane at any f, producing an highly efficient control. However, when $\phi = (2n+1)\pi/2$ m_z depends strongly on f. The pulse actually inverts moving spins when f is less than about 20 Hz ($m_z = -1$), which results in $\alpha_{AM} = 0$ because $m_{z\_control} = m_{z\_label}$. At the highest f (f = 200 Hz or f = 500 Hz) the effect of the AM pulse varies less with ϕ and m_z is much closer to the ideal of +1 at all ϕ.

The evolution of m_z as a spin moves through the two AFPs of the AM control is shown in *Figure 4.3* with $\phi = 0$, $\phi = \pi/4$ and $\phi = \pi/2$ at f = 50 Hz and f = 500 Hz. The change in m_z produced by the first AFP is not perfectly reversed by the second AFP unless $\phi = n\pi$. We see from *Figure 4.3a* that full inversion is not necessary for restoration of m_z to +1. However, *Figure 4.3c* and *4.3e* demonstrate that without full inversion, the AM pulse is effective only for spins with $\phi = 0$. At f = 500 Hz the AFP processes are almost independent of one another because the two inversion planes are 10 times further apart than at f = 50 Hz. The first AFP inverts m, the second AFP re-inverts m and there is no net effect on m_z.

Rapid oscillations in m_z occur when the evolution of m is determined predominantly by its precession about $\underline{B}_{eff}$, rather than by the change in $\underline{B}_{eff}$, caused by the frequency sweep. This happens when the adiabatic condition is not satisfied (see Appendix A). When f = 50 Hz, m_z oscillates at a frequency of approximately 100 Hz close to the centres of the AFPs (this frequency may be calculated from the spatial frequency of m_z shown in *Figure 4.3* and the velocity of the spin (200 mm/s)) This may be explained by an interruption of the precession of m_z every time $B_1 = 0$, which occurs at a frequency twice as great as the modulation frequency. At f = 500 Hz ΔB does not change as much during a single period of the modulation function and the slower frequency sweep dominates the evolution of m_z, although oscillations in m_z are still observed (see also *Figure 4.5*). For further explanation of the dependence of the double inversion on ϕ see Appendix B.

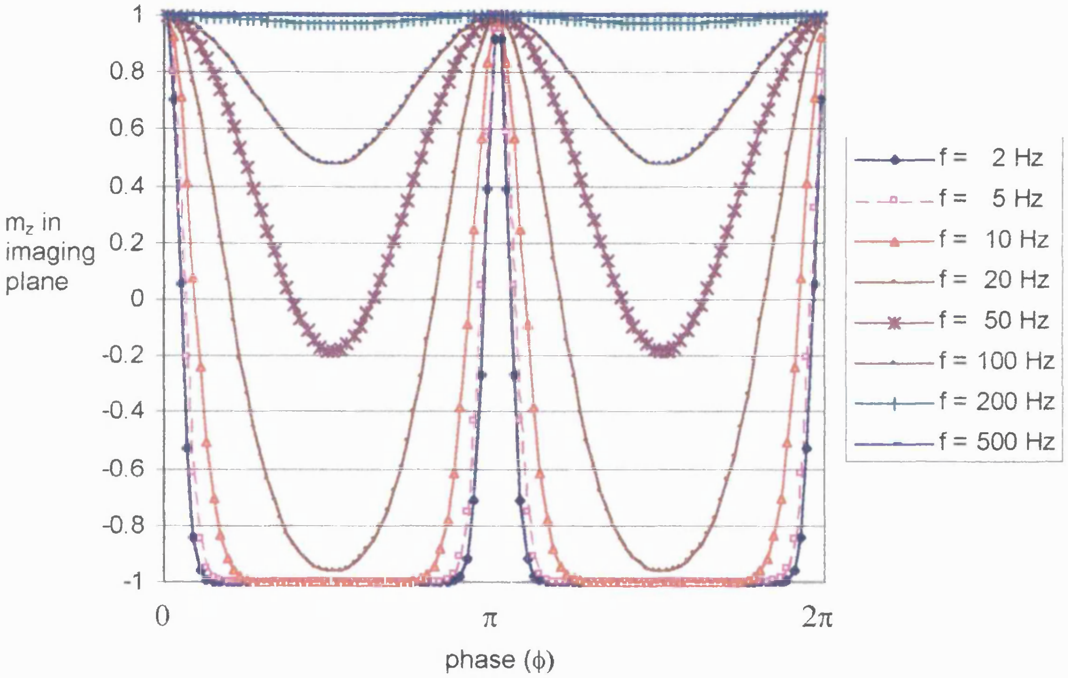

Figure 4.2

The performance of the AM control over a range of ϕ at different modulation frequencies

5kHz offset at 100 mm from the imaging plane (G = 50 Hz/mm), $B_1 = 212$ Hz, v = 200 mm/s, $T_1 = T_2 = 10^6$ ms

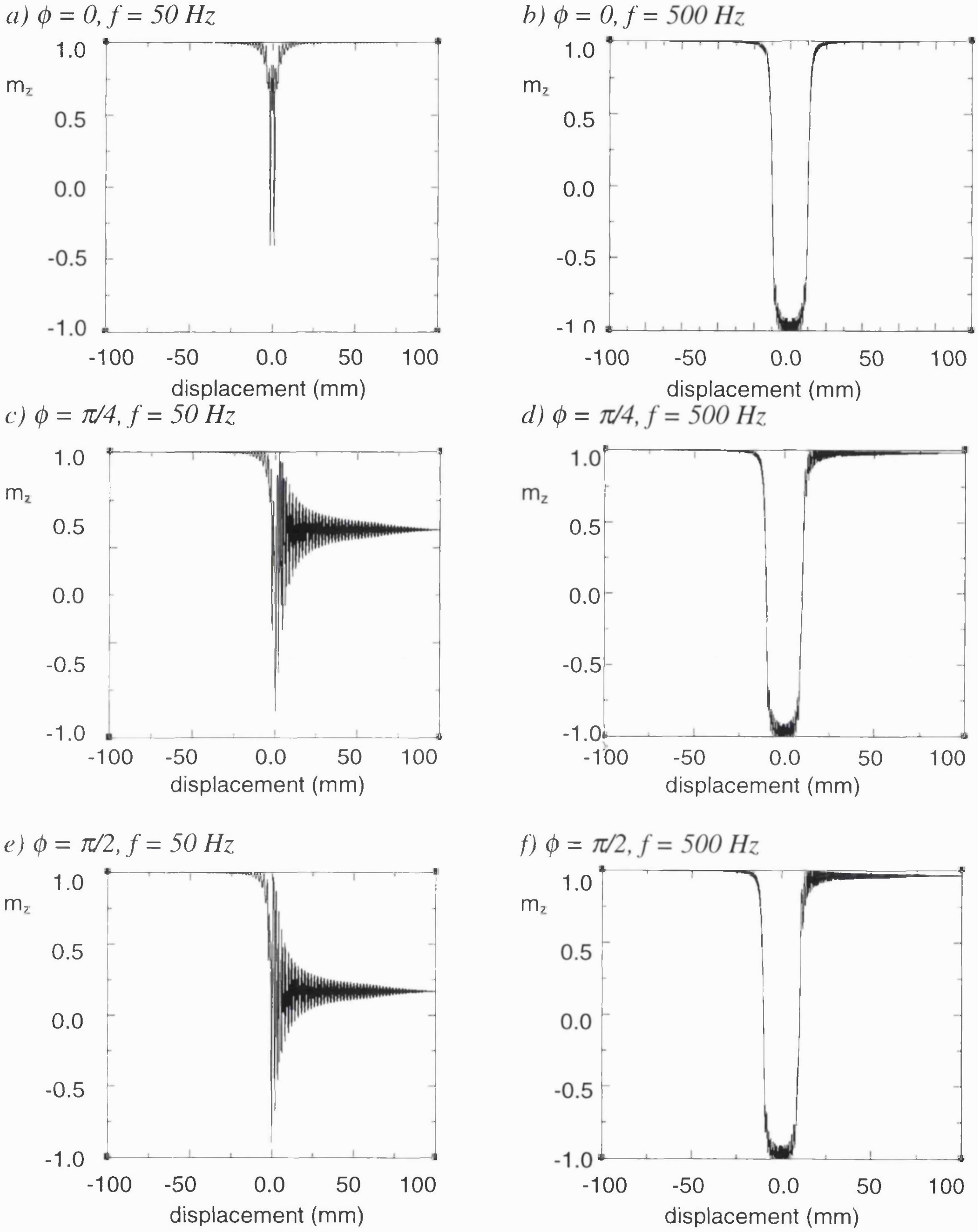

Figure 4.3

Effect of the AM control on m_z of a proton

The proton moves from – 100 mm to + 100 mm when $\phi = 0, \pi/4, \pi/2$ at f = 50 Hz (a,c,e) and f = 500 Hz (b,d,f).

5 kHz offset at 100 mm from the imaging plane (G = 50 Hz/mm), B_1 = 212 Hz, v = 200 mm/s, $T_1 = T_2 = 10^6$ms.

4.4.2 Modulation Frequency (f)

Figure 4.4 shows the mean m_z of 100 spins, calculated with values of ϕ at intervals of $\pi/100$, in the range $0 < \phi < \pi$. This provides a realistic approximation to the situation when the AM pulse is applied for CASL since the period of the modulation function (1/f) is much less than the duration of the labelling or control pulse (e.g. when f = 100 Hz, 1/f = 0.01 seconds compared with a typical pulse duration of 3 seconds). Spins with the whole range of ϕ, $0 < \phi < \pi$, contribute to the signal in the control image. Two sets of data are shown, one without spin-relaxation effects ($T_1 = T_2 = 10^6$ ms) and one with typical T_1 and T_2 for imaging the human brain at 1.5 T.

When f is greater than 180 Hz, spin relaxation reduces m_z by 20 % relative to the case without spin-relaxation. If the labelling pulse was perfect (giving $m_z = -1.0$) α_{AM} (equation [4.2]) would be 1.0 without relaxation and 0.9 with relaxation. At modulation frequencies below 100 Hz, the efficiency of the control is higher when spin relaxation is included in the model. This is because after the second inversion, the magnetisation of partially inverted spins returns to equilibrium ($m_z = +1$), through T_1 relaxation.

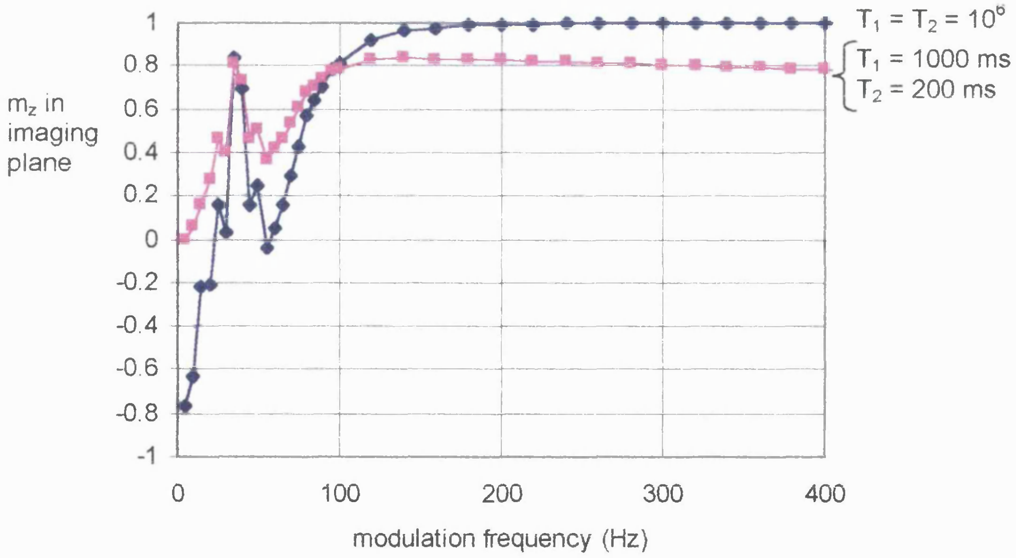

Figure 4.4

Mean response to AM control at different modulation frequencies

m_z values are the means of 100 values of m_z, calculated with ϕ at intervals of $\pi/100$.

5 kHz offset at 100 mm from imaging plane (G = 50 Hz/mm), B_1 = 212 Hz, v = 200 mm/s, $T_1 = T_2 = 10^6$ ms when relaxation effects are neglected, or T_1 = 1000 ms, T_2 = 200 ms.

4.4.3 Spin Relaxation (T_1 and T_2)

Figure 4.5 shows the evolution in space of the magnetisation of single spins when T_1 and T_2 relaxation are included in the model and $\phi = 0$. Comparison with *Figure 4.3* (where $T_1 = T_2 = 10^6$ ms) shows that relaxation reduces the value of m_z immediately after the second AFP. m_z then recovers slightly through T_1 relaxation after the second AFP before the spin arrives in the imaging plane. Spin relaxation causes a more significant reduction in m_z at f = 500 Hz than at f = 50 Hz.

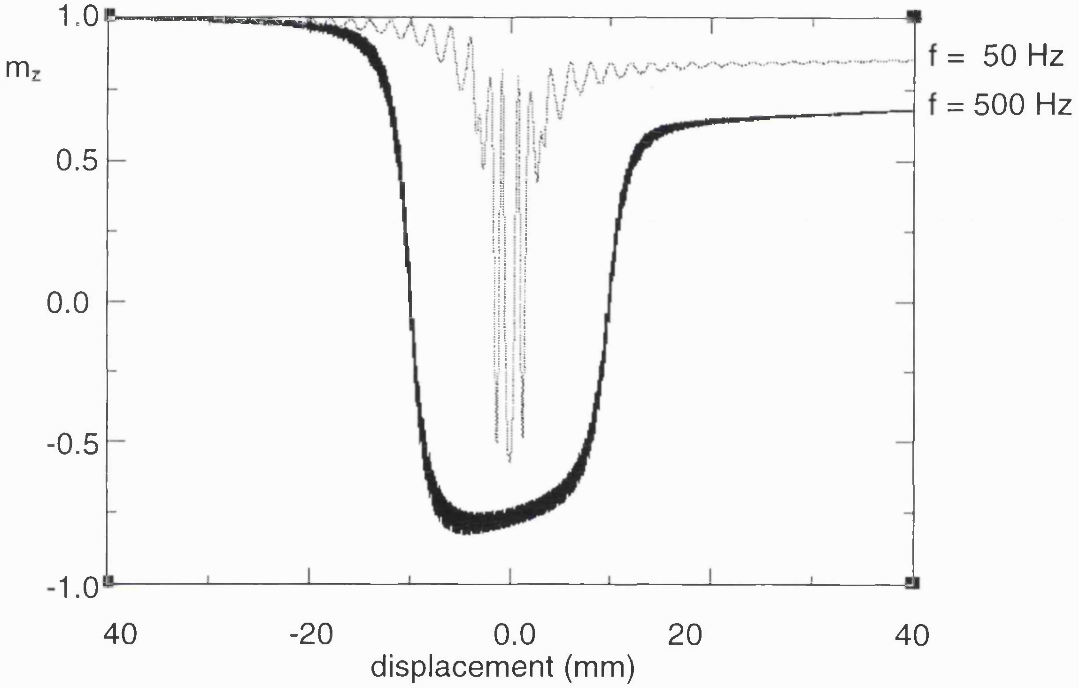

Figure 4.5

Spin relaxation during the double inversion of the AM control.

In the computer model a spin travels a total distance of 200 mm. Only the central 80 mm is shown here.

5kHz offset at 100 mm from imaging plane (G = 50 Hz/mm), B_1 = 200 Hz, v = 200 mm/s, T_1 = 1000 ms, T_2 = 200 ms, f = 50Hz and f = 500 Hz, $\phi = 0$.

The effects of T_1 and T_2 relaxation on m_z are shown separately and in combination with respect to f in *Figure 4.6*. At low f, T_2 relaxation reduces m_z more significantly than T_1 relaxation. Losses due to T_2 relaxation reach a plateau at about f = 300 Hz. Losses due to T_1 relaxation increase as f increases, particularly when f is greater than 200 Hz. The influence of T_1 relaxation is more pronounced at higher f. This is because spin relaxation starts as soon as m departs from equilibrium, and at larger f, the first AFP occurs further from the imaging plane, allowing more time for relaxation before a spin arrives in the imaging plane. Results with both T_1 and T_2, compared with results with T_2 relaxation alone, indicate that T_1 relaxation after the second inversion mitigates losses in efficiency due to T_2 relaxation during each inversion when f is less than approximately 750 Hz.

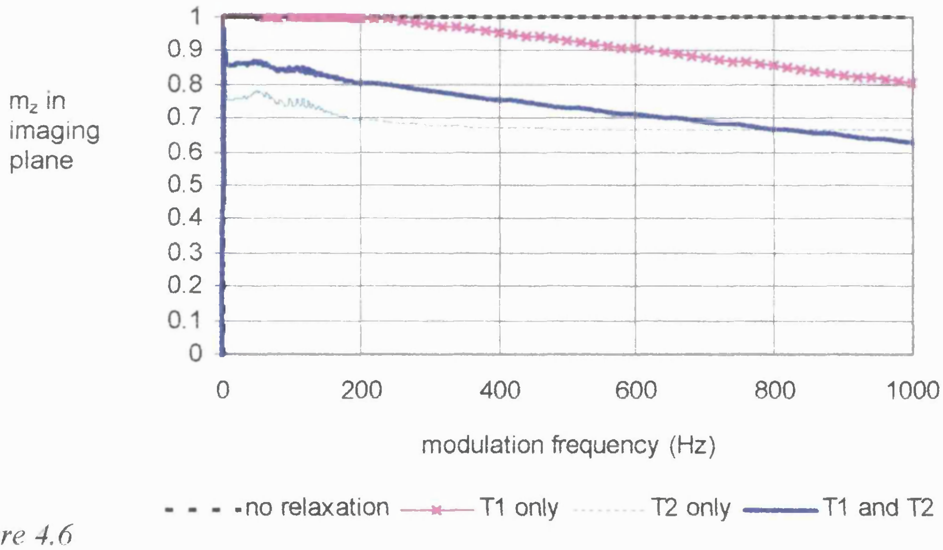

Figure 4.6

The effect of spin relaxation on the efficiency of the AM control over a range of modulation frequencies.

The effects of T_1 and T_2 relaxation are shown separately and in combination.

5 kHz offset at 100 mm from imaging plane (G = 50 Hz/mm), B_1 = 270 Hz, v = 200 mm/s, T_1 = 1000 ms, T_2 = 200 ms, $\phi = 0$.

4.4.4 B_1 Amplitude

Figure 4.7 demonstrates the sensitivity of the AM pulse to B_1 amplitudes typical of those used in human (*4.8a*) and animal (*4.8b*) studies. The mean of 100 values of m_z with ϕ at intervals of $\pi/100$ was calculated at a range of B_1, with and without spin relaxation effects.

If B_1 is too small, neither inversion is very efficient because the adiabatic condition is not satisfied (Chapter 3 and Appendix A). The overall effect of the control is then some degree of labelling ($m_z < +1$). As B_1 becomes larger, both inversion and re-inversion become more efficient and m_z approaches +1 (in the absence of relaxation). When B_1 is too large, m_z decreases due to interference between the components of $\underline{B}_1$ (seen at f = 100 Hz). As B_1 increases, $\underline{B}_{eff}$ departs from alignment with the $\underline{\Delta B}$ axis sooner and the duration of each AFP increases. This effect is observed at the lowest f because the centres of the AFPs are closest together and any increase in their duration is more likely to cause them to overlap.

It is interesting to note that the effect of relaxation may improve the efficiency of the AM control at the highest B_1 (most apparent when f = 100 Hz in the human model, *Figure 4.7a*). If $m_z < +1$ immediately after the second inversion, T_1 relaxation acts to restore m_z as blood moves into the imaging plane, effectively improving the efficiency of the AM control. This effect is seen also in *Figures 4.5* and *4.6*.

Optimal values of B_1 for the AM control when relaxation effects are included are lower than optimal values without relaxation, approximately 140 Hz compared with 180 Hz in the human model (at f = 200 Hz) and approximately 220 Hz compared with over 300 Hz in the animal model (at f = 250 Hz).

The MT produced by a continuous RF pulse depends on B_1^2 (Eng et al. 1991). The time-averaged mean of a sine-modulated B_1 pulse is $B_{10}^2/2$, where B_{10} is the peak amplitude of B_1 (equation [4.1]). Therefore B_1 amplitudes for the label that produce the same power deposition as the AM control are $B_{10}/\sqrt{2}$, producing $140/\sqrt{2} = 100$ Hz in the human model and $220/\sqrt{2} = 155$ Hz in the animal model. The optimum B_1 values found in Chapter 3 for the label with a 5 kHz offset are $B_1 = 74$ Hz and $B_1 = 118$ Hz in the human and animal models respectively (Chapter 3, section 3.4.1). The values of B_1 required to optimise the AM control are approximately 30 – 35 % greater than optimum values derived from the optimum B_1 values for the labelling pulse (if B_1 is the amplitude of the labelling pulse, $B_{10} \approx 1.3 * \sqrt{2} * B_1$).

a) human model

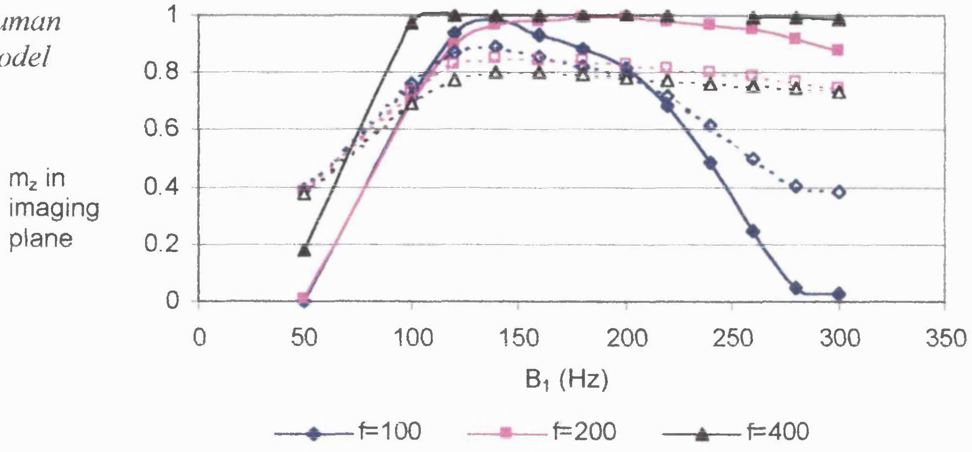

b) animal model

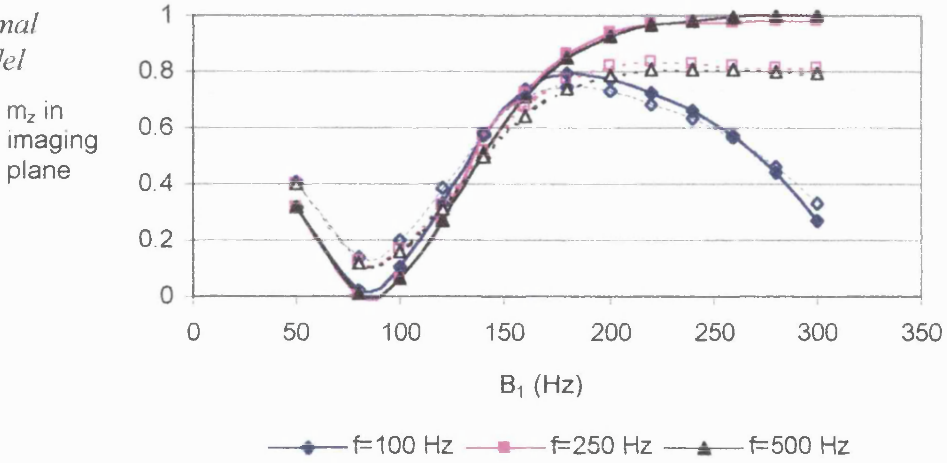

Figure 4.7

The effect of B_1 on the efficiency of the AM Control with and without spin relaxation. Open data points show results with spin relaxation.

5 kHz offset at 100 mm from imaging plane ($G = 50$ Hz/mm), $v = 200$ mm/s, $T_1 = 1000$ ms, $T_2 = 200$ms for the human model (a)

5 kHz offset at 20 mm from imaging plane ($G = 250$ Hz/mm), $v = 100$ mm/s, $T_1 = 1500$ ms, $T_2 = 150$ ms for the animal model (b)

Values of m_z are means over 100 values of ϕ at intervals of $\pi/100$. Closed data points show results without spin relaxation ($T_1 = T_2 = 10^6$ ms).

4.4.5 Velocity

Figure 4.8 shows the dependence of the AM control and the labelling pulse on velocity in the human and animal models. The mean of 100 values of m_z with ϕ at intervals of $\pi/100$ was calculated at a range of v with and without spin relaxation.

The value of B_1 employed for this study is close to the optimum for spins moving at v = 200 mm/s in the human model, but these data show that even at velocities as great as 400 mm/s, B_1 is sufficient to satisfy the adiabatic condition for the labelling pulse (*Figure 4.8a*). When spin relaxation is included, the label becomes very inefficient at low v, reflecting the limit imposed by the left hand side of the adiabatic condition (Chapter 3, equation [3.6]). There is more T_2 relaxation at low v because the duration of each AFP is greater and m_z spends more time in the transverse plane. Also, the amount of T_1 relaxation is greater because the time it takes a spin to move to the imaging plane after inversion increases.

The AM control in the human model is fairly insensitive to velocity (*Figure 4.8a*), with or without relaxation. Two different effects maintain $m_z \approx +1$ at low and high v. At low v, the adiabatic condition is not satisfied for either inversion and m_z does not deviate significantly from +1 at any point. At high v, inversion and re-inversion are successful and relaxation effects are reduced, so that m_z is restored to almost +1 after double inversion.

In the animal model (*Figure 4.8b*), when relaxation effects are not included, the label becomes inefficient at the highest v. G in the animal model is 5 times greater than in the human model, making it more difficult to satisfy the right hand side of the adiabatic condition at high v (equation [3.5]). When spin relaxation is included in the model, the efficiency of the label is most significantly compromised when v < 150 mm/s.

The AM control is more sensitive to velocity than the labelling pulse in the animal model with or without spin relaxation (*Figure 4.8b*). As v increases from 20 mm/s to 120 mm/s, increased efficiency of the double inversion mirrors the increasing efficiency of the single inversion for labelling. However, the control is most efficient at a lower velocity than the labelling pulse (approximately 120 mm/s compared with approximately 260 mm/s). The effects of spin relaxation become insignificant at v greater than 240 mm/s, where there is no difference between m_z with or without spin relaxation.

a) human model

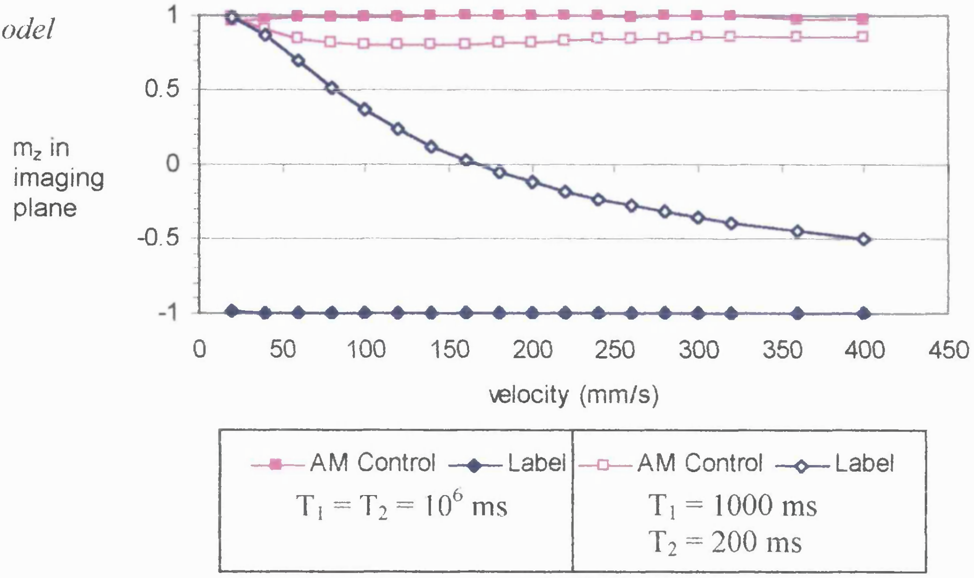

b) animal model

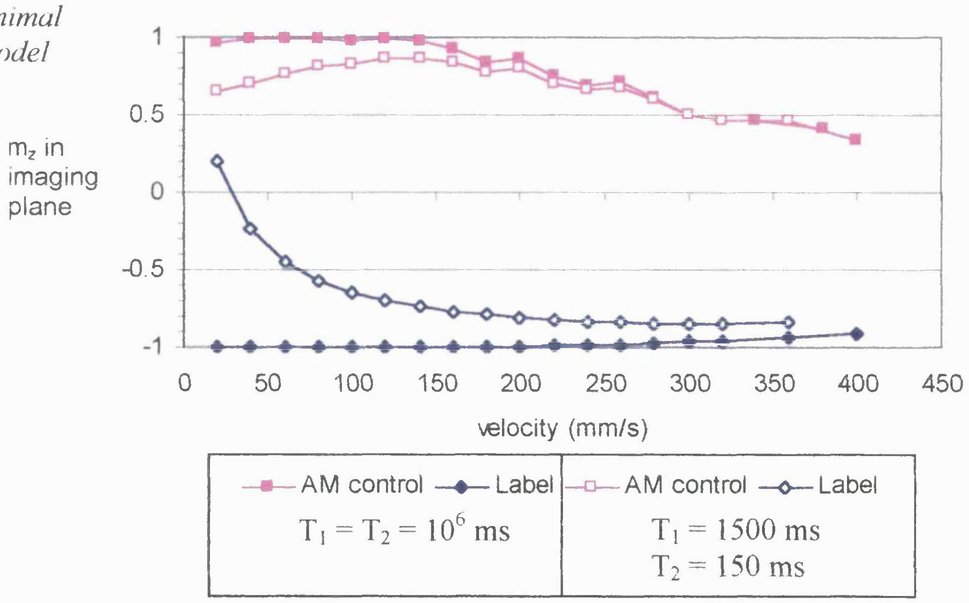

Figure 4.8

The effect of velocity on the AM control and labelling pulses

Values of m_z are means over 100 values of ϕ at intervals $\pi/100$.

5 kHz offset at 100 mm from imaging plane (G = 50 Hz/mm), B_1 = 140 Hz for the label, B_1 = 200 Hz for AM control, f = 250 Hz, T_1 =1000 ms, T_2 = 200 ms in the human model (a)

5 kHz offset at 20 mm from imaging plane (G = 250 Hz/mm), B_1 = 177 Hz for the label, B_1 = 250 Hz for AM control, f = 250 Hz, T_1 =1500 ms, T_2 = 150 ms in the animal model (b)

There are at least two factors that contribute to greater loss in efficiency of the AM pulse than the single inversion. Firstly, because there are two inversions, any imperfection in a single AFP is repeated, amplifying the loss in m_z. A single inversion reduces m_z to $(1 - 2\alpha)$, where α is the inversion efficiency. If $\alpha = 0.9$, $m_z = m_{z\_label} = -0.8$ after one inversion and $m_z = m_{z\_control} = 0.64$ after two inversions. In this case $\alpha_{AM} = (0.64 - (-0.8)) / 2 = 0.72$. Secondly, the temporal separation of the two AFPs is reduced at high v, increasing the possibility of interference between them (see Appendix C).

4.5 Discussion

A control technique for ASL imaging must provide the same image contrast as the labelling pulse in all respects except the contribution of blood flow. The AM control was designed to fulfil these criteria, but in practice there is always a degree of partial labelling by the pulse, which reduces the contrast between label and control images and hence reduces the sensitivity of rCBF measurements. The following discussion focuses on practical considerations for achieving maximum sensitivity to perfusion with the AM control technique. Further discussion of the effects of the pulse on moving spins may be found in Appendices A, B and C.

The most efficient labelling of blood for CASL requires optimisation of both the labelling and control schemes. The ideal experiment would produce (i) $m_z = -1$ after labelling; (ii) $m_z = +1$ after the control and (iii) equal MTC in both label and control images. There are several variables to consider, three of which are common to both schemes, the magnetic field gradient, $\underline{G}$, the velocity, $\underline{v}$, and the spin relaxation rates of the blood. B_1 for the control must produce the same MTC as the label. The remaining parameters for the AM pulse are the phase, ϕ, and the frequency, f, of the sine modulation function. Each of these parameters is now discussed.

The pulse parameters for the AM control may be optimised in the following order. $\underline{G}$ is selected to produce the desired frequency offset and position of the labelling plane. An estimate of the blood velocity is made in order to select the optimal amplitude of B_1, and finally f is selected. Each variable is now discussed in turn.

B_1 must satisfy the adiabatic condition for each AFP (Appendix A). Optimum B_1 amplitudes are lower when spin relaxation is included in the model than when it is neglected (*Figure 4.7*). This indicates that both inequalities of the condition are important when selecting B_1, as was found also for the labelling pulse (*Figure 3.4*). As

B_1 increases, the duration of each AFP increases (equation [3.9]), causing more significant losses due to T_2 relaxation during the passage of blood through resonance. The greater duration of each AFP also increases the possibility of overlap between the two inversions of the control (*Figures 4.3, 4.5* and *4.7* and Appendix C). The $\underline{B}_1$ amplitude of the label must be multiplied by $\sqrt{2}$ for the peak of the AM control pulse, B_{10}, to ensure equivalent MTC in the images (Eng J et al. 1991; Alsop DC and Detre JA 1998). This is because MTC depends on B_1^2 and the mean B_1^2 of a sine-modulated pulse with peak amplitude B_{10} is $B_{10}^2/2$. In fact, B_{10} values for the AM control, which produce the highest values of m_z in the imaging plane, are more than $\sqrt{2}$ times greater than the optimum values of B_1 for labelling, found in Chapter 3, by approximately 30 % (*Figure 4.7*).

The sensitivity of the AM control to velocity depends on the magnitude of $\underline{G}$. In the animal model $\underline{G}$ is 5 times greater than in the human model and at large v the right hand side of the adiabatic condition limits the inversion efficiency of the label and the control (Chapter 3 and Appendix B). The efficiency of the AM control in the animal model is more severely compromised at high v than the efficiency of the label because poor inversion by the first AFP is compounded by a poor inversion by the second AFP. Differences in v during an experiment or between different animals may lead to significant uncertainty in calculated values of the labelling efficiency, α_{AM}, and hence of rCBF. This should be taken into account if exceptionally high v may compromise the efficiency of the control pulse and an increase in B_1 may be necessary.

The effect of spin relaxation on m_z depends on the duration and separation of the two AFPs, and their distance from the imaging plane. T_2 relaxation is more significant with small G, low velocities, or large B_1 values because $\underline{m}$ then spends more time in the transverse plane. T_1 relaxation begins as soon as the first inversion is complete. Therefore at larger f (or lower v), the total time available for T_1 relaxation is greater because there is more time between the first inversion and arrival of blood in the imaging plane (*Figure 4.5*).

For maximum efficiency the control must be effective at any ϕ because spins with the full range of ϕ pass through the labelling plane during the 2 or 3 seconds of the control pulse. At sufficiently high f the condition $f \gg B_{10}$ (Appendices A and B) is satisfied and the control becomes insensitive to ϕ. When spin relaxation is neglected and $f > B_{10}$ all spins enter the imaging slices with $m_z = +1$, as required for an effective control, (*Figures 4.2* and *4.4* and *4.6*). When spin relaxation is taken into account, lower values of f generally result in greater efficiency of the AM control (*Figures 4.5* and *4.6*). The choice of modulation frequency demands a compromise between large f to minimise interactions between the components of B_1 and small f to minimise losses through T_1 and T_2 relaxation. Optimal values of f lie in the range $100\ \text{Hz} < f < 300\ \text{Hz}$ with typical values for G, v and B_1 (*Figure 4.4*). A value of f that is approximately equal to B_{10} may be an appropriate choice under typical conditions (*Figure 4.4* and Appendices A and B).

In summary, the AM control may be optimised by selecting each parameter as follows. $\underline{G}$ is selected to give the required frequency offset and position of the labelling plane. B_1 is optimised for the labelling pulse, then if B_1 is the amplitude of the labelling pulse, and B_{10} is the peak amplitude of the AM control, $B_{10} = \sqrt{2}\ B_1$ to produce equal MTC in label and control images. B_1 for both pulses is increased by about 30 % to provide optimum conditions for the AM control. The modulation frequency should be approximately equal to B_1, in order to minimise spin-relaxation and approach the requirement that $f > B_1$ (Appendix A).

The standard, single slice control produces $m_z = 1$. When fully optimised, the double inversion of spins by the AM control may return the magnetisation to 80 % of its optimum value ($m_z = +\ 0.8$, *Figure 4.4*). If m_z after labelling is $-\ 0.8$, $\alpha_{AM} = 0.8$ when the AM control is fully optimised.

4.6 Conclusions

The performance of the AM pulse is subject to complex interactions between the two components of $\underline{B}_1$ and spin relaxation effects. Valuable insight has been gained into the dependence of the AM pulse on ϕ, f, B_1, G, v, T_1 and T_2. If multiple slice imaging is essential, the AM control may provide a more time efficient technique than separate acquisitions of images in different slice positions, but at the cost of lower overall sensitivity to flow. The results of these investigations may inform the optimisation of the AM control for multiple-slice CASL.

5 Implementation of the amplitude modulated control for multiple-slice continuous arterial spin labelling

5.1 Introduction

The amplitude modulated (AM) control was devised to produce equivalent magnetisation transfer (MT) to the labelling pulse for continuous arterial spin labelling (CASL) over a large volume of tissue to facilitate multiple-slice perfusion imaging (Alsop DC and Detre JA 1998). Sine modulation of the amplitude of the labelling RF pulse, B_1, divides the pulse into two frequency components. In the presence of a gradient, each component defines an inversion plane. Ideally, spins in blood move through one plane and are inverted, then move through the other plane and they are re-inverted so that there is no net change in magnetisation. In fact, the AM control does have an overall effect on the magnetisation of moving spins and the sensitivity of the AM technique is always lower than that of the standard, single slice technique (Chapter 4; and Wong EC et al. 1998a; Alsop DC and Detre JA 1998). Despite this drawback, the AM control remains the most effective approach for multiple-slice CASL and it has been employed by several groups to map regional cerebral blood flow (rCBF) in multiple image planes, particularly in human studies (Detre JA et al. 1999; Chalela JA et al. 2000; Ye FQ et al. 1999; Wolf RL et al. 2001).

In Chapters 3 and 4 a computer model of velocity driven adiabatic fast passage (AFP) was modified to investigate the effects on moving spins of the labelling and AM pulses respectively. The computer model is useful to study the effects of both the label and AM control techniques on moving protons in blood, under specified, controlled conditions. However, the labelling RF pulse also changes the magnetisation of static brain tissue through MT effects and the computer model does not give any information on this static tissue.

Aspects of the pulse that are not amenable to evaluation with the computer model are the subjects of this chapter. The effects include (i) the equivalence of MT contrast (MTC) in label and control images; (ii) the duration of B_1 required to saturate protons in the macromolecular pool to an extent where the magnetisation of the tissue reaches a new equilibrium level, M_{0sat}; and (iii) the duration of the delay required after the labelling pulse to allow all labelled blood to flow out of large vessels in the imaging slice(s) and to minimise the sensitivity of rCBF measurements to the transit time (Alsop DC and Detre JA 1996). Each of these effects was assessed in rat brain at 2.35 T in a small bore MR system. Finally, a direct comparison of the standard and AM control techniques for CASL was performed *in-vivo* in rat brain. The results of such comparisons in human brain have been reported (Alsop DC and Detre JA 1998) but similar data for animal experiments are not available. In Chapter 4 some significant differences between the behaviour of the AM control in humans and animals were found (*Figure 4.8*). Therefore it is possible that conclusions drawn from human studies of the AM control may not be valid in rats.

This chapter is divided into three sections. The first section describes experiments on MT effects of the AM control in multiple imaging slices in samples of meat. The second section describes experiments to verify the efficacy of CASL measurements using the AM control *in-vivo* in rat brain. The third section describes a series of experiments, in which CASL measurements were performed repeatedly over a period of several hours to compare the sensitivity of the AM control and the standard control techniques.

5.2 General Methods

Images were acquired in a 2.35 T magnet with a 120 mm clear bore. RF pulses were transmitted by a volume saddle coil and signals were received by a single loop surface coil, of diameter 3 cm. For *in-vivo* studies, the surface coil for signal reception was placed beneath the brain of an animal, as it lay prone in a Perspex holder. The head was held by ear bars to minimise motion and the holder was positioned within the magnet, such that the brain lay at the centre of the magnetic field. Details of anaesthesia and physiological monitoring are given in the methods section for each *in-vivo* study.

CASL was implemented with a 3 second, continuous RF pulse for labelling, applied at the same time as a low amplitude gradient along the bore of the magnet. A labelling plane was selected at a position where blood flow through the carotid arteries was predominantly parallel to the labelling gradient, close to the brain. The control pulse for multiple slice experiments was implemented by modulating the amplitude of B_1 by sin $2\pi ft$ to produce two inversion planes, proximal to the imaging plane(s) (*Figure 5.1*).

The amplitude of the RF pulse, B_1, experienced by a particular spin at time, t, is given by the expression:

$$B_1 = B_{10} \sin(2\pi ft + \phi) \qquad \text{equation [5.1]}$$

where B_{10} is the peak amplitude of B_1

f is the modulation frequency

ϕ is the phase of the modulation when the spin passes through the labelling plane (half way between the two inversion planes for the AM control)

CASL images were also acquired using the standard control, i.e. by reversing the frequency offset applied for labelling to select a control plane distal to the imaging slice (*Figure 5.1*). It is possible to implement the standard control by reversing the polarity of the labelling gradient, while maintaining the same frequency offset for the label and the control. This approach is preferable in theory because there is evidence that the resonance of protons bound to macromolecules may be asymmetric (Pekar J et al. 1996; Barbier EL et al. 1999), leading to differences in MT unless the labelling and control pulse are applied at exactly the same frequency offset. However, CASL images that were acquired by reversing the gradient polarity produced artifacts in subtraction images due to translation of the object within the field of view in the control image relative to the label image. This is most likely to be a result of eddy currents produced by the labelling gradient, which affect the imaging sequence. Therefore reversal of the frequency offset of B_1 was employed for the standard CASL control in all studies reported here.

A post-labelling delay, w, was inserted after the labelling or control period and before image acquisition. During the delay, w, labelled blood in the macrovasculature washes out of the imaging slices, leaving signal only from spins that perfuse the tissue. In addition, T_1 relaxation of the tissue restores the magnetisation from M_{0sat} (its equilibrium level when the magnetisation of macromolecular protons is saturated) to M_0 (the equilibrium level in the absence of the labelling or control pulse). Values of w were selected according to the objectives of each study. Long post-tagging delays were employed to study perfusion signals and short w to observe the maximum effects of MT. Slices were acquired consecutively, and therefore w was greater in slices that were acquired later.

A multiple-slice, spin-echo echo planar imaging (EPI) sequence was employed for acquisition of CASL images. The images had a 64 x 128 matrix, TE = 35.2 ms, TR = 4 s (labelling time + 1 s). Up to 7 slices were acquired with slice thickness 2 mm, 2.1 mm separation (centre to centre) and a delay of 78.2 ms between slice acquisitions.

T_1 was calculated from inversion recovery images that were acquired at a range of inversion times (TI) as part of most *in-vivo* experiments. Differences in signal between label and control were generally normalised to the signal intensity in the inversion recovery image with the longest inversion time, to approximate the signal intensity at M_0. If no inversion recovery data were acquired, difference signals were normalised to the signal intensity in the control image.

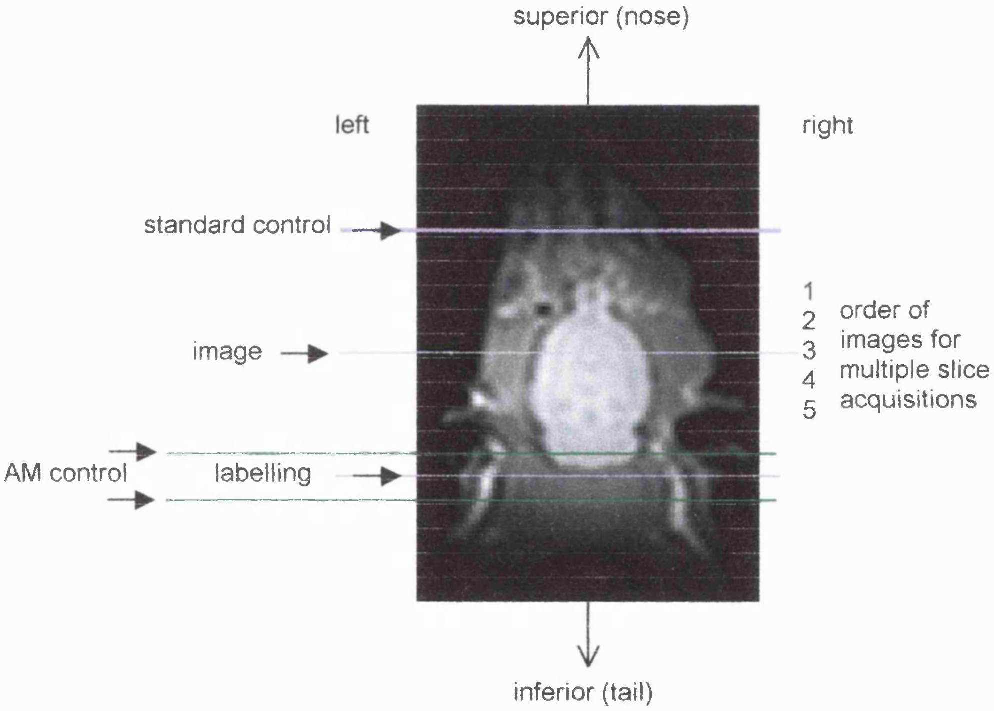

Figure 5.1

Positions of labelling and control planes for CASL in rat brain.

Proton spins in arterial blood are labelled by AFP as they pass through the labelling plane at the back of the brain.

For the standard control, a single control plane lies superior to the image, at the same distance from the image as the labelling plane. For the AM control two inversion planes produce a double inversion of moving protons, one inversion on either side of the labelling plane.

5.3 Magnetisation transfer in CASL images

The standard control pulse for CASL has a frequency offset of the same magnitude as the label, but the opposite sign. It is effective over only a thin region, where the control pulse and the labelling pulse result in the same degree of excitation of macromolecular protons. Ideally, amplitude modulation of B_1 produces the same MT as the labelling pulse at all imaging positions.

MT is determined by the combination of the frequency offset and power deposition of the labelling or control pulse (Graham SJ and Henkelman RM.1997). If the modulation frequency is small relative to the frequency offset for the labelling pulse, both components of the AM pulse act at approximately the same frequency offset as the labelling pulse. As long as this approximation is valid, the AM pulse may be treated as a single RF pulse. The mean power deposited by a RF pulse of peak amplitude B_{10}, whose amplitude is modulated by a sine wave, is $B_{10}^2/2$. Therefore, equal power deposition by the labelling and control pulses is achieved by multiplying the amplitude of B_1 for the label by $\sqrt{2}$ to give B_{10} for the control. This approach was adopted by Alsop and Detre when they introduced the technique (Alsop DC and Detre JA 1998) (and by all other groups since then).

The experiments described in this section were designed to assess the MT effects of the AM control in several slice positions in the absence of blood flow. Samples of pork were used to assess MT effects in label and control images at different frequency offsets, B_1 amplitudes and modulation frequencies. The advantages of using samples of meat are that MT effects are similar to those *in-vivo*, signal differences due to blood flow are absent, image artifacts and noise due to motion are absent and the sample is more uniform across several slice positions than the brain.

5.3.1 Method

For each study, a sample of pork escalope was placed into a plastic tube with a screw top lid. The tube was secured on top of the surface coil and placed within the magnet, on the Perspex holder used for the *in-vivo* experiments. CASL measurements were performed as described in Section 5.2, using the AM control or the standard control.

Normalised differences in signal intensity, ΔS_{MT}, between label (S_{label}) and control ($S_{control}$) images are reported for each experiment described below. The ideal control would produce no differences in MTC, $\Delta S_{MT} = 0$.

In all these studies the post-labelling delay (w) was small to maximise the sensitivity of both label and control images to magnetisation transfer. Any differences between the images due to MT were thus emphasised.

The first study was performed to determine the amplitude of B_{1O} for the AM control at which MT effects are the same as those in label images. B_l for the labelling pulse was maintained at a constant amplitude. AM control images were acquired at frequency offsets of 5 kHz and 10 kHz with six amplitudes of B_1.

In the second study, the maximum MT effect of the labelling pulse was observed. B_l for the label was set at a typical value for CASL (*in-vivo*) and B_{1O} for the control pulse was set at zero. Images were acquired at seven slice positions with frequency offsets between the labelling plane and central imaging plane of 5 kHz, 8 kHz and 10 kHz.

In the third experiment, the sensitivity of ΔS_{MT} to the amplitude of B_l was investigated. The ratio of B_l for the label to B_{1O} for the AM control was maintained at $(1/\surd 2)$. ΔS_{MT}, was calculated in five image slices, using both the standard control and the AM control, at two different modulation frequencies.

The final experiment was designed to study MT effects at different modulation frequencies. Images were acquired in five slices with f = 100 Hz, f = 250 Hz, f = 500 Hz. A further set of images was acquired with f = 100 Hz and the frequency offset of the labelling and control pulses was reversed (from + 5 kHz to − 5 kHz), while the labelling gradient was kept the same. The labelling and AM control planes were thus placed in the position of the standard control for *in-vivo* experiments.

5.3.2 Results of magnetisation transfer in CASL images

Typical EPI images of a sample of pork are shown in *Figure 5.2.*

Figure 5.3 shows the results of the first experiment to determine the peak amplitude, B_{10}, for the AM control, relative to B_1 for the label, at which MTC is the same in label and control images. B_1 for the labelling pulse was set to a constant value and images were acquired with different B_{10} for the AM control. In *Figure 5.3* values of ΔS_{MT} are shown for the central slice, but results were similar in other slices.

S_{label} was employed for normalisation of ΔS_{MT} in this experiment because S_{label} should have been constant, while $S_{control}$ decreased at higher B_1. Therefore

$$\Delta S_{MT} = 100 * (S_{label} - S_{control}) / S_{label} \qquad \text{equation [5.2]}$$

ΔS_{MT} tends to be larger at an offset of 5 kHz than at 10 kHz, as might be expected because a larger proportion of the macromolecules is saturated at a lower frequency offset. ΔS_{MT} approached zero when B_1 for the AM control was 1.4 times greater than B_1 for the label, a factor of approximately $\sqrt{2}$. Ideally, higher amplitudes of B_{10} would have been employed, but the maximum amplitude of B_{10} was limited by the practical consideration of possible damage to the RF transmission coil at very high amplitudes of the long RF pulse for CASL.

Figure 5.2

CASL images of a sample of pork after a labelling pulse

B_1 = 175 Hz, w = 50 ms to the first slice. Slices were acquired in the order 2,4,6,1,3,5,7.

The second experiment was performed to measure the maximum difference in signal intensity (ΔS_{MT}) produced by a labelling pulse with a typical amplitude of B_1 for the labelling pulse for CASL. These data are shown in *Figure 5.4.* The amplitude of the control pulse was set to zero and ΔS_{MT} was measured at frequency offsets of 5 kHz, 8 kHz and 10 kHz. The normalised difference in signal intensity is

$$\Delta S_{MT} = 100 * (S_{control} - S_{label}) / S_{control} \qquad \text{equation [5.3]}$$

In fact in this experiment:

$$\Delta S_{MT} = (S_0 - S_{label}) / S_0$$

where S_0 is the value of $S_{control}$ when B_1 for the AM control is zero.

If there were no reduction in signal intensity due to the labelling pulse, $S_{control} = S_{label} = S_0$ and ΔS_{MT} would be zero.

Images were acquired at 7 slice positions in the order 2, 4, 6, 1, 3, 5, 7, (slice positions are shown in *Figure 5.1*). This means that the post-labelling delay, w, was greatest in slice 7 and the frequency offset was greatest in slice 1. ΔS_{MT} varies between 42 % in slice 4 at a 5 kHz offset and 18 % in slice 1 at a 10 kHz offset.

Figure 5.4 shows that ΔS_{MT} tends to be lower in slices further from the labelling plane, where the frequency offsets are higher. This behaviour is expected because at higher frequency offsets the pulse excites a smaller fraction of the bound protons in the imaging slice, increasing S_{label} and reducing ΔS_{MT}. The pattern of variation in ΔS_{MT} between slices is due to different, competing effects. Firstly, MT may be expected to be smaller in slices where the post tagging delay, w, was longer because there was more time for the magnetisation to relax back to equilibrium after the labelling pulse, before the image was acquired. However, between slices 2, 4, and 6 and between slices 1, 3, 5, and 7, the progressively smaller frequency offsets tend to increase MT effects, cancelling out the effect of longer w in slices that were acquired later. In the step from slice 6 to slice 1 both the increased frequency offset and the longer delay, w tend to reduce ΔS_{MT} and, in combination, they produce the greatest "step" in ΔS_{MT} in *Figure 5.4.*

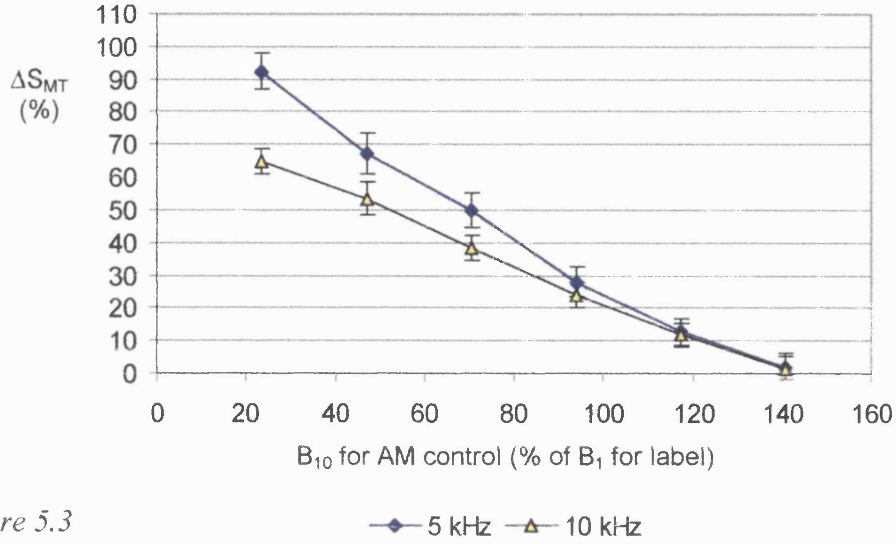

Figure 5.3

MT effects of CASL with a range of B_1 using the AM control in a sample of pork

Frequency offsets of 5 kHz and 10 kHz, at 11.5 mm from the imaging plane, $B_1 = 120$ Hz for the label, w = 128 ms to this slice (slice 4 of 7), f = 250 Hz.

$\Delta S_{MT} = 100 * (S_{label} - S_{control}) / S_{label}$

Errors bars were calculated from the SNR in the label and control images.

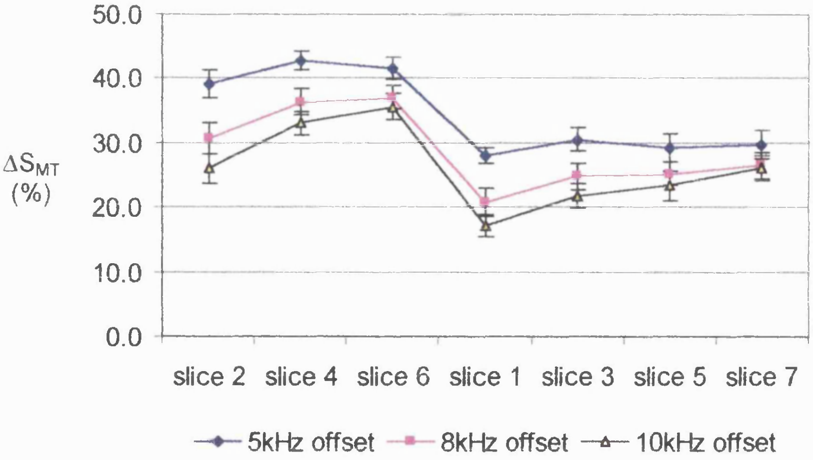

Figure 5.4

Maximum MT effects of CASL in a sample of pork

Labelling plane at 11.5 mm from the central slice (4), $B_1 = 150$ Hz for the label, $B_1 = 0$ Hz for the control, f = 250 Hz, w = 50 ms to the first slice. Slices were acquired in the order 2,4,6,1,3,5,7.

$\Delta S_{MT} = 100 * (S_{control} - S_{label}) / S_{control}$

Errors bars were calculated from the SNR in the label and control images in each slice.

In a third experiment, images were acquired at two different amplitudes of B_1 using the standard control and the AM control at f = 100 Hz and f = 250 Hz. B_{10} for the AM control was fixed at $\sqrt{2}$ times B_1 for labelling. *Figure 5.5* shows ΔS_{MT} (equation [5.3]), for the AM and standard control techniques at five slice positions.

The departure from $\Delta S_{MT} = 0$ was most significant in slices other than the central image (slice 3), when the standard control was applied. The variation in ΔS_{MT} between slices using the AM control was less ± 1 %, while the variation with the standard control was ± 5 % and ± 12 % when B_1 = 85 Hz and B_1 = 120 Hz respectively

ΔS_{MT} with the standard control had a greater magnitude at B_1 = 120 Hz than at B_1 = 85 Hz in slices other than the central slice. A slight trend to larger magnitude ΔS_{MT} at higher B_1 may be observed also for the AM control (dashed lines are below solid lines). All acquisitions with the AM control produced slightly negative ΔS_{MT}.

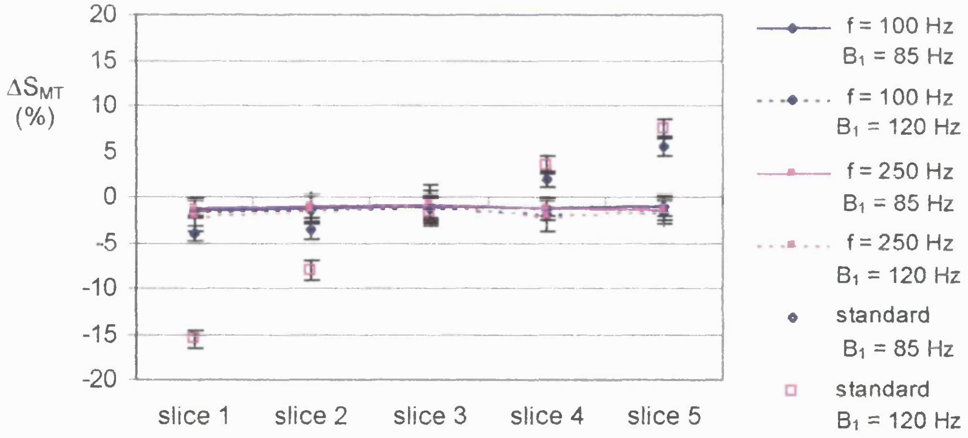

Figure 5.5

MT effects of CASL at different B_1 amplitudes in a sample of pork

Data were acquired using the standard, single slice control and the AM control at 5 slice positions.

5 kHz offset to slice 3 at 14mm, w = 10 ms to slice 1. Slices were acquired in the order 1,2,3,4,5. B_{10} for the AM control was $\sqrt{2}$ times greater than B_1 for the labelling pulse.

$\Delta S_{MT} = 100 * (S_{control} - S_{label}) / S_{control}$

Errors bars were calculated from the signal-to-noise ratios in the label and control images in each slice.

The final experiment was designed to measure MTC in CASL images with the AM control at different modulation frequencies. ΔS_{MT} was measured in five slices with f = 100 Hz, f = 250 Hz and f = 500 Hz with a typical B_1 for CASL (*Figure 5.6*). ΔS_{MT} was consistently negative with the AM control, as in *Figure 5.5*.

Differences between ΔS_{MT} at different values of f were nearly always smaller than the measurement error in each slice. Slightly lower ΔS_{MT} in slice 5 when f = 500 Hz than at other f may indicate that the AM control caused greater MT in this slice when f = 500 Hz than when f = 100 Hz or f = 250 Hz.

One data set shows the effect of reversing the frequency offset of both the label and AM control with f = 100 Hz (dashed line). There is no evidence of different MT effects with labelling and AM control pulses applied in this location at f = 100 Hz.

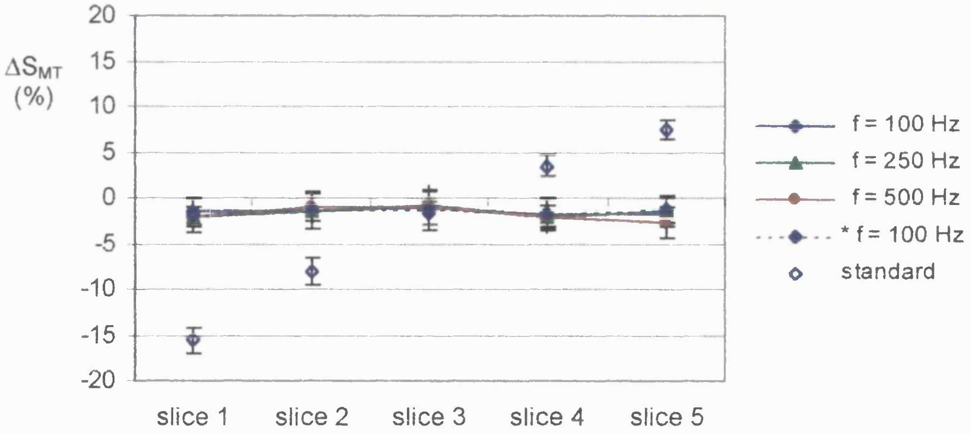

Figure 5.6

MT effects of CASL in a sample of pork at different modulation frequencies.

B_1 for the labelling pulse was 120 Hz, B_1 for the AM control was $120*\sqrt{2}$ Hz

5 kHz offset to slice 3 at 14 mm, w = 10 ms to slice 1. Slices were acquired in the order 1,2,3,4,5.

* the frequency offset of the labelling and the AM control pulses were reversed for one acquisition.

$\Delta S_{MT} = 100 * (S_{control} - S_{label}) / S_{control}$

Errors bars were calculated from the signal-to-noise ratios in the label and control images in each slice.

5.3.3 Discussion of magnetisation transfer in CASL images

Magnetisation transfer contrast in CASL images using the AM control depends on the amplitude of the labelling pulse, B_1, the frequency separation of each imaging plane from the labelling plane and the delay between the end of the labelling pulse and image acquisition (w). Each of these factors has been studied in order to determine its impact on MTC cancellation between label and control images.

Results shown in *Figures 5.3* indicate that MTC is equivalent in AM control and label images when the peak B_1 of the sine modulated RF pulse is approximately $\sqrt{2}$ times greater than B_1 for the labelling pulse. This is consistent with the theory for continuous wave pulses (Graham SJ and Henkelman RM 1997, Eng et al. 1991). The maximum signal difference, ΔS_{MT}, due to the labelling pulse varied from 18 % to 42 % of the signal in control images, depending on slice position, the frequency offset of the pulse and the delay after labelling (*Figure 5.4*). The MTC equivalence of the AM control in non-central slice positions was shown to be superior to that of the standard control (*Figures 5.5* and *5.6*).

The standard control produced more significant mismatches in MTC at higher B_1 (*Figure 5.5*). B_1 must be large for efficient labelling of moving blood, but these results suggest that high B_1 values may accentuate differences between MTC in label and control images.

The modulation frequency, f, and the gradient, G, determine the positions at which the two inversion pulses of the AM control act. At small f, each pulse has approximately the same frequency offset as the labelling pulse and the MTC in control images is approximately equivalent to that in label images, when the correct amplitude of B_1 is applied. At higher f, one control plane moves further away from and the other moves towards the imaging planes. When the separation of the two inversion planes of the AM control is too large, the assumption that the combined MT of the two components of the AM control is equivalent to that of the label becomes invalid. The results in *Figure 5.6* show that all modulation frequencies below 500 Hz at a frequency offset of 5 kHz produce equally good MTC cancellation across 5 slices. The other criterion for selection of f is sensitivity to flow. This will be considered in the next section.

Consistently negative ΔS_{MT} were observed in *Figure 5.5* and *Figure 5.6*, although the differences from zero were barely greater than the experimental error. Both data sets were acquired using the same sample, in the same imaging session. The causes of such an offset are most likely to be different for the standard control and the AM control experiments. The offset in ΔS_{MT} with the standard control may be due to asymmetry in the resonance of macromolecules (the bound pool) in pork. If the ^1H resonance of the bound pool was asymmetric, the degree of saturation of the bound pool at positive and negative frequency offsets would not be identical. Then MT contrast in labelled and control images would be different and ΔS_{MT} would be always non-zero. This asymmetry in brain tissue has been reported in studies of cat brain (Pekar J et al. 1996) and in rat brain (Barbier EL et al. 1999). For the standard control, the same B_1 amplitude is employed for both label and control pulses, but B_{10} for the AM control pulse was set independently of B_1 for the labelling pulse. Although B_{10} was nominally $\sqrt{2}$ times greater than B_1 for the label, RF power deposition resulting from the label and control may not have been identical in practice.

5.4 Multiple slice CASL with the AM control in normal rat brain

The aim of the studies described in this Section was to verify that perfusion weighted images at multiple slice positions in rat brain may be obtained using the AM control for CASL at 2.35 T. Experimental verification of findings in Chapters 3 and 4 was sought and the effects of the pulse on static brain tissue were assessed. The variables considered in this section are the amplitude, B_1, and duration of the labelling pulse, the duration of a post-labelling delay, w, and the modulation frequency of the AM control, f. Animal preparation was performed by Dr Mark Lythgoe (Institute of Child Health, UCL, London) and I acquired and analysed the CASL images.

As discussed in Section 5.3, the labelling pulse for CASL excites the magnetisation of the macromolecular proton pool in brain tissue and MT reduces the bulk magnetisation of the free protons. Calculations of rCBF are greatly simplified if the labelling pulse is long enough to establish a new equilibrium magnetisation in the brain, M_{0sat} and the standard formulas for these calculations are based on the assumption of saturation (equation 2.9 in Chapter 2). Therefore, it is important to confirm that the labelling pulse is long enough for the magnetisation to reach an equilibrium, M_{0sat}.

A post-labelling delay, w, for CASL measurements was introduced by Alsop and Detre to minimise the influence of arterial transit times (δ) on calculated values of rCBF (Alsop DC and Detre JA 1996). The arterial transit time is the time it takes for blood to move from the labelling plane to the capillary bed, where it exchanges into tissue. Transit times depend on the relative positions of labelling and imaging planes and the velocity of the blood. These parameters vary between brain regions and in different physiological states. Therefore systematic errors in calculated flow values may result if values of rCBF are very sensitive to δ and if the estimate of δ is incorrect.

A post-labelling delay also allows labelled blood to flow out of the macrovasculature before image acquisition. Immediately after labelling a large proportion of the labelled blood resides in major blood vessels, which may appear as focal bright regions in subtraction images. This blood does not perfuse the slice where it is seen, and its contribution to the signal in labelled images causes rCBF to be over-estimated. If w is greater than the longest transit time (δ) to the tissue of interest, all signal from large blood vessels disappears and calculations of rCBF are much less sensitive to δ. However, excessively long w are not desirable because the flow-dependent signal decays due to T_1 relaxation after the end of the labelling pulse.

The value of f affects both the efficiency of labelling and errors due to differences in MTC in label and control images. The AM control partially labels moving spins, reducing the perfusion-dependent difference in signal between label and control images, and thereby reducing the sensitivity of the technique to regional blood flow. This partial labelling was investigated in Chapter 4, using a computer model of velocity driven AFP. Differences in the MT effects of labelling and AM control pulses were considered in Section 5.3 in samples of meat. Simultaneously analysis of the effects of f on flow and MTC cancellation is performed in this section *in-vivo.*

The variables considered in this section are (i) the magnitude of B_1 for maximum flow-dependent differences in signal in label and control images; (ii) the duration of labelling pulse required to ensure that M reaches an equilibrium level, M_{0sat}, in brain tissue; (iii) the length of post-labelling delay necessary to remove focal artifacts in subtraction images due to labelled blood in large vessels; (iv) the modulation frequency for the AM control that produces maximum flow weighting and the most effective cancellation of MTC in subtraction images.

5.4.1 Method

The study was approved by the Home Office, UK. CASL imaging was performed in normal male rats, as described in Section 5.2. Anaesthesia was maintained with halothane in O_2 and N_2O.

A labelling plane was located at the back of the brain, between 14 and 18 mm from the central imaging plane (*Figure 5.1*). Pairs of label and AM control images were obtained in five slice positions and normalised differences in signal intensity in regions of interest were calculated:

$$\Delta S_{CASL} = 100 * (S_{control} - S_{label}) / S_0 \qquad \text{equation [5.4]}$$

where S_0 is the signal in an inversion recovery image with an inversion time of 3.65 seconds (an approximation to the signal from magnetisation at equilibrium).

The minimum B_l required for optimum labelling efficiency was assessed by acquiring image pairs at different magnitudes of B_l while maintaining the peak amplitude of the AM pulse (B_{l0}) at $\sqrt{2}$ times B_l for the label. ΔS_{CASL} was calculated in regions of interest to indicate the degree of perfusion weighting achieved by the label/control combination.

The duration of the labelling pulse required to reach M_{0sat} was determined by acquiring images after labelling pulses with durations in the range 400 ms to 3800 ms, with a typical amplitude for the labelling pulse of $B_l = 180$ Hz.

Images were acquired at different post-labelling delays, w, to find the shortest delay, at which no focal bright spots appeared in subtraction images.

Modulation frequencies of f = 100 Hz, 250 Hz, 500 Hz and 1000 Hz were employed to obtain AM control images at five slice positions. The experiment was repeated after the frequency offsets of both the label and the control were reversed. In this way, equivalent MTC to that in labelled images was achieved, without either the label or control pulses affecting flowing blood. The labelling experiment was repeated post-mortem.

5.4.2 Results in normal rat brain

Subtraction images at the central slice position at a range of B_l amplitudes are shown in *Figure 5.7*. The labelling efficiency increased at increasing values of B_l, up to

180 Hz. ΔS_{CASL} (equation 5.4) in a cortical region of interest in this slice were 0.6 % at 80 Hz, 1.7 % at 100 Hz, 4.0 % at 150 Hz and 4.6 % at 180 Hz. Although acquisitions at greater B_1 amplitudes would be required to prove that this is the optimum B_1, the fact that ΔS_{CASL} changes little from $B_1 = 150$ Hz to $B_1 = 180$ Hz suggests that 180 Hz is close to the optimum. In order to compare this result with results from the computer model, the differences between the model and the situation *in-vivo* must be accounted for. The frequency offset was 5 kHz in both cases but the distance from the labelling plane to the imaging plane was 20 mm in the computer model and 15 mm for images shown in *Figure 5.7*, corresponding to labelling gradient amplitudes of G = 250 Hz/mm and G = 333 Hz/mm respectively. The optimum amplitude of B_1 is determined by G. The optimum B_1 using G = 333 Hz/mm was found to be between 130 Hz and 140 Hz using the computer model (*Figure 3.5* Chapter 3). However, all CASL images acquired in this section employed the AM control and it was found in Chapter 4 that optimum B_1 values for labelling using the AM control are approximately 30 % greater than those required when the standard control is employed (*Figure 4.7* Chapter 4). On this basis the optimum B_1 is predicted to be between 169 Hz and 182 Hz, which is consistent with $B_1 = 180$ Hz for the highest labelling efficiency *in-vivo.*

The progressive saturation of magnetisation in the bound pool at increasing pulse durations is shown in *Figure 5.8*. A new equilibrium value of M_{0sat} was established in regions of interest in cortex and basal ganglia when the signal intensity reached a plateau at pulse durations greater than approximately 2.5 seconds.

Subtraction images of the brain of a rat at a range of post-tagging delays, w, are shown in *Figure 5.9*. The uniformity of the signal across the brain increased at greater w. In particular, a bright region along the midline of the cortex became less prominent. Average signal-to-noise ratios over images at all w in label and control images were 120 ± 17 and 147 ± 26 in the cortex and 89 ± 13 and 106 ± 18 in the basal ganglia. Signal intensities in the label and control images in regions of interest in the cortex and basal ganglia are plotted with respect to w in *Figure 5.10*. Signal intensities increased at longer w as the magnetisation relaxed back from M_{0sat} to M_0 in both label and control images. The rate of relaxation back to M_0 was greater in label images due to the combination of the wash out and T_1 relaxation of labelled spins. Therefore ΔS_{CASL} decreased at greater w.

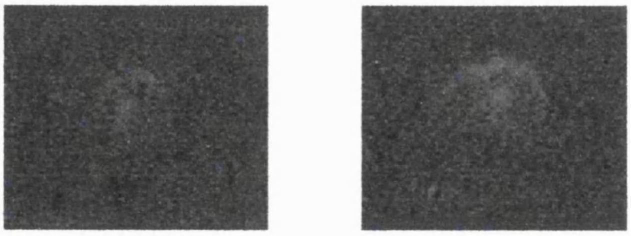

B_1= 80Hz B_1= 100Hz

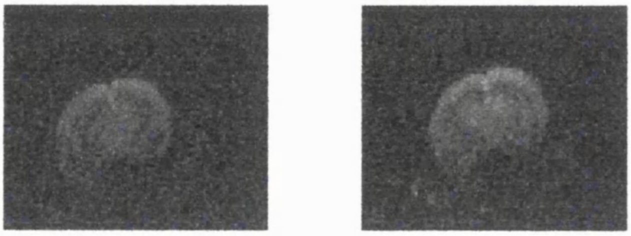

B_1= 150Hz B_1= 180Hz

Figure 5.7

Subtraction images with different B_1 amplitudes using the AM control.

Images shown are at the central slice position

Frequency offset = 5 kHz at 15mm, w = 50 ms, f = 250 Hz.

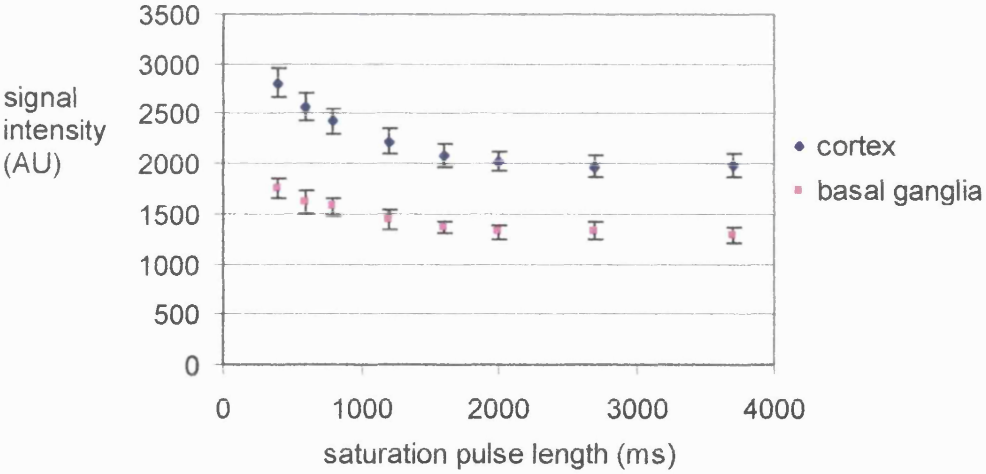

Figure 5.8

Progressive saturation of the bound proton pool in rat brain.

Frequency offset = 5 kHz at 15 mm, B_1 = 180 Hz. Signal intensities were measured in the central slice. Measurements are shown in arbitrary units and errors are the standard deviations of the intensity in the region of interest. The ROI in the cortex had an area of 12 mm^2 and the ROI in the basal ganglia had an area of 6 mm^2

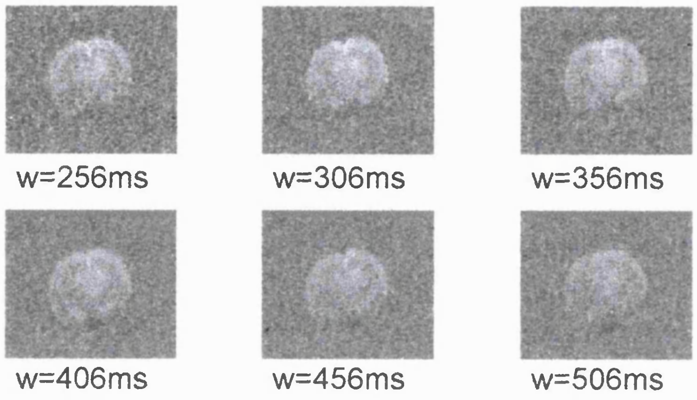

Figure 5.9

CASL subtraction images at different post-tagging delays (w)

Frequency offset = 5 kHz at 15 mm, B_1 = 100 Hz, f = 250 Hz.

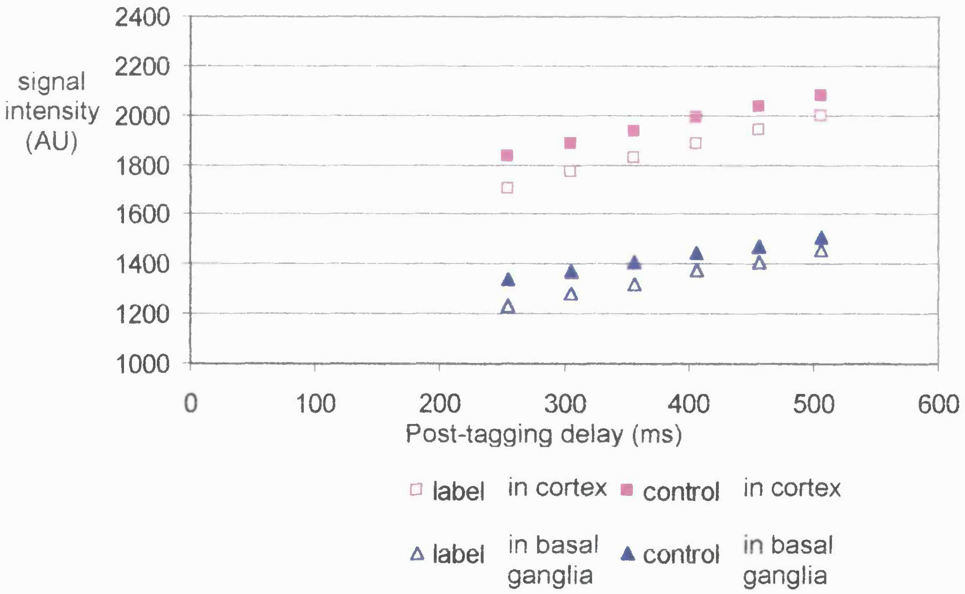

Figure 5.10

Signal intensities in the central slice at different post-labelling delays (w)

Frequency offset = 5 kHz at 15 mm, B_1 = 100 Hz, f = 250 Hz. Signal intensities are shown in arbitrary units. The ROI in the cortex had an area of 27 mm^2 and the ROI in the basal ganglia had an area of 10 mm^2.

Cancellation of MTC due to label and AM control preparations was assessed by eliminating the sensitivity of the preparation pulses to blood flow, while retaining their MT effects in the brain. This was achieved by placing the labelling and AM control planes in the position of the standard control (*Figure 5.1*). With this arrangement neither preparation pulse had any effect on spins in arterial blood. For comparison, images were acquired with the conventional geometry of the labelling and AM control planes *in-vivo* and post mortem. These data are shown in *Figure 5.11*. A short value of w was selected to produce maximum flow-dependence and MTC. ΔS_{CASL} was calculated in small ROIs in the cortex (*Figure 5.12*).

When the labelling and AM control planes were proximal to the imaging slices (below the brain), perfusion-related contrast appeared in all five image slices (*Figure 5.11a*). When both planes were distal to the imaging slices, ΔS_{CASL} in brain parenchyma was minimal (*Figure 5.11b* and *Figure 5.12*). Images acquired post mortem, with the planes proximal to the imaging slices showed no signal differences at any slice position (*Figure 5.11c*).

Slices were acquired in the order 1 to 5 (*Figure 5.1*). ΔS_{CASL} decreased in consecutive slices, especially between slices 3 and 4. (*Figure 5.12*). This is largely due to greater wash-out and T_1 relaxation of labelled blood in slices that were acquired later. In the first slice the contribution to signal differences from macrovascular flow is greatest and T_1 relaxation of labelled protons was least significant. Reduced amounts of labelled blood within large vessels and increased T_1 relaxation result in smaller signal differences in slices that are acquired later.

However, signal differences when the labelling pulse was applied distal to the imaging planes *in-vivo* had no detectable dependence on slice number, suggesting that differences in ΔS_{CASL} between slices when blood is labelled are dominated by flow effects and not MTC.

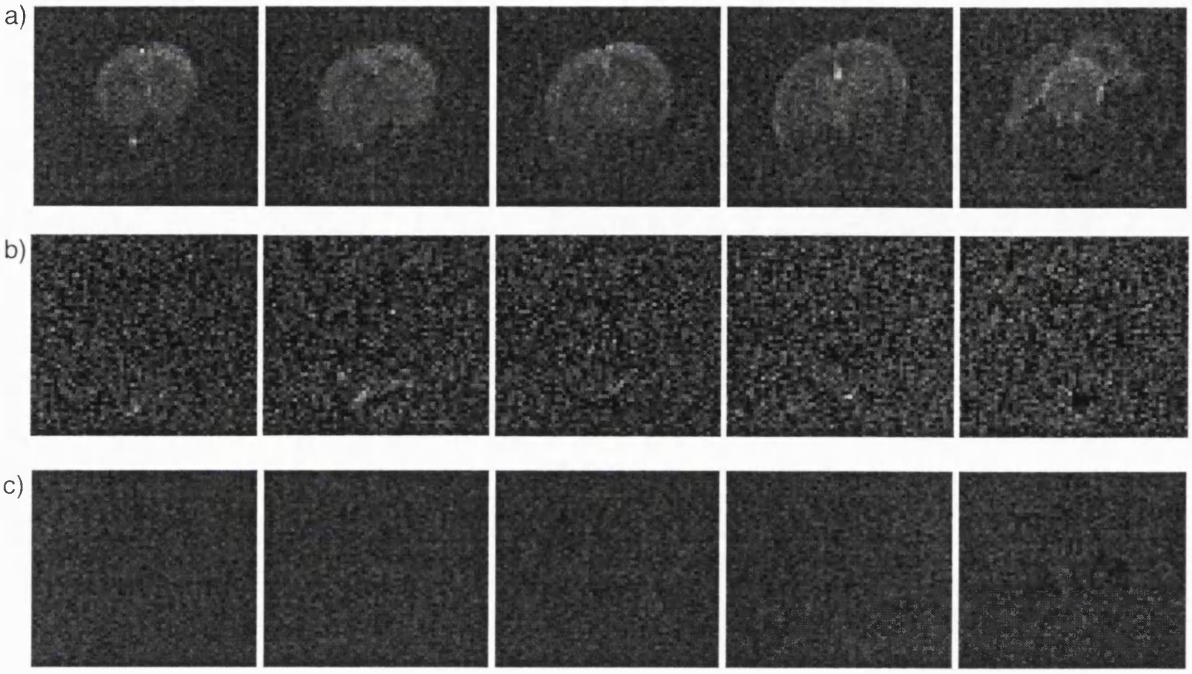

Figure 5.11

CASL subtraction images using the AM control with the labelling and control planes proximal (a) and distal (b) to the imaging slices, and proximally post-mortem (c). Images are shown at 5 slice positions.

Frequency offset = 5 kHz at 15 mm, B_1 = 150 Hz, f = 250 Hz, w = 50 ms. Slices were acquired in the order 1 to 5.

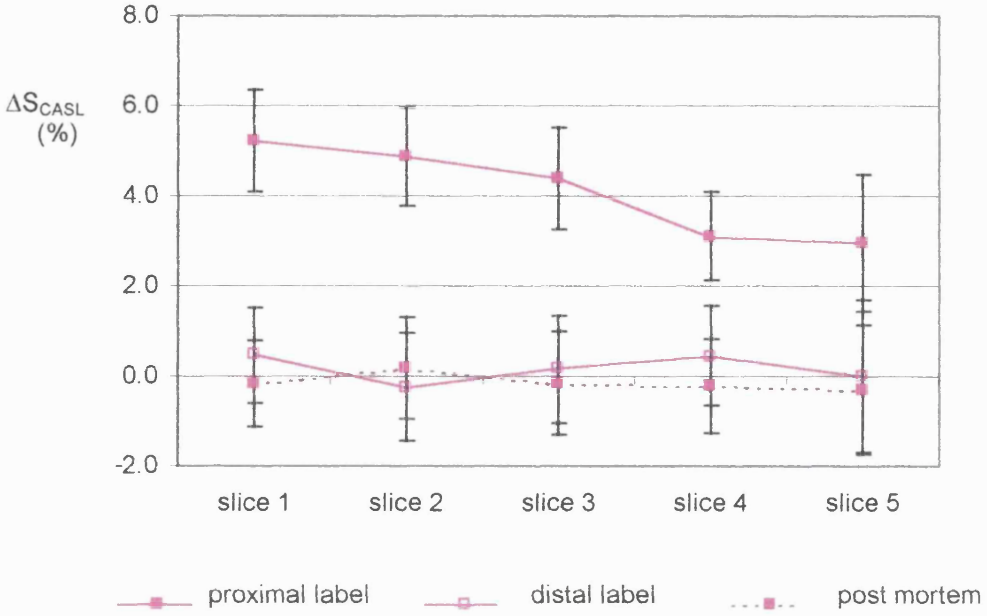

Figure 5.12

Signal differences in the cortex of a normal rat using the AM control (data from images in *Figure 5.11*). The ROIs were approximately 24 mm^2.

Frequency offset = 5 kHz at 15 mm, B_1 = 150 Hz, f = 250 Hz, w = 50 ms, slices were acquired in the order 1 to 5.

$\Delta S_{CASL} = 100 * (S_{control} - S_{label}) / S_0$

Errors were calculated from the signal-to-noise ratios in the label, control and S_0 images in each slice.

The last experiment was designed to detect any differences in ΔS_{CASL} at a range of modulation frequencies. Such differences may be due to variations in the efficiency of labelling or MT in brain parenchyma. Modulation frequencies of f = 100 Hz, 250 Hz, 500 Hz and 1000 Hz were employed to acquire CASL images at 5 slice positions. Subtraction images are shown in *Figure 5.13.* A second set of images was acquired with the same f, but with the label and AM control planes above the brain, distal to the imaging slices. ΔS_{CASL} is shown in *Figure 5.14* at each f, with the label and control planes proximal (*Figure 5.14a*) and distal (*Figure 5.14b*) to the imaging planes.

Comparison of *Figure 5.14a* with *Figure 5.14b* shows that when the label and control pulses are applied behind the brain (proximal to the imaging planes), the labelling of protons in blood flowing into the brain results in greater ΔS_{CASL} at all modulation frequencies, than when the label and control are applied above the head of the animal. However, *Figure 5.14b* shows non-zero ΔS_{CASL} in all slices, despite the absence of labelled blood. These signal differences may be indicative of poor MTC cancellation. A positive offset may be associated with higher M_{0sat} in the control image than in the label image, which would occur if B_{10} for the AM control was too low. This might be expected to affect slices closer to the labelling plane more significantly, where the frequency offset of the labelling pulse is smaller although w is greater.

When f = 500 Hz or f = 1000 Hz, the signal differences are smaller in slices 2 and 4 than when f = 100 Hz or f = 250 Hz. This is observed both with and without flow weighting, indicating that this pattern is an MT effect. The result is that sensitivity to flow was lower at f = 500 Hz and f = 1000 Hz than at f = 100 Hz or f = 250 Hz in slices 2 and 4.

A constant difference in MTC in label and control images was measured in some experiments presented in this Section (for example *Figures 5.5*, *5.6* and *5.14*). This might be explained by asymmetry of the proton resonance of the bound pool. A procedure to detect asymmetry in the frequency dependent MT response of a sample, described by Barbier et al. (Barbier EL et al. 1999) was applied *in-vivo* in brain tissue. CASL images were acquired with alternately positive and negative frequency offsets of the labelling pulse without a labelling gradient. Moving spins in blood were not subject to a frequency sweep, as they would be in the presence of a gradient, but the MT effects of the pulse were the same as for the CASL experiment in the central slice. Slightly negative $\Delta S_{standard}$ of -0.6 ± 0.5 % and -0.6 ± 0.2 % were found at frequency offsets of 5 kHz and 10 kHz respectively (mean ± standard deviation in 4 ROIs in two separate experiments at each offset frequency). However, these differences were no greater than the error in the measurement of 0.9 %, which was calculated from the SNR in each image.

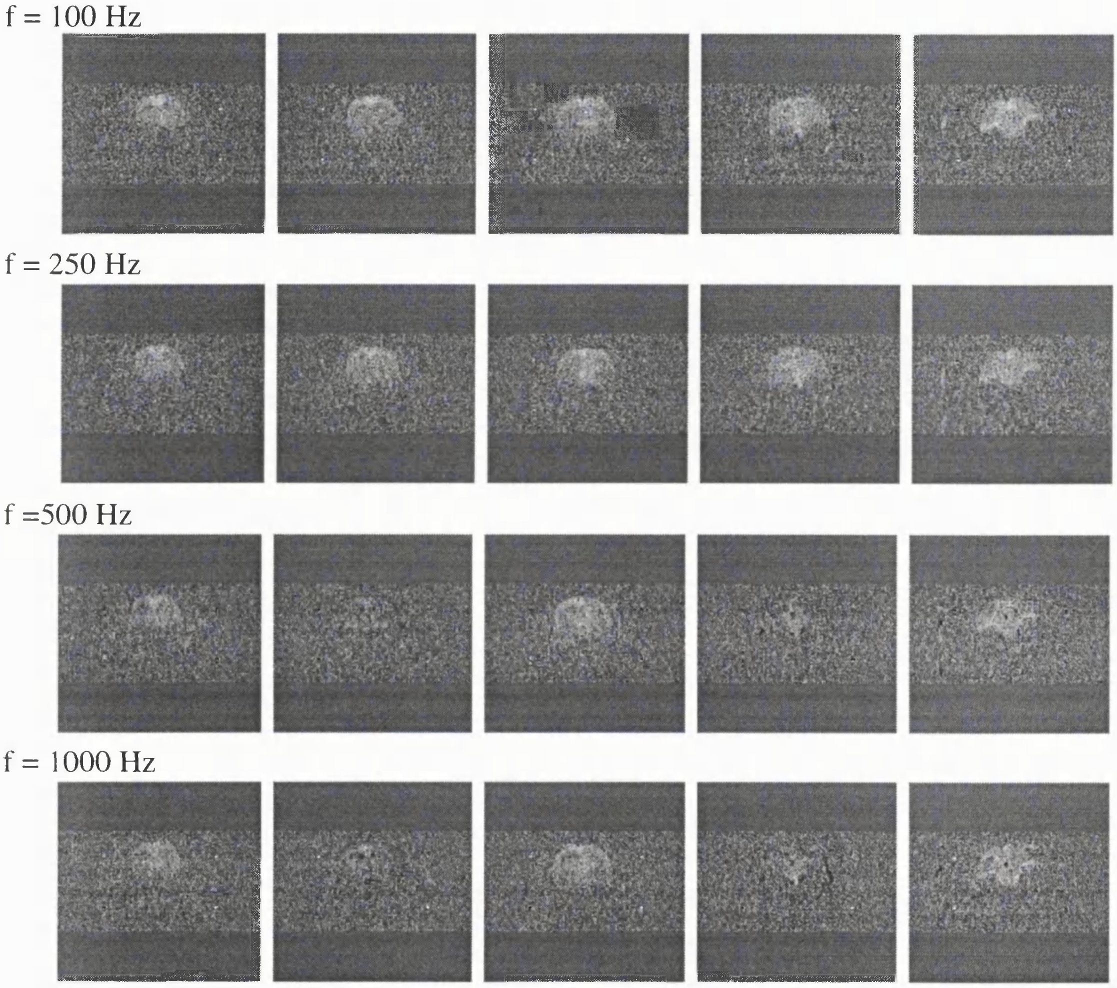

Figure 5.13

Subtraction images with different modulation frequencies for the AM control.

Images are shown at 5 slice positions.

Frequency offset = 5 kHz at 18 mm to the central slice, B_1 = 130 Hz, w = 50ms *a) proximal label*

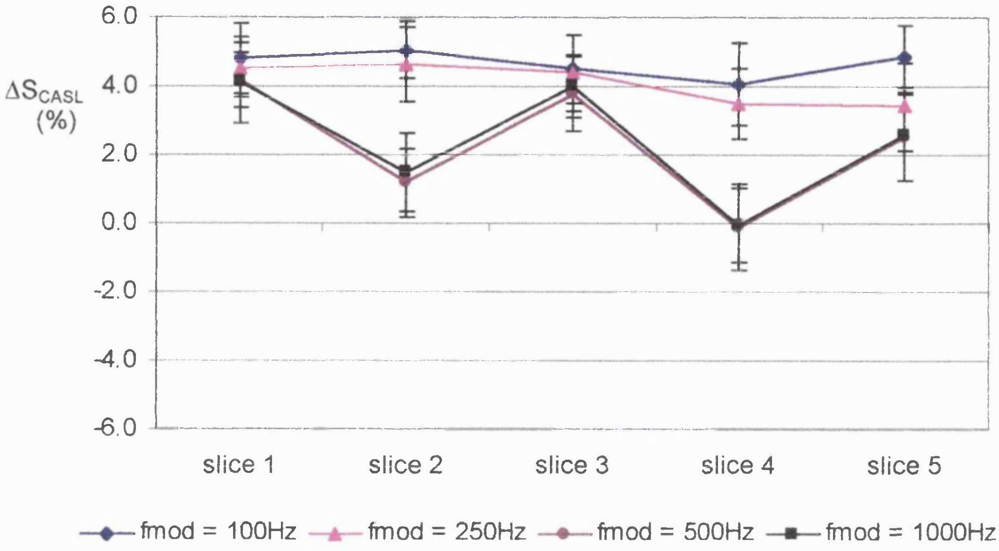

b) distal label

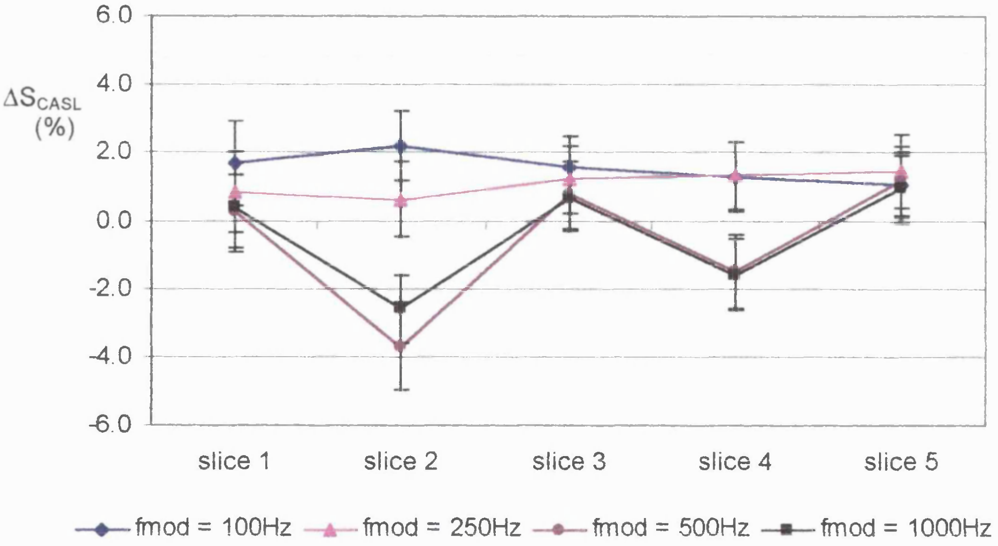

Figure 5.14

Signal differences in the cortex when labelling and control planes were proximal (a) and distal (b) to the imaging planes (data for *5.14a* are from images in *Figure 5.13*).

Frequency offset = 5 kHz at 18 mm, B_1 = 130 Hz, w = 50ms.

$\Delta S_{CASL} = 100 * (S_{control} - S_{label}) / S_{control}$

The sizes of the ROIs were 18 mm^2, 17 mm^2, 20 mm^2, 13 mm^2 and 8 mm^2 in slices 1, 2, 3, 4 and 5.

Errors bars were calculated from the signal-to-noise ratios in the label and control images in each slice.

5.4.3 Discussion of CASL imaging in normal rat brain

The sensitivity of CASL images to perfusion depends on several parameters and the first point to consider is the labelling process itself. The degree of labelling increases with increasing B_1, in a given magnetic field gradient, G, as demonstrated by increased contrast in subtraction images at higher B_1 in *Figure 5.7.* Ideally CASL images would have been obtained at higher B_1 to confirm that the degree of labelling did not increase further at higher B_1. This procedure was employed in the next part of this Chapter (Section 5.5) at a frequency offset of 10 kHz. However, an optimum B_1 of 180 Hz is compatible with the optimum value predicted from the computer model of labelling by velocity driven AFP.

It is important that B_1 is sufficient for efficient AFP, but excessive B_1 amplitudes are unnecessary and even undesirable for several reasons. If B_1 is greater than the optimum the labelling efficiency, α, actually decreases due to increased T_2 relaxation during the inversion (Chapter 3, *Figure 3.4*). This effect may be too small to detect in practice. However, further considerations at higher amplitudes of B_1 are the worse MTC cancellation (*Figure 5.5*), the increased risk of heating the animal through RF power deposition and the greater demands on RF amplifiers and transmission coils.

After the RF pulse for labelling a post-tagging delay was introduced before image acquisition, w. A long delay minimises both contributions from macrovascular flow and the dependence of the flow-dependent signal on arterial transit times, δ. The dependence of the optimum value of w on values of δ is problematic in two ways. Firstly, values of δ vary between different parts of the brain and they depend on the separation of the labelling plane from the imaging plane. Thus there may be apparent differences in rCBF due to different transit times in brain regions with the same actual rCBF. Secondly, arterial transit times are liable to change in certain physiological states. Reduced δ have been measured, for example, in activation studies in humans (Gonzalez-At JB et al. 2000) and in hypercarbia in rats (Zhang W et al. 1992). A reduction in δ increases the possibility of over-estimation of rCBF (Gonzalez-At JB et al. 2000). For multiple-slice acquisitions, δ and w vary with slice position. There is a case for acquiring images closest to the labelling plane first because they have the shortest δ (i.e. in the order 5,4,3,2,1 for the set up described in this Chapter (*Figure 5.1*)), but this is unlikely to eliminate the problem entirely. Another consideration for the choice of slice acquisition order is the sensitivity to any residual MT differences. If slices were acquired in the order 5,4,3,2,1 any residual differences in MTC between the label and control would be accentuated in slice 5 both because it has the smallest frequency offset from the labelling plane and because the least T_1 relaxation would have occurred to restore the tissue magnetisation to M_0 during w.

Focal bright spots appear in subtraction images when w is too short for labelled blood to leave the macrovasculature in the imaging plane. A significant proportion of the labelled blood then resides within large blood vessels and signal differences due to this blood do not reflect perfusion. The subtraction images in *Figure 5.9* show that bright spots became less prominent when w is greater than approximately 350 ms. Macrovascular contributions disappear if w is greater than δ, suggesting that δ is close to 350 ms in this slice. This is consistent with values of δ reported by other groups. Zhang et al. measured $\delta = 310$ ms at a 20 mm offset of the labelling plane in normal rat brain (Zhang W et al. 1992) and Barbier et al. found similar values (Barbier EL et al. 1999).

Visual inspection of subtraction images reveals the most obvious macrovascular contributions but contrast to noise ratios decrease with w, reducing the sensitivity of subtraction images to differences in flow. This calls into question the reliability of this subjective approach to selection of w. Direct measurement of δ would provide a more robust method for selecting w. In theory this may be done by repeated measurements of ΔS_{CASL} at different w to identify the arrival time of the first labelled blood after a brief labelling pulse (Zhang W et al. 1993; Ye FQ et al. 1997). Many measurements would be required to determine δ accurately. On our system each measurement lasts approximately nine minutes in order to achieve adequate signal-to-noise, making the total measurement time very long. Such a procedure may be valuable to determine normal values of δ, but is of limited use in situations where δ changes rapidly.

Contrast in CASL images is a combination of MTC and perfusion weighting. MTC must be equivalent in label and control images for accurate quantification of microvascular blood flow. A means of confirming MT equivalence without blood flow effects *in-vivo* was devised by placing both the label and AM control pulses distal to the imaging slices, so that no arterial spins were labelled, but similar MT effects to those of the true labelling and AM control pulses were produced. Using this procedure it was found that the difference in signal intensity between label and control images, ΔS_{CASL}, was dominated by perfusion, even when cancellation of MTC was imperfect (*Figures 5.11* and *5.12*) (see also ΔS_{CASL} when f = 100 Hz and f = 250 Hz in *Figure 5.14*).

Once the labelling pulse is optimised, the modulation frequency of the AM control must be selected to satisfy two requirements. The efficiency of labelling must be as great as possible and MTC in control and labelled images must be identical.

The double inversion of the AM control pulse never restores the magnetisation of moving spins to equilibrium, resulting in partial labelling. This partial labelling is discussed in Chapter 4, where the effects of the AM pulse on the magnetisation of protons in blood was determined independently of MT effects. In practice it appears that MT effects at high f may be as great a limitation as low labelling efficiency (*Figures 5.13* and *5.14*). *In-vivo* MTC appears to have a stronger dependence on slice position than MTC in images of pork (compare results with f = 500 Hz in *Figure 5.14* and *Figure 5.6*), although differences in the labelling gradient, G, for the two experiments also influence these results.

It is not clear why lower sensitivity to perfusion was observed in slices 2 and 4 when f = 500 Hz or 1000 Hz while ΔS_{CASL} in the central slice is similar to ΔS_{CASL} when f = 100 Hz or 250 Hz (*Figure 5.13* and *Figure 5.14*). This may be due to a complicated combination of MT effects from the two components of the AM pulse, one of which moves further from the imaging plane, and one of which moves closer as f increases. A frequency offset of 5 kHz when the labelling plane is 15 mm from the imaging plane results in a separation of the AM control planes of ± 0.6 mm when f = 100 Hz and ± 3.0 mm when f = 500 Hz. Lower ΔS_{CASL} at higher f is consistent with reduced signal in control images, and therefore more magnetisation transfer. This suggests that the component of the AM pulse closest to the images may make an excessive MT contribution when f is greater than about 500 Hz.

In summary, preliminary CASL images of normal rat brain have been acquired using the AM control in five imaging slices. The optimum B_1 is approximately 180 Hz when a frequency offset of 5 kHz is employed at a separation of 15 mm from the central imaging plane. A three second labelling pulse is sufficient for magnetisation in the brain to reach a new equilibrium level, $M_{0sat.}$. A post-labelling delay of at least 350 ms is required to allow blood to leave the macrovascular compartment within the central imaging slice of the brain of normal rats. A modulation frequency of 250 Hz or 100 Hz produced maximum sensitivity of the AM control to rCBF and minimal residual MT differences in five slice positions.

5.5 Comparison of AM control with standard single slice control

In the Section 5.3 of this chapter, the AM control was shown to produce MT cancellation far superior to that of the standard control in non-central slices (*Figures 5.5* and *5.6*). However, increased spatial coverage with the AM technique is gained at the expense of reduced flow-sensitivity, as described in Chapter 4. The following section describes an experiment to evaluate the sensitivity of CASL images with the AM control, relative to the sensitivity of CASL with the standard control.

A series of *in-vivo* experiments, lasting several hours permitted repeated comparisons of the two control techniques under almost identical conditions. The experiments were part of an investigation into the link between circadian rhythms and the incidence of stroke (Helliar RW 2001). Animal preparation was performed by Robert Hellier and I acquired and analysed the CASL images.

The aim of the physiological experiment was to mimic low blood pressure during sleep in order to create the physiological conditions under which strokes frequently occur. Rats were made hypotensive by intravenous injection of the pharmacological agent, clonidine. The rats were imaged continuously at 2.35 T before and after administration of clonidine to detect signs of spontaneous stroke. The imaging protocol included diffusion weighted imaging, T_2 and T_2* and CASL measurements.

5.5.1 Method

CASL was performed as described in Section 5.2 every half hour with the following parameters for the labelling and control pulses: offset frequency = 10 kHz, labelling plane 15 or 16 mm from the central imaging plane (to lie at the back of the brain, as in *Figure 5.1*), B_1 = 200 Hz for the label and $200*\sqrt{2}$ = 283 Hz for the AM control, w = 300 ms, number of averages = 56, acquisition time = 8 minutes and 45 seconds, f = 250 Hz for the AM control, for the standard control the sign of the frequency offset was reversed to define a control plane distal to the imaging plane(s). CASL images were acquired in slices of thickness 2 mm, separated by 2.1 mm, with a FOV of 40 mm. Five slices were acquired with the AM control and only the central slice was acquired with the standard control.

Adult, male, Sprague-Dawley rats were maintained under anaesthesia with isofluourane in O_2 and N_2O. Mean arterial blood pressure was monitored through a catheter inserted into the femoral artery. Temperature and ECG were monitored continuously and temperatures remained within the normal range ($37.5 \pm 1.0\ ^0$C).

After a period of baseline imaging the pharmacological agent, clonidine, was injected into the femoral artery to lower mean arterial blood pressure to approximately 80 % of its baseline value (n = 3). Further injections were administered to maintain the hypotensive state, as necessary. Normal, control rats were monitored in the same way and imaged for a time equivalent to the duration of the clonidine experiments, but clonidine was not injected into these animals (n = 2).

Preliminary experiments were performed to select the amplitude of B_1 for maximum efficiency of labelling and to determine T_{1sat} for quantification of rCBF.

In order to confirm that B_1 = 200 Hz yielded the maximum degree of inversion four pairs of experiments with the standard control were performed with B_1 = 200 Hz and 250 Hz then four pairs with B_1 = 200 Hz and 300 Hz (an experiment comprises one label and one control image). Normalised subtractions of the signal intensity in control ($S_{control}$) and labelled (S_{label}) images were calculated from a ROI in the cortex, using equation [5.4].

The longitudinal relaxation in the presence of a saturation pulse, T_{1sat}, is required for calculation of rCBF (equation [2.9] on page 25). T_{1sat} was measured in one animal by inversion recovery with a saturation pulse applied before inversion and in the interval between the inversion pulse and image acquisition (the inversion time). The amplitude of the saturation pulse was equal to that of the labelling pulse for CASL (200 Hz). Inversion times were 3, 100, 200, 500, 800, 1200, 2000, 3500 ms.

An inversion recovery (IR) experiment was performed for each animal to calculate T_1 on a pixel by pixel basis. A global, hyperbolic secant inversion pulse was applied and EPI images were acquired after an inversion time, TI. Measurements in each slice were separated by 78.2 ms and TI values in the central slice were 256, 356, 556, 756, 1156, 1656, 2656, 3656 ms. T_1 maps were produced using a routine in the Interactive Data Language (IDL, RSI, Boulder, Co. USA).

S_0 is the signal intensity in the IR image with the longest TI. It was used to normalise ΔS_{CASL}. The inversion recovery experiment was performed only once and therefore only one value for S_0 was obtained. In order to account for the possibility of drift in the RF receiver over the course of the experiment, the ratio, R_{norm}, of $S_{control}$ in the first CASL control image to S_0 was employed to normalise all ΔS_{CASL},

$$R_{norm} = S_{control}(t = 0) / S_0(t = 0)$$

Then ΔS_{CASL} becomes

$$\Delta S_{CASL} = 100 * R_{norm} (S_{control} - S_{label}) / S_{control} \qquad \text{equation [5.5]}$$

The normalised signal differences in images acquired with the AM control and the standard control are denoted ΔS_{AM} and $\Delta S_{standard}$, respectively.

One CASL experiment with the AM control was followed immediately by a CASL experiment with the standard control every thirty minutes. Time courses of $\Delta S_{standard}$ and ΔS_{AM} were determined and the ratio $\Delta S_{AM} / \Delta S_{standard}$, was calculated to estimate the labelling efficiency of the AM control relative to that of the standard control.

rCBF was calculated on a pixel-by-pixel basis, using a program written in the Interactive Data Language (IDL, RSI, Boulder, Colorado, USA), following the model described by Alsop and Detre (Alsop DC and Detre JA 1996). I adapted the code from that employed by David Thomas (Thomas DL 1999).

Equation [5.6] describes the calculation required to determine rCBF from label and control CASL images (Alsop and Detre 1996 and Appendix E).

$$rCBF = \lambda(S_{control} - S_{label})/(2\alpha S_0(C_{T1} + C_{T1sat})\exp[-\delta/T_{1a}]) \quad \text{equation [5.6]}$$

where

λ is the partition coefficient (ml of water per ml of blood/ml of water per ml of brain tissue)

$S_{control}$ and S_{label} are the signal intensities in the control and label CASL images

α is the efficiency of labelling

δ is the arterial transit time

T_{1a} is the T_1 relaxation time of arterial blood

C_{T1sat} and C_{T1} describe the relaxation of labelled spins during the labelling pulse and during the post-labelling delay respectively

$C_{T1sat} = T_{1sat}\exp[-w/T_1]$

$C_{T1} = T_1(\exp[(-w+\delta)/T_1] - \exp[-w/T_1])$

in the cases where $\delta < w$ (slices 2,3,4,5)

$C_{T1} = T_1(1 - \exp[-w/T_1]) + T_{1a}(\exp[-w/T_{1a}]-\exp[-\delta/T_{1a}])$

in the case where $\delta > w$ (slice 1)

T_{1sat} is the observed spin - lattice relaxation time of brain tissue in the presence of the labelling pulse

T_1 is the observed spin – lattice relaxation time of brain tissue

S_0 is the signal when the magnetisation is at equilibrium. This was found in the process of fitting for T_1.

In this study the following values were assumed:

$\lambda = 0.9$

$\delta = 350, 300, 250, 200, 150$ ms in slices 1, 2, 3, 4, 5,

$T_{1a} = 1500$ ms

$\alpha = 0.9$ for the standard, single slice experiment

5.5.2 Results of comparison of AM control with standard single slice control

The pharmacological agent, clonidine, was administered to rats to maintain the mean arterial blood pressure at 80 % of normal level for up to six hours. No changes were observed in apparent diffusion coefficient, T_2 or T_2* values in the brains of hypotensive animals, indicating that the animals remained physiologically stable over the course of the experiment and justifying the use of these rCBF data to compare control techniques for CASL.

Table 5.1 shows ratios of $\Delta S_{standard}$ with B_1 = 250 Hz and B_1 = 300 Hz to $\Delta S_{standard}$ with B_1 = 200 Hz in a region of interest in the cortex of a normal rat's brain. $\Delta S_{standard}$ was not significantly greater at B_1 = 250 Hz or B_1 = 300 Hz than at B_1 = 200 Hz, suggesting that labelling efficiency was maximal at B_1 = 200 Hz. A frequency offset of 10 kHz at 15 mm from the central imaging plane requires a gradient of 667 Hz/mm. The optimum B_1 values predicted using the computer model (Chapter 3) for labelling gradients of 650 Hz/mm and 700 Hz/mm are 199 Hz and 207 Hz respectively (*Figure 3.5*), in agreement with these results *in-vivo*.

	Ratio of $\Delta S_{standard}$
$B_1 = 250$ Hz	1.02 ± 0.11
$B_1 = 300$ Hz	1.02 ± 0.02

Table 5.1

Ratios of $\Delta S_{standard}$ with B_1 = 250 Hz and B_1 = 300 Hz to $\Delta S_{standard}$ with B_1 = 200 Hz. (mean ± standard deviation of 4 pairs of measurements).

Frequency offset = 10 kHz at 15 mm from the imaging plane.

$\Delta S_{standard} = 100 * R_{norm} (S_{control} - S_{label}) / S_{control}$

Comparison of sensitivity to rCBF using AM and standard controls

Examples of subtraction images with the AM control and the standard single slice control during the baseline period in an hypotensive animal are shown in *Figure 5.15*. Regions of perfused tissue may be identified in each subtraction image but the superior contrast with the single slice control is evident. This reflects the poorer sensitivity of the AM control.

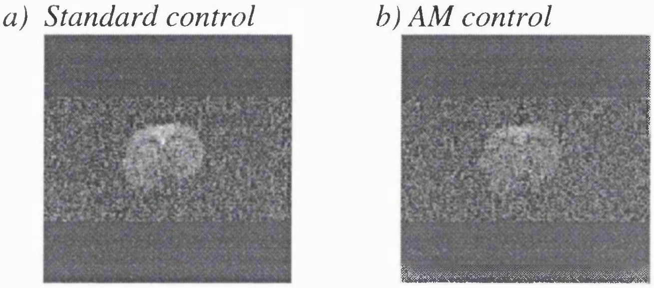

CNR = 3.1 ± 0.3 CNR = 1.7 ± 0.3

Figure 5.15

CASL subtraction images with the standard control (a) and the AM control (f = 250 Hz) (b) in the central slice position.

10 kHz offset at 15 mm, B_1 = 200 Hz, w = 300 ms.

Contrast-to-noise ratios are quoted as mean ± standard deviation of four regions of interest with areas between 3 and 4 mm^2 in the left and right cortex and basal ganglia.

Time courses of ΔS_{CASL} in cortical regions of interest in two normal, control rats and three hypotensive rats are shown in *Figure 5.16*. Results were similar in other brain regions. The times at which clonidine was injected are indicated by arrows in each plot. A reduction in $\Delta S_{standard}$ and ΔS_{AM} occurred after the first injection of clonidine in every hypotensive animal, suggesting that the clonidine caused a small reduction in perfusion (although it is possible that the apparent reduction was due to lower labelling efficiency as a result of a reduction in arterial blood velocity).

$\Delta S_{standard}$ was measured in the second normal rat post-mortem to confirm that the contrast observed in subtractions was not caused by different MT effects in label and control images. $\Delta S_{standard}$ was 0.1 % post-mortem, much lower than $\Delta S_{standard}$ during the *in-vivo* part of the experiment (5.5 ± 0.5 %).

ΔS_{AM} was lower than $\Delta S_{standard}$ in every animal, although variations in ΔS_{AM} with time generally followed the same pattern as $\Delta S_{standard}$.

In the first normal rat only four CASL experiments were performed using the AM control (*Figure 5.16a*). In the second normal, ΔS_{AM} was significantly lower than in the other animals (*Figure 5.16b*). The fact that $\Delta S_{standard}$ in this animal was similar to $\Delta S_{standard}$ in other animals makes it unlikely that low ΔS_{AM} are due to lower rCBF. It is possible that the AM control caused more significant partial labelling of the arterial blood in this animal than in the other animals, reducing the signal difference between label and AM control images.

The first hypotensive animal (*Figure 5.16c*) died shortly after the second injection of clonidine, after about 240 minutes of imaging. Values of $\Delta S_{standard}$ were generally higher in the third hypotensive animal than in the second, while values of ΔS_{AM} were approximately the same in both animals.

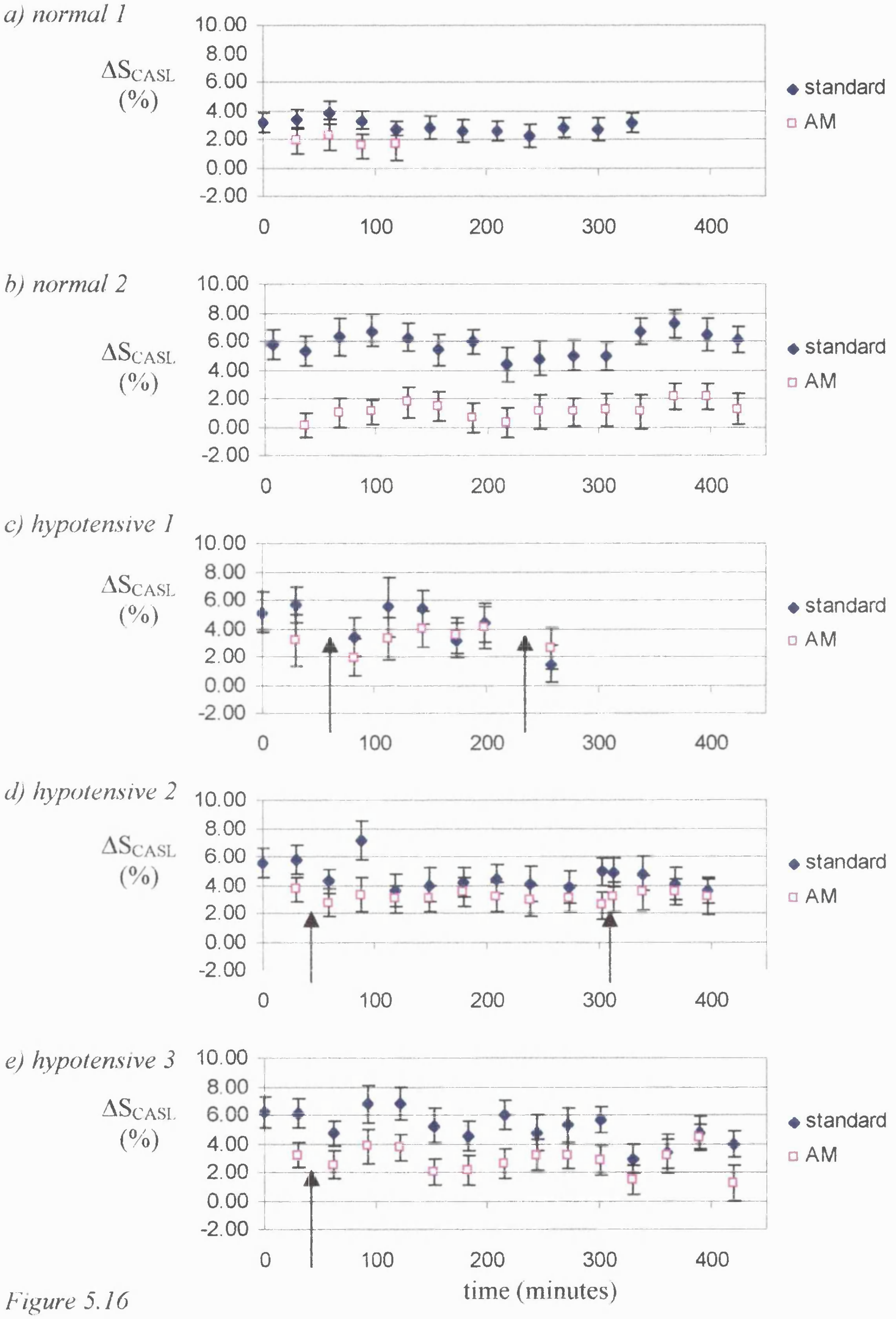

Figure 5.16

ΔS_{CASL} in five animals using the standard control and the AM control (f = 250 Hz). Arrows indicate times at which clonidine was injected.

$\Delta S_{CASL} = 100 * R_{norm} (S_{control} - S_{label}) / S_{control}$

Error bars = $(S_{label} / S_{control}) * \sqrt{[(1/SNR_{label}{}^{2} + (1/SNR_{control})^{2}]}$

Calculation of rCBF

Values of $\Delta S_{standard}$ and ΔS_{AM} are shown for each animal in *Table 5.2*, averaged over four regions of interest over the whole time course for each animal, but excluding the first point after each injection of clonidine for the hypotensive animals. The mean $\Delta S_{AM}/\Delta S_{standard}$ of all animals is 0.7 ± 0.2, excluding the second normal animal. The ratio $\Delta S_{AM}/\Delta S_{standard}$ is proportional to the ratio of labelling efficiencies for the two experiments, α_{AM} / α, where α is defined in Chapter 2 by equation [2.10] and α_{AM} is defined in Chapter 4 by equation [4.2]:

$$\alpha = (1 - m_{a\_label}) / 2$$

$$\alpha_{AM} = (m_{a\_control} - m_{a\_label}) / 2$$

In order to calculate rCBF from the AM control images the mean $\Delta S_{AM}/\Delta S_{standard}$ of 0.7 was employed as a calibration factor for the labelling efficiency of the AM control. Maps of rCBF were made using $\alpha = 0.9$ for the standard control and $\alpha_{AM} = 0.7 * 0.9 = 0.63$ for the AM control.

Experiment	Normal		Hypotensive		
	1	2	1	2	3
mean $\Delta S_{standard}$	4.2 ± 0.7	5.5 ± 0.5	4.9 ± 0.4	4.9 ± 0.4	5.1 ± 0.1
mean ΔS_{AM}	2.8 ± 0.9	1.4 ± 0.3	3.4 ± 0.3	3.4 ± 0.3	3.2 ± 0.4
$\Delta S_{AM}/\Delta S_{standard}$	0.64	0.25	0.72	0.72	0.64
Number of measurements	4	14	5	12	13

Table 5.2

$\Delta S_{standard}$ and ΔS_{AM} *in-vivo*

Values are means ± standard deviations, excluding measurements immediately post-injection. The number of measurements used to calculate $\Delta S_{AM}/\Delta S_{standard}$ is shown.

$\Delta S_{standard} = 100 * R_{norm} (S_{control} - S_{label}) / S_{control}$ (same calculation for ΔS_{AM})

T_{1sat} in one normal animal within a cortical ROI was calculated to be 800 ± 14 ms. This value was used in the rCBF calculation. T_1 maps were produced for each animal and values of T_1 in each pixel were employed to calculate rCBF.

The mean values of T_1 (for all animals) in cortical regions were 1405 ± 63 ms, 1271 ± 15 ms, 1219 ± 18 ms, 1215 ± 27 and 1264 ± 29 ms in slices 1 to 5. Values of T_1 in slice 1 were greater than 1300 ms in all animals. This may be due to partial volume effects in this slice.

Maps of perfusion at five slice positions acquired with the AM control are shown in *Figure 5.17*. A map of rCBF in the central slice in the same animal acquired with the standard CASL control is shown at an equivalent time in the experiment.

Time courses of rCBF measurements in normal animals are shown in *Figure 5.18a* and in hypotensive animals in *Figure 5.18b*. Data are shown for 5 slice positions using the AM control and the central slice position using the standard CASL control.

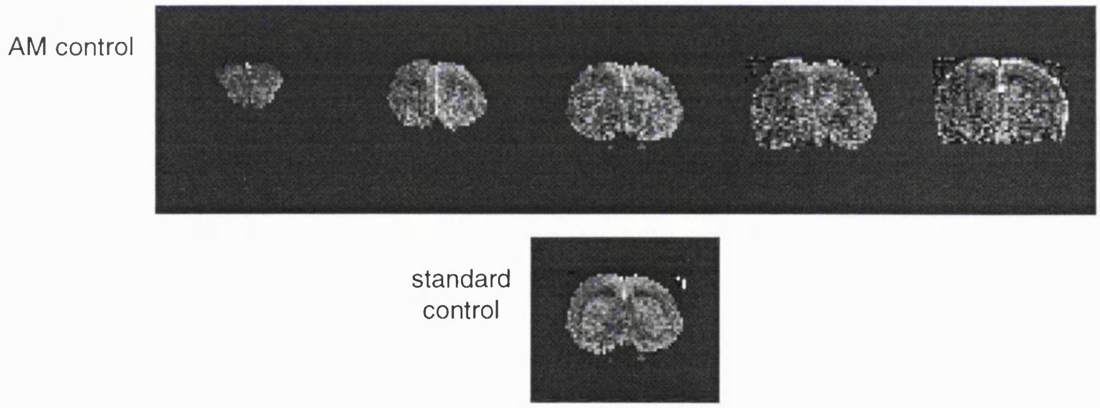

Figure 5.17

Maps of rCBF calculated from CASL images in normal control animal 1.

The AM control was used to acquire images in five slices (top) and the standard control was used to acquire images in the central slice position.

B_1 = 200 Hz for labelling pulse (and $200\sqrt{2}$ Hz for B_{10} of the AM control), f = 250 Hz *normal 1*

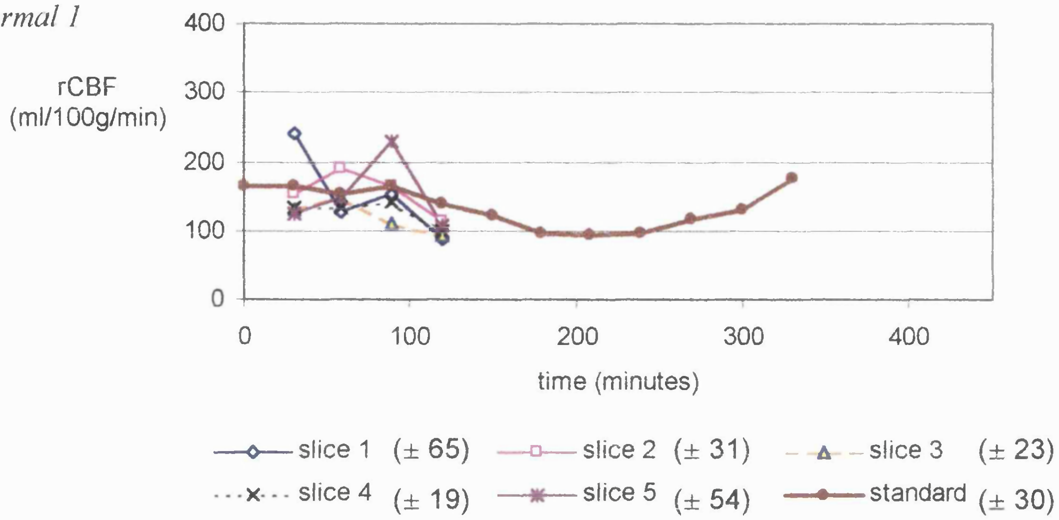

normal 2

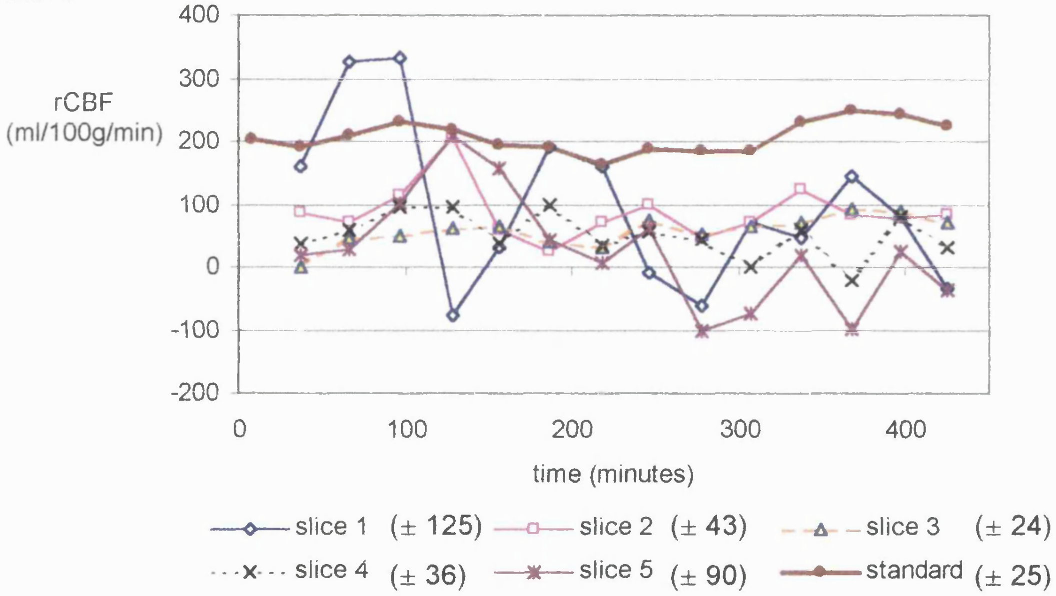

Figure 5.18 a)

Time courses of rCBF in cortical regions of interest in normal rats

Measurements are shown in 5 image slices using the AM control and the standard control in the central slice (slice 3). Values of rCBF are corrected for the lower degree of labelling with the AM control.

Shown in the key of each plot are the standard deviations of all rCBF values over the whole time course, excluding points immediately after injections of clonidine.

hypotensive 1

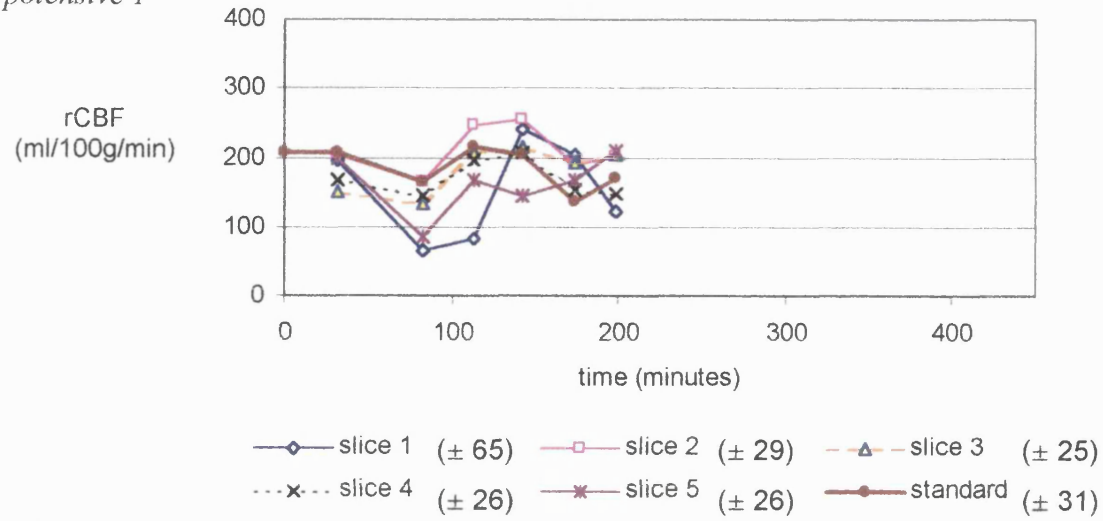

hypotensive 2

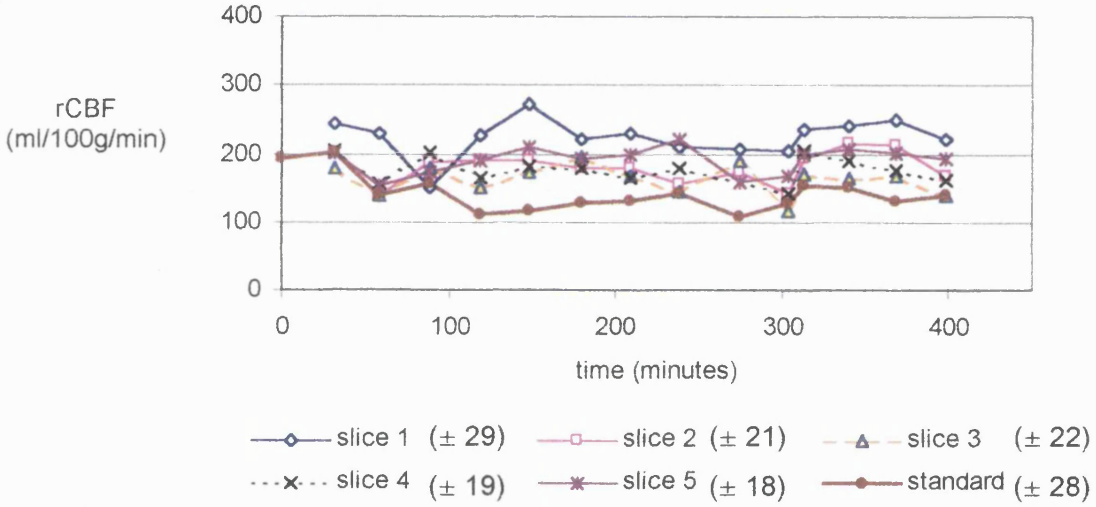

hypotensive 3

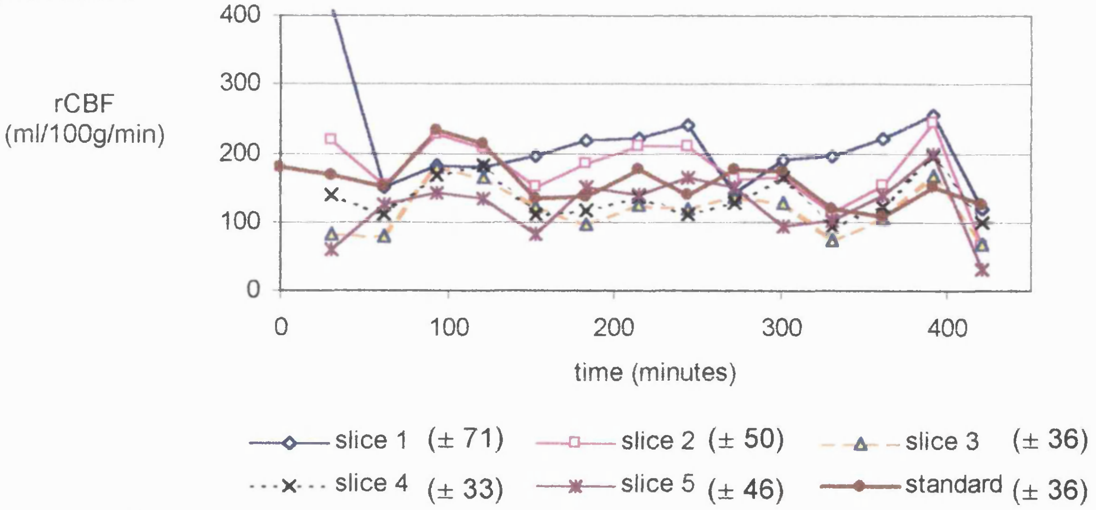

Figure 5.18 b)

Time courses of rCBF in hypotensive rats

(all parameters as in *Figure 5.18a*)

5.5.3 Discussion of comparison of AM control with standard single slice control

These experiments compared the AM control with the standard control for CASL. The ratio of the labelling efficiencies with the AM and standard control schemes (α_{AM} / α) was found to be 0.7, which is comparable to values determined in humans (Alsop DC and Detre JA 1998). Calculations of rCBF using the AM control and the standard control agree to within about ± 30 ml/100g/min. Values of rCBF are comparable with those in previous reports of CASL measurements in rat brain (for example 127 ± 44 ml/100g/min (Zaharchuk G et al. 1999a), approximately 200 ml/100g/min (Barbier EL et al. 1999), 200 ± 40 ml/100g/min, 180 ± 10 ml/100g/min (Zhang W et al. 1993). The discussion that follows is divided into sections on i) the AM and standard controls, and ii) the quantification of rCBF and the choice of post-tagging delay.

Comparison of the AM control and the standard control

From the definitions of α_{AM} and α, the mean m_{a_label} and $m_{a\_control}$ for the AM experiments described in this chapter may be estimated as follows. Setting $\alpha_{AM} = 0.7\alpha$ and assuming $\alpha = 0.9$ gives:

$$0.9 = (1 - m_{a\_label}) / 2$$

$$m_{a\_label} = -0.8$$

and:

$$\frac{\alpha_{AM}}{\alpha} = \frac{(m_{a\_control} - m_{a\_label})}{(1 - m_{a\_label})}$$

$$0.7 = (m_{a\_control} + 0.8) / (1.8)$$

$$m_{a\_control} = 0.46$$

Ideally $m_{a\_control} = +1.0$. Clearly the behaviour of the AM pulse falls far short of this ideal. In Chapter 4 it was predicted that the maximum value of $m_{a\_control}$ that is achievable with the AM control is + 0.8 (*Figure 4.4*). However, in this comparative study the same mean amplitude of B_1 was employed with both controls, in order to produce the same mean power deposition. This makes it likely that B_1 was lower than the optimum for the AM control, which may at least partly account for the low value of $m_{a\_control}$.

The labelling pulse is sensitive to B_1 and v but the AM control pulse is much more sensitive (*Figures 3.4* and *3.10* in Chapter 3 and *Figures 4.7* and *4.8* in Chapter 4). In the second normal animal (*Figure 5.16b*) ΔS_{AM} was constantly and significantly lower than in the other rats in all imaging slices, despite similar values of $\Delta S_{standard}$ to those in other animals. Reduced α_{AM} may be due to sub-optimal B_1, or a difference in the amplitude of the labelling gradient relative to that employed for other animals.

In normal rat 2 the labelling plane was 16 mm from the imaging plane, but in the other animals this distance was 15 mm. This did not significantly affect the labelling process ($\Delta S_{standard}$ for normal rat 2 is comparable to $\Delta S_{standard}$ in other animals) but the lower value of G for a 16 mm offset also increased the physical separation of the two AFPs for the AM control. This increased the possibility of a change in the velocity or direction of blood flow between one AFP and the next. If such a change occurred, the degree of inversion by the first AFP of the AM pulse may not be the same as the degree of re-inversion by the second AFP, leading to partial labelling by the AM control and reduced α_{AM}.

While the preceding argument illustrates one of the problems with the AM control, it seems to be unlikely that the very low perfusion sensitivity of the AM control in normal rat 2 is attributable solely to a slightly lower amplitude labelling gradient. The long RF pulse for the label or control pulse is very demanding on the RF transmit coil and it may be that the AM control pulse, which has a higher peak amplitude than the label, was not transmitted accurately (in terms of peak amplitude and / or duration). This demonstrates the greater demands on RF hardware made by the AM control and the greater possibility of failure of the measurement.

In order to obtain the same contrast-to-noise ratio (CNR) in CASL with the AM control as with the standard control, greater SNR in the images is required. The necessary improvement in SNR may be calculated from the ratio α_{AM} / α. Assuming that the noise in label and control images is approximately the same in both experiments, the SNR of images for the AM control experiment must be 1/0.7 times greater than the SNR of images for the standard control experiment. This would require an increase of $1/(0.7)^2 = 2.0$ in the number of averages, equivalent to a doubling of the image acquisition time (retaining the same FOV, image matrix and slice thickness).

Values of rCBF and the choice of post-tagging delay

The differences in signal intensities, $\Delta S_{standard}$, and hence the values of rCBF measured with the standard control tend to be lower in normal rat 1 and hypotensive rat 2 than in the other animals (*Figure 5.18*). Systematic errors in calculated values of rCBF may be caused by inaccurate estimation of α or δ, or poor cancellation of MT effects in label and control images. The last of these possibilities was excluded in one animal in which $\Delta S_{standard}$ was 5.5 ± 0.5 % *in-vivo*, but only 0.1 % post mortem, confirming that cancellation of MT effects in this case were adequate.

α depends on numerous factors, including the amplitude of B_1 and the velocity of blood flowing through the carotid arteries (Chapter 3). If any of these factors changed between different experiments, an assumption of uniform α across all experiments would be invalid. For example, if $\alpha = 0.8$ rather than 0.9, an actual rCBF of 150 ml/100g/min would be measured as 133 ml/100g/min (under-estimation by 11 %).

Differences in δ may reflect physiological variations between animals or variations in the same animal over time. If $\delta = 300$ ms or 200 ms instead of 250 ms, an actual rCBF of 150 ml/100g/min would be measured as 159 ml/100g/min or 142 ml/100g/min respectively (over- or under-estimating true values by 6 %). This variation in rCBF is within the range of experimental error found here, suggesting that errors in δ of ± 50 ms would not introduce significant errors to rCBF values with a post-tagging delay of 300 ms.

A post-tagging delay of w = 300 ms is similar to measurements of δ in normal rat brain (Zhang W et al. 1992; Barbier EL et al. 1999). However, some CASL subtraction images showed bright regions in the brain around and above the sagittal sinus, in the territory of the anterior cerebral artery, especially following periods of hypoxia in an extension of the original study (data not shown). This suggests that w may not have been long enough to allow labelled blood to wash through the larger blood vessels supplying that territory. During hypoxia, δ may increase if vasodilation occurs. In the case of an hypotensive animal, arterial blood velocity may be reduced, again increasing δ. If perfusion decreased at the same time, the measured rCBF may not reflect the total change in perfusion. Although lower perfusion would reduce ΔS_{CASL}, longer δ would increase ΔS_{CASL} because labelled spins relax with the longer T_1 of arterial blood for longer and the magnetisation returns to equilibrium more slowly.

5.6 General discussion and conclusions

CASL images have been acquired in three studies. In the first, MTC effects of the AM control in samples of meat were assessed. In the second, the AM control was optimised *in-vivo* in rat brain. In the final study rCBF was measured in rat brain using the AM control and the standard control. The following discussion comprises sections on the AM control, measuring α and α_{AM} *in-vivo*, arterial transit times and differences between CASL experiments in humans and in animals.

5.6.1 The AM control

The AM control has lower sensitivity than the standard control for CASL (Wong EC et al. 1998a; and Chapter 4), making it imperative to maximise the performance of the double inversion for the AM control and the equivalence of MTC in control and label images. It has been found that the amplitudes of the labelling and control pulses and the modulation frequency for the AM control pulse influence both flow sensitivity and MTC cancellation (Section 5.4).

Velocity driven AFP does not occur if B_1 is too small, but several disadvantages of excessively large amplitudes of B_1 have been highlighted. Firstly, B_1 values above the optimum reduce the degree of labelling (Chapters 3 and 4, *Figures 3.5* and *4.9*). Secondly, differences in MT between the label and control may be emphasised at higher B_1, increasing the likelihood of erroneous rCBF values (*Figure 5.5*). Further important considerations are high RF power deposition, which may result in heating the animal, and greater demands on hardware.

Predictions of optimum B_1 values for labelling, made from the computer model, agree well with estimates of optimum B_1 values found at offsets of 5 kHz and 10 kHz *in-vivo* (*Figure 5.6* and *Table 5.1*). For the AM control the computer model predicted that the optimal mean value of B_1 was approximately 30 % higher than the optimal value for the labelling pulse. However, in order to compare the techniques under conditions that were as similar as possible, the same mean B_1 was employed for the standard and AM controls in the study described in Section 5.5. Therefore the value of B_1 was probably less than the optimum for the AM control.

The choice of modulation frequency (f) affects both the efficiency of the double inversion of moving spins and the cancellation of MT effects in tissue. The double inversion was studied in Chapter 4 and the condition that f must be approximately equal to B_{10} for independent inversion and re-inversion was found (see also Appendix A). The results of this chapter indicate that poor MTC cancellation at high f (in this case greater than 500 Hz) may also reduce the sensitivity of the AM control (*Figures 5.12b, 5.13b, 5.5*). Furthermore, the greater the physical separation of the AM control planes the greater the possibility of a change in the velocity of blood as it moves between the planes of inversion and re-inversion. In the worst case, there may be only one inversion if the adiabatic condition is satisfied for only one AFP.

In order to achieve the same contrast to noise ratios in CASL images with the AM control as with the standard control, the signal to noise ratio of the individual labelling and control images must be increased, as described in Section 5.5.3. If CASL with the AM control produced 0.8 times the contrast of CASL with the standard, single slice control (as predicted for the optimised AM pulse in Chapter 4) image acquisition times would have to increase by a factor of $1/0.8^2 = 1.56$ for the same CNR. However, with a relative contrast of 0.7 the imaging time for the AM control experiment must be increased by a factor of 2 relative to the imaging time for the standard, single slice control. This represents a severe limitation of the AM technique, when one considers that the imaging time for the standard control is already on the order of several minutes (about nine minutes with the scanner used for these experiments).

The AM control technique requires higher B_1 and more averages to achieve sensitivity that is comparable to the standard control. Even with these adjustments, the AM control is more prone to reductions in labelling efficiency at high velocities of blood and sub-optimal B_1 amplitudes (Chapter 4, *Figures 4.9* and *4.10*) and apparent low rCBF values may be due to failure of the AM control (*Figure 5.16b*).

5.6.2 Measuring α and α_{AM}

α may be determined *in-vivo* by measuring the magnetisation of blood in an artery immediately after labelling (Zhang W et al. 1992). Application of the same technique may be employed to determine the magnetisation of blood after application of the AM control, to calculate α_{AM} (equation [4.2]). However, the measurement of m_{a_label} or $m_{a\_control}$ presents some significant difficulties. Firstly, the lumen of the carotid arteries occupies at most one or two pixels in an image and partial volume effects are likely to introduce errors into the measurement. Secondly, although the flow through the vertebral arteries is a small fraction of the total cerebral inflow, this may increase if flow through the carotid arteries is compromised and for accurate calculation of rCBF the contribution of the vertebral arteries should be taken into account. The measurement of α in the vertebral arteries would be much more challenging than in the carotid arteries because they are considerably smaller and partial voluming is more likely. Lastly, it may not be possible to measure m_{a_label} with the geometrical arrangement employed for experiments described in this chapter because the carotid arteries are too narrow "downstream" of the labelling position. In the experiment performed by Zhang et al. the labelling plane was 20 mm from the region where rCBF was measured. In their experiment m_{a_label} was measured in a position where blood entered the brain, the location of the labelling plane for the experiments described in this chapter. Measuring α is very challenging and to determine α_{AM} even greater sensitivity would be required to detect relatively small changes in $m_{a\_control}$ due to the AM pulse.

5.6.3 Arterial transit times

Any labelled spins within the slice of interest contribute to the perfusion signal, including those in arterial blood, which does not perfuse tissue in the slice where it is seen. If signal from arterial blood is included in the calculations, perfusion is overestimated. There are two approaches to reduce the contribution of macrovascular flow through large vessels to signal differences in ASL images. Either a delay is introduced between the end of the labelling period and image acquisition (w) (Alsop DC and Detre JA 1996); or low amplitude spoiler gradients are applied to crush the signal in large vessels (Pekar J et al. 1996). If crusher gradients are applied after labelling, the amplitude of these gradients is chosen to eliminate signal from any vessel that is larger than a required threshold. If labelled spins have arrived in the imaging voxel where they are destined to enter the tissue, but remain within the vascular compartment at the time of imaging, crusher gradients may lead to underestimation of perfusion (Buxton RB et al. 1998).

A post-labelling delay, w, was employed for experiments described in this chapter. The delay mitigates two possible sources of error in calculations of rCBF. If w is long enough, labelled blood leaves large vessels and reaches capillary exchange sites before images are acquired and secondly the sensitivity of calculated values of rCBF to δ is reduced. Another argument in favour of long w is reduced MTC, and hence a smaller possibility of signal differences due to MT rather than perfusion (*Figure 5.4*). However, the benefit of a long post-tagging delay must be weighed against the reduction in perfusion contrast at long w, due to increased T_1 relaxation of the labelled protons.

There is some evidence that w was shorter than would be optimal for the experiments in Section 5.5. Ideally w is greater than the longest arterial transit time (δ). Measurements of δ would give an indication of the variation in δ throughout the brain and inform the choice of a suitable w in a more objective way than by visual inspection of subtraction images. While a pixel-by-pixel analysis might not be feasible, the sensitivity of CASL images acquired after a range of w may be sufficient to yield average δ within the territories of individual cerebral arteries.

5.6.4 CASL in animals and humans

Larger gradient amplitudes are required to induce velocity driven adiabatic fast passage (AFP) in animals than in humans due to the greater proximity of the imaging plane to the labelling plane. The product of the labelling gradient and the velocity of arterial blood, Gv, determines the duration of the AFP as well as the minimum amplitude of the RF pulse for successful labelling (equations [3.9] and [3.5]). The product Gv is generally larger in animals due to larger values of G, despite higher blood velocities in humans. Therefore velocity driven AFP occurs more quickly and hence suffers less from T_2 relaxation in animals (*Figures 3.10* and *3.11*). In addition, arterial transit times are shorter in animals, so less T_1 relaxation occurs than in humans. Larger values of Gv and shorter transit times tend to make single slice CASL more sensitive to perfusion in small animals than in humans. This effect is emphasised by the fact that animal studies are often performed at higher magnetic field strengths, at which T_1 values are longer (Chapter 3 *Figure 3.8*).

For multiple-slice CASL using the AM control technique, the situation may be different. Larger values of Gv for the AM control in animals mean that at a given modulation frequency (f), the temporal separation of the two AFP processes (2f/(Gv) Appendix C) is reduced, and the possibility of interference between the two inversion processes is greater (Chapter 4 and Appendix C). Larger values of Gv also demand greater B_1 amplitudes, which increase the duration of each AFP (equation [3.9]), further increasing the possibility of interference between the inversion and re-inversion processes. The modulation frequency may be increased to increase the separation of the AFPs, but this risks invalidating the assumption that the two components of the AM pulse act at the same frequency offset as the labelling pulse (important for accurate MT cancellation). Large modulation frequencies also increase the time available for relaxation, and increase the possibility of a change in blood velocity between inversion and re-inversion, making it less likely that the adiabatic condition is satisfied for both AFPs.

5.6.5 Final Remarks on the AM control

It has been demonstrated that perfusion-weighted images may be acquired in up to five slice positions in rat brain using the AM control. Several non-ideal aspects of the AM control have been highlighted, but it remains the most widely used technique for multiple-slice CASL imaging. There are several factors, which may make the AM control more useful in humans than in small animals, and it has been employed in humans by several groups (Chalela JA et al. 2000; Ye FQ et al. 1999; Parkes LM and Tofts PS 2001).

The choice of standard, single slice or multiple-slice CASL measurements with the AM control must depend on the priorities for a given application. If the locations of regions where perfusion is abnormal are not known, the AM control may provide a more time efficient way to detect such areas than by repeated single slice CASL. However, due to the lower sensitivity to perfusion and higher RF power deposition (for optimal conditions), there is a strong case for using the standard, single slice technique in most cases.

6 MRI of liver during intestinal ischaemia-reperfusion

6.1 Introduction

Magnetic resonance signals may be sensitised to several physiological parameters that are linked with the delivery of oxygen to tissue and its utilisation in tissue. These include tissue perfusion, the diffusive movement of protons and the presence of deoxyhaemoglobin (dHb). The work described in this chapter was designed to exploit the sensitivity of MRI to dHb through blood-oxygen-level-dependent (BOLD) contrast, to investigate liver damage in an animal model of intestinal ischaemia-reperfusion (I/R). The results are also reported of an investigation of inflow to the liver in the same animal model using transonic ultrasound. Animal preparation was carried out by Dr Paisarn Vejchapipat (Institute of Child Health, UCL, London) and I performed the MR imaging and analysis. Statistical modelling for Study 2 was performed by Dr Martin King (Institute of Child Health, UCL, London).

6.1.1 BOLD MRI

BOLD MRI is best known for its application in functional studies of the brain, where it is employed to detect activation-induced changes in the microcirculation. However, BOLD also has applications as an indicator of oxygen debt in normal and pathological states. It has been employed to study oxygenation-dependent changes in brain (Harris NG et al. 2001; Grüne M et al. 1999), muscle (Donahue KM et al. 1998), kidney (Prasad PV et al. 1996) and heart (Bauer WR et al. 1999; Atalay MK et al. 1995).

The BOLD effect arises through the sensitivity of the transverse relaxation rates, R_2 and R_2^*, to the presence of dHb. R_2 and R_2^* are related by the equation $R_2^* = R_2 + R_2^`$, where $R_2^`$ accounts for the reversible component of R_2^*. Molecules of dHb are paramagnetic and they perturb local magnetic fields in tissue, affecting both R_2 and $R_2^`$ (and hence R_2^*). The transverse relaxation rates depend on the concentration and distribution of molecules of dHb and the diffusion rate of protons through the local magnetic field gradients created around these molecules.

R_2^* is more sensitive than R_2 to perturbations in the magnetic field, and hence more sensitive to the presence of dHb (Bandettini PA et al. 1994; Kennan RP et al. 1994). A linear relationship between R_2^* and tissue concentrations of dHb, measured with near infrared spectroscopy (NIRS) has been found in neonatal piglet brain

(Punwani S et al. 1998). The high correlation between R_2* and [dHb] indicates that changes in R_2* may serve as a surrogate marker for changes in tissue oxygenation. This approach has been employed to study ischaemia - reperfusion in brain (eg. (Grüne M et al. 1999; Ono Y et al. 1997)) and the heterogeneous distribution of oxygen in human kidney (Prasad PV et al. 1996).

The concentration of dHb at the microvascular (capillary) level is influenced by oxygen consumption and the oxygen extraction fraction of the tissue as well as the haematocrit fraction (Hct) and oxygenation of inflowing blood, and the flow rate and volume of blood. T_2*- weighted images ($1/R_2^* = T_2^*$) are sensitive to the balance between microvascular inflow and tissue oxygen demands. Additional measurements must be made to distinguish changes in R_2* due to blood flow and volume from changes in R_2* due to Hct and blood oxygenation. However, BOLD MRI provides rapid, quantitative measurements without the need for an exogenous contrast agent, which makes it an attractive, non-invasive approach in experimental and clinical investigations.

6.1.2 Intestinal Ischaemia-Reperfusion (I/R)

This chapter describes a study of the liver using MRI, during intestinal I/R. Intestinal I/R is a feature of many serious clinical conditions including shock, sepsis, abdominal surgery, multiple trauma and birth asphyxia. Treatment options for patients with intestinal I/R are limited and consist mainly of supportive interventions (Macdonald P.H. and Beck I.T.2000). For example, antibiotics may be administered to reduce systemic levels of bacteria or the smooth muscle relaxant, paperverine, may be infused to dilate blood vessels of the mesenteric circulation, and thereby ameliorate nutritional and oxygen levels. Surgery is performed to assess damage and remove necrotic sections of bowel or to bypass or remove vascular obstructions.

It is important to realise that damage to the intestine itself is not the main cause of the acute morbidity and mortality associated with intestinal I/R. The most serious consequence of intestinal I/R is remote organ injury, leading to the possibility of multiple organ dysfunction syndrome (MODS) (Thompson JS.1995; Pastores SM et al. 1996). Injury to liver, lung, kidney, heart and central nervous system following intestinal I/R is caused by the release of a cascade of toxins and mediators from the damaged intestine. A series of local and systemic reactions is set in train by various substances leaving the gut. Liver damage may occur as a direct result of the inflow of toxins from the damaged intestine (exogenous reaction), or as a result of the action of mediators from the intestine, which stimulate an excessive immune response in the liver (endogenous reaction).

The intimate connection between the gut and the liver is illustrated in *Figure 6.1*. The liver is unique in having two input blood vessels, the portal vein and the hepatic artery. Under normal physiological conditions nutrient-rich blood flows from the gut, stomach and spleen, through the portal vein to the liver, while highly oxygenated blood enters through the hepatic artery. When the intestine is damaged, the portal vein carries the products of this damage directly to the liver.

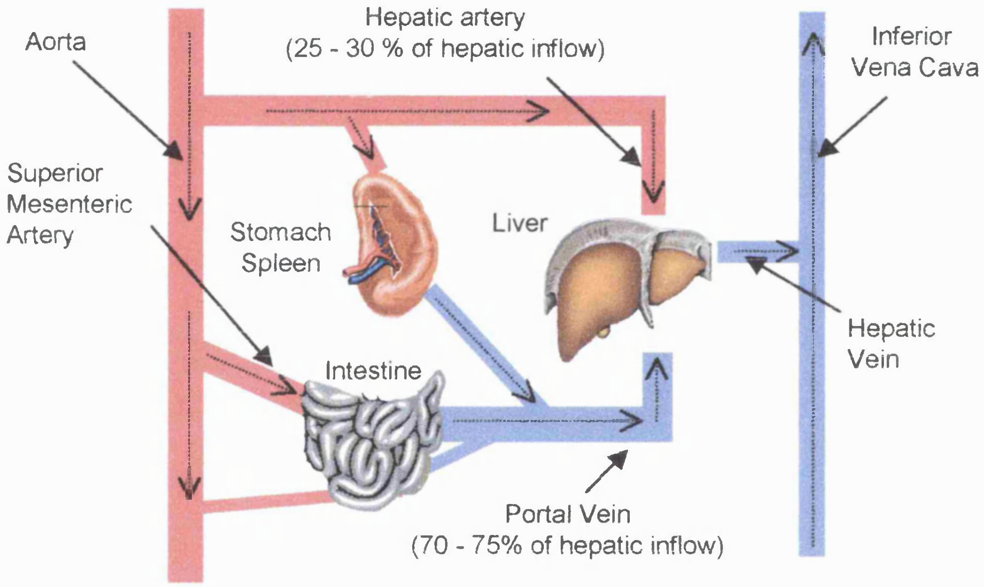

Figure 6.1 Schematic diagram of mesenteric circulation

The cascade of pathological processes set in train by intestinal I/R exacerbates intestinal damage and initiates derangement of the function of remote organs. Intestinal I/R initiates the production and release of cytokines, such as interleukin and tumour-necrosis factor α, which propagate an inflammatory response. It promotes the release of bacteria and bacterial products such as endotoxin, which cause over-activation of the reticulo-endothelial system in liver and lung. Activated neutrophils are also produced in the damaged intestine. They roll on and adhere to the endothelium before migrating into the tissue and promoting the production of oxygen free radicals and enzymes, which damage the surrounding tissue (Pastores SM et al. 1996; Deitch EA.1992). Activated neutrophils may migrate to other organs, or may be produced in these organs as a secondary response to the intestinal insult. Another possible contributory factor to tissue damage is the release of xanthine oxidase as ATP breaks down during ischaemia. Xanthine oxidase acts on oxygen upon reperfusion to form oxygen-free radicals (Poggetti RS et al. 1992).

Previous work in our laboratory using *in-vivo* and *in-vitro* MRS of liver has shown that intestinal reperfusion is the trigger for the failure of hepatic energy metabolism after a 90 minute period of intestinal ischaemia (Vejchapipat P et al. 2001a). Similar results were found *in-vitro* after 60 minutes of ischaemia (Vejchapipat P et al. 2001b). Energy metabolism is critically dependent on oxygen and therefore hepatic oxygenation is an important factor in liver injury due to intestinal I/R.

A series of studies is described in this chapter. For the first study T_2*-weighted images were acquired repeatedly to monitor changes in the liver during 90 minutes of intestinal ischaemia and 120 minutes of reperfusion. Decreasing signal intensity in these images over the course of the experiment suggested that T_2* decreased in the liver, due to the insult. In the light of these initial results, a second study was designed to quantify changes in R_2* and R_2 during intestinal I/R in a model of 60 minutes ischaemia. These data were related to measurements of hepatic inflow obtained using transonic ultrasound of the hepatic artery and portal vein.

6.2 Methods

Experimental protocols for animal preparation differed only in the duration of intestinal ischaemia (90 minutes or 60 minutes). Aspects of the experimental method that are common to all studies are described first and then specific details are given for each one.

6.2.1 Animal Preparation

Studies were approved by the Home Office, UK. Male Sprague Dawley rats weighing between 300 g and 350 g were anaesthetised with 1.0 % to 1.5 % halothane in oxygen and nitrous oxide in the ratio 40:60.

Laparotomy was performed by midline incision. The superior mesenteric artery (SMA) was isolated and the origin was located. A silicone thread was passed behind the SMA, then across the front and behind once more to exit after forming a complete loop.

No traction was applied to the vascular loop during surgery. Normal saline (20ml/kg) was infused intra-peritoneally to prevent dehydration.

Animals were divided into two groups, I/R and control. In the control group a sham operation was performed. In the I/R group intestinal ischaemia was induced by applying traction to the loop of silicone thread to occlude the SMA. Reperfusion was achieved by releasing the loop, without having to move the animal. The same force was applied to the loop in all studies by using a constant length of thread and pulling it to a point at a fixed distance from the origin of the SMA. Rectal temperature was monitored continuously and maintained between approximately 35 ^{0}C and 39 ^{0}C, either by adjusting the temperature of air flowing into the bore of the magnet or with a heating mat and lamp for the experiments on the bench. The large range of temperatures is an effect of the nature of the insult, which severely impairs the ability of an animal to maintain its body temperature. It is particularly difficult to control body temperature within the bore of the magnet, where the source of heat is some distance from the animal.

Imaging the abdomen presents the challenges of motion due to respiration and peristalsis and the presence of tissue/air boundaries in the intestine. Respiratory-gating or -triggering increases image acquisition times and requires additional hardware. Measurements made with transonic ultrasound are also sensitive to motion. Ultrasound probes detect the movement of blood and the signal is very sensitive to the position and physical stability of the probes. We minimised motion-induced artifacts by minimising motion. A plastic (acrylic) insert was positioned between the liver and the diaphragm to minimise respiratory-induced movement of the liver in all studies (*Figure 6.2*). It did not touch blood vessels or exert any pressure on the liver.

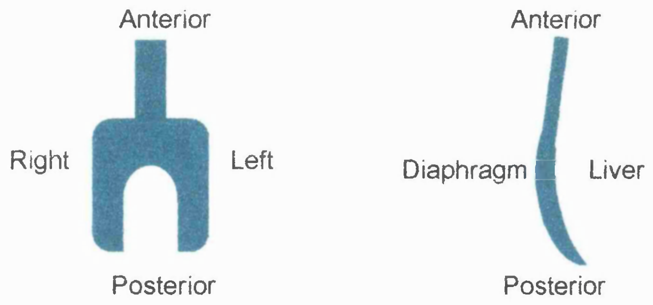
a) View from tail
b) View from side

The insert is 1.25 mm thick and 32 mm wide (left to right) at its widest point.

Figure 6.2 Schematic diagram of the plastic insert to isolate the liver from respiratory motion.

6.2.2 Study 1: T_2* - Weighted Imaging

After surgery the abdomen was closed, the rat was put into a perspex cradle and placed within a 2.35 T magnet interfaced to a Surrey Medical Imaging Systems (SMIS, Surrey UK) console. The animal was positioned with the liver at the centre of the magnet. A saddle RF coil was used for transmission and reception.

Gradient echo MR images were acquired in a transverse plane through the liver to detect relative changes in T_2*. Images were acquired repeatedly during a baseline period of 30 minutes and then throughout 90 minutes of intestinal ischaemia and 120 minutes of reperfusion (I/R group, n = 5) or under general anaesthetic for four hours (control group, n = 4). All images had the following parameters, TR = 500 ms, TE = 12 ms FOV = 60 mm, slice thickness = 2 mm, matrix = 128 x 64 with oversampling in the frequency encoding direction. One image was acquired at least every seven minutes.

A large region of interest (ROI) was defined for each animal and projected onto all images of that animal for analysis. Signal intensities within this ROI in all images were normalised to the average signal intensity in the first four images (acquired during the baseline period in the I/R group). These data were then grouped into blocks of 10 minutes.

6.2.3 Study 2: R_2 and R_2* Measurements

The animal was prepared in the same way as for Study 1 and images were acquired with the same RF coil, in a transverse plane. After a baseline period of 30 minutes 60 minutes of intestinal ischaemia was followed by up to 150 minutes of reperfusion (I/R group, n = 9) or the animal was maintained under general anaesthetic for four hours (control group, n = 5).

R_2 was determined from spin-echo images, acquired at four echo times in the range TE = 16 to 60 ms with TR = 1000 ms. R_2* was determined from gradient-echo images, acquired at four echo times in the range TE = 8 to 30 ms with TR = 1000 ms. One set of R_2 and R_2* measurements was performed approximately every 15 minutes throughout each experiment.

A large region of interest (> 65 mm^2) in the liver of each animal was selected and projected onto all images of that animal for analysis. R_2 and R_2* were calculated from two parameter fits for T_2 and T_2* respectively, using non-linear regression analysis (Graphpad Prism, Graphpad Software, Inc. San Diego, USA) to the equation

$$S = S_0 \exp(-TE/T_2) \qquad \text{[equation 6.1]}$$

Analysis was performed on the time courses of R_2 and R_2^* values in the liver, by fitting each data set to a linearly time-dependent model. The model allows different time dependencies in the ischaemia and reperfusion phases of the experiment. The mean temporal behaviour of R_2 and R_2^* was determined for each group. Tests of the significance of temporal trends and differences between trends in the intestinal I/R group and the control group were performed by mixed model regression analysis. The threshold for significance was set at a p-value of 0.01.

6.2.4 Study 3: Ultrasonic measurement of hepatic inflow

In a separate experiment using 3 animals (250g – 300g), ultrasonic microvascular flow probes (Transonic, Ithaca, NY, U.S.A.) were placed around the portal vein (PV) and the hepatic artery (HA) to measure blood flow to the liver during 60 minutes of intestinal ischaemia and 120 minutes of reperfusion. Occlusion of the SMA was achieved with a vascular loop, as for the MRI experiments. The abdomen was partially closed to prevent dehydration, without disturbing the vascular flow probes. Rectal temperature was monitored and was maintained using a heating mat and lamp. Measurements of PV and HA flow were made for 3 hours before occlusion of the SMA. The long baseline period provided control data for comparison with the I/R part of the experiment.

Blood flow through the HA and PV was recorded on line at a rate of 100 Hz. Data were pooled into blocks of 2.5 seconds for analysis. Mean flow values over periods of 1 minute were calculated for each animal. Flow values for each animal were then normalised relative to their individual baseline measurements (recorded 1 minute before occlusion). Mean normalised flows in three animals were calculated at times 3 minutes after occlusion, 3 minutes before and 3 minutes after de-occlusion, and at half hour intervals throughout reperfusion.

A student's t-test was used to detect significant differences in mean flows relative to pre-occlusion values $p < 0.01$ is reported.

6.3 Results

In order to select a transverse imaging slice through the liver for studies 1 and 2, coronal, spin-echo images were acquired, as shown in *Figure 6.3*. Air in the lung and bowel produces regions of low signal intensity above and below the liver.

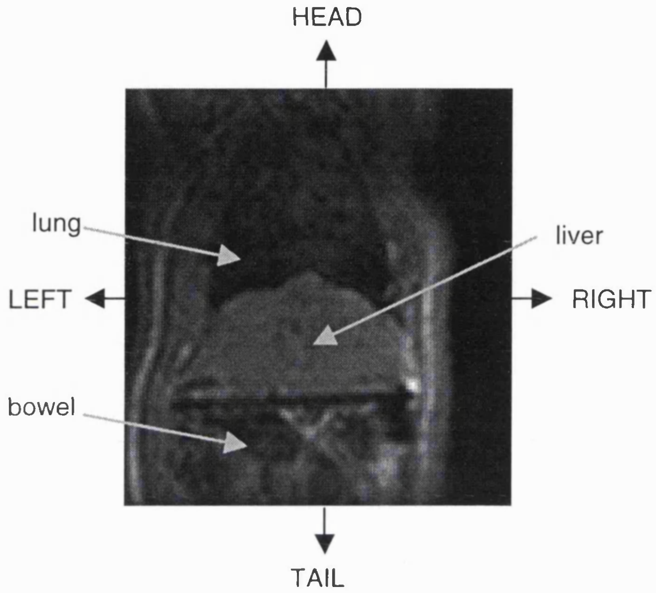

Figure 6.3

Coronal spin echo image for localisation of the transverse image plane for analysis

6.3.1 Study 1: T_2* - Weighted Imaging

Normalised signal intensities (SI) in the liver of I/R (n = 5) and control (n = 4) animals are shown in *Figure 6.4*. Data are grouped in ten-minute blocks. No significant differences appear during the baseline period. At time zero the SMA was occluded to induce intestinal ischaemia in the I/R group. SI in the I/R animals was lower during ischaemia than in controls after an equivalent time under anaesthetic. Upon de-occlusion of the SMA after 90 minutes of ischaemia, SI in the I/R animals decreased progressively until the end of the experiment. Larger standard errors in SI during reperfusion than during baseline imaging reflect considerable heterogeneity in individual responses to gut I/R.

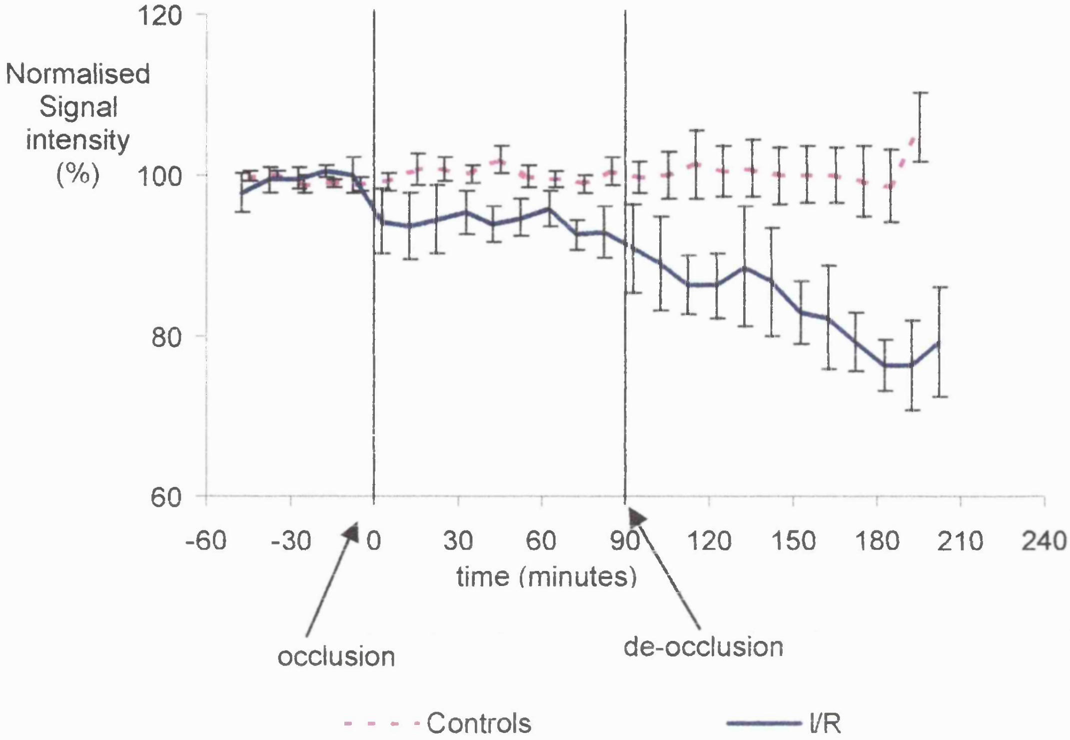

Figure 6.4

Normalised signal intensities in T_2*-weighted images of the liver during intestinal I/R. TE = 12 ms, TR = 500 ms.

Error bars are standard errors of the means in 5 (I/R group) and 4 (control group) animals.

6.3.2 Study 2: R_2 and R_2* Measurements

Study 1 showed that changes in the liver during intestinal I/R may be detected in T_2*-weighted images. A second study was designed to quantify these changes in terms of the relaxation rates R_2 and R_2*. The duration of ischaemia was reduced from 90 minutes to 60 minutes to reduce the severity of the insult, and hence to reduce the risk of animals dying before the end of the experiment (based on the experience of my colleague, Dr Paisarn Vejchapipat). Spin-echo and gradient-echo images were acquired at four different echo times to quantify R_2 and R_2* respectively in animals subject to intestinal I/R (n = 9) and in a control group (n = 5).

Gradient-echo and spin-echo images of one animal are shown in *Figure 6.5*. The animal was positioned to lie on its back. The abdominal wall was closed after surgery, but there is an air gap between the liver and the abdominal wall. The ends of the insert between the diaphragm and the liver may be seen on either side of, and anterior to the spinal cord. Blood vessels passing through the liver appear as bright spots in the gradient-echo image and as dark regions at equivalent points in the spin-echo image, because blood moving through the imaging slice does not experience both the 90^0 and the 180^0 RF pulses of the spin-echo acquisition.

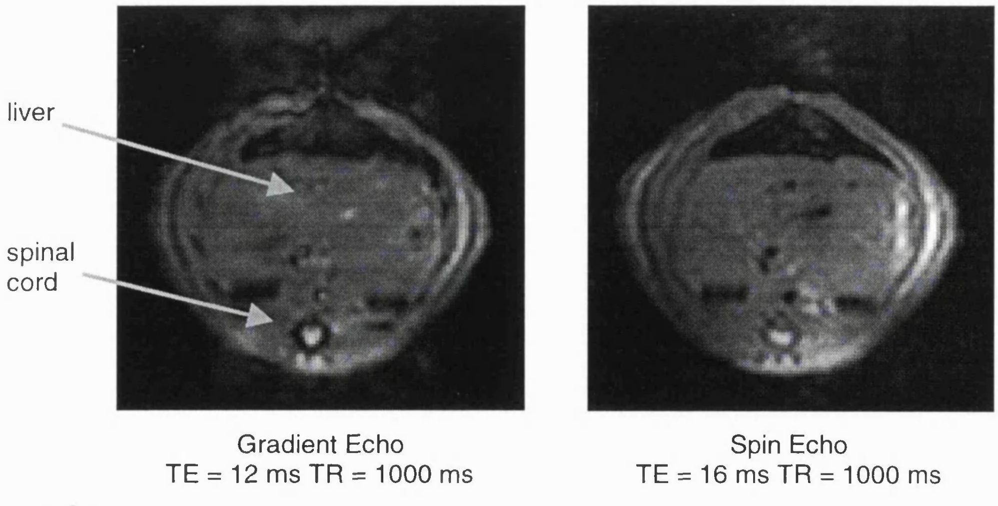

Figure 6.5

Transverse images of the liver used for analysis in Study 2

Figures 6.6 and *6.7* show time courses of R_2 and R_2* in each animal. Data for the control group are shown with time = 0 after a 60 minute baseline period, for comparison with the I/R group. R_2 values are consistently much lower than R_2* values, indicating that there is a significant $R_2`$ contribution to $R_2*$ in the liver ($R_2* = R_2 + R_2`$). There are considerable random variations within each animal in both R_2 and R_2*, which reflect the relatively large uncertainty in R_2 and R_2* due to low signal-to-noise ratios in the images.

One animal in the intestinal I/R group had particularly high R_2* values throughout, although R_2 values in that animal were similar to those in other animals, indicating that $R_2`$ was very high. $R_2`$ depends, on the homogeneity of the static magnetic field and high values of $R_2`$ may be due to background gradients resulting from poor homogeneity of B_0.

The time courses of R_2 and R_2* shown in *Figures 6.6* and *6.7* were fit to a first order polynomial, time dependent model. The model allows R_2 or R_2* to increase (or decrease) linearly with time at different rates during ischaemia and reperfusion. Statistical tests were performed using mixed model regression analysis to address the following questions for R_2 and R_2*

(i) Does the mean R_2 (or R_2*) depend on time in either group (intestinal I/R or control) or in either phase (ischaemia or reperfusion)?

(ii) Does the mean time dependence differ between phases?

(iii) Does the mean time dependence differ between groups?

(iv) Does the mean R_2 (or R_2*) change between the end of ischaemia and the beginning of reperfusion?

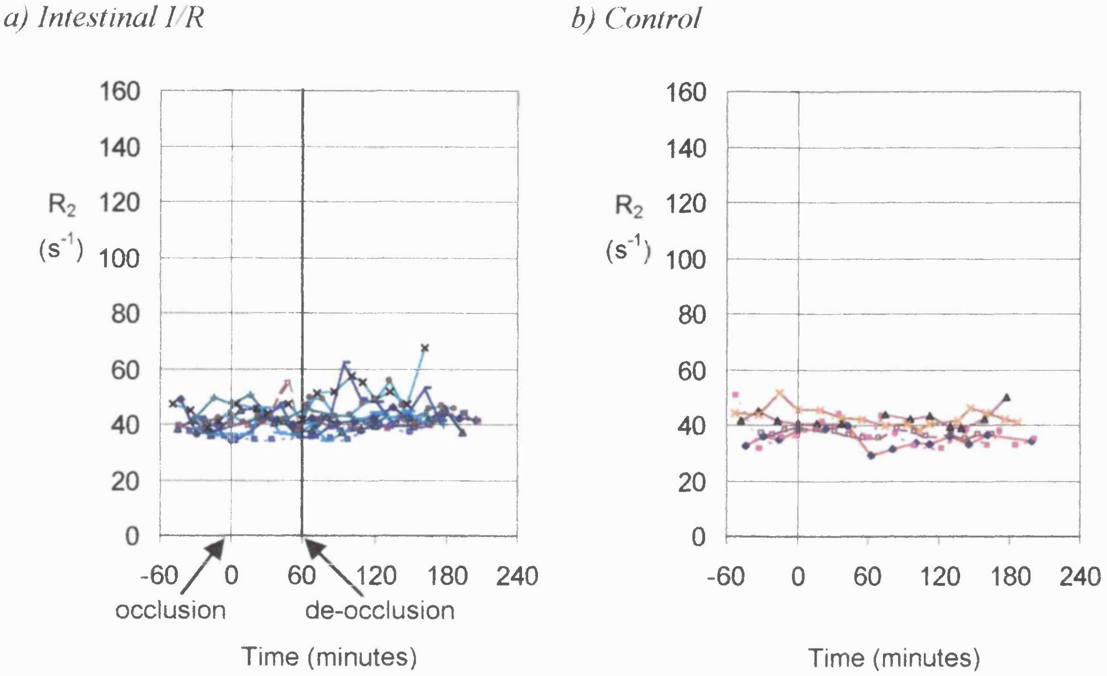
a) Intestinal I/R

b) Control

Figure 6.6

R_2 of liver in the intestinal I/R group (n = 9) (a) and control group (n = 5) (b). The time is shown relative to the time at which the SMA was occluded.

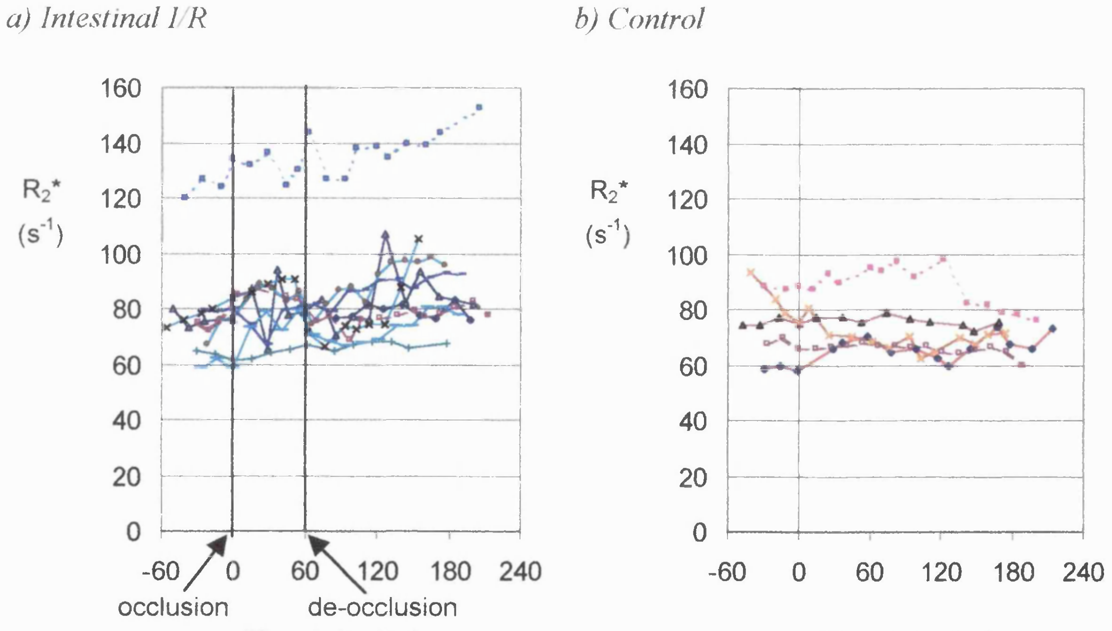
a) Intestinal I/R

b) Control

Figure 6.7

R_2* of liver in the intestinal I/R group (n = 9) (a) and control group (n = 5) (b). The time is shown relative to the time at which the SMA was occluded.

Mean rates of change of R_2 and R_2* were determined for each group, using the regression model. *Figure 6.8* shows R_2* in the reperfusion phase for every individual animal and the mean behaviour of each group.

R_2 had no significant time dependence in either group or in either phase. There was no significant difference between the time dependencies of R_2 in the I/R and control groups during ischaemia ($p = 0.98$) or reperfusion ($p = 0.86$).

R_2* during ischaemia did not have a significant time dependence in either group, nor was there a significant difference between groups ($p = 0.7$). Conversely, during reperfusion R_2* in the I/R group increased significantly with time and this time dependence was significantly different from that of the control group ($p = 0.0001$). No significant differences between the time dependencies of R_2* during ischaemia and reperfusion were found in either group and there is no evidence for a step change in R_2 or R_2* between ischaemia and reperfusion. This means that we cannot exclude the possibility that a gradual rise in R_2* starts during ischaemia and continues during reperfusion.

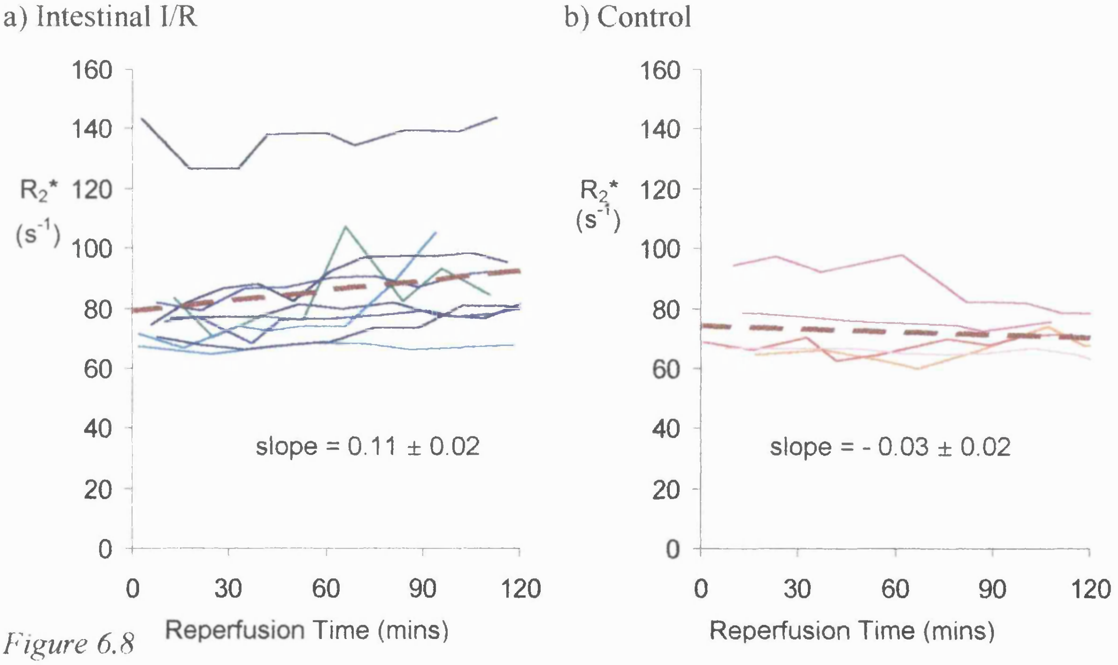

Figure 6.8

R_2* in liver following 60 minutes of intestinal ischaemia (a). The individual and mean behaviours of R_2* during reperfusion are shown with solid lines and a dashed line respectively. The mean behaviour of control animals is shown over an equivalent time under anaesthesia (b). The rate of increase of R_2* in the intestinal I/R group was significantly different from that of the R_2* in the control group ($p < 0.01$).

6.3.3 Study 3: Ultrasonic measurement of hepatic inflow

Oxygenation of the liver depends on the supply of oxygen it receives from the blood. This depends in turn on two factors, the volume of inflow and the amount of oxygen carried by the blood. This study was designed to measure hepatic inflow. Simultaneous measurement of inflow, R_2 and R_2* in individual animals would elucidate the relationship between these parameters more clearly. However, the ultrasound probes employed for measurements of flow through the portal vein and hepatic artery in rats are not MR-compatible. Therefore this study was performed on the bench, using the same animal model as that used for Study 2.

Portal venous (PV) and hepatic arterial (HA) flow during intestinal ischaemia and reperfusion are shown for one animal in *Figure 6.9*. There was a severe and immediate reduction in portal venous flow upon occlusion of the superior mesenteric artery (at time = 0). A slight recovery of PV flow in the first five minutes of intestinal ischaemia was followed by a steady and persistent decline. Upon de-occlusion of the SMA, PV flow was restored initially, but then it decreased gradually throughout reperfusion. Flow through the HA increased upon occlusion of the SMA to compensate somewhat for reduced PV flow. This rise in HA flow was more gradual than the fall in PV flow. De-occlusion of the SMA elicited a reduction in HA flow to below pre-ischaemic levels. The pattern of total hepatic inflow followed the pattern of PV flow closely, reflecting the fact that a greater proportion of blood enters the liver through the portal vein, than through the hepatic artery.

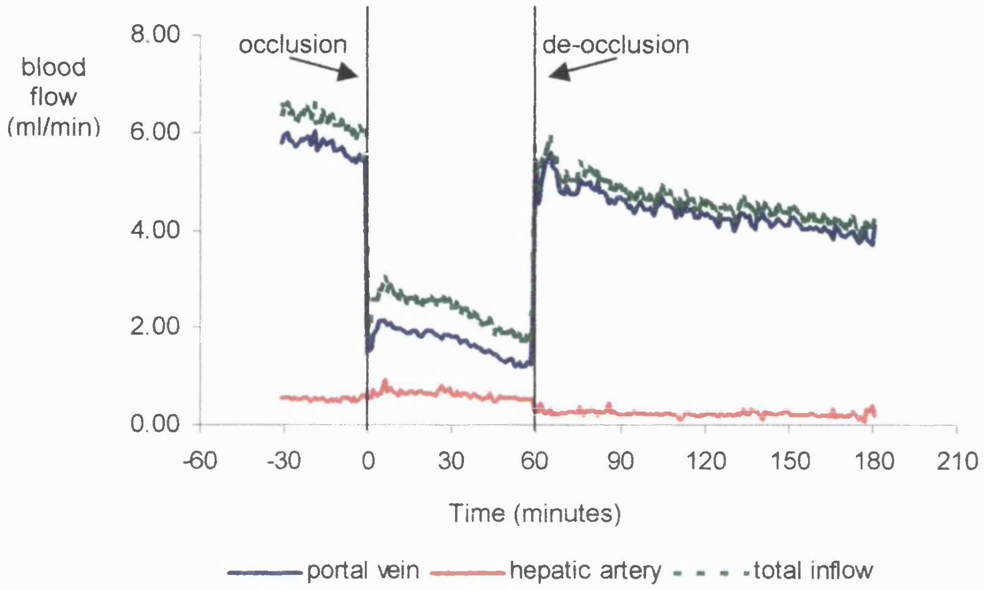

Figure 6.9

Typical response of hepatic blood supply to intestinal ischaemia-reperfusion
The time is shown relative to the time at which the SMA was occluded.

Mean values of normalised flows in 3 animals are shown at selected time points throughout intestinal I/R and throughout three hours of general anaesthetic in *Figure 6.10*. During a 3-hour period under anaesthesia blood flow through the PV did not change significantly (*Figure 6.10 a*). Flow through the HA fell slightly during the first hour, but the change was not significant (*Figure 6.10 b*).

During intestinal ischaemia blood flow through the PV was reduced to 40 % of pre-occlusion values. Flow through the HA increased to 140 % of baseline but total inflow was reduced to below 50 % of pre-occlusion values. Immediately upon de-occlusion, blood flow through the PV was restored to 93 % of baseline, but HA flow fell to less than 40 % of baseline. Flow through both vessels decreased continuously throughout 120 minutes of reperfusion. The total inflow was 67 % of pre-occlusion values by the end of reperfusion.

a) Portal Venous Flow

b) Hepatic Arterial Flow

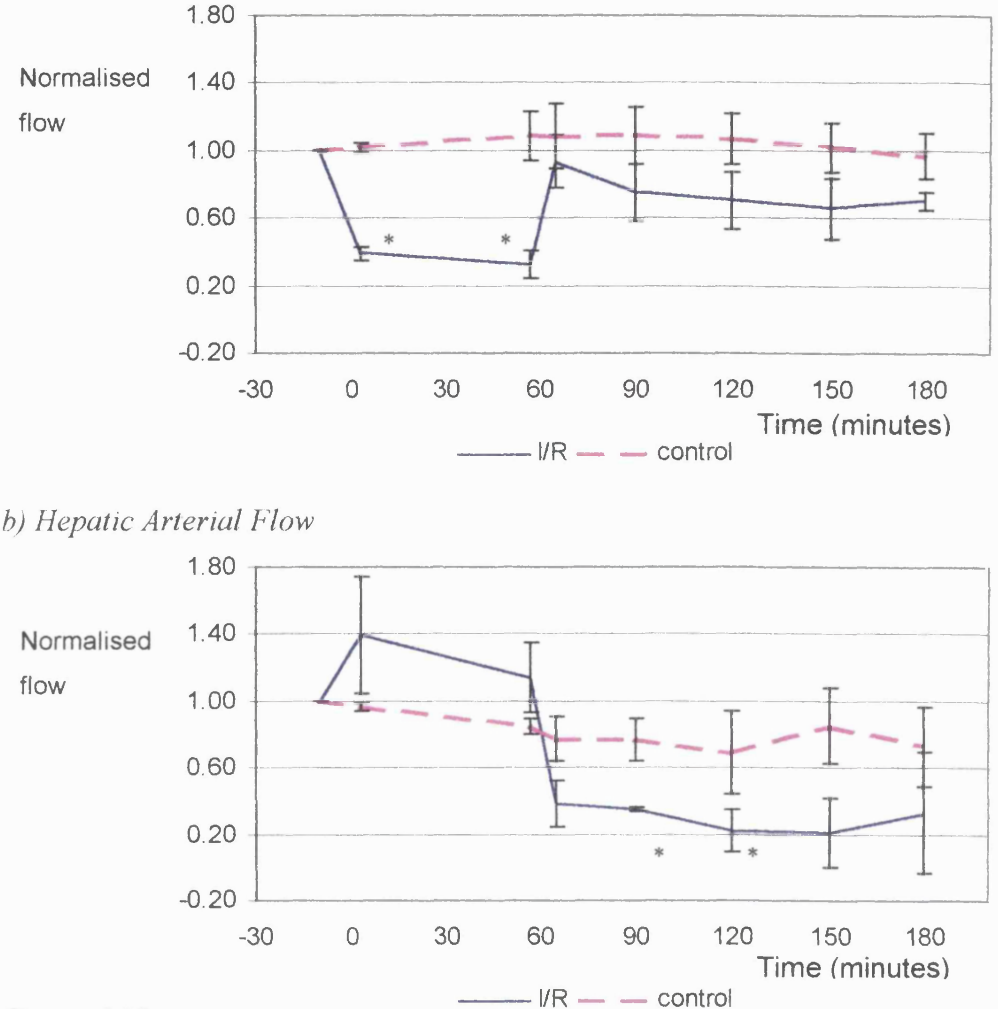

Figure 6.10

Blood flow through the portal vein (a), hepatic artery (b) (mean ± standard deviation) (n = 3). Mean values are shown, normalised to the flow one minute before occlusion of the SMA. The time is shown relative to the time of occlusion.

* = $p < 0.01$ compared with baseline.

6.4 Discussion

The pathophysiological processes that characterise intestinal I/R are numerous and complex. This work has focussed on the effect of intestinal I/R on the liver, one of the first remote organs to suffer functional impairment due to the insult. MRI has offered some insight into hepatic oxygenation changes and transonic ultrasound has been used to study the effects of intestinal I/R on hepatic inflow. The main finding of these studies was a rise in R_2* during reperfusion, following 60 minutes of intestinal ischaemia.

R_2 and R_2* depend on the static magnetic field strength, differences in magnetic susceptibility between tissue and blood, the sizes of blood vessels and the diffusion distance of protons. The contributions of each of these factors to changes in hepatic R_2* during intestinal I/R are now discussed in the light of evidence from the literature on the pathophysiology of intestinal I/R.

No significant changes in R_2 were observed during ischaemia or reperfusion, despite changes in R_2*. This is consistent with the lower sensitivity of R_2 to dHb than R_2*. Another factor is the hepato-toxic effects of halothane anaesthesia, which has been shown to cause increased T_2 in the liver after prolonged exposure in rats (Noseworthy MD et al. 1997). This corresponds to decreasing R_2, which may mask a rise in R_2 due to intestinal I/R.

The behaviour of R_2 and R_2* in brain has been modelled (Kennan RP et al. 1994; Hoppel BE et al. 1993; Kiselev VG and Posse S.1999) and a model has been developed for R_2 and R_2* in the myocardium (Bauer WR et al. 1999). The microcirculation of liver differs from that of brain and myocardium in at least two important respects. Firstly, the volume of blood within the liver is much greater under normal conditions (25ml/100g (Gurll N J.1989) compared with typically 2 - 4 % in the brain) and secondly, hepatic sinusoids are larger than cerebral or myocardial capillaries (7 - 15 μm in diameter, compared with 2 - 5 μm). Both greater blood volume and greater vessel radii produce bigger changes in R_2* in response to changes in flow and oxygenation in computer models of BOLD (Bandettini PA and Wong EC 1995; Kennan RP et al. 1994). This suggests that R_2* should be at least as sensitive, and may be more sensitive to changes in [dHb] in the liver than in the brain. However, high R_2 in normal liver at 2.35 T results in lower signal-to-noise ratios in images of the liver than in images of the brain, which limit the sensitivity of R_2 and R_2* measurements.

R_2 and R_2* depend on the amount of paramagnetic dHb in tissue and adjacent vessels, which is determined by the volume, the haematocrit fraction and the oxygenation of the blood. An increase in dHb may be due to de-oxygenation of a constant volume of haemoglobin or an increase in haematocrit with no change in oxygenation (or increased total blood volume). Measurements of blood gases in a model of 90 minutes intestinal ischaemia and 60 minutes of reperfusion highlight possible causes of increased hepatic R_2* during intestinal reperfusion (Williams SB et al. 2001).

Immediately after reperfusion blood in the superior mesenteric vein (SMV), the outflow from the intestine (*Figure 6.1*), had elevated haematocrit and pO_2, but normal pH. After sixty minutes of reperfusion blood in the SMV, inferior vena cava and aorta was significantly more haemo-concentrated and acidic, despite normal pO_2 suggesting that the response was systemic at this stage. Increasing haematocrit fraction and acidity during reperfusion would both contribute to raised [dHb], as the total Hb content of blood increased and the lower pH shifted the oxygen dissociation curve for Hb, to increase the proportion of Hb that was de-oxygenated (Martin DW Jr.1985).

As mentioned previously, high R_2 and R_2* values in liver, especially at 2.35 T, result in low signal-to-noise ratios and correspondingly large uncertainties in calculated values of R_2 and R_2*. It is possible that changes in R_2* occurred during ischaemia, but our measurements were not sensitive enough to detect them. However, changes in [dHb] during reperfusion are compatible with the observations of Horie et al., who reported an increased number of non-perfused sinusoids upon intestinal reperfusion following occlusion of the SMA in rats and mice, measured with intra-vital microscopy (Horie Y et al. 1996; Horie Y et al. 1997). As the number of viable sinusoids decreased, oxygen extraction from the remaining sinusoids would have to increase for the liver to extract sufficient oxygen to maintain normal energy metabolism. Haemoglobin would become more de-oxygenated and any blood trapped in the non-perfused sinusoids would continue to lose oxygen, creating pools of dHb within the liver.

It has been predicted that R_2* increases with increasing blood fraction, especially when the vessel radius increases, rather than the number of perfused blood vessels (Ogawa S et al. 1993; Kennan RP et al. 1994). There are, to our knowledge, no reports of altered hepatic blood volume in intestinal I/R, but the number of perfused sinusoids has been shown to decrease during reperfusion following 30 minutes of intestinal ischaemia (Horie Y et al. 1996; Horie Y et al. 1997). The redistribution of blood may enlarge those sinusoids that remain viable, contributing to a local rise in blood volume and increased R_2*.

R_2* is also sensitive to iron concentration and the liver stores much of the body's iron. An accumulation of iron in the liver would lead to an increase in R_2*. However, hepatic iron accumulation is not a recognised feature of remote organ injury and disruption of iron storage mechanisms usually occurs over a longer time-scale than the duration of this experiment (Grace ND and Powell LW 1974).

It is interesting to consider the direct insult on the liver in the case of liver I/R. In liver ischaemia, vacuole formation and oedema have been reported (Vollmar B et al. 1994). Studies of liver ischaemia-reperfusion using Laser Doppler (Chavez-Cartaya RE et al. 1994) and intra-vital microscopy (Vollmar B et al. 1994) have shown that microvascular flow is compromised after reperfusion. A larger number of non-perfused sinusoids, and an increase in the number of adherent leukocytes on the endothelium has been observed during reperfusion, which may indicate that congestion of sinusoids by activated leukocytes compromises hepatic perfusion, leading to flow-dependent oxygen extraction, and derangement of oxygen metabolism. Hepatic damage due to intestinal I/R is not as severe as the damage due to liver I/R. However, if liver damage during intestinal reperfusion were severe enough to produce hepatic oedema, the associated reduction in diffusion might also contribute to increased R_2* (Ogawa S et al. 1993; Kennan RP et al. 1994).

Measurements of flow through the PV and the HA using vascular ultrasound probes showed that total hepatic inflow was severely reduced during 60 minutes of ischaemia and did not return to normal levels upon reperfusion. Turnage et al. (Turnage RH et al. 1996) and Williams et al. (Williams SB et al. 2001) have measured HA and PV flow during intestinal I/R, produced by occlusion of the SMA for 120 and 90 minutes of ischaemia respectively. In both experiments there were similar patterns of change in HA and PV flow to those demonstrated here. It is interesting to note that the proportion of the total hepatic inflow from the hepatic artery was significantly lower during reperfusion than at baseline, or during ischaemia. A significant proportion of the oxygen supplied to the liver under normal conditions enters via the hepatic artery. Therefore restoration of total inflow to near normal levels upon reperfusion does not necessarily mean that the oxygen supply was restored to normal and the total amount of oxygen that entered the liver may have been lower during reperfusion than at baseline. Reduced HA flow during reperfusion may lead to very low hepatic oxygen supply, which may be inadequate for normal energy metabolism.

Impaired microcirculation and inflammation may initiate, promote or sustain one another. Ischaemia activates neutrophils and primes macrophages, while inflammation damages the micro-vessels (Grace PA.1994; Horie Y et al. 1997). This makes it difficult to classify liver hypoxia as a cause or an effect of hepatic energy failure, initiated by intestinal I/R. If reduced hepatic inflow during intestinal I/R were to cause a sufficient degree of hypoxia, it might elicit an excessive immune response in the liver. Conversely, if the inflow of inflammatory mediators upon intestinal reperfusion were to damage the hepatic sinusoids, oxygen delivery and extraction might be compromised, causing liver hypoxia. Further studies are required to classify hypoxia and inflammation as the cause and effect of hepatic damage due to intestinal I/R. One approach would be to use a combination of R_2* and perfusion imaging (Appendix D). If a rise in R_2* preceded a reduction in hepatic perfusion, it would imply that increased oxygen demand due to inflammatory processes reduced the number of perfused sinusoids and thereby reduced perfusion. On the other hand, if reduced perfusion were to precede increased R_2*, the implication would be that liver energy metabolism was compromised by reduced perfusion leading to hypoxia.

Liver perfusion has been monitored previously with MRI, using a contrast agent, gadolinium diethylenetriamine penta-acetic acid (Gd-DTPA), both clinically and in an animal model (Uematsu H et al. 1998; Materne R et al. 2002). Use of Gd-DTPA would preclude repeated measurements of R_2 and R_2*. Therefore the use of blood water as an endogenous contrast agent would be very useful. To this end non-invasive MRI arterial spin labelling technique, FAIR, has been implemented for liver perfusion imaging (Appendix D). The sensitivity of these measurements is very low and it remains to be seen whether changes in hepatic perfusion during intestinal I/R may be detected using ASL.

Early detection of organ dysfunction is crucial to the effectiveness of appropriate intervention. Markers of hepatic function include bile flow, serum aspartate aminotransferase (AST) and alanine aminotransferase (ALT). Changes in these markers correlate well with hepatic oxygenation, as demonstrated, for example, in models of liver ischaemia, using NADH autofluorescence (Horie Y et al. 1996) and NIRS measurements of cytochrome oxidase and concentrations of oxy- and deoxy-haemoglobin (El Desoky AE et al. 2001). Bile flow is a useful indicator because it is closely correlated with hepatic ATP levels (Kamiike W et al. 1985). However, each of these techniques has serious disadvantages, whether applied in experimental models or clinical practice. Collection of bile or serum is invasive and may disrupt the physiological state one wishes to monitor. NIRS is a promising technique, but it only provides absolute measurements of oxy-Hb and dHb if calibrated when the oxygen saturation is zero in each individual subject. This may not be possible in all animal models and is not acceptable clinically.

NMR offers repeated measurements of absolute quantities (metabolite concentrations using MRS, NMR relaxation times, apparent diffusion coefficients and perfusion) non-invasively and *in-vivo*. This study has shown that gradient-echo MRI is sensitive to changes resulting from the indirect effects on the liver of intestinal ischaemia-reperfusion. There is potential for detecting more severe changes due to more serious insults in clinical studies and in experimental models.

Although MRI may not be ideal for monitoring critically ill patients, such as those suffering from intestinal I/R, measurements of R_2* as an indicator of hepatic oxygenation have potential applications in various patient groups. One example is liver transplant recipients. MRI investigations are performed to assess the patency of the portal vein and to measure the volume of the liver in the assessment of candidates for liver transplant (Kuo PC et al. 1995; Lewis WD et al. 1993) and measurements of transverse relaxation rates could be added to existing imaging protocols.

The studies described in this chapter makes a contribution to understanding of the effects of intestinal I/R on the liver. Ideally, hepatic inflow, perfusion and R_2 / R_2* would be measured as part of the same experiment. A comprehensive set of measurements of perfusion, dHb levels and hepatic inflow would provide a more detailed understanding of hepatic haemodynamics during intestinal ischaemia-reperfusion.

6.5 Conclusions

The signal intensity in T_2*-weighted images of the liver decreased as a result of intestinal I/R, following a 90 minute period of ischaemia.

R_2* in liver increased during reperfusion after sixty minutes of intestinal ischaemia, although there was no detectable change in R_2. There were no changes in either R_2 or R_2* during intestinal ischaemia. This is consistent with the accumulation of dHb during reperfusion, despite significantly greater total inflow of blood to the liver than during intestinal ischaemia. However, the significant reduction in hepatic arterial flow upon reperfusion may correspond to lower total oxygen delivery, despite almost normal levels of total blood inflow. This suggests that liver hypoxia may contribute to the failure of hepatic energy metabolism following intestinal I/R.

7 Final discussion and future work

This thesis covers aspects of two MRI techniques for studying the microcirculation, arterial spin labelling (ASL) and blood-oxygen-level-dependent (BOLD) contrast. This concluding chapter begins with a brief summary of the main findings of each chapter. Some of the issues raised by the results of this work are then discussed and future work is proposed.

7.1 Thesis summary

Chapter 3 focused on the process of velocity driven adiabatic fast passage (AFP) for continuous ASL (CASL). One significant finding from this computer modelling study is the importance of relaxation effects during velocity driven AFP. It is not sufficient to consider only the right hand side of the adiabatic condition to select optimal pulse parameters. Results from the model show that although variations in velocity over the course of the cardiac cycle have a great influence on the degree of inversion for individual spins, the time-averaged degree of inversion over the cardiac cycle is the same as for a spin moving at a constant velocity equal to the time-averaged mean. Dividing the RF pulse for labelling into a train of RF pulses has a significant effect on the inversion, and the dependence of the mean degree of inversion on the duty cycle of the pulse train is highly non-linear. Predictions of the efficiency of labelling based on the assumption of linearity may lead to inaccurate calculations of perfusion.

Chapter 4 describes a study of the amplitude modulated (AM) RF pulse, designed as a control for multiple-slice CASL. It is clear from these investigations that the perfusion sensitivity of CASL with the AM control is intrinsically lower than that of the standard, single slice CASL experiment. This is because interference between the two components of the AM pulse reduces the efficiency of double inversion. As the frequency of the amplitude modulation increases, interference effects diminish, but greater T_1 relaxation compromises the efficiency of the control more significantly. The optimal RF pulse amplitude, and hence the mean RF power deposition, is higher with the AM control than with single slice CASL. Also it was found that the technique is more sensitive to velocity in animals than in humans.

In Chapter 5 the efficacy of multiple-slice CASL using the AM control was demonstrated for imaging rat brain at 2.35 T. Magnetisation transfer effects of the pulse in samples of meat and in rat brain were equivalent to those of the labelling pulse over several image slices. Comparison with the standard, single slice control showed that the perfusion-dependent contrast-to-noise ratio (CNR) of the optimised AM control was only 70 % of the CNR of the standard control, given the same RF power deposition.

Chapter 6 presents MRI results in an animal model of intestinal ischaemia-reperfusion (I/R). R_2* increased during reperfusion following sixty minutes of intestinal ischaemia, which is consistent with the accumulation of deoxyhaemoglobin (dHb) in the liver. These results support the view that reperfusion initiates the derangement of hepatic oxygenation, which causes failure of liver energy metabolism. Transonic ultrasound measurements showed that hepatic inflow fell dramatically during ischaemia, but was restored almost to baseline levels when reperfusion began. Therefore changes in the total inflow of blood do not account for an increased amount of dHb in the liver during reperfusion.

7.2 Discussion

Computer modelling was employed to study the characteristics of the labelling and AM control pulses, as described in Chapters 3 and 4. Ideally further experimental verification of the results from the computer model would be obtained *in-vivo* or, failing that, with a flow phantom. However, this requires the calculation of α, or α_{AM}, which are difficult measurements *in-vivo*, as outlined in Section 5.6.2. The computer model provides great flexibility, allowing one to model the process of AFP under a range of conditions that would be difficult, or even impossible, to mimic in the laboratory. For example, one may, in effect, account for changes in the static magnetic field strength (by altering T_1 and T_2) and the physiological state or the species in which measurements are made (by altering the velocity of blood and the distance between the labelling plane and the imaging plane). It was possible to examine the effects of a train of RF pulses and pulsatile blood flow on individual spins, which would not be possible *in-vivo* or in a flow phantom, where estimates of α are averages over all the spins within a vessel.

A fundamental question that remains about the validity of the computer model is the appropriate relaxation times for spins as they undergo velocity driven AFP. Some authors favour T_1 and T_2 (Maccotta L et al. 1997; Alsop DC and Detre JA 1998) while others view the process as a spin locking experiment (Lee HK et al. 1991; Marro KI et al. 1997). If velocity driven AFP is treated as a spin-locking experiment, the adiabatic condition must be stated in terms of relaxation times in the rotating reference frame, $T_{1\rho}$ and $T_{2\rho}$. These relaxation times depend on the amplitude of B_{eff}, which evolves throughout AFP, by definition. Therefore, modelling velocity driven AFP as a spin-locking experiment would require the calculation of estimates of $T_{1\rho}$ and $T_{2\rho}$ at every individual time point. Values of $T_{1\rho}$ are close to values of T_2 on resonance and it may be that the degree of inversion would be similar with either set of relaxation times but this has not been shown.

Another difference between the computer model and the situation *in-vivo* is the movement of blood through vessels of smaller diameter, at reduced velocities, as it approaches capillary exchange sites. Models that assume that blood moves at a constant velocity may underestimate the amount of T_1 relaxation of the label.

The effects of normal, pulsatile flow on a single inversion and the influence of a train of RF pulses on spins moving at constant velocity have been studied. In practice, the combination of a train of RF pulses and pulsatile flow influences the degree of inversion (especially for clinical studies) and the effect of this combination has not been examined. Furthermore, the influences on the AM control of variations in the blood velocity and discontinuous RF pulses remain to be explored.

The continuous version of ASL offers a larger perfusion-dependent signal than the pulsed version, and the goal of multiple-slice CASL remains attractive for global monitoring of regional blood flow. However, one of the most important findings of this thesis is the failure of the AM control to provide optimum perfusion-dependent contrast. The experimental arrangements differ for humans and animals, suggesting that different solutions may be required in these two situations.

In human studies one of the major concerns is high RF power deposition due to the labelling pulse, especially at higher static magnetic field strengths. This is exacerbated by the AM control, which demands higher RF pulse amplitudes than the equivalent standard, single slice control for optimal performance (Section 4.4.4). However, the AM control continues to be the most widely applied technique for multiple-slice CASL in humans at 1.5 T, suggesting that despite its relatively low sensitivity, it offers significant advantages, namely that no additional hardware is necessary, and it is relatively easy to implement. The AM control may be of value as a diagnostic tool to locate perfusion abnormalities in any image plane throughout the brain. Nevertheless, single slice CASL is preferable for maximum sensitivity and accurate quantification and the single slice technique should be employed when any abnormality is well localised.

In small animals the higher amplitude gradients for CASL and shorter arterial transit times tend to produce greater sensitivity for single slice CASL than in humans. Conversely, higher amplitude gradients may reduce the sensitivity of CASL with the AM control to perfusion in animals (Section 5.6.4). For multiple-slice imaging in animals a different approach may produce better results. Possible alternatives include the use of a separate coil for labelling and imaging, a different control to cancel MT effects (for example Talagala SL et al. 1998; Williams DS et al. 2001), or pulsed ASL.

The measurement of R_2 and R_2* is ideally suited to the type of experimental study presented in Chapter 6 (monitoring over time to detect oxygenation changes). The technique offers high time resolution and is easy to implement and perform. However, R_2* is not an absolute measure, as it depends on the local homogeneity of the static magnetic field, and R_2 is less sensitive to changes in [dHb] than R_2* (no change in R_2 in the liver was seen to result from intestinal I/R). Interpretation of changes in transverse relaxation rates is complicated due to their dependence on several factors, including blood flow and blood volume, haematocrit fraction and the oxygenation of haemoglobin. Ideally, BOLD imaging would be combined with other measures to distinguish between contrast due to blood flow and contrast due to the composition of the blood.

One such measure is perfusion. Clinical MR perfusion studies are routinely performed with contrast agent techniques. These approaches are not so well suited to longitudinal studies in animal models, because time must be allowed after each measurement for the agent to clear the circulation and the presence of the contrast agent complicates the quantification of other MR parameters. The case for using ASL in such studies is strong and initial work to apply the technique in the liver has been performed (Appendix D). Measurements of R_2 and perfusion may be combined in a single sequence, as applied for example by Thomas et al. in brain, using double-echo FAIR (DEFAIR) (Thomas DL et al. 2001). In this way, changes in blood volume could be detected because this approach also has the potential to discriminate blood from tissue in a voxel due to their different T_2 values and the different magnetisation of inflowing blood and tissue after a slice selective inversion.

7.3 Future work

As mentioned in the previous section, the computer model of velocity driven AFP may be extended to examine the magnetisation of blood under different conditions, including:

- gradually decreasing blood velocity as a spin approaches the imaging plane to mimic the movement of blood through the vasculature after labelling
- the combination of pulsatile flow and a train of RF pulses
- the combination of pulsatile flow and the AM control

Much work in this thesis has focussed on the performance of the AM control technique for multiple-slice measurements of perfusion. Severe disadvantages of the technique have been found and although means to optimise the pulse have been determined, an alternative method for multiple-slice measurements, especially in small animals, may be preferable. In order to benefit from the greater sensitivity of continuous in comparison with pulsed ASL, while avoiding MT effects in tissue, the use of separate labelling and imaging RF coils has much to recommend it. Future work to implement two-coil CASL would extend the range of applications for perfusion imaging, including the option to selectively label blood in a single artery and thereby map perfusion territories.

The application of MRI to image the liver during intestinal I/R could be extended to further elucidate the pathological changes due to the insult. Results from BOLD imaging have been reported here, but it would be particularly informative to measure a range of different parameters in the same animal, in order to determine causal links between changes in flow through the hepatic artery (HA) and portal vein (PV), perfusion, R_2* and concentrations of energy metabolites in the liver. Combined perfusion and BOLD imaging may permit assessment of the relative contributions of compromised perfusion and oxygenation to the derangement of hepatic energy metabolism. CASL is less suitable for imaging the liver than the brain because the orientation of the PV and HA is quite variable and the optimum direction for the labelling gradient would change between animals. On the other hand, refinement of the FAIR technique for liver imaging may make it possible to map perfusion in the liver during intestinal I/R. Implementation of DEFAIR with a FLASH acquisition may provide data on both perfusion and blood volume.

Other possible measurements include MR angiography (MRA) and phosphorus MR spectroscopy (MRS). MRA may be employed to measure the relative contributions to hepatic inflow of the portal vein and hepatic artery. Phosphorus MRS may be used to study changes in the energy metabolism of the liver during intestinal I/R. Such a multi-modal approach may help to elucidate the mechanisms underlying intestinal I/R injury.

Appendix A

The adiabatic condition for the AM control

The AM control depends on adiabatic fast passage to produce two inversions. It is therefore of interest to consider the adiabatic condition. A general form of the condition for the AM control has a complicated mathematical form, but consideration of some particular cases sheds light on the choice of parameters for successful double inversion by the AM pulse.

The condition may be expressed as:

$$1/T_1,\ 1/T_2 \ll d\theta/dt \ll \gamma B_{eff} \qquad \text{equation [A1]}$$

where $\underline{B}_{eff} = \underline{B}_1 + \underline{\Delta B}$

$\cos\theta = \Delta B / B_{eff}$

(see *Figure 3.1* and Section 3.2.1 for definition of terms). In the following analysis all magnetic field strengths and gradients are expressed in Hz and Hz/mm respectively. Velocities are expressed in mm/s.

By differentiation with respect to time of cos θ and $\underline{B}_{eff}$, as in Chapter 3, the right hand side of the condition for velocity driven AFP may be written:

$$(\Delta B^2 + B_1^2)^{3/2} \gg \left(B_1 \frac{d\Delta B}{dt} - \Delta B \frac{dB_1}{dt}\right) \qquad \text{equation [A2]}$$

For labelling by velocity driven AFP, $\underline{B}_1$ is constant and $\Delta B = vGt$,

$$((vGt)^2 + B_1^2)^{3/2} \gg B_1 vG$$

The condition is most difficult to satisfy when t = 0 and the condition simplifies to

$$B_1^2 \gg vG \qquad \text{equation [A3]}$$

For the AM pulse,

$$B_1 = B_{10} \sin(2\pi ft + \phi)$$

$$dB_1/dt = 2\pi f B_{10} \cos(2\pi ft + \phi)$$

and the adiabatic condition becomes:

$$((vGt)^2 + B_{10}^2\sin^2(2\pi ft+\phi))^{3/2} >> B_{10}(vG)\{\sin(2\pi ft + \phi) - 2\pi ft\cos(2\pi ft + \phi)\}$$
equation [A4]

This function may be evaluated in a few particular cases. When $t = 0$ equation [A4] is independent of f. When $t = 0$ and $\phi = 0$ equation [A4] reduces to $0 >> 0$, making the condition meaningless. When $t = 0$ and $\phi=\pi/2$ the condition reduces to [A3]. At the centres of the AFPs $t = \pm f/(Gv)$ and

$$(f^2 + B_{10}^2\sin^2(2\pi f(\pm f/(Gv))+\phi))^{3/2} >>$$
$$B_{10}\{Gv*\sin((2\pi f(\pm f/(Gv))+\phi) - (\pm 2\pi)f^2\cos(2\pi f(\pm f/(Gv))+\phi)\}$$
equation [A5]

The condition [A5] is most difficult to satisfy when $\sin(\pm 2\pi f^2/(Gv)+\phi) = 0$, i.e. when $\underline{B}_1 = 0$ at the centre of an inversion. In this case [A5] becomes

$$f >> -(\pm B_{10})$$
equation [A6]

Equations [A5] and [A6] show that the adiabatic condition is different at ± f . If only one AFP satisfies the condition, the result is a single inversion ($m_z \approx -1$).

Another case in which the adiabatic condition may be simplified is if the term $d\underline{B}_1/dt$ does not contribute to the AFP and therefore may be neglected. This may be because B_1 changes too rapidly for $\underline{m}$ to follow so that the change in $\underline{m}$ is dominated by the frequency sweep, or in the specific case where $\cos(\pm 2\pi f^2/(Gv)+\phi) = 0$. If $d\underline{B}_1/dt$ is neglected, equation [A5] becomes

$$f^2 >> (B_{10}Gv)^{2/3} - B_{10}^2$$
equation [A7]

or $$f^2/Gv >> (B_{10}^2/Gv)^{1/3} - B_{10}^2/Gv$$

The condition [A7] is always satisfied if [A3] is satisfied, independent of f. Therefore the adiabatic condition for the AM control, neglecting relaxation effects, may be summarised by the conditions for two extreme cases, firstly when $B_1 = 0$ at the centre of the AFPs [A6] and secondly when B_1 changes so rapidly that the change in $\underline{m}$ is dominated by the frequency sweep of $\underline{B}_{eff}$:

$B_1^2 >> Gv$ and $f >> B_{10}$

Appendix B

Phase of the modulation of B_1 (ϕ) for the AM control

Figure B1 shows the double inversion of the AM control at $\phi = 0$ and at $\phi = \pi/2$. An explanation for the dependence of the AM control on ϕ may be found by considering the effective magnetic fields that describe the first and second AFP of the AM control, $\underline{B}_{eff1}$ and $\underline{B}_{eff2}$. The velocity of the spin, $\underline{v}$, and the gradient, $\underline{G}$, determine the direction of the frequency sweep, which is therefore the same for both AFPs. However, at the position half way between the inversions, where $t = 0$, $\underline{\Delta B} = + f$ for $\underline{B}_{eff1}$ and $\underline{\Delta B} = -f$ for $\underline{B}_{eff2}$. This may be regarded as the end of the first AFP and the beginning of the second AFP.

Spins undergo AFP when B_1 has different amplitudes, at different phases of the modulation function $\sin(2\pi ft + \phi)$. Let us consider B_1 at positions symmetrically displaced about $t = 0$, at $\pm t_A$, where t_A is a small increment of time, corresponding to regions where the 2 effective magnetic fields, $\underline{B}_{eff1}$ and $\underline{B}_{eff2}$, dominate the evolution of $\underline{m}$ (*Figure B1*).

From [equation 4.1]

$$B_1(\pm t_A) = B_{10} \sin(2\pi f(\pm t_A) + \phi)$$

$\underline{B}_1$ is periodic in both ϕ, and $2\pi ft$.

When $\phi \approx n\pi$,

$$B_1(+t_A) \approx -B_1(-t_A)$$

and

$$|B_1(t=0)| \approx 0$$

In this case, there is a smooth transition from one AFP to the next (*Figure B1(i)*). At $t = 0$ nutation about $\underline{B}_{eff1}$ is equivalent to nutation about $-\underline{B}_{eff2}$. The magnetisation can move smoothly from the first to the second AFP and the second AFP reverses the effect of the first AFP.

$$d\underline{B}_{eff1}/dt \approx -d\underline{B}_{eff2}/dt$$

and

$$d\underline{m}(-t_A)/dt \approx -d\underline{m}(+t_A)/dt$$

m nutates about + $\underline{B}_{eff1}$ for the first AFP and then follows - $\underline{B}_{eff2}$ for the second AFP and double inversion is achieved.

On the other hand, when $\phi \approx (2n+1)\pi/2$,

$$\underline{B}_1(+t_A) \approx +\underline{B}_1(-t_A)$$

and

$$|\underline{B}_1(t=0)| \approx B_{10}$$

In this case, $\underline{B}_{eff2}$ is not aligned with $\underline{B}_{eff1}$ at $t = 0$ and the evolution of $\underline{m}$ is disrupted, as nutation about $\underline{B}_{eff1}$ is not equivalent to nutation about $\underline{B}_{eff2}$ (or $-\underline{B}_{eff2}$).

The preceding argument applies to small f. If $f >> B_{10}$ the frequency sweep $d\underline{\Delta B}/dt$ dominates the change in $\underline{B}_{eff}$. As t approaches 0, $\underline{B}_{eff1} \approx -f$ and $\underline{B}_{eff2} \approx +f$ for any value of ϕ and the phase of B_1 is not important because $\underline{B}_{eff1}(t = 0) \approx -\underline{B}_{eff2}(t = 0)$, at any value of ϕ.

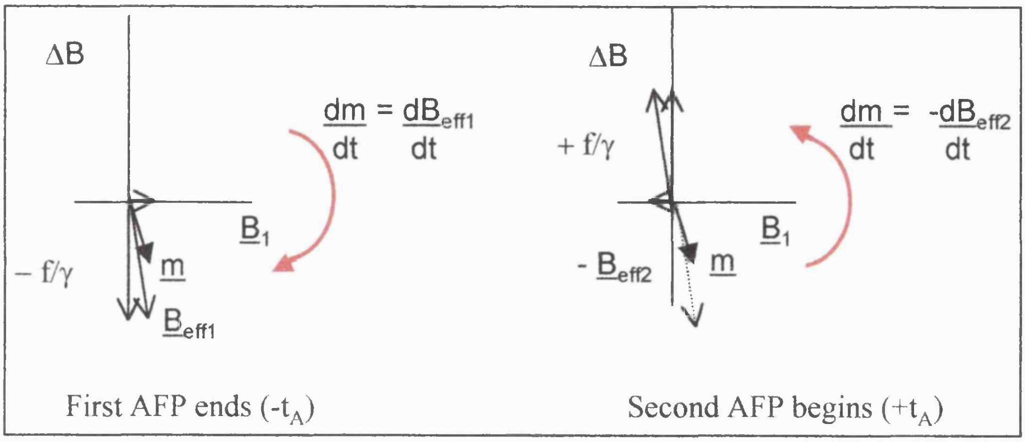

i) $\phi = n\pi$ when $t = 0$

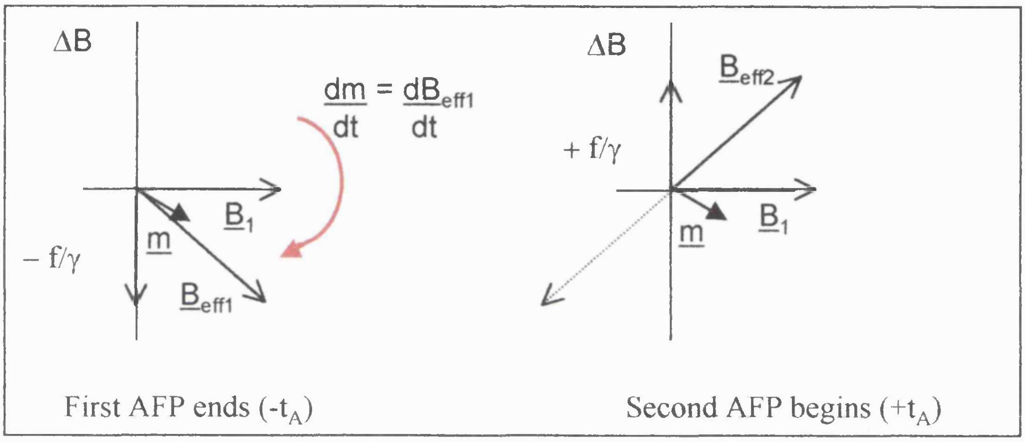

ii) $\phi = (2n+1)\pi/2$ when $t = 0$

Figure B1

The evolution of $\underline{B}_{eff}$ and $\underline{m}$ in the rotating reference frames for inversion ($\underline{B}_{eff1}$) and re-inversion ($\underline{B}_{eff2}$). $\underline{m}$ is shown at times just before and just after the spin passes through the plane at $\underline{z} = 0$ when $\phi = 0$ (i) and when $\phi = \pi/2$ (ii).

Appendix C

Further studies of the AM control

C.1 Introduction

In Chapter 4 it was shown that the performance of the AM control is a complicated function of ϕ, f, G, v and B_1. Three further studies were performed in order to determine whether the dependence of the AM control on f, G, v and B_1 might be explained in terms of the separation the AFPs from one another and the duration of each individual AFP. The separation depends on G, f and v, while the duration of each AFP depends on G, v and B_1. In the following analysis all magnetic field strengths and gradient amplitudes are expressed in Hz and Hz/mm respectively. Velocities are expressed in mm/s.

The separation of the AFPs may be defined in terms of frequency, distance or time, as follows. Inversions are centred on $\Delta B = \pm f$. Therefore the inversion planes are separated in frequency by 2f. In the presence of a magnetic field gradient, $\underline{G}$, this corresponds to a physical separation of

$$\Delta z = 2f/G \qquad \text{equation [C1]}$$

Denoting t_{inv} as the time at which a spin passes through the centre of one AFP (where $\Delta B = \pm f$) and recalling that $t = 0$ when $\Delta B = 0$,

$$t_{inv} = \pm f/(Gv)$$

and the temporal separation of the inversions is

$$2t_{inv} = 2f/(Gv) \qquad \text{equation [C2]}$$

Spins in blood spend less time travelling from one AFP to the next when v is large or when $\Delta z = 2f/G$ is small.

The separation of the planes is unique to the AM pulse, but another temporal parameter influences any AFP, namely its duration, Δt, as discussed in Chapter 3 (equation [3.9]). Δt is inversely proportional to the rate of the frequency sweep, $d\Delta B/dt = Gv$, and increases linearly with the amplitude of B_1 (at larger B_1, $\underline{B}_{eff}$ moves away from the $\underline{\Delta B}$ axis to begin the velocity driven AFP sooner (*Figure 3.1*)).

Some indication of the roles of the separation and duration of the AFPs may be gained from Chapter 4. The efficiency of the AM control decreases when f is too small (*Figure 4.4*) or when v is too great, meaning that the time it takes for a spin to travel from one inversion plane to the other is too short (especially apparent in the animal model, *Figure 4.8b*). These results suggest that it would be possible to select f/(Gv) to be large enough to separate the centres of the AFPs and thereby eliminate any overlap between them. However, B_1 also influences the efficiency of the AM control (*Figure 4.7*). B_1 does not affect the separation of the inversions, but as B_1 increases the duration of each AFP increases and it becomes more likely that the second inversion begins before the first inversion is complete (*Figure 4.3a*).

The investigations described in this section were designed to elucidate the dependence of the AM control on the parameters (i) v and (ii) the product Gv; (iii) the amplitude of B_1. v and the product Gv affect the separation of the centres of the AFPs and the duration of each one. B_1 affects the duration of a single AFP, without changing the separation of the centres of the AFPs.

C.2 Velocity

The variation in m_z over a range of f at three different v is shown in *Figure C1*. At the lowest f, all spins are inverted (m_z = -1). At the highest f, the AM control performs as required and $m_z \approx +1$. There are two points to note here. Firstly, the lowest value of f, at which some degree of re-inversion takes effect is greater at higher velocities. Secondly, the last minimum in m_z is reached, and m_z approaches its maximum (plateau) level at lower f when v is higher. The performance of the AM control appears to be dominated by different effects at low f (less than 50 Hz) and high f (greater than 50 Hz).

At a given f and G, the physical separation of the planes is the same at any v, but the temporal separation is greater for smaller v. This may explain the behaviour at low f shown in *Figure C1*. If a minimum temporal separation of the centres of the control planes were required for two distinct inversions, it would be achieved at lower f when v was smaller and m_z would depart from –1 at lower f (compare v = 50 mm/s with v = 100 mm/s). The first maxima occur at greater f at higher velocities, although this is not a simple linear dependence on v^{-1} that might be predicted by consideration only of the temporal separation of the AFPs.

At high f, the duration of the inversions becomes more important. At v = 100 mm/s each AFP takes longer than at v = 200 mm/s and the centres of each AFP must be separated by greater f when v = 100 mm/s than when v = 200 mm/s for two completely independent inversions (*Figure C1*).

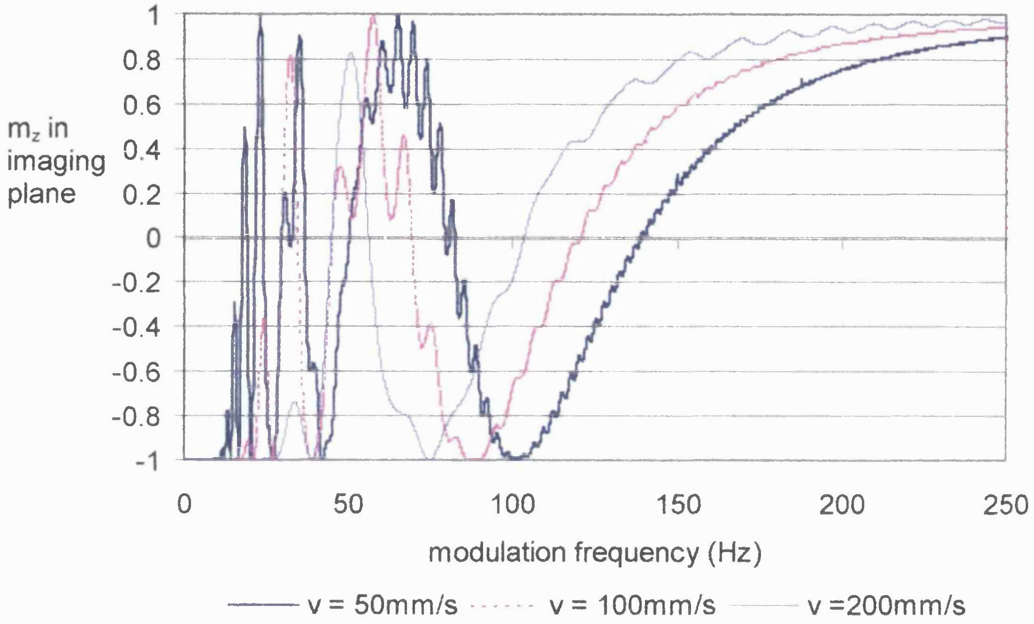

Figure C1

m_z at three different velocities with respect to modulation frequency

m_z values were calculated from f = 0 Hz to f = 250 Hz in steps of 0.1 Hz.

10 kHz offset at 100 mm (G = 100 Hz/mm), $\phi = \pi/2$, $B_1 = 270$ Hz, $T_1 = T_2 = 10^6$ms.

C.3 The product Gv

The dependence of m_z on f is illustrated in *Figure C2* for different values of the product Gv. We see that the variation in m_z with f depends on the product Gv, rather than on either v or G. For example, m_z behaves differently in *Figure C2(a)* and *Figure C2(b)*, although G is the same in both, while m_z follows the same pattern when Gv is the same (as in *Figures C2(c)* and *(a)* or *Figures C2(b)* and *(d)*). This suggests that the behaviour of the AM control depends not on the physical separation of the inversions, $2\Delta z = 2f/G$ but on the temporal separation, $\Delta t = 2f/(\gamma Gv)$

Two forms of oscillatory behaviour may be distinguished in the complicated dependence of m_z on f. Firstly, there are large-scale variations with f. When Gv = 5 x 10^3 Hz/s, these variations have a minimum at about f = 40 Hz, a maximum at about f = 70 Hz and a final minimum at f = 100 Hz. Secondly, more rapid variations in m_z with smaller amplitudes are observed. The period of these rapid oscillations is twice as great when Gv = 10 x 10^3 Hz/s, as when Gv = 5 x 10^3 Hz/s.

The envelope of larger scale variations in m_z has a similar form at both values of Gv. However, when Gv is 10 x 10^3 Hz/s, the final minimum is at a lower f than when Gv is 5 x 10^3 Hz/s (the last minimum is at f = 89 Hz when Gv = 10 x 10^3 Hz /s (*Figure C2(a)* and *(c)*) and at f = 100 Hz when Gv = 5 x 10^3 Hz /s (*Figure C2(b)* and *(d)*). When Gv = 10 x 10^3 Hz/s the frequency sweep for AFP is faster, the duration of each AFP is shorter and therefore the AFPs become independent of one another at lower f.

The halving of the frequency of the more rapid oscillations in m_z when Gv = 10 x 10^3 Hz /s relative to the cases where Gv = 5 x 10^3 Hz /s suggests that these small oscillations may be related to the temporal separation of the inversion planes, $2t_{inv} = 2f/(Gv)$. The time it takes a spin to move from the centre of the first AFP to the centre of the second AFP at a given f is twice as great when Gv = 5 x 10^3 Hz /s as when Gv = 5 x 10^3 Hz / s.

a) Gv = 5 x 10^3 Hz / s
G = 100 Hz/mm, v = 50 mm/s

b) Gv = 10 x 10^3 Hz / s
G = 100 Hz/mm, v = 100mm/s

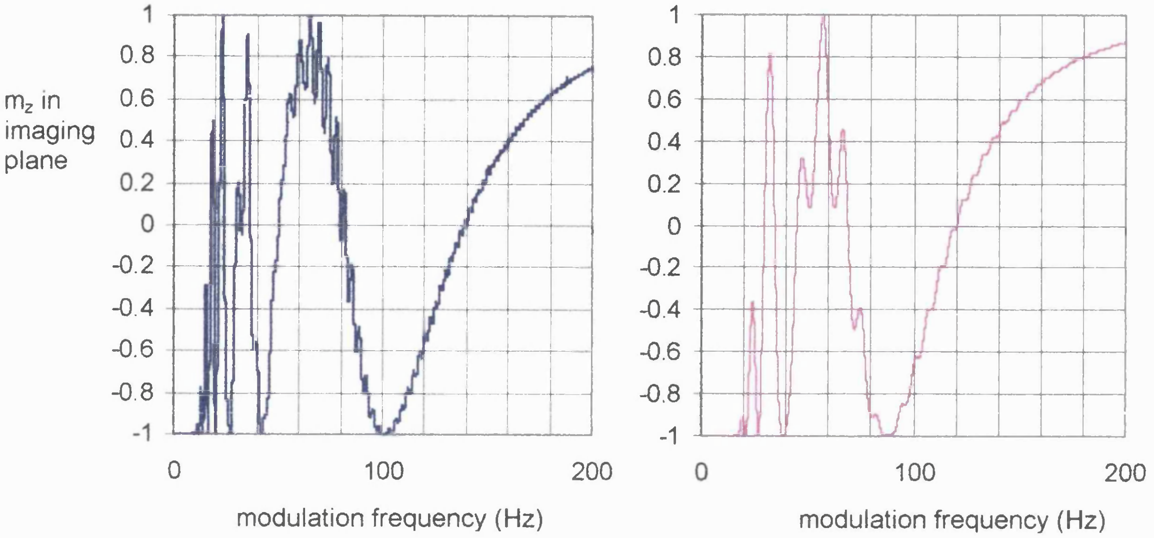

c) Gv = 5 x 10^3 Hz / s
G = 50 Hz/mm, v = 100mm/s

d) Gv = 10 x 10^3 Hz / s
G = 50 Hz/mm, v = 200mm/s

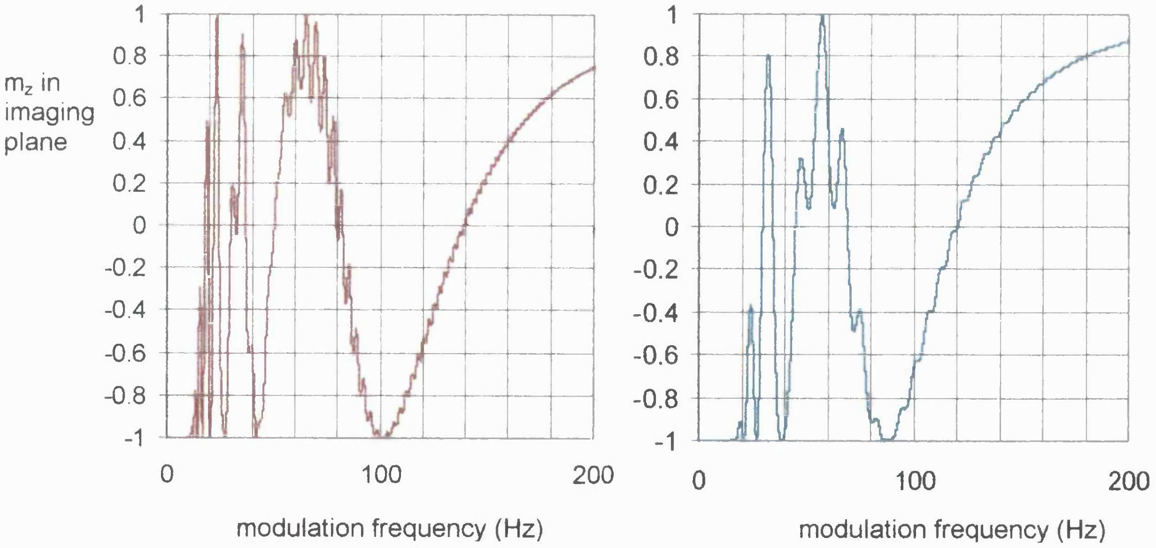

Figure C2

Dependence of m_z on the product Gv

B_1 = 270 Hz, $T_1 = T_2 = 10^6$ ms, $\phi = \pi/2$

m_z values were calculated from f = 0 Hz to f = 200 Hz in steps of 0.1 Hz.

C.4 The amplitude of B_1

The dependence of the AM control on the amplitude of B_1 with ranges of B_1 that would be employed in practice was shown in *Figure 4.8.* Unlike the variables f, G and v, B_1 determines only the duration of the AFP. It does not influence the separation of the centres of the inversions. The aim of this investigation was to calculate the effects of a greater range of B_1 values, in order to infer something about the dependence of the AM control on the duration of each AFP.

Figure C3 shows m_z in the imaging plane with respect to B_1 at three f without relaxation effects ($T_1 = T_2 = 10^6$ ms). Data are shown with $\phi = \pi/2$ (*Figure C3 a*) and $\phi = 0$ (*Figure C3 b*). Note the different scales for m_z in the two plots. The sensitivity of the control to B_1 when $\phi = 0$ is minimal, but variations in m_z with f have the same period, whether $\phi = \pi/2$ or $\phi = 0$.

The dependence of m_z on the amplitude of B_1 has a similar, pseudo-periodic form at each f. At B_1 values greater than 130 Hz the period of variations with respect to B_1 is proportional to f. The second minima appear at $B_1 = 185$ Hz when f = 50 Hz, $B_1 = 300$ Hz when f = 100 Hz and $B_1 = 490$ Hz when f is 200 Hz. A larger B_1 corresponds to a greater duration of the AFP. Therefore, overlap between the two AFPs of the AM control might be expected at lower B_1 when f is smaller. However, the reason for a series of maxima and minima of m_z at increasing B_1 is not apparent.

a) $\phi = \pi/2$

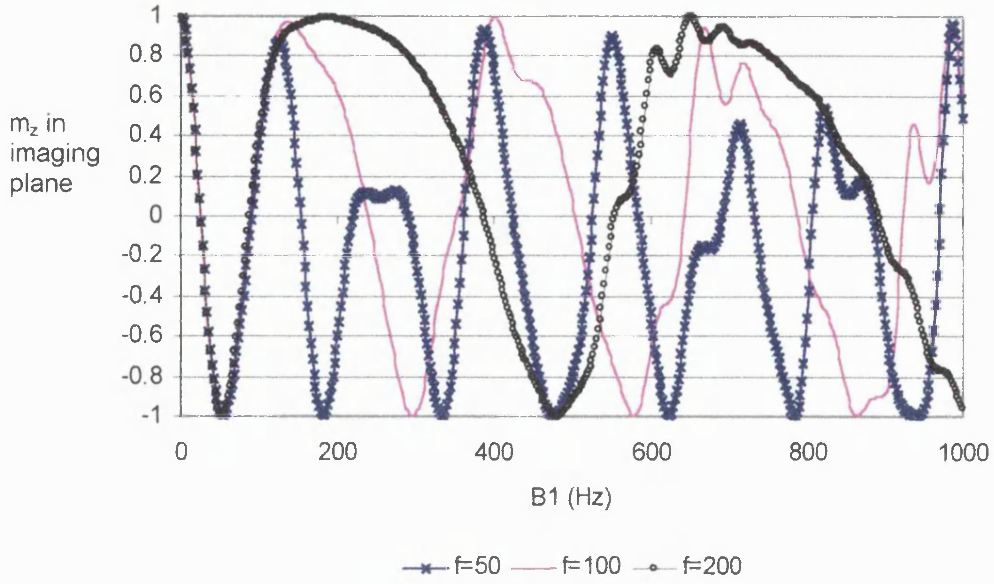

b) $\phi = 0$

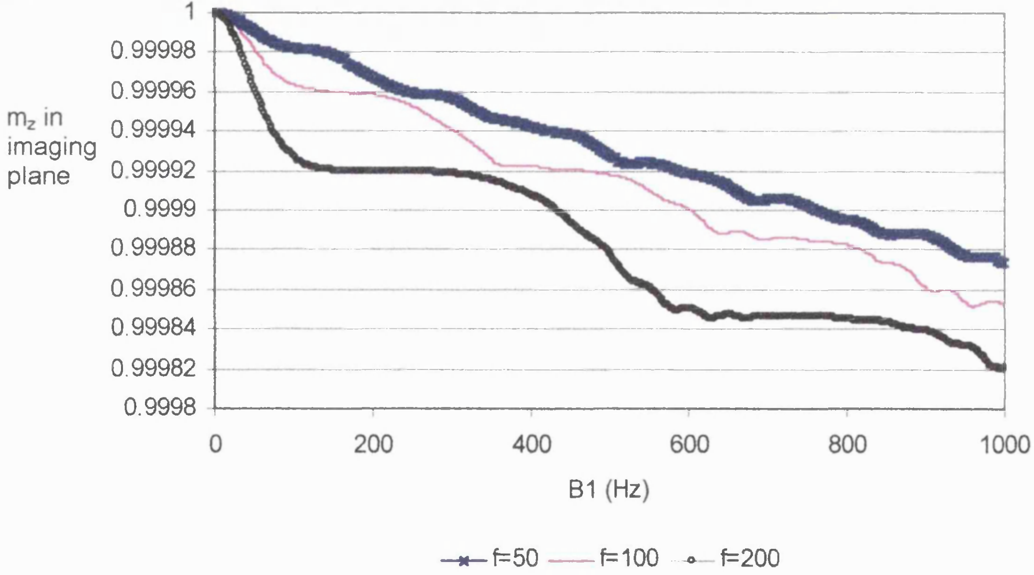

Figure C3

The dependence of m_z on B_1

m_z depends on f and B_{10} when $\phi = \pi/2$ (a) but when $\phi = 0$ this dependence is minimal (b).

5 kHz offset at 100 mm from the imaging plane (G = 50 Hz/mm), v = 200 mm/s, $T_1 = T_2 = 10^6$ ms

m_z values were calculated from f = 0 Hz to f = 1000 Hz in steps of 0.1 Hz.

C.5 Discussion

Interactions between the two components of B_1 for the AM control reduce the efficiency of the technique, as shown in Chapter 4. The studies in this appendix were designed to investigate further the functional dependence of m_z on key parameters of the AM control pulse, namely the magnetic field gradient amplitude, G, the velocity of blood, v, and the amplitude of the RF pulse, B_1.

The modulation frequency, f, dictates the frequency separation of the centres of the AFPs. However, there are two other ways of defining the separation of the components of the AM pulse, which are related to one another, as follows:

1) the physical distance between the centres of the inversions, $\Delta z = 2f/G$;
2) the time it takes for a spin to move from the centre of one AFP to the other, $2t_{inv} = \Delta z/v = 2f/(Gv)$.

Results presented here indicate that the temporal separation influences the efficiency of the AM control, rather than the physical separation, indicated by the behaviour of m_z when Δz is the same at different v (*Figure C1*) and the dependence of m_z on the product Gv, rather than G alone (*Figure C2*).

The amplitude of B_1 has no effect on the separation of the centres of the 2 AFPs, but it has a profound effect on the efficiency of the control (*Figures 4.7* and *C3*). If each AFP takes more time, it is more likely that the two AFPs of the AM control overlap, leading to imperfect inversion and re-inversion. This becomes more likely at larger B_1 because $\underline{B}_{eff}$ moves away from the $\underline{\Delta B}$ axis sooner and the duration of a single AFP increases. The behaviour of the AM pulse depends on B_1 in a periodic way with a period that is proportional to f. The reasons for this dependence are not clear. However, if the condition $f > B_1$ is met (see also Appendix A) the overlap between AFPs should be minimal.

These further studies demonstrate the complexity of the AM pulse. Despite the remaining unexplained features of the pulse, it has been possible to devise a practical procedure for optimisation of the pulse as a control for CASL imaging, detailed in Chapter 4.

Appendix D

Flow-sensitive alternating inversion recovery (FAIR) MRI in liver

D.1 Introduction

The measurement of perfusion provides an invaluable tool in the study of any ischaemic injury. One such injury occurs in the liver as a result of intestinal ischaemia-reperfusion (I/R). A model of this condition was studied in Chapter 6 using blood-oxygen-level-dependent (BOLD) contrast. The MR technique of arterial spin labelling (ASL) provides non-invasive measurements of perfusion. This study was designed to test the feasibility of the flow-sensitive-alternating-inversion-recovery (FAIR) technique in the liver of a rat.

D.2 Methods

FAIR was implemented with alternate slice selective (SS) and non-selective (NS) inversion pulses before a refocused, fast low angle shot (FLASH) image acquisition (Haase A et al. 1986). Inversion was achieved using an adiabatic, frequency offset corrected inversion (FOCI) RF pulse (t-shape, 1440 Hz bandwidth) in order to minimise interference between the profiles of the inversion and imaging slices (Ordidge RJ et al. 1996; Yongbi et al. 1999). FLASH was selected in preference to EPI, because EPI is more prone to signal drop-out in areas of large susceptibility gradients at interfaces between different materials, which are prevalent in the abdomen.

The refocused FLASH acquisition had a slice thickness of 2 mm, Gaussian shaped RF pulse (600 Hz bandwidth), 64 phase encoding steps with centre-out phase encoding, effective TE = 2.06 ms, 65 mm^2 field of view, 80 averages. The inversion slab for the SS image was 5 mm thick to give a ratio of inversion:slice thickness of 5:2. There were four dummy cycles prior to image acquisition (one cycle comprises a pair of SS and NS inversions, each followed by an imaging sequence). The repetition time for a single loop of the experiment, following either SS or NS inversion was TR = 1264 ms + TI, giving a total acquisition time of 8 minutes and 6 seconds for an inversion time of 1600 ms with 80 averages. Pairs of SS and NS images were acquired at a range of inversion times, TI = 250, 500, 750, 1100, 1600, 2500, 2700, 2900 ms.

The animal was maintained under anaesthesia with halothane and oxygen as for experiments described in Chapter 6. A plastic insert was positioned between the liver and the diaphragm to minimise the effects of respiratory motion (*Figure 6.2*), but there was no other surgical intervention.

Normalised signal differences were calculated at each TI in regions of interest in the liver:

$$\Delta S = 100 * (S_{SS} - S_{NS}) / S_0$$

where S_{SS} and S_{NS} are the signal intensities in SS and NS images,

S_0 is the signal in the NS image with the longest TI

D.3 Results

FLASH-FAIR images are shown in *Figure D1*. Images on the left were acquired after a non-selective (NS) inversion pulse. When the NS image is subtracted from the SS image a difference in signal appears due to the flow of fully relaxed blood into tissue after the SS inversion (images on the right of *Figure D1*). Blood flowing through large vessels is clearly visible and there are smaller signal differences in the liver parenchyma (*Figure D1 a*). There is no signal difference in the post-mortem images, confirming that there was no significant residual signal difference in the absence of flow (*Figure D1 b*).

a) In-vivo

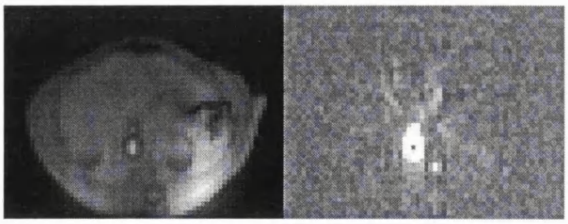

NS inversion Subtraction (SS – NS)

b) Post-mortem

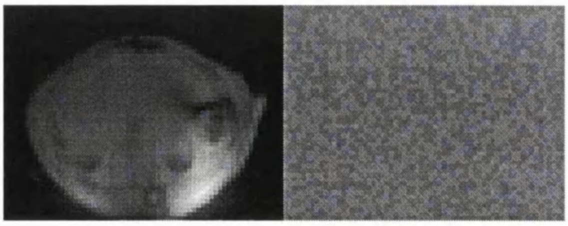

NS inversion Subtraction (SS – NS)

Figure D1

FAIR images of liver

TI = 2500 ms TR = 3765 ms, TE (effective) = 2.06 ms, number of averages = 80, FOV = 65 mm, 64 x 64 matrix, ratio of inversion thickness: slice thickness = 5:2.

Figure D2 shows subtraction images at a range of TI. The regions of interest selected for analysis are shown also. ROI 1 is in the parenchyma of the liver and ROI 2 is in a region encompassing a small blood vessel.

Differences in signal, ΔS (equation [D1]), are shown in *Figure D3* at a range of inversion times. ΔS increased with increasing TI, as fully relaxed blood washed into the liver after the SS inversion until TI = 500 ms, then ΔS decreased due to T_1 relaxation in the tissue. ΔS is not as great in ROI 1 as in ROI 2. The variation in ΔS with TI in ROI 1 was only a little greater than measurement error, reflecting the low sensitivity of these measurements to true tissue perfusion. Post mortem values of ΔS were 0.0 ± 1.0 and ΔS = 0.5 ± 1.0 in ROI 1 and ROI 2 respectively (with an inversion time of 2500 ms), much lower than ΔS at the same TI *in-vivo* (ΔS = 1.4 ± 1.6 % and 4.6 ± 1.6 % in ROI 1 and ROI 2 respectively).

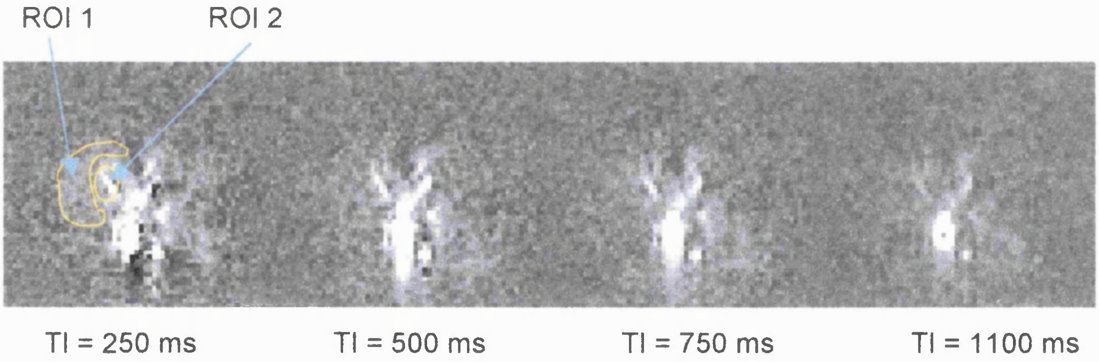

Figure D 2

FAIR subtraction images of liver at short TI

Positions of the ROIs used for analysis are shown.

TR = 3764 ms, TE (effective) = 2.06 ms, number of averages = 80, FOV = 65 mm, 64 x 64 matrix, ratio of inversion thickness: slice thickness = 5:2.

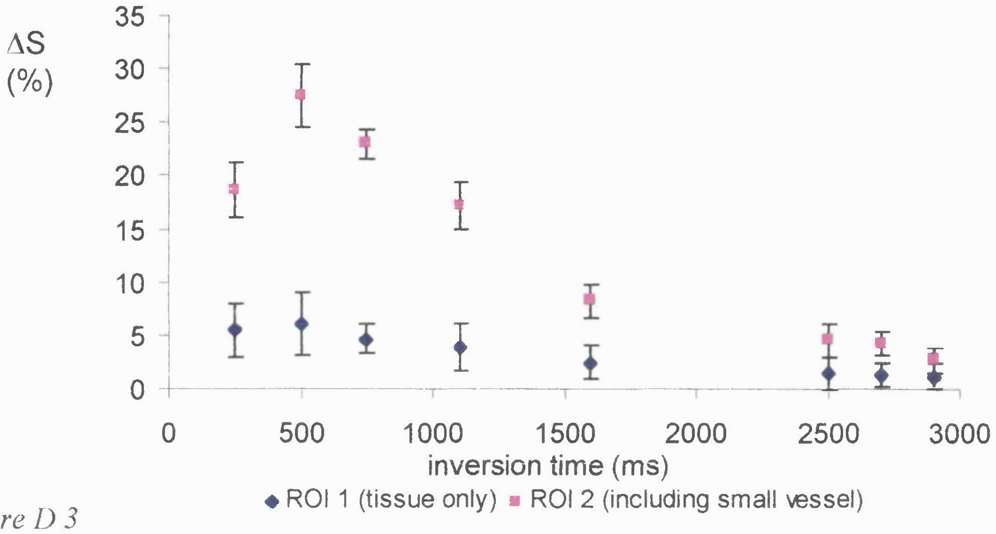

Figure D 3

Signal differences in liver

$\Delta S = 100*(S_{SS} - S_{NS}) / S_0$

Error bars are calculated from the SNR of the three images used to calculate ΔS.

D.4 Discussion and Conclusion

The application of ASL in the liver presents some additional challenges to those for ASL in the brain. The first of these is motion. Motion artifacts due to respiration may be overcome by fast imaging, in this case FLASH, but gross motion, possibly resulting from peristaltic movement in the abdomen, still poses a problem, especially when several minutes of averaging are necessary, as for FAIR. Also, short T_1 and T_2 in the liver reduce the sensitivity of ASL. Short T_2 produce low signal-to-noise ratios in all images of the liver. This reduces the CNR in FAIR subtraction images of the liver. Short values of T_1 in liver parenchyma are a particular problem for ASL because as soon as labelled spins enter the liver tissue they begin to relax with the short T_1 of tissue (approximately 210 ms at 2.35 T), reducing the difference in signal intensity produced by the label.

It has been shown that MR perfusion-weighted imaging of the liver is possible in rats, using FAIR, despite considerable technical difficulties. This adds a possible further source of information on hepatic haemodynamics during intestinal I/R and other conditions that affect the circulation of the liver.

Appendix E

Quantification of perfusion from the CASL experiment

The starting point for the calculation of microvascular blood flow, f, is the modified Bloch equation, given in Chapter 2.

$$\frac{dM_t}{dt} = \frac{(M_{0sat} - M_t)}{T_{1sat}} + f\,M_a(t) - \frac{f\,M_t}{\lambda} \qquad \text{equation [2.9]}$$

where M_t is the tissue magnetisation per 100g of tissue

M_{0sat} is the equilibrium value of M_t in the presence of the labelling pulse

M_a is the magnetisation of inflowing (arterial) blood per 100 ml of blood

f is microvascular blood flow (ml /100g tissue/sec)

λ is the blood / brain partition coefficient $\dfrac{\text{(ml of water / g of tissue)}}{\text{(ml of water / g of blood)}}$

T_{1sat} is the spin-lattice relaxation time of the tissue in the presence of the labelling pulse.

In equation [2.9] the first term describes the longitudinal relaxation of the tissue, the second term describes the inflow of protons in arterial blood and the last term describes the venous outflow from the tissue. In addition to inverting moving spins the labelling pulse acts as a saturation pulse on tissue in the imaging plane. Therefore the equilibrium magnetisation of tissue while the labelling pulse is on is M_{0sat} and the spin-lattice relaxation time is T_{1sat}.

The difference in tissue magnetisation between the label and control experiments is reduced by relaxation in the blood as it moves into the imaging plane. The magnetisation that arrives in the imaging plane after the label or the control is

$$M_a = (1 - 2\alpha\, e^{-\delta / T1a})\, M_{0a}$$

where α is the efficiency of inversion. Ideally $\alpha = 1$ and $\alpha = 0$ for the label and control experiments respectively.

δ is the is the arterial transit time (the time between labelling a spin and its arrival in the imaging plane)

T_{1a} is the T_1 relaxation time of arterial blood

M_{0a} is the equilibrium magnetisation of arterial blood water

Using the relationship $M_{a0} = M_0 / \lambda$,

where M_0 is the equilibrium magnetisation of tissue water,

we may write

$$M_a = (1 - 2\alpha\, e^{-\delta / T_{1a}})\, M_0 / \lambda \qquad \text{equation [E1]}$$

It may be shown by integration of equation [2.9] after substitution of [E1] that the difference in magnetisation that develops during the labelling time is:

$$\Delta M = M^{label} - M^{control} = \frac{-2\alpha\, M_0\, f\;\, e^{-\delta/T1a}}{\lambda} \int_{\delta}^{\tau} \exp[-(t-\delta)/T_{1app}]\, dt$$

equation [E2]

where $1 / T_{1app} = 1 / T_{1sat} + f / \lambda$

τ is the duration of the pulse

$$\Delta M = \frac{-2\alpha\, M_0\, f\;\, e^{-\delta/T1a}}{\lambda}\, T_{1app}\, (1 - \exp[-(\tau-\delta)/T_{1app}]) \qquad \text{equation [E3]}$$

In the limit where τ tends to infinity ($\tau >> T_{1sat}$) f is then (Detre JA et al. 1992):

$$f = \frac{-\lambda}{T_{1app}}\; \frac{\Delta M}{2\,\alpha\, M_0\, e^{-\delta/T1a}} \qquad \text{equation [E4]}$$

The simplifying assumption that $\delta = 0$ reduces equation [E4] equal to equation [2.10] (Chapter 2).

The experiments described in Chapter 5 have a post-labelling delay to reduce the sensitivity of the measurement to transit times. During a post-labelling delay two populations of labelled spins may be distinguished. Firstly, labelled spins that have already entered the tissue continue to relax with the longitudinal relaxation time T_1 (not T_{1sat}, as it is in the presence of the labelling pulse). Secondly, fresh labelled spins continue to enter the tissue until the post-labelling delay is longer than δ. This second population of spins changes the magnetisation by an amount ΔM_{new_blood}.

$$\Delta M_{new\_blood} = \frac{-2\alpha M_0 f \ e^{-\delta/T1a}}{\lambda} \int_{\tau}^{t} \exp[-(t-\tau)/T_{1ns}]\, dt \qquad \text{equation [E5]}$$

where $1 / T_{1ns} = 1 / T_1 + f / \lambda$, the observed relaxation time with no saturation pulse (ns)

The sum of the two components of labelled water in tissue, in the limit $\tau >> T_{1app}$ is

$$\Delta M = \left[\frac{-2\alpha M_0 f e^{-\delta/T1a}}{\lambda}\right]\{T_{1app} \exp[-(t-\tau)/T_{1ns}] + T_{1ns}(1 - \exp[-(t-\tau)/T_{1ns}])\}$$

equation [E6]

If w is the post-labelling delay, and $t = w + \tau$, the difference in magnetisation is:

$$\Delta M(w < \delta) = \left[\frac{-2\alpha M_0 f e^{-\delta/T1a}}{\lambda}\right]\{T_{1app} \exp[-w/T_{1ns}] + T_{1ns}(1 - \exp[-w/T_{1ns}])\}$$

equation [E7]

Equation [E7] pertains when $w < \delta$. After a time $t = \tau + \delta$ all of the labelled blood has arrived and ΔM continues to relax. ΔM may be determined for the case where $w > \delta$ by evaluating equation [E6] when $t = \tau + \delta$ and multiplying the result by $\exp[-t-(\tau + \delta))/T_{1ns}]$.

Writing $t = \tau + w$ in the limit $\tau >> T_{1app}$

$$\Delta M(w > \delta) = \left[\frac{-2\alpha M_0 f e^{-\delta/T1a}}{\lambda}\right]\{T_{1app} \exp[-w/T_{1ns}]$$

$$+ T_{1ns}(\exp[-(w-\delta)/T_{1ns}] - \exp[-w/T_{1ns}])\} \qquad \text{equation [E8]}$$

Equations [E7] and [E8] are equivalent to the expressions derived by Alsop and Detre (1996). From equations [E7] and [E8] f may be calculated in the cases where $w < \delta$ and $w > \delta$ (Chapter 5, equation [5.6], where T_{1app} and T_{1ns} are called the observed values of T_{1sat} and T_1 respectively).

References

Abragam A; The principles of nuclear magnetism: Clarendon Press (1961)

Alsop DC and Detre JA; Reduced transit-time sensitivity in noninvasive magnetic resonance imaging of human cerebral blood flow; J Cereb Blood Flow Metab 16(6): p1236 - 1249 (1996)

Alsop DC and Detre JA; Multisection cerebral blood flow MR imaging with continuous arterial spin labeling; Radiology 208(2): p410 - 416 (1998)

Atalay MK, Reeder SB, Zerhouni EA, and Forder JR; Blood oxygenation dependence of T1 and T2 in the isolated, perfused rabbit heart at 4.7T; Magn Reson Med 34(4): p623 - 627 (1995)

Bandettini PA and Wong EC; Effects of Biophysical and Physiologic Parameters of Brain Activation-Induced R_2* and R_2 Changes: Simulations Using a Deterministic Model; International Journal of Imaging Systems and Technology 6: p133 - 152 (1995)

Bandettini PA, Wong EC, Jesmanowicz A, Hinks RS, and Hyde JS; Spin-echo and gradient-echo EPI of human brain activation using BOLD contrast: a comparative study at 1.5 T; NMR Biomed 7(1-2): p12 - 20 (1994)

Barbier EL, Silva AC, Kim HJ, Williams DS, and Koretsky AP; Perfusion analysis using dynamic arterial spin labeling (DASL); Magn Reson Med 41(2): p299 - 308 (1999)

Barbier EL, Silva AC, Kim SG, and Koretsky AP; Perfusion imaging using dynamic arterial spin labeling (DASL); Magn Reson Med 45(6): p1021 - 1029 (2001)

Bauer WR, Nadler W, Bock M, Schad LR, Wacker C, Hartlep A, and Ertl G; The relationship between the BOLD-induced T(2) and T(2)(*): a theoretical approach for the vasculature of myocardium; Magn Reson Med 42(6): p1004 - 1010 (1999)

Blicharski JS; Nuclear magnetic resonance relaxation in rotating frame; Acta Physica Polonica A41(2): p223 - 236 (1972)

Bloch F; Nuclear Induction; Physical Review 70(7,8): p460 - 473 (1946)

Bottomley PA, Foster TH, Argersinger RE, and Pfeifer LM; A review of normal tissue hydrogen NMR relaxation times and relaxation mechanisms from 1-100 MHz: dependence on tissue type, NMR frequency, temperature, species, excision, and age; Med Phys 11(4): p425 - 448 (1984)

Busza AL, Allen KL, King MD, van Bruggen N, Williams SR, and Gadian DG; Diffusion-weighted imaging studies of cerebral ischemia in gerbils. Potential relevance to energy failure; Stroke 23(11): p1602 - 1612 (1992)

Buxton RB, Frank LR, Wong EC, Siewert B, Warach S, and Edelman RR; A general kinetic model for quantitative perfusion imaging with arterial spin labeling; Magn Reson Med 40(3): p383 - 396 (1998)

Calamante F, Lythgoe MF, Pell GS, Thomas DL, King MD, Busza AL, Sotak CH, Williams SR, Ordidge RJ, and Gadian DG; Early changes in water diffusion, perfusion, T1 and T2 during focal cerebral ischemia in the rat studied at 8.5 T; Magn Reson Med 41(3): p479 - 485 (1999)

Calamante F, Williams SR, van Bruggen N, Kwong KK, and Turner R; A model for quantification of perfusion in pulsed labelling techniques; NMR Biomed 9(2): p79 - 83 (1996)

Capuro NL, Goldstein RE, Aamodt R, Smith HJ, and Epstein SE; Loss of microspheres from ischemic canine cardiac tissue; An important technical limitation; Circ Res 44: p223 - 227 (1979)

Chalela JA, Alsop DC, Gonzalez-Atavales JB, Maldjian JA, Kasner SE, and Detre JA; Magnetic resonance perfusion imaging in acute ischemic stroke using continuous arterial spin labeling; Stroke 31(3): p680 - 687 (2000)

Chavez-Cartaya RE, Ramirez-Romero P, Calne RY, and Jamieson NV; Laser-Doppler flowmetry in the study of in vivo liver ischemia and reperfusion in the rat; J Surg Res 56(5): p473 - 477 (1994)

Conn HL; Measurement of organ blood flow without blood sampling; J Clin Invest 34: p916 - 917 (1955)

Davis TL, Kwong KK, Weisskoff RM, and Rosen BR; Calibrated functional MRI: mapping the dynamics of oxidative metabolism; Proc Natl Acad Sci USA 95(4): p1834 - 1839 (1998)

Deitch EA; Multiple organ failure. Pathophysiology and potential future therapy; Ann Surg 216(2): p117 - 134 (1992)

Detre JA, Alsop DC, Vives LR, Maccotta L, Teener JW, and Raps EC; Noninvasive MRI evaluation of cerebral blood flow in cerebrovascular disease; Neurology 50(3): p633 - 641 (1998)

Detre JA, Leigh JS, Williams DS, and Koretsky AP; Perfusion imaging; Magn Reson Med 23(1): p37 - 45 (1992)

Detre JA, Samuels OB, Alsop DC, Gonzalez-At JB, Kasner SE, and Raps EC; Noninvasive magnetic resonance imaging evaluation of cerebral blood flow with acetazolamide challenge in patients with cerebrovascular stenosis; J Magn Reson Imaging 10(5): p870 - 875 (1999)

Dijkhuizen RM, Ren J, Mandeville JB, Wu O, Ozdag FM, Moskowitz MA, Rosen BR, and Finklestein SP; Functional magnetic resonance imaging of reorganization in rat brain after stroke; Proc Natl Acad Sci USA 98(22): p12766 - 12771 (2001)

Dixon WT, Du LN, Faul DD, Gado M, and Rossnick S; Projection angiograms of blood labeled by adiabatic fast passage; Magn Reson Med 3(3): p454 - 462 (1986)

Donahue KM, Van Kylen J, Guven S, El Bershawi A, Luh WM, Bandettini PA, Cox RW, Hyde JS, and Kissebah AH; Simultaneous gradient-echo/spin-echo EPI of graded ischemia in human skeletal muscle; J Magn Reson Imaging 8(5): p1106 - 1113 (1998)

Drayer BP, Wolfson SK, Reinmuth OM, Dujovny M, Boehnke M, and Cook EE; Xenon enhanced CT for analysis of cerebral integrity, perfusion, and blood flow; Stroke 9(2): p123 - 130 (1978)

Edelman RR, Siewert B, Darby DG, Thangaraj V, Nobre AC, Mesulam MM, and Warach S; Qualitative mapping of cerebral blood flow and functional localization with echo-planar MR imaging and signal targeting with alternating radio frequency; Radiology 192(2): p513 - 520 (1994)

Edelstein WA, Bottomley PA, Hart HR, and Smith LS; Signal, noise, and contrast in nuclear magnetic resonance (NMR) imaging; J Comput Assist Tomogr 7(3): p391 - 401 (1983)

Edelstein WA, Hutchison JM, Johnson G, and Redpath T; Spin warp NMR imaging and applications to human whole-body imaging; Phys Med Biol 25(4): p751 - 756 (1980)

El Desoky AE, Delpy DT, Davidson BR, and Seifalian AM; Assessment of hepatic ischaemia reperfusion injury by measuring intracellular tissue oxygenation using near infrared spectroscopy; Liver 21(1): p37 - 44 (2001)

Eng J, Ceckler TL, and Balaban RS; Quantitative 1H magnetization transfer imaging in vivo; Magn Reson Med 17(2): p304 - 314 (1991)

Fazio F, Fieschi C, Nardini M, Collice M, and Possa M; Assessment of regional cerebral blood flow by continuous infusion of krypton-81m and emission computed tomography: Acta Neurologica Scandanavia 60 Suppl: p192 (1979)

Ferris EB; Objective measurement of relative intracranial blood flow in man with observations concerning the hydrodynamics of the craniovascular system; Arch Neurol and Psychiatry 46: p377 - 401 (1941)

Fick A; Ueber die Messung des Blutquantums in den Herzventrikeln; Sitz ber Physik-Med Ges Wurzburg 2: p16 - 28 (1870)

Frackowiak RS, Lenzi GL, Jones T, and Heather JD; Quantitative measurement of regional cerebral blood flow and oxygen metabolism in man using 15O and positron emission tomography: theory, procedure, and normal values; J Comput Assist Tomogr 4(6): p727 - 736 (1980)

Francis ST, Gowland PA, and Bowtell RW; Continuous saturation EPI with diffusion weighting at 3.0 T; NMR Biomed 12(7): p440 - 450 (1999)

Franke C, van Dorsten FA, Olah L, Schwindt W, and Hoehn M; Arterial spin tagging perfusion imaging of rat brain: dependency on magnetic field strength; Magn Reson Imaging 18(9): p1109 - 1113 (2000)

Gach HM, Kam AW, Reid ED, and Talagala SL; Quantitative analysis of adiabatic fast passage for steady laminar and turbulent flows; Magn Reson Med 47(4): p709 - 719 (2002)

Garwood M and Ugurbil K; B1 insensitive adiabatic RF pulses, in: In-vivo magnetic resonance spectroscopy 1: Probeheads and radiofrequency pulses, spectrum analysis; ed. Diehl P, Fluck E, Kosfeld R, and Seelig J: Springer Verlag (1992)

Gonzalez-At JB, Alsop DC, and Detre JA; Cerebral perfusion and arterial transit time changes during task activation determined with continuous arterial spin labeling; Magn Reson Med 43(5): p739 - 746 (2000)

Grace ND and Powell LW; Iron storage disorders of the liver; Gastroenterology 67(6): p1257 - 1283 (1974)

Grace PA; Ischaemia-reperfusion injury; Br J Surg 81(5): p637 - 647 (1994)

Graham SJ and Henkelman RM; Understanding pulsed magnetization transfer; J Magn Reson Imaging 7(5): p903 - 912 (1997)

Grüne M, van Dorsten FA, Schwindt W, Olah L, and Hoehn M; Quantitative T*(2) and T'(2) maps during reversible focal cerebral ischemia in rats: separation of blood oxygenation from nonsusceptibility-based contributions; Magn Reson Med 42(6): p1027 - 1032 (1999)

Gurll N J; Ischemia of the liver and pancreas, in: Splanchnic ischemia and multiple organ failure; ed. Marston A, Bulkley GB, Fiddian-Green RG, and Haglund UH: Edward Arnold (1989)

Haase A, Frahm J, Matthaei D, and Merboldt KD; FLASH imaging:Rapid NMR imaging using low flip-angle pulses; Journal of Magnetic Resonance 67: p258 - 266 (1986)

Harper HA; The blood, lymph and cerebrospinal fluid, in: Review of physiological chemistry; ed. Harper HA: Blackwell Scientific Publications (1971)

Harris NG, Lythgoe MF, Thomas DL, and Williams SR; Cerebrovascular reactivity following focal brain ischemia in the rat: a functional magnetic resonance imaging study; Neuroimage 13(2): p339 - 350 (2001)

Helliar RW; Development of a novel model for stroke using magnetic resonance imaging (MRI); MSc Thesis, University of London (2001)

Helpern JA, Branch CA, Yongbi MN, and Huang NC; Perfusion imaging by un-inverted flow-sensitive alternating inversion recovery (UNFAIR); Magn Reson Imaging 15(2): p135 - 139 (1997)

Henkelman RM, Huang X, Xiang QS, Stanisz GJ, Swanson SD, and Bronskill MJ; Quantitative interpretation of magnetization transfer; Magn Reson Med 29(6): p759 - 766 (1993)

Hillman EM, Hebden JC, Schweiger M, Dehghani H, Schmidt FE, Delpy DT, and Arridge SR; Time resolved optical tomography of the human forearm; Phys Med Biol 46(4): p1117 - 1130 (2001)

Hoge RD, Atkinson J, Gill B, Crelier GR, Marrett S, and Pike GB; Linear coupling between cerebral blood flow and oxygen consumption in activated human cortex; Proc Natl Acad Sci USA 96(16): p9403 - 9408 (1999)

Holdsworth DW, Norley CJ, Frayne R, Steinman DA, and Rutt BK; Characterization of common carotid artery blood-flow waveforms in normal human subjects; Physiol Meas 20(3): p219 - 240 (1999)

Holloway V, Gadian DG, Vargha-Khadem F, Porter DA, Boyd SG, and Connelly A; The reorganization of sensorimotor function in children after hemispherectomy. A functional MRI and somatosensory evoked potential study; Brain 123(12): p2432 - 2444 (2000)

Hoppel BE, Weisskoff RM, Thulborn KR, Moore JB, Kwong KK, and Rosen BR; Measurement of regional blood oxygenation and cerebral hemodynamics; Magn Reson Med 30(6): p715 - 723 (1993)

Horie Y, Wolf R, Anderson DC, and Granger DN; Hepatic leukostasis and hypoxic stress in adhesion molecule-deficient mice after gut ischemia/reperfusion; J Clin Invest 99(4): p781 - 788 (1997)

Horie Y, Wolf R, Miyasaka M, Anderson DC, and Granger DN; Leukocyte adhesion and hepatic microvascular responses to intestinal ischemia/reperfusion in rats; Gastroenterology 111(3): p666 - 673 (1996)

Horn EP, Standl T, Wilhelm S, Jacobs EE, Freitag U, Freitag M, and Schulte am EJ; Bovine hemoglobin increases skeletal muscle oxygenation during 95% artificial arterial stenosis; Surgery 121(4): p411 - 418 (1997)

Ingvar DH and Lassen NA; Quantitative determination of regional cerebral blood flow in man; The Lancet: p806 - 807 (1961)

Kam AW and Talagala SL; Decreasing the residual magnetization transfer effects in SPDI-CASL perfusion MRI by pulsed magnetization transfer; Proceedings of the 8th meeting of the ISMRM: p709 (2000)

Kamiike W, Nakahara M, Nakao K, Koseki M, Nishida T, Kawashima Y, Watanabe F, and Tagawa K; Correlation between cellular ATP level and bile excretion in the rat liver; Transplantation 39(1): p50 - 55 (1985)

Kennan RP, Zhong J, and Gore JC; Intravascular susceptibility contrast mechanisms in tissues; Magn Reson Med 31(1): p9 - 21 (1994)

Kety S and Schmidt CJ; The determination of cerebral blood flow in man by the use of nitrous oxide in low concentrations; American Journal of Physiology 143: p53 - 66 (1945)

Kim SG; Quantification of relative cerebral blood flow change by flow-sensitive alternating inversion recovery (FAIR) technique: application to functional mapping; Magn Reson Med 34(3): p293 - 301 (1995)

Kiselev VG and Posse S; Analytical model of susceptibility-induced MR signal dephasing: effect of diffusion in a microvascular network; Magn Reson Med 41(3): p499 - 509 (1999)

Klar E, Kraus T, Bleyl J, Newman WH, Bowman HF, Hofmann WJ, Kummer R, Bredt M, and Herfarth C; Thermodiffusion for continuous quantification of hepatic microcirculation - validation and potential in liver transplantation; Microvasc Res 58(2): p156 - 166 (1999)

Kumar A, Welti D, and Ernst RR; NMR Fourier Zeugmatography; Journal of Magnetic Resonance 18: p69 (1975)

Kuo PC, Li K, Alfrey EJ, Jeffrey RB, Garcia G, and Dafoe DC; Magnetic resonance imaging and hepatic hemodynamics: correlation with metabolic function in liver transplantation candidates; Surgery 117(4): p373 - 379 (1995)

Kwong KK, Chesler DA, Weisskoff RM, Donahue KM, Davis TL, Østergaard L, Campbell TA, and Rosen BR; MR perfusion studies with T1-weighted echo planar imaging; Magn Reson Med 34(6): p878 - 887 (1995)

Landau WH, Freygang WH Jnr, Roland LP, Sokoloff L, and Kety S; The local circulation of the living brain: Values in the unanaesthetised and anaesthetised cat; Trans Am Neurol Assoc 80: p125 - 129 (1955)

Lauterbur P; Image formation by induced local interactions: examples employing nuclear magnetic resonance; Nature 242: p190 - 191 (1973)

Lee HK, Nalcioglu O, and Moran PR; Spatially resolved flow velocity measurements and projection angiography by adiabatic passage; Magn Reson Imaging 9(1): p115 - 127 (1991)

Lewis WD, Finn JP, Jenkins RL, Carretta M, Longmaid HE, and Edelman RR; Use of magnetic resonance angiography in the pretransplant evaluation of portal vein pathology; Transplantation 56(1): p64 - 68 (1993)

Ljunggren S; A simple graphical representation of Fourier-based imaging methods; Journal of Magnetic Resonance 54: p338 - 343 (1983)

Lythgoe MF, Thomas DL, Calamante F, Pell GS, King MD, Busza AL, Sotak CH, Williams SR, Ordidge RJ, and Gadian DG; Acute changes in MRI diffusion, perfusion, T(1), and T(2) in a rat model of oligemia produced by partial occlusion of the middle cerebral artery; Magn Reson Med 44(5): p706 - 712 (2000)

Maccotta L, Detre JA, and Alsop DC; The efficiency of adiabatic inversion for perfusion imaging by arterial spin labeling; NMR Biomed 10(4-5): p216 - 221 (1997)

Macdonald PH and Beck IT; Ischemic disease of the intestine, in: First principles of gastroenterolgy; ed. Macdonald PH and Beck IT: AstraZeneca Canada Inc. (2000)

Majid DS, Godfrey M, and Omoro SA; Pressure natriuresis and autoregulation of inner medullary blood flow in canine kidney; Hypertension 29(1 Pt 2): p210 - 215 (1997)

Mallett BL and Veall N; Investigation of cerebral blood-flow in hypertension, using radioactive-xenon inhalation and extracranial recording; Lancet: p1081 - 1082 (1963)

Mansfield P; Multi-Planar image formation using NMR spin echoes; J Phys C:Solid State 10(3): pL55 - L58 (1977)

Marro KI, Hayes CE, and Kushmerick MJ; A model of the inversion process in an arterial inversion experiment; NMR Biomed 10(7): p324 - 332 (1997)

Martin DW Jr; Structure and function of a protein-hemoglobin, in: Harper's review of biochemistry; ed. Martin DW Jr, Martin DW, Mayes PA, Rodwell VW: Lange Medical (1985)

Materne R, Smith AM, Peeters F, Dehoux JP, Keyeux A, Horsmans Y, and Van Beers BE; Assessment of hepatic perfusion parameters with dynamic MRI; Magn Reson Med 47(1): p135 - 142 (2002)

McLaughlin AC, Ye FQ, Pekar JJ, Santha AK, and Frank JA; Effect of magnetization transfer on the measurement of cerebral blood flow using steady-state arterial spin tagging approaches: a theoretical investigation; Magn Reson Med 37(4): p501 - 510 (1997)

Meiboom S and Gill D; Modified spin echo method for measuring nuclear relaxation times; Rev Sci Instrum 29: p688 - 691 (1958)

Noseworthy MD, Janzen EG, Towner RA, and Yamashiro S; In vivo study of halothane hepatotoxicity in the rat using magnetic resonance imaging and 31P spectroscopy; J Biochem Biophys Methods 34(2): p107 - 122 (1997)

Ogawa S, Menon RS, Tank DW, Kim SG, Merkle H, Ellermann JM, and Ugurbil K; Functional brain mapping by blood oxygenation level-dependent contrast magnetic resonance imaging. A comparison of signal characteristics with a biophysical model; Biophys J 64(3): p803 - 812 (1993)

Ohta S, Meyer E, Thompson CJ, and Gjedde A; Oxygen consumption of the living human brain measured after a single inhalation of positron emitting oxygen; J Cereb Blood Flow Metab 12(2): p179 - 192 (1992)

Ono Y, Morikawa S, Inubushi T, Shimizu H, and Yoshimoto T; T2*-weighted magnetic resonance imaging of cerebrovascular reactivity in rat reversible focal cerebral ischemia; Brain Res 744(2): p207 - 215 (1997)

Ordidge RJ, Wylezinska M, Hugg JW, Butterworth E, and Franconi F; Frequency offset corrected inversion (FOCI) pulses for use in localized spectroscopy; Magn Reson Med 36(4): p562 - 566 (1996)

Østergaard L, Sorensen AG, Chesler DA, Weisskoff RM, Koroshetz WJ, Wu O, Gyldensted C, and Rosen BR; Combined diffusion-weighted and perfusion-weighted flow heterogeneity magnetic resonance imaging in acute stroke; Stroke 31(5): p1097 - 1103 (2000)

Parkes LM and Tofts PS; Modelling of arterial spin labelled perfusion data with varying delay time, including permeability effects; Proceedings of the 9th meeting of the ISMRM: p100 (2001)

Pastores SM, Katz DP, and Kvetan V; Splanchnic ischemia and gut mucosal injury in sepsis and the multiple organ dysfunction syndrome; Am J Gastroenterol 91(9): p1697 - 1710 (1996)

Pauli W; Naturwissenschaften 12: p741 (1924)

Pekar J, Jezzard P, Roberts DA, Leigh JS, Jr., Frank JA, and McLaughlin AC; Perfusion imaging with compensation for asymmetric magnetization transfer effects; Magn Reson Med 35(1): p70 - 79 (1996)

Poggetti RS, Moore FA, Moore EE, Koeike K, and Banerjee A; Simultaneous liver and lung injury following gut ischemia is mediated by xanthine oxidase; J Trauma 32(6): p723 - 727 (1992)

Prasad PV, Edelman RR, and Epstein FH; Noninvasive evaluation of intrarenal oxygenation with BOLD MRI; Circulation 94(12): p3271 - 3275 (1996)

Punwani S, Ordidge RJ, Cooper CE, Amess P, and Clemence M; MRI measurements of cerebral deoxyhaemoglobin concentration [dHb] - correlation with near infrared spectroscopy (NIRS); NMR Biomed 11(6): p281 - 289 (1998)

Rein H; Ueber Besonderheiten der Blutzirkulation in der Arteria carotis; Z Biologie 89: p309 - 318 (1929)

Roberts DA, Bolinger L, Detre JA, Insko EK, Bergey P, and Leigh JS Jr.; Continuous inversion angiography; Magn Reson Med 29(5): p631 - 636 (1993)

Roberts DA, Detre JA, Bolinger L, Insko EK, and Leigh JS Jr.; Quantitative magnetic resonance imaging of human brain perfusion at 1.5 T using steady-state inversion of arterial water; Proc Natl Acad Sci USA 91(1): p33 - 37 (1994)

Rudolph AM and Heyman MA; The circulation of the fetus in utero; Circulation Research 21: p163 (1967)

Schmidt CF and Pierson JC; The intrinsic regulation of the blood vessels of the medulla oblongata; Am J Physiol 108: p241 - 263 (1934)

Silva AC and Kim SG; Pseudo-continuous arterial spin labeling technique for measuring CBF dynamics with high temporal resolution; Magn Reson Med 42(3): p425 - 429 (1999)

Talagala SL, Barbier EL, Kam AW, and Koretsky AP; A method to extend the spatial coverage of SPDI-CASL perfusion MRI; Proceedings of the 9th meeting of the ISMRM: p1563 (2001)

Talagala SL, Barbier EL, Williams DS, Silva AC, and Koretsky AP; Multi-slice perfusion MRI using continuous arterial water labeling: Controlling for MT effects with simultaneous proximal and distal RF; Proceedings of the 6th meeting of the ISMRM: p381 (1998)

Thomas DL; Magnetic Resonance Imaging of Diffusion and Perfusion: Techniques and Applications to Cerebral Ischaemia; PhD Thesis, University of London (1999)

Thomas DL, Lythgoe MF, Calamante F, Gadian DG, and Ordidge RJ; Simultaneous noninvasive measurement of CBF and CBV using double-echo FAIR (DEFAIR); Magn Reson Med 45(5): p853 - 863 (2001)

Thome C, Vajkoczy P, Horn P, Bauhuf C, Hubner U, and Schmiedek P; Continuous monitoring of regional cerebral blood flow during temporary arterial occlusion in aneurysm surgery; J Neurosurg 95(3): p402 - 411 (2001)

Thompson JS; The intestinal response to critical illness; Am J Gastroenterol 90(2): p190 - 200 (1995)

Turnage RH, Kadesky KM, Myers SI, Guice KS, and Oldham KT; Hepatic hypoperfusion after intestinal reperfusion; Surgery 119(2): p151 - 160 (1996)

Twieg DB; Acquisition and accuracy in rapid NMR imaging methods; Magn Reson Med 2(5): p437 - 452 (1985)

Uematsu H, Yamada H, Sadato N, Muramoto S, Inoue H, Hayashi K, Yonekura Y, Kimura H, Sakuma H, Matsuda T, Hayashi N, Yamamoto K, and Ishii Y; Assessment of hepatic portal perfusion using T2 measurements of Gd-DTPA; J Magn Reson Imaging 8(3): p650 - 654 (1998)

van Dorsten FA, Olah L, Schwindt W, Grüne M, Uhlenkuken U, Pillekamp F, Hossmann KA, and Hoehn M; Dynamic changes of ADC, perfusion, and NMR relaxation parameters in transient focal ischemia of rat brain; Magn Reson Med 47(1): p97 - 104 (2002)

Vejchapipat P, Williams SR, Proctor E, Lauro V, Spitz L, and Pierro A; Moderate hypothermia ameliorates liver energy failure after intestinal ischaemia-reperfusion in anaesthetised rats; J Pediatr Surg 36(2): p269 - 275 (2001a)

Vejchapipat P, Williams SR, Proctor E, Spitz L, and Pierro A; The effects of moderate hypothermia on intestinal ischaemia-reperfusion: High resolution ^{1}H and ^{31}P magnetic resonance spectroscopy study; Proceedings of the 9th meeting of the ISMRM: p1055 (2001b)

Villringer A, Rosen BR, Belliveau JW, Ackerman JL, Lauffer RB, Buxton RB, Chao YS, Wedeen VJ, and Brady TJ; Dynamic imaging with lanthanide chelates in normal brain: contrast due to magnetic susceptibility effects; Magn Reson Med 6(2): p164 - 174 (1988)

Vollmar B, Glasz J, Leiderer R, Post S, and Menger MD; Hepatic microcirculatory perfusion failure is a determinant of liver dysfunction in warm ischemia-reperfusion; Am J Pathol 145(6): p1421 - 1431 (1994)

Walsh EG, Minematsu K, Leppo J, and Moore SC; Radioactive microsphere validation of a volume localized continuous saturation perfusion measurement; Magn Reson Med 31(2): p147 - 153 (1994)

Williams DS, Detre JA, Leigh JS, and Koretsky AP; Magnetic resonance imaging of perfusion using spin inversion of arterial water; Proc Natl Acad Sci USA 89(1): p212 - 216 (1992)

Williams DS, Qing Y, Koretsky AP, and Ho C; Multislice perfusion MRI using arterial spin labeling: Controlling for MTC effects in adiabatic fast passage inversion using proximal slab selective saturation pulses; Proceedings of the 9th meeting of the ISMRM: p1558 (2001)

Williams SB, Williams SR, Spitz L, and Pierro A; Hepatic Blood Flow and Portal and Systemic Blood gases during intestinal ischaemia-reperfusion; British Association of Parenteral and Enteral Nutrition (BAPEN) (2001)

Willis T; Dr Willis's Practice of Physick: T Dring, C Harper and J Leigh (1684)

Wolf RL, Alsop DC, Levy-Reis I, Meyer PT, Maldjian JA, Gonzalez-Atavales J, French JA, Alavi A, and Detre JA; Detection of mesial temporal lobe hypoperfusion in patients with temporal lobe epilepsy by use of arterial spin labeled perfusion MR imaging; AJNR Am J Neuroradiol 22(7): p1334 - 1341 (2001)

Wong EC, Buxton RB, and Frank LR; Implementation of quantitative perfusion imaging techniques for functional brain mapping using pulsed arterial spin labeling; NMR Biomed 10(4-5): p237 - 249 (1997)

Wong EC, Buxton RB, and Frank LR; A theoretical and experimental comparison of continuous and pulsed arterial spin labeling techniques for quantitative perfusion imaging; Magn Reson Med 40(3): p348 - 355 (1998a)

Wong EC, Buxton RB, and Frank LR; Quantitative imaging of perfusion using a single subtraction (QUIPSS and QUIPSS II); Magn Reson Med 39(5): p702 - 708 (1998b)

Ye FQ, Mattay VS, Jezzard P, Frank JA, Weinberger DR, and McLaughlin AC; Correction for vascular artifacts in cerebral blood flow values measured by using arterial spin tagging techniques; Magn Reson Med 37(2): p226 - 235 (1997)

Ye FQ, Yang Y, Duyn J, Mattay VS, Frank JA, Weinberger DR, and McLaughlin AC; Quantitation of regional cerebral blood flow increases during motor activation: A multislice, steady-state, arterial spin tagging study; Magn Reson Med 42(2): p404 - 407 (1999)

Yongbi MN, Yang Y, Frank JA, and Duyn JH; Multislice perfusion imaging in human brain using the C-FOCI inversion pulse: comparison with hyperbolic secant; Magn Reson Med 42(6): p1098 - 1105 (1999)

Zaharchuk G, Ledden PJ, Kwong KK, Reese TG, Rosen BR, and Wald LL; Multislice perfusion and perfusion territory imaging in humans with separate label and image coils; Magn Reson Med 41(6): p1093 - 1098 (1999b)

Zaharchuk G, Mandeville JB, Bogdanov AA Jr., Weissleder R, Rosen BR, and Marota JJ; Cerebrovascular dynamics of autoregulation and hypoperfusion. An MRI study of CBF and changes in total and microvascular cerebral blood volume during hemorrhagic hypotension; Stroke 30(10): p2197 - 2204 (1999a)

Zhang W, Silva AC, Williams DS, and Koretsky AP; NMR measurement of perfusion using arterial spin labeling without saturation of macromolecular spins; Magn Reson Med 33(3): p370 - 376 (1995)

Zhang W, Williams DS, Detre JA, and Koretsky AP; Measurement of brain perfusion by volume-localized NMR spectroscopy using inversion of arterial water spins: accounting for transit time and cross-relaxation; Magn Reson Med 25(2): p362 - 371 (1992)

Zhang W, Williams DS, and Koretsky AP; Measurement of rat brain perfusion by NMR using spin labeling of arterial water: in vivo determination of the degree of spin labeling; Magn Reson Med 29(3): p416 - 421 (1993)

Zhou J, Mori S, and van Zijl PC; FAIR excluding radiation damping (FAIRER); Magn Reson Med 40(5): p712 - 719 (1998)